Master Thesis, Department of Geosciences

L-band differential interferometric SAR in difficult conditions

Kristine H. H. Ekseth

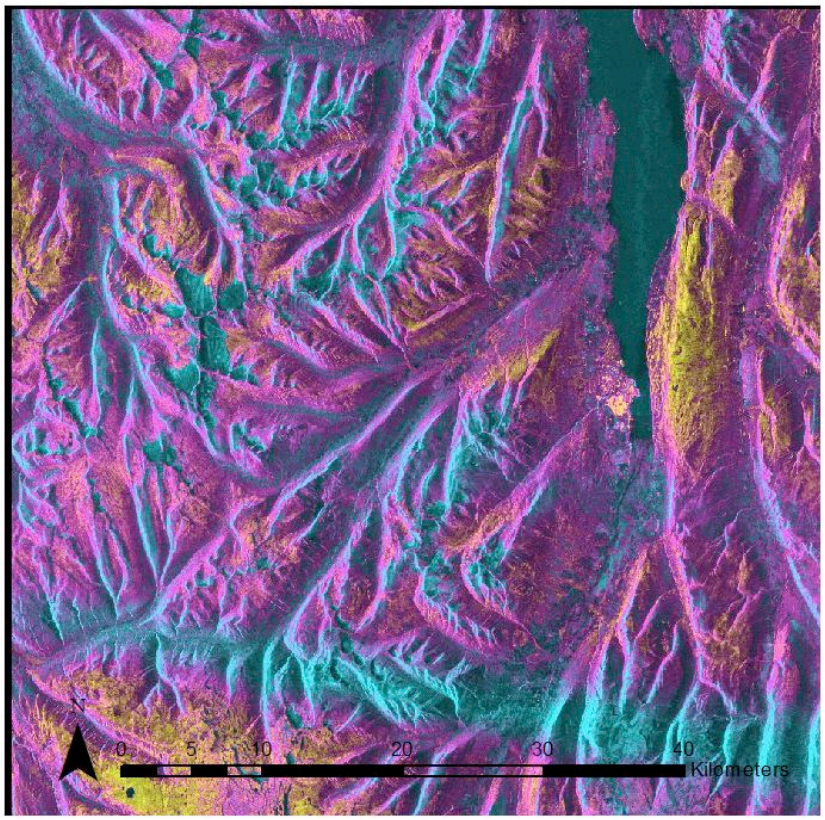

UNIVERSITY OF OSLO
FACULTY OF MATHEMATICS AND NATURAL SCIENCES

L-band differential interferometric SAR in difficult conditions

Kristine H. H. Ekseth

Master thesis in Geoscience, Geomatics discipline, Institute of Geoscience, Faculty of Mathematics and Natural Sciences

UNIVERSITETET I OSLO

01.12.2012

L-band differential interferometric SAR in difficult conditions

Front page image: Coherence image from ALOS PALSAR scenes 16.08.2007-01.10.2007.

2012

L-band differential interferometric SAR in difficult conditions

Kristine H. H. Ekseth

http://www.duo.uio.no

Trykk: Reprosentralen, Universitetet i Oslo

Abstract

In this study, the potential of L-band differential interferometric synthetic aperture radar (DInSAR) to detect slope instabilities under difficult topographic and climatic conditions is evaluated. In which areas and under which conditions does L-band interferometry still produce useful results? The results are dependent on the temporal, geometric and processing decorrelation between the used SAR scenes. The goal is to extract mass movements and displacements on a millimetre to centimetre scale per year. This is to test the limits of the method, and to quantify any problems with the method in difficult areas. Tröllaskagi, north Iceland, Austurland, east Iceland and Tafjord, west Norway is chosen as study sites.

The Icelandic and Norwegian study sites have difficult topographic and climatic conditions, and the factors impacting interferometric products the most are directly related to the geometrical properties of the SAR systems combined with the difficult topography, where particularly layover and shadow have a large effect/impact on the end results. DEM errors and the difficulty of removing the topographic phase component in the SAR signal also contribute to erroneous results.

The main error source for the data used in this thesis is the DEMs. In image pairs with a large baseline, the DEM does not entirely remove the topographic phase, and residual phase is found across the differential interferograms. In image pairs with a small baseline, displacement and mass movement is detected in some areas in the differential interferograms, but the image geometry and temporal decorrelation (including atmospheric decorrelation) add to the uncertainty of the detected displacement. Displacements of up to 11.8 cm is detected in radar line-of-sight, and up to 8.5 cm in steepest direction of slope (assuming 34° look angle).

L-band DInSAR can be a useful tool for displacement measuring and surveillance in difficult conditions if a high quality DEM is available and the baseline is of an optimal length, particularly in hard to reach areas or in combination with other methods of surveillance.

Acknowledgements

The European Space Agency (ESA), allowing access to ALOS PALSAR data under AOALO.3579, made this work possible.

The author would like to thank professor Andi Kääb, UiO, for his supervision and the freedom he has given me with regard to the thesis work. Thanks also go to the International Centre for Geohazards, NGI, for the contribution to the printing of this thesis.

A big thank you goes out to study room 219 – thank you for the endless cups of coffee and all the helpful discussions on relevant and irrelevant topics.

Last, but not least: thank you, Torstein, for all your patience with me the last 12 months.

Table of Contents

List of Figures

1 Introduction and research question

1.1 Introduction

Unstable slopes and mountainsides are well-known problems in both Iceland and Norway. These are a threat to both infrastructure and buildings, and can, in some cases, be a threat to entire communities. In Norway, Åknesfjellet in Møre og Romsdal and Nordnesfjellet in Troms are the best known unstable mountainsides, where enormous blocks could plunge into the fjords and create tsunamis/flood waves of several tens of meters in height. Similar rockslides are not found in Iceland, but slow moving mass movements and landslides are found in several places on the island, for example at Almenningsnöf, Tröllaskagi and above Seyðisfjörður, Austurland. An effective surveillance method for large areas, particularly in areas where access to the instabilities is difficult, is differential interferometric synthetic aperture radar (DInSAR).

DInSAR is an effective method to measure displacements, where points with a high spatial distribution provide a dense network for accurate measurements (Massonet and Feigl 1998). Based on SAR scenes acquired from remote sensing, the high return periods mean that large areas can be monitored efficiently. Many have used DInSAR to monitor land subsidence or landslides (Strozzi et al. 2005; Cascini et al. 2010), or to measure displacement over large areas after earthquakes (Atzori et al. 2009; Chini et al. 2009; Hernandez et al. 1997) and some have measured displacement in permafrost areas (Lilleøren and Etzelmüller 2011; Strozzi et al. 2010; Kenyi and Kaufmann 2003; Strozzi et al. 2004). Some have looked at interferometry in areas with difficult meteorological conditions (Sandwell et al. 2008; Weydahl 2001). However, the performance of L-band DInSAR in difficult conditions, both topographic and meteorological, has not been explored to a larger extent, and this thesis will try to amend this.

The factors impacting interferometric products the most are directly related to the geometrical properties of the SAR systems combined with the difficult topography, where particularly layover and shadow have a large effect/impact on the end results. DEM errors and the difficulty of removing the topographic phase component in the SAR signal is also contribute to erroneous results. Atmospherical conditions also have an

effect, more so in L-band scenes than in C- and X-band (Sandwell et al. 2008). Ionospherical disturbances as well as tropospherical disturbances due to water vapour, clouds or height dependent atmosphere can produce distortions and erroneous displacement features in differential interferograms (Massonet and Feigl 1998; *Gamma* manual 2008), but the surface properties of the areas of interest also have an effect. Vegetation, heavy rains and swelling of the ground or dry patches, snow cover and geological effects have an effect on the results (Weydahl 2001). These factors have to be considered both during processing of the data and when interpreting the results.

The results will be used to evaluate the potential and precision of DInSAR for monitoring and detecting mass movements and displacements in these types of areas, where conventional methods are difficult to use.

1.2 Goal of thesis

The goal of this thesis is to perform differential interferometric SAR analysis on scenes acquired by the ALOS PALSAR satellite sensor in areas with difficult conditions to extract mass movements and displacements on a millimetre to centimetre scale per year. This is to test the limits of the method, and to quantify any problems with the method in these difficult areas. Difficult areas are defined as areas with coarse topography, where steep mountainsides and deep valleys create problems with layover, shadow and height-dependent atmosphere, with large areas covered by vegetation such as trees, bushes and grass and where the climate is wet.

Sub-goals that are explained and expanded on in this thesis are:

- Analysis and processing of DInSAR datasets from Northern and Eastern Iceland and Western Norway with the associated methods, and gathering of information.
- Analysis of the results from Iceland and Norway.
- The information that can be extracted from these results, and what relevance it has to geoscientific applications.
- How comparable the information from DInSAR is to information from more traditional methods of surveillance and measure in areas with mass movements/landslides/displacements.

Five different datasets have been processed and analysed in the commercial program package *Gamma* Remote Sensing in order to try to explain and expand on the above. The first two datasets cover the Tröllaskagi peninsula in northern Iceland; two datasets cover Austurland in north-eastern Iceland and one dataset covers the Tafjord area in western Norway. All areas have a climate and topography corresponding to "difficult" for radar remote sensing, with little urban development and coarse topography, and differential interferometric analyses are expected to be difficult (Strozzi 2005).

1.3 Structure of thesis

This thesis has eight chapters, including references, and two appendixes A and B. Chapter two presents the theory behind SAR and differential interferometry. In chapter three the study areas and datasets are presented and described, while chapter four describes the data processing method for differential interferometry, and chapter five contains the results from this processing. Discussion of the results is found in chapter six, while a conclusion is tentatively reached in chapter seven. All the references used in the thesis are found in chapter eight. Appendix A contains all the differential interferograms processed in the thesis with corresponding coherence images and histograms showing the coherence distribution. Appendix B contains tables with the meteorological data for August, September and October in eastern Iceland in the years 2007, 2009 and 2010, and meteorological data for August, September and October in northern Iceland in the years 2007, 2008 and 2010.

2 Theory

2.1 InSAR (Interferometric Synthetic Aperture Radar)

2.1.1 Principles and operation

In the late 1970s, the first radar remote sensing satellites were sent into space, both for planetary surface investigations as well as Earth observation. The SEASAT satellite, a NASA satellite, was the first Earth observation radar satellite (Bamler and Hartl 1998; Massonnet and Feigl 1998; Gens and van Genderen 1996). Early use of the radar technology first considered the ground echo images as noise, since this was at first a ranging and detecting tool, mostly used for distance measures. However, the usefulness of the radar images became apparent when the intensity images were acquired. Synthetic aperture radar is an active imaging sensor system, usually monostatic and mounted on a satellite, a spacecraft or an airplane. In the next section, the principles of space- and airborne synthetic aperture radars will be discussed.

Interferometric Synthetic Aperture Radar (InSAR) exploits phase differences between two (or more) complex-valued images acquired from different orbits and/or at different times (Bamler and Hartl 1998). However, the complexity of the images as well as the method of acquiring necessitates a considerable amount of image and signal processing to get adequate results. A lot has been published on the subject, and several different algorithms are available, both for processing the images and analysis made on the images. A short introduction to the principles of SAR is given here. More thorough discussions are found in Curlander and McDonough (1991), Franceschetti and Lanari (1999), and Bürgmann et al. (2000).

A SAR image is acquired in a side-looking fashion, either from space or air. The sensor, perpendicular to the azimuth direction, moves along an assumed straight path, at an altitude H, above a reference surface (here, the Earth's surface). Microwave signals are transmitted to the surface, in the antenna's illumination footprint, and these pulses are scattered back to the SAR receiver, where the receiver registers both phase and amplitude from the signal, as well as the signal's travel time. Distance to the target is calculated from the travel time. The pulses are registered as a stream of Doppler echoes

which are separated into individual echoes, each corresponding to a transmitted pulse. Most modern radar satellites use *chirps*, compressed signals in the frequency domain. The echoes are separated in range (cross-track) dimension, and the Doppler history is used to separate surface pixels in the azimuth (along-track) dimension. See figure 2.1. The images can be recorded from strip mode, spot mode or scan mode satellite sensor, but here strip mode satellite sensors are discussed, all the while they are the common sensor type at present. This technique is similar to optical sensors acquiring images by the push broom-technique (Elachi and van Zyl 2006).

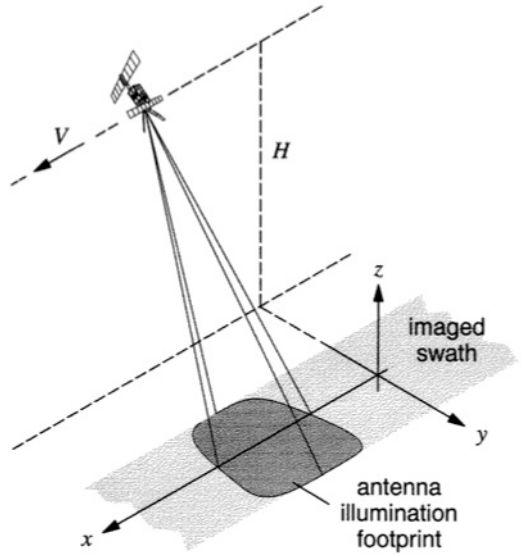

Figure 2.1:Geometry of a side-looking SAR system. From Bamler and Hartl (1998).

The synthetic aperture method improves the resolution by focusing the image. An array of antennas is equivalent to one single antenna, moving along the array line, as long as the received signals are coherently recorded and then added in the same way as the array of antennas would have been combined. As the sensor moves in space, it records the successive echoes along the flight line at points x_1, x_2, …, x_i. An onboard stable oscillator is used as a reference, the echoes recorded coherently with phase and amplitude as a function of time. A processor synthesizes these echoes into a linear array. For a continuous antenna, the distribution of the signals takes a $\sin \alpha / \alpha$ pattern whenever there is uniform rectangular distribution (Elachi and van Zyl 2006). The signals then have to be reconstructed and sorted according to which pixel and geographical location they belong to. This is the focusing, creating a synthetic aperture equivalent to 40 km (for ALOS PALSAR) on an imaginary antenna.

In traditional radar systems, also known as RAR systems (Real Aperture Radar), spatial resolution is governed by the physical length of the antenna and the distance to target. However, in space, the satellite has a distance of 800-1000 km to the target, and the antennas used for RAR would not be adequate. To acquire the necessary resolution, the antenna length is synthesized as described over. There are two general types of radar systems, continuous wave and pulsed wave (Elachi and van Zyl 2006). Pulsed wave systems radiate pulses. The pulse repetition frequency (PRF) is the number of pulses radiated per second from the radar. The bandwidth of a pulse is defined as (Elachi and van Zyl 2006:229):

$$B = \frac{1}{\tau} \tag{2.1}$$

Where B is the bandwidth, and τ is the length of the pulse. The length of the pulse defines the bandwidth size, either as wide or narrow. The range resolution, given by (Elachi and van Zyl 2006:229)

$$\Delta r = \frac{c\tau}{2} = \frac{c}{2B} \tag{2.2}$$

where c is the speed of light, Δr is the shortest separation between targets that the sensor can measure and the factor of 2 accounts for the round trip propagation from the sensor to the target. From the equations, it is clear that the achievable resolutions are related to the signal bandwidth. The energy in a signal is given by (Elachi and van Zyl 2006:229):

$$E = P\tau \tag{2.3}$$

where P is the instantaneous peak power. The longer the bandwidth, the higher the energy and the better the target detection is. However, this presents a problem, namely if a high detection ability is needed as well as high resolution. If these abilities are to be combined, a modulated signal is needed.

Pulse modulation is a way to achieve a long pulse with high energy, bypassing the incompatibility found in equations 2.2 and 2.3, providing high resolution with a good signal-to-noise ratio (SNR) (Curlander and McDonough 1991). This modulation is usually achieved by either linear frequency modulation (also known as FM chirp) or binary pulse modulation. The FM chirp method is more commonly used (Franceschetti and Lanari 1999), and is done by modulating the signal up or down, making the bandwidth independent of the pulse length. By compressing the signal using a matched filter, the signal is shortened and the total energy output is compressed into a much shorter pulse (Elachi and van Zyl 2006). This enables the sensor to transmit signals at average energy output and still receive signals enabling images of high quality and resolution. The received signal is a combination of several echoes from a large number of point targets in the scene. The goal is to combine the appropriate received contributions backscattered by each target to achieve the best resolutions, and it is shown that each received pulse will compress to have its maximum at a time equal to the round-trip of the transmitted pulse to the point target. This is known as range compression and is a convolution done in the frequency domain and is a fast Fourier Transformation (FFT), based on a matched filter (Elachi and van Zyl 2006). The next step is to compress the signal in the azimuth direction, also a matched filter operation implemented by FFTs.

Travel time of the signal takes the form of a hyperbola based on the sensor's movement in the azimuth direction. Using signal processing and the geometrical properties of the signal, the hyperbola can become linear (this process is also known as range migration) (Cumming and Wong 2005). Range curvature and range walk are collectively referred to as range migration. Range migration happens in the frequency domain as a Doppler shift, leading to a chirp signal differing from the transmitted signal since its rate is both range and azimuth-frequency dependent. The compensation of this factor is an induced change and is considered as an additional range compression step. In practice, this is a rectangular algorithm, consisting of three main steps. First, range compression, followed by resampling to compensate for range walk and lastly azimuth compressions. The compressions and resampling into a point, where the position of the measured point is known, is the basic principle behind stripmap processing, the most common

system in remote sensing SAR (Curlander and McDonough 1991; Bamler and Hartl 1998; Franceschetti and Lanari 1999).

A SAR imaging system will have a range resolution projected into the image plane equal to (Elachi and van Zyl 2006):

$$x_r = \frac{c}{2B \sin \theta} \tag{2.4}$$

Where c is the speed of light, B is the bandwidth of the transmitted signal and θ is the look angle. The look angle is dependent on the range distance from the satellite, and if the equation is solved for parameters from the ALOS PALSAR system (see table 2.1), the theoretical range resolution is found to be between 14 and 88 meters (Jaxa 2012), the resolution increasing from near-range to far-range.

Mode	**Fine Beam Dual Polarization**
Centre Frequency	1270 MHz
Chirp Bandwidth	14 MHz
Polarization	HH+HV and VV+VH
Incident Angle	60° – 8°
Range Resolution	14 – 88 m
Observation Swath	40 – 70 km
Bit Length	5 bits
Radiometric Accuracy	Scene: 1 dB/Orbit: 1.5 dB

Table 2.1: ALOS PALSAR Characteristics

A SAR imaging system will have a spatial azimuth resolution equal to (Elachi and van Zyl 2006):

$$x_a = \frac{L}{2} \tag{2.5}$$

Where L is the physical length of the antenna. ALOS PALSAR has a physical antenna length of 8.9 meters, providing a theoretical azimuth resolution of ca 4.5 meters. The derivation of equation 2.5 is shown in most texts on SAR; see Curlander and McDonough (1991), Franceschetti and Lanari (1999) or Bamler and Hartl (1998) for further reading on the subject. The resolution of the image is decoupled (to some extent) from the distance of the sensor to the object it is sensing, and this makes SAR a practical instrument for remote sensing.

On azimuth spatial frequency bandwidth: *L/2*, meaning that subsequent SAR data processing, an all-pass (phase-only) filter operation, is able to focus the raw data to an azimuth resolution of about half the physical length of the physical antenna length, independent of range, wavelength and sensor velocity (Bamler and Hartl 1998). However, there is a trade-off between antenna size and the SNR, where smaller antennas give a larger signal-to-noise-ratio. ALOS PALSAR has the advantage of an advanced subdivision of the antenna, enabling ScanSAR and an experimental polarimetric mode as well as single and dual polarization images for the conventional SAR images (Rosenqvist et al. 2007). Polarization is an important factor in the use of SAR images, and is a mathematical operation on the transmitted and received signals from/to the antenna, as a synthesized radar cross section (Elachi and van Zyl 2006). PALSAR images can be obtained in Fine Beam Single mode (FBS), transmitting HH or VV polarization, or in Fine Beam Dual mode (FBD), transmitting HH+HV or VV+VH. ScanSAR has single polarization only, while polarimetric mode can transmit at all four polarizations (Rosenqvist et al. 2007).

ALOS PALSAR has an L-band sensor, meaning that the transmitted signal from the sensor has a wavelength λ equal to 23.6 cm and bandwidth *Bw* equal to 1.27GHz. These are two of the most important parameters for the sensor, as well as the look angle θ, pulse-repetition rate *PRF* and the Doppler-centroid f_{dc} (f_{dc} is specific to sensors like ERS-1 and 2). Other systems operate with different bands, such as C-band (6 cm, 5.3GHz) or X-band (3 cm, 9.6GHz). Atmospheric interaction with electromagnetic waves (EM waves) is shown in figure 2.2. The figure shows the atmospheric windows where propagation of EM waves pass more or less unhindered through the atmosphere. Wavelengths equal to or longer than some centimetres pass easily through the

atmosphere, and the active radar sensors benefit from this, making them independent of atmospheric disturbances such as clouds, precipitation or the lack of sunlight (Franceschetti and Lanari 1999). Some disturbance due to atmospherical disturbances can still be found in SAR scenes, either ionospherical or topographical. More on this is found in chapter 2.2.6.

The sensitivity of the SAR products, particularly interferograms, is directly connected to the wavelength λ, and shorter wavelengths are more sensitive to topography and deformation of the ground (Curlander and McDonough 1991).

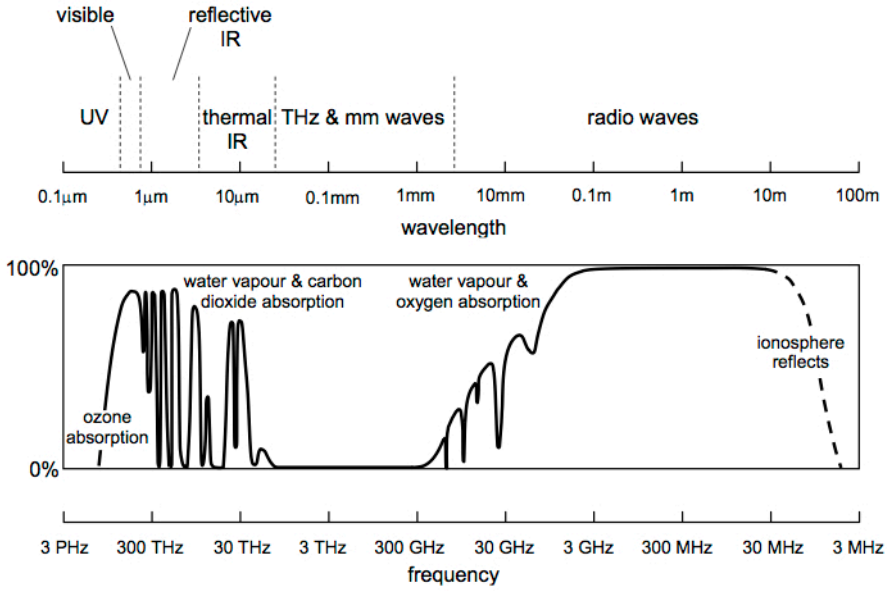

Figure 2.2: The electromagnetic spectrum of the Earth's atmosphere. From Richards (2009).

2.1.2 Complex SAR data

SAR sensors register both amplitude and frequency in the coherent return signal, making them into complex images consisting of both a real and an imaginary part (Massonnet and Feigl 1998). The real and imaginary parts of any complex pixel are mutually uncorrelated, as well as magnitude and phase (Bamler and Hartl 1998). The returned amplitude in an image is the sum of distributed point targets, recording the variable ability of the terrain to send the incident energy back to the radar, with a Rayleigh distribution. The returned phase is dependent on travel time to the point target as well as the surface backscatter properties, the scatterer's orientation to the

sensor and the electromagnetic properties of the scatterer's material. Its values are uniformly distributed between 0 and 2π, making the image appear noisy. For a moving system these values change with time, also called fading (Massonnet and Feigl 1998; Franceschetti and Lanari 1999). The deduction of the distributions of the phase and amplitude is given in Franceschetti and Lanari (1999), and will not be mentioned here.

The phase in an image is the component used in interferometric SAR (InSAR), and the backscatter values from the detected targets are what the amplitude registers in an image, also called the surface backscatter cross section, σ. Surface properties determine the intensity of the backscattered energy, and the image pixels have different grey scale values depending on the terrain's roughness and moisture content (Elachi and van Zyl 2006). Targets with a low backscatter are dark or even black (smooth surfaces such as water bodies, wet surfaces) and corresponding; targets with a high backscatter are seen as bright in the image. The roughness of the terrain affect the backscattered radar wave differently depending on the radar's wavelength; if the roughness of the terrain, measured by its root mean square (r.m.s.) height is much larger than the wavelength, more of the backscattered energy is incoherent. See figure 2.3 for an example of a SAR amplitude image.

The coherent SAR image is made from the phase and amplitude of the backscattered signal. As mentioned above, the amplitude signal is used for the image processing, while the phase signal is uniformly distributed and much smaller than the image pixels, creating a noisy image (Curlander and McDonough 1991; Franceschetti and Lanari 1999). Even two very similar terrain elements are physically different at the scale of the radar wavelength, making their backscattered fields independent random variables. However, the phase is still used in the image processing, and the fading and noise mentioned above creates *speckle*, a grainy appearance in image of the terrain in view of the SAR, sometimes called a salt and pepper texture (CCRS 2010). Speckle is usually not a wanted feature in the SAR image (unless speckle tracking is the chosen analysis method), and utilizing the independent looks acquired by the sensor at different aspect angles, an average can be computed, reducing the speckle, but also reducing the resolution of the image. Even though speckle is unwanted, it is a result from the

coherent processing of the images and therefore unavoidable (Franceschetti and Lanari 1999).

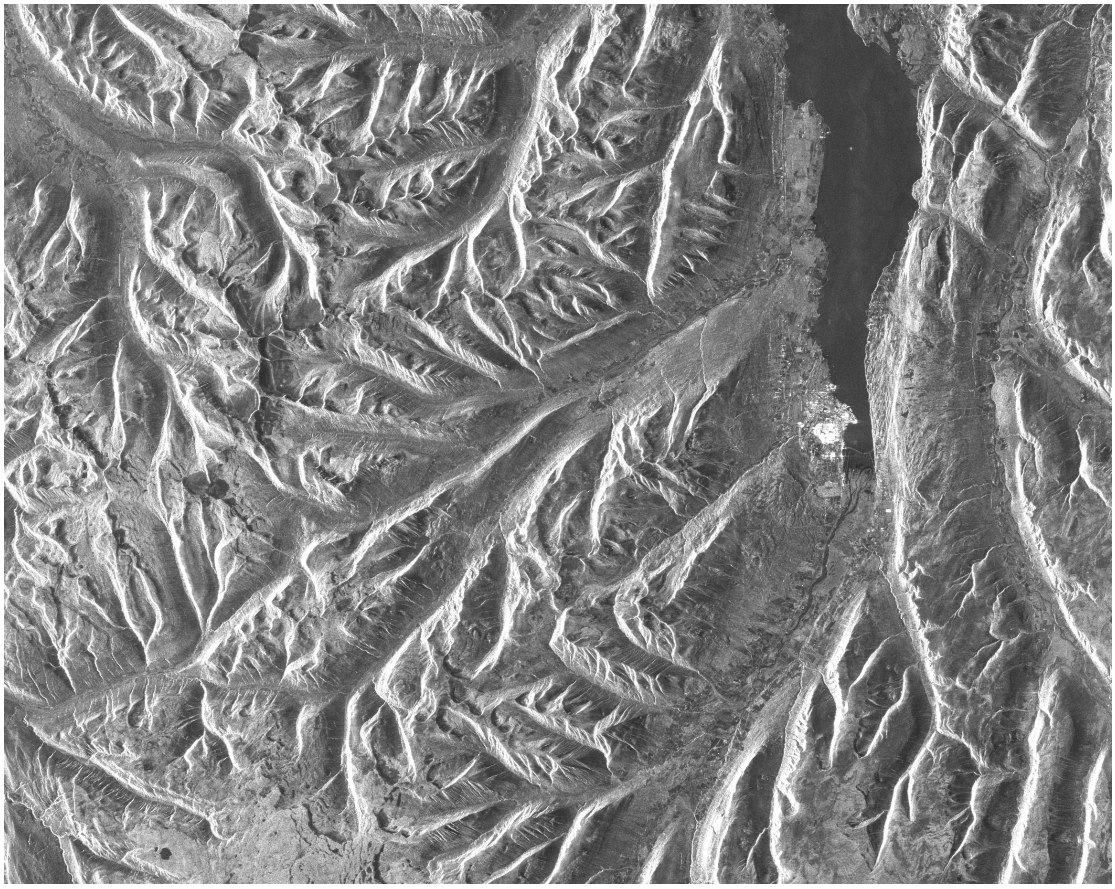

Figure 2.3: ALOS PALSAR 20071001HH intensity image from Tröllaskagi, Northern Iceland. ALOS PALSAR data © ESA (AOALO.3579).

2.1.3 ALOS PALSAR L-band

ALOS (the Advanced Land Observing Satellite) was launched on January 24, 2006 and went into power-saving mode on April 22, 2011 and then shut down on May 12, 2011 (Jaxa 2012). The ALOS satellite was the successor to the JERS-1 (1992-1998), and included full polarimetric capabilities, a conventional SAR as well as ScanSar options. The Phased Array L-band SAR (PALSAR) was onboard, in addition ALOS carried the Advanced Visible and Near Infrared Radiometer type 2 (AVNIR-2), an optical sensor with a 10 m resolution at nadir, and Panchromatic Remote-sensing Instruments for Stereo Mapping (PRISM), an instrument that measures precise land elevation.

ALOS had a 46-day repeat cycle; it required 671 passes to complete full global coverage. One out of four passes were acquired in ScanSAR mode. The swath width is 70 km for both fine beam modes, with a ground resolution of 10´10 and 10´20 m in HH and HH/HV polarization, respectively. The 34.3° off-nadir angle corresponded to an incidence angle of 36.6-40.9° from near to far range. The drawback of the ALOS repeat cycle was the heterogeneous time structure, making the data less suitable for analysis of multipass data over extensive regions (Rosenqvist et al. 2007). For more information on the ALOS PALSAR, consult table 2.1.

2.1.4 Geometrical distortions

The sensors' emitted signals will, in almost all cases be distorted when they return to the sensor due to ground-based conditions. Three main types of geometrical distortions are found in SAR images: shadow, layover and foreshortening (Franceschetti and Lanari 1999; Curlander and McDonough 1991). Other effects are also considered as geometrical distortions, such as sensor errors, target location errors, platform ephemeris errors and errors in target ranging such as atmospheric distortions and target elevation errors. However, most of these errors are attempted corrected through the image processing and are not treated in this chapter. See chapter 2.2.4 and its subchapters.

Shadow is defined by (Franceschetti and Lanari 1999):

$$\alpha \leq \vartheta - \frac{\pi}{2} \tag{2.6}$$

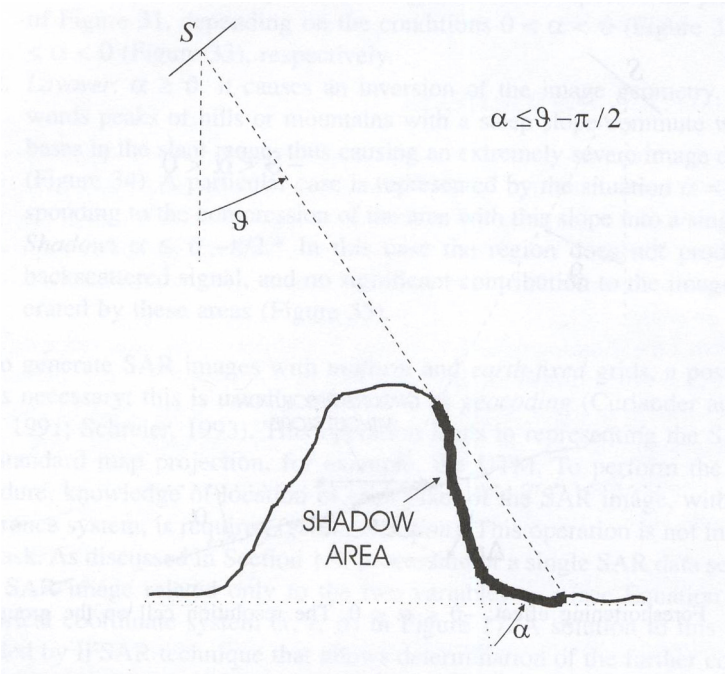

Figure 2.4: Shadow. Figure from Franceschetti and Lanari (1999).

ϑ is the system's incidence angle, α is the surface slope. A radar sensor, being an active sensor system, will not register any signals from an area in shadow, except for the inherent noise from the radar system.

Foreshortening is defined by:

$$-\vartheta < \alpha < \vartheta \tag{2.7}$$

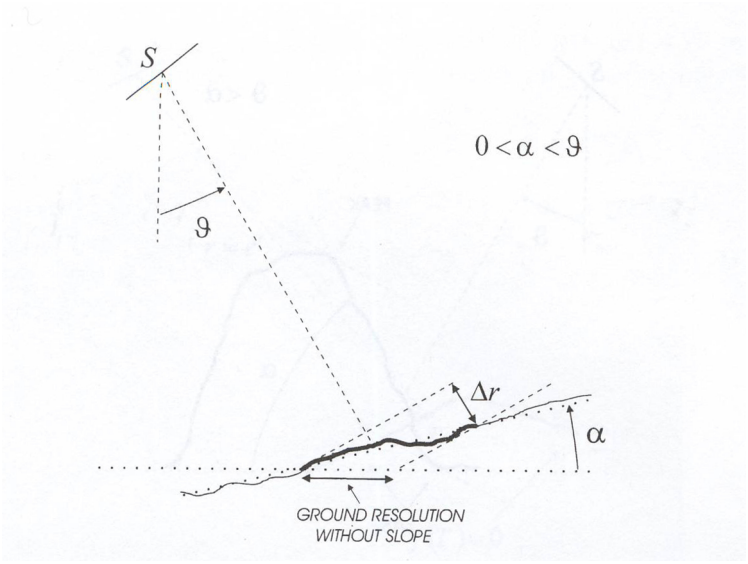

Figure 2.5: Foreshortening. From Franceschetti and Lanari (1999).

The pixel is compressed or dilated on the ground with respect to projection to the reference plane. The effect is depending on the look angle and the terrain's incidence angle: if $0 < \alpha < \vartheta$ the pixel is compressed on the ground, meaning "more" terrain is contained in the resolution cell. If the opposite case is true, i.e. $-\vartheta < \alpha < 0$, "less" terrain is spread out (dilated) in the resolution cell.

Layover is defined as:

$$\alpha \leq \vartheta \tag{2.8}$$

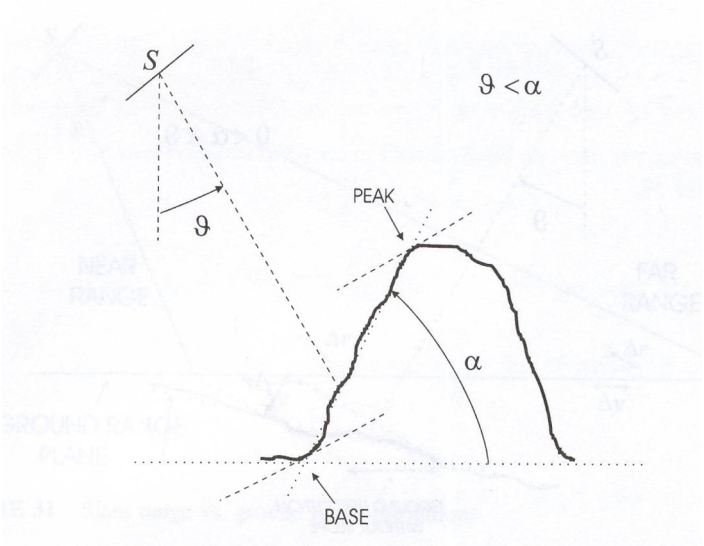

Figure 2.6: Layover. From Franceschetti and Lanari (1999).

Layover is an inversion of the geometry of the image, meaning that peaks and mountains with a steep slope, in the worst case, will be compressed into a single pixel. This effect is due to how the returned signal is registered in the sensor and the way it is processed into single pixels. In a sidelooking SAR, any signal with the same return time is assumed to belong to the same target, and the fraction of scattered power cannot be resolved. For a mountain, this means that the peak is at a nearer slant range than the base of the mountain, with the peak appearing in a nearer range position than the base, a "folding over" effect. As mentioned earlier, some geometrical effects can be corrected at a later processing stage, but for the most severe effects (i.e. shadow, layover and foreshortening) this is not an option. These areas have to be identified and for the areas with shadow and layover the data loss is irreversible, while the areas with foreshortening the results will be distorted. Through geocoding, the SAR images are reprojected from a range-Doppler projection into a standard map projection such as UTM, but areas with severe geometrical errors will not have any data.

If the local topography is known, either through a digital elevation model (DEM) or personal knowledge, it is possible to make some assumptions about the SAR products from the area of interest, particularly if the area has many mountains and steep slopes. Any area with a, for a SAR sensor, difficult topography has to be considered carefully before any image purchases are made. If the satellite acquires images in both ascending and descending orbits this has to be considered as well, since the geometric distortions due to topography will be different; ascending images will have distortions on slopes with an East aspect while descending images will have distortions on slopes with a western aspect.

2.2 Interferometry

2.2.1 Principles and introduction

SAR interferometry was first demonstrated in 1974 (Franceschetti and Lanari 1999; Elachi and van Zyl 2006). The basic principle is that two different scenes can provide a stereoscopic vision based on phase interference fringes from the two images. In a single SAR image, no information on terrain height or deformations is available. By calculating

the phase difference between two SAR images in an interferogram, the position of any pixel can be calculated in three dimensions. After the launch of ESA satellite ERS-1, a large number of SAR images became available and a considerable amount of research has been done on the subject since (Bamler and Hartl 1998). The method is usually called interferometric SAR (InSAR), and several different methods are available, such as repeat-pass interferometry and single-pass interferometry. Here, the most interesting technique is the dual-pass or repeat-pass method, since this technique utilizes two or more images acquired at different times unlike the single-pass method, where two sensors are mounted on the same vehicle (Franceschetti and Lanari 1999). Several SAR satellites have been active the last 30 years, and images from these sensors can be used for interferometry. However, some conditions have to be fulfilled, namely a known sensor position and satellite ephemeris and a regular repeat interval, both of which are needed if interferometry is to be successful. If at least one image parameter is different between the images (flight path, acquisition time, wavelength), interferometry can provide additional information. However, in many cases noise is a contributing factor to these differences (Elachi and van Zyl 2006).

Taking a closer look at the baseline, this can be shown as seen in figure 2.8. $B_{\perp}$ and $B_{\parallel}$ denote respectively the normal component of the baseline and the parallel component. The phase received by the satellite sensor is given as (Rosen et al. 2000):

$$\varphi(t) = -\frac{4\pi}{\lambda}\rho(t) \tag{2.8}$$

Where λ is the radar wavelength and ρ is the range. This is the equation for a monostatic system, where the range is found twice. The phase provides no information in and of itself, since it is given as modulo 2π.

The interferometric process is dependent on the baseline B, the separation of the sensor's flight tracks, and the *effective baseline*, $B_{\perp}$, the component of the baseline that is perpendicular to the look direction. When the sensor locations and the corresponding ranges ρ_1 and ρ_2 are known for two (or more) images, every pixel in the images can be mapped back into space by triangulation (Bamler and Hartl 1998). The advantage of

SAR images is the known phase of each pixel, meaning that each pixel contributes to measure the parallax $\Delta\rho = \rho_2 - \rho_1$. Figure 2.7 shows the geometry of a repeat-pass SAR system. ρ is the slant range, $\delta\rho$ is the path length difference between the two antennas, B the physical interferometric baseline length and θ is the look angle to the point being imagined. θ_0 is the look angle corrected to the reference plane, h the height of the sensor above the reference plane, z terrain height over the reference plane and A_1 and A_2 are the sensor positions at time$_1$ and time$_2$. α is the the baseline orientation, not to be confused with slope angle.

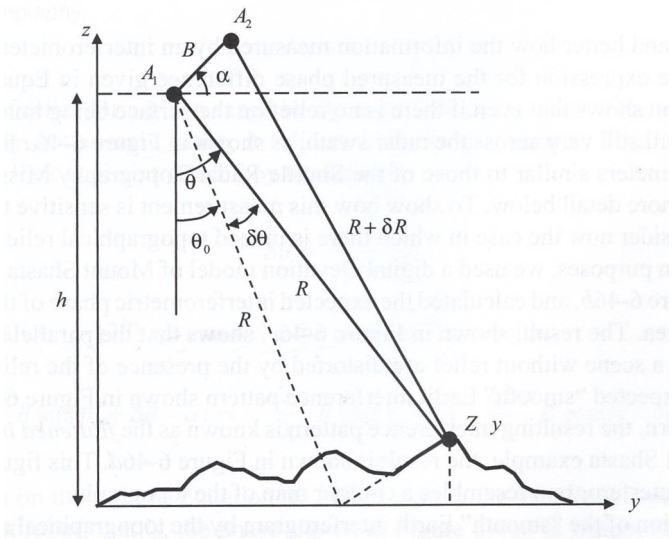

Figure 2.7: The SAR interferometry imaging geometry with a slightly different notation. R is ρ in this thesis. From Elachi and van Zyl (2006). Range is along the y-axis and azimuth is into the paper plane.

If two images are used, the signal from both are taken and the interferometric phase is given as (Rosen et al. 2000):

$$\Phi = \varphi_1 - \varphi_2 = \frac{4\pi}{\lambda}(\rho_2 - \rho_1) = \frac{4\pi}{\lambda}\Delta\rho \qquad (2.9)$$

The signal from A_1 is taken as reference, and $\rho_1 = \rho_2 + \delta\rho$. When the phase difference is calculated, the position of any point present in the images can be found. However, the principal value can only be measured in modulo 2π, and that the difference between the observation points can be many multiples of the radar wavelength (i.e. many multiples

of 2π). The result is a so-called wrapped interferogram and is what produces the fringes (colour cycles) in the interferogram image.

If the interferogram and following unwrapping of the phase is to get any meaning, the interferometric phase and other measurable values (such as the

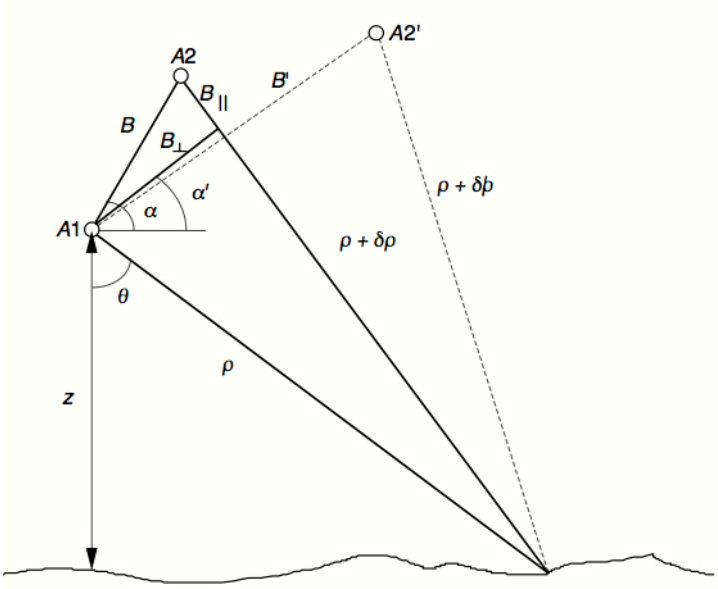

Figure 2.8: The baseline of an interferometric SAR system. $B_{\perp}$ is the normal component to the baseline B, $B_{\parallel}$ is the parallel component to B, and B is the baseline due to separation of the satellite flight tracks. Figure from Zebker (2000).

baseline) have to be related to the topographic height. As equation 2.9 shows, the interferometric phase is proportional to the range difference from two antenna locations (A_1 and A_2) to a point on the surface. The interferometric baseline is dependent on the orbit parameters. If figure 2.7 is the basic geometric setup of an interferometric radar system, then the path length difference $\delta\rho$ can be easily rewritten. Using the law of cosine, it is given (Elachi and van Zyl 2006; Zebker 2000):

$$\rho + \delta\rho = \sqrt{\rho^2 + B^2 - 2B\rho\cos\left(\frac{\pi}{2} - \theta + \alpha\right)} \qquad (2.10)$$

From this equation, $\delta\rho$ can be solved, assuming that $\rho \ll$ B due to parallel ray approximation (the orbits of the SAR sensor will usually not be perfectly parallel from t_1 to t_2 and lead to point-dependent azimuth and range geometric distortions, but these

are slow variations and local constants, and do not produce as large distortions as could be feared due to patches in the images with a rigid transformation from t_1 to t_2. A more thorough discussion is found in Franceschetti and Lanari (1999).). $\delta\rho$ is then (Franceschetti and Lanari 1999; Elachi and van Zyl 2006):

$$\delta\rho \approx -B\sin(\theta - \alpha) \tag{2.11}$$

If equations 2.9 and 2.11 are combined, the interferometric phase difference is measured through a relation to the path length difference (Bamler and Hartl 1998; Elachi and van Zyl 2006):

$$\Phi = \frac{4\pi}{\lambda}\delta\rho = -\frac{4\pi}{\lambda}B\sin\theta - \alpha \tag{2.12}$$

The point elevation z is found through (Elachi and van Zyl 2006):

$$z(y) = h - \rho\cos\theta \tag{2.13}$$

As mentioned earlier, the range ρ changes with the terrain height z, meaning that there is a contribution to the interferometric phase difference Φ through the image, even if the terrain height is 0 over the entire image. This is called the flat earth phase, and has to be compensated in the interferograms (i.e., the flat earth phase has to be subtracted from the interferogram). The terrain distorts the interferogram; this is due to the slightly modified radar look angles. From equation 2.13, the actual look angle from the measured interferometric phase is inferred (Elachi and van Zyl 2006):

$$\theta = \alpha - \sin^{-1}\left(\frac{\lambda\phi}{4\pi B}\right) \tag{2.14}$$

The SAR systems measure phase with a high accuracy, but not the look angle. This is why the look angle has to be estimated from 2.14. Terrain height can then be written as, combining 2.13 and 2.14 (Elachi and van Zyl):

$$z(y) = h - \rho \cos\left[\alpha - \sin^{-1}\left(\frac{\lambda\phi}{4\pi B}\right)\right] \tag{2.15}$$

From 2.14, if the look angle in the absence of relief for a given range is θ_0 and z is the elevation of the pixel including topography at the same range, then the change in the look angle due to relief is (Elachi and van Zyl 2006):

$$\delta\theta \approx \frac{z}{\rho_0 \sin(\theta_0)} \tag{2.16}$$

$\delta\theta$ is the change in the look angle θ due to topography (eq. 2.14). A spaceborne system making multiple passes over an area might acquire images with motion on the surface from t_1 to t_2. The change in look angle due to different orbits, viewing the topography from different look angles, is unwanted, and follows the base line length and the transmitted wavelength. The topographic contribution yields fringes that hug the topography like contour lines. If displacement takes place from t_1 to t_2, topographic phase has to be removed from the interferogram to acquire the displacement, since $\phi_{obs} = \phi_{topography} + \phi_{displacement}$ (Rosen et al. 2000). This creates a so-called flattened interferogram. Due to the geometrical set-up of the SAR sensors, only deformation in the sensor's line-of-sight (LOS) can be measured (Rosen et al. 2000; Bamler and Hartl 1998; Franceschetti and Lanari 1998).

Looking at equation 2.9, the deformation from t_1 to t_2 will contribute to the interferometric phase Φ through the range measurements:

$$\Phi_{deformation} = \frac{4\pi}{\lambda}\delta\rho_{deformation} \tag{2.17}$$

Taking into account the contributions to deformation, the equation for interferometric phase can be written as:

$$\Phi = \Phi_{flat\ earth} + \Phi_{topography} + \Phi_{deformation} \tag{2.18}$$

If the equation is expanded (no sign):

$$\Phi = \frac{4\pi}{\lambda}\delta\rho_{flat\ earth} + \left(\frac{4\pi}{\lambda}\frac{B_{\perp}z}{\rho \sin\theta}\right) + \frac{4\pi}{\lambda}\delta\rho_{deformation} \quad (2.19)$$

This does not include any other error sources such as errors due to propagation through the ionosphere and atmosphere or errors due to a change in scattering behaviour of the target (Bamler and Hartl 1998). If the geometry in fig. 2.7 is used:

$$B_{\perp} = B\cos(\theta_0 - \alpha) \quad (2.20)$$

And the final equation for the phase difference Φ can be written as (Elachi and van Zyl 2006):

$$\Phi \approx \frac{4\pi}{\lambda}B\sin(\theta_0 - \alpha) + \left(\frac{4\pi}{\lambda}\frac{B\ z}{\rho \sin\theta}\cos(\theta_0 - \alpha)\right) + \frac{4\pi}{\lambda}\delta\rho_{deformation} \quad (2.21)$$

The first term is the phase change due to flat earth, second term is phase change due to topography and the following change to look angle, and the third term is the phase change due to any deformation. $\delta\rho_{deformation}$ is the projection of the displacement vector onto the line-of-sight (range) direction (Bamler and Hartl 1998).

The baseline, as it is expressed in eq. 2.20, is an important part of the interferometric processing. The interferograms are sensitive to the baseline, both with regard to correlation between the images used for the interferometric processing and what the end goal of the processing is (extraction of topography or displacements). This sensitivity translates into a limitation on the baseline length; there is a rapid change in phase as the baseline length is increased causing the interferometric phase in the image to appear as noisy. Since the phase in the interferograms is measured in modulo 2π, any enlargement in the baseline causing the phase changes over one pixel to increase with more than 2π. If this happens, unwrapping of the phase in these areas is not possible and the reconstruction of the elevation profile is not possible (Elachi and van Zyl 2006). If topographic mapping is the end goal, a large baseline is helpful, as eq. 2.21 shows. The closer the baseline is to zero, the more sensitive the interferogram is to any

deformation. The critical baseline, the maximum baseline projected orthogonally to the look direction is given as (Elachi and van Zyl 2006):

$$B_{\perp crit} = B_f \cos(\theta - \alpha) = \rho|\delta\theta_{max}| = \left|\frac{\lambda_0 \rho B_f \tan(\theta - \alpha)}{c}\right| \quad (2.22)$$

Where B_f is the total bandwidth of the system, ρ is the distance between the electromagnetic source and the surface and c is the speed of light. If the equation is solved for the ALOS PALSAR parameters, a critical baseline of 6500 m is found.

The next step in the processing of an interferogram is finding the elevation value of one fringe (2π), the height ambiguity. From Bamler and Hartl (1998), this equation is given:

$$\Delta z_{ambig} = \frac{\lambda \rho \sin\theta_0}{2B_\perp} \quad (2.23)$$

From the equation is follows that the height ambiguity is dependent on the length of the baseline and the look angle. The local fringe frequency, meaning the interferogram's sensitivity to topography, is given by (Rott and Nagler 2006):

$$\frac{\delta\Phi}{\delta z} = \frac{\lambda}{2}\frac{R \sin\theta}{B_\perp} \quad (2.24)$$

As mentioned over, there are some error sources in the interferometric equation (eq. 2.16/2.19) that cannot be removed by the help of DEMs. These errors are $\Phi_{scattering}$, changes in the terrain's scattering behaviour, e.g., changes to the dielectric constant or a random phase as a consequence of temporal scene decorrelation, and $\Phi_{propagation}$, a phase delay difference du to atmospheric and ionospheric propagation conditions (Bamler and Hartl 1998). Added to these error sources is the random noise from the radar system, thermal noise (see Franceschetti and Lanari (1999) for a thorough discussion on this error source). This leads to an expansion in eq. 2.18:

$$\Phi = \Phi_{flat\ earth} + \Phi_{topography} + \Phi_{deformation} + \Phi_{atmosphere} + \Phi_{noise} \quad (2.25)$$

Any phase in an interferogram contains these individual contributions, but depending on what the end goal is, some are either separated (topographic phase or deformation phase contributions) and the other contributions are either compensated or ignored (particularly the atmosphere noise contribution is ignored in DInSAR, this is more thoroughly discussed in 2.2.6).

2.2.2 Interferograms

An interferogram is calculated by extracting the phase in one image from the phase in the second. This is done in practice by the equation:

$$\Phi = [\omega_1 \omega_2^*] \tag{2.26}$$

Where ω is the complex radar signal for images 1 and 2, and the * denotes the complex conjugate. This equation calculates the phase difference for each pixel in the images. The phase is restricted to the interval]-π, π] (Franceschetti and Lanari 1999), meaning that the phase is wrapped and the phase differences are only known in this interval. To make the differences absolute, the phase has to be unwrapped (which will be treated more thoroughly in chapter 2.2.9).

2.2.3 Differential interferometry (DInSAR)

Differential interferometry (DInSAR) is a method used to extract the phase difference due to deformation by trying to separate the different phase components in eq. 2.25. There are several methods to extract the displacement between interferograms, but two of the more common techniques is to either use a DEM and extract the simulated topographic phase from the interferogram (2-pass interferometry) or to use three or more interferograms to calculate the topographic phase (3- or 4-pass interferometry) (Bamler and Hartl 1998). The method used is dependent on the availability and quality of a DEM in the area of interest as well as the type of motion, baseline and time separation between the images (Rosen et al. 2000). In this thesis, the 2-pass DInSAR technique is the main theme, and will mostly focus on the different parameters that contribute to errors and misregistrations in the resulting differential interferograms.

For the 2-pass technique, equation 2.15 is used to simulate the topographic phase. Any atmospheric contributions and thermal noise are difficult to simulate or eliminate from the phase, meaning that they usually are ignored in the processing of the interferograms. If the user has access to 25+ images over the same area, the persistent scatterer (PS) or Small BAseline Subset algorithm (SBAS)-techniques can be used, thus enabling elimination of the atmospheric contribution in the phase. The satellite ephemeris and orbit data for most SAR systems are known, and this, in combination with the simulated topography enables the creation of interferograms and the successive differential interferograms.

Several error sources are present in most DInSAR-analysis, most notably the atmospheric noise, errors in the DEM used and differences (temporal) between the images. However, due to the flattened interferogram the phase differences are more sensitive to changes in topography, i.e., surface displacements or deformation, than to the topography itself (Elachi and van Zyl 2006):

$$\Phi_{flat} \approx -\frac{4\pi}{\lambda} B_{\perp} \frac{z}{\rho_1 \sin\theta_0} + \frac{4\pi}{\lambda} \Delta\rho \qquad (2.27)$$

Equation 2.27 shows the phase difference sensitivity to changes in topography; the elevation has to change by one ambiguity height to cause one cycle in phase difference while the surface displacement has to change by $\lambda/2$ to cause the same amount of phase change. An interferogram created with images with a large baseline will, however, be more sensitive to errors in the DEM and could possibly lead to large errors in the height estimates (cf. eq. 2.23). In the case of ERS with a 100 m perpendicular baseline and 23° look angle, the scale factor is 2.8 x 10^{-4}. Therefore, a 10 m error in topography will map into a 2.8 mm error in LOS. In the case of ALOS with a 100 m baseline and 34° look angle, the scale factor is nearly the same: 1.9 x 10^{-4} (Sandwell et al. 2008). However, no interferometric image pairs have a baseline smaller than 444.5 m in this thesis, and topographic errors will therefore map into a much larger error in LOS.

If enough images are available, this type of error as well as atmospheric and image difference errors can be compensated and to some degree eliminated through the PS technique. Errors in the DEM, however, will impact each interferogram and create errors in the same location in each interferogram. For traditional DInSAR, the errors are intrinsic to the technique, and the end results have to be treated with caution (Massonet and Feigl 1998).

One of the largest sources of errors in the DInSAR analysis is the *decorrelation* of the data. Decorrelation is an increase in the phase noise in the interferograms, creating random fringes. This decorrelation is expressed mathematically. One way to measure this decorrelation is to calculate the coherence, an estimate of the complex correlation coefficient of the two SAR images.

2.2.4 Coherence

Coherence is a mathematical expression of the similarities both in phase and amplitude from the coregistered images: image_1 acquired at time_1 to image_2 acquired at time_2. This is done through a cross-correlation function using the complex data (Weydahl 2001; Just and Bamler 1994, Bamler and Hartl 1998):

$$\gamma = \frac{E\{\omega_1 \omega_2^*\}}{\sqrt{(E\{|\omega_1|^2\} \cdot E\{|\omega_2|^2\})}} \tag{2.28}$$

and $0 \leq \gamma \leq 1$. E denotes the expectation value; this is calculated for each pixel. The signals are assumed to be Gaussian distributed, and this enables a probability density function (*pdf*) to be calculated and estimates for the coherence to be made. However, this is often done by estimating the coherence in windows of size $M \times N$. In *Gamma*, this window is often of the size of 5x5 (*Gamma* manual 2008), but due to the different sampling in SAR images (range:azimuth is often 1:5) M, N can be given values that correspond to this. However, the estimated coherence values are often overestimated, particularly for low coherence values. Additionally, the processing is dependent on a large number of averaged pixels in such a way that the higher the coherence accuracy, the lower spatial resolution and details. Coherence estimation techniques also rely on the hypothesis that all the signals involved in the estimation process are stationary and,

in particular, are locally stationary processes. When this is not the case, biased coherence values result (López-Martínez and Pottier 2007). Even if a DEM is available to correct this bias, the DEM itself might be of a lesser quality.

Figure 2.9 shows a coherence estimate plotted against the phase noise standard derivation, clearly showing how the phase noise increases while the coherence decreases. With a high coherence value, i.e., coherence close to 1.0, the function approaches a δ-function (Just and Bamler 1994) and gives a unambiguous fringe pattern. The most common technique to lower the phase noise is the multilooking-technique (Franceschetti and Lanari 1999; López-Martínez and Pottier 2007), which assumes that the SAR images can be described by Gaussian pdfs with a subsequent trade-off in spatial resolution. See figure 2.10.

A common way of denoting the coherence (Weydahl 2001):

$$\gamma_{total} = \gamma_{thermal} + \gamma_{processing} + \gamma_{temporal} + \gamma_{geometric} + \gamma_{DC} \qquad (2.29)$$

Decorrelation due to thermal noise and processing (or Signal-to-Noise Ratio, SNR) can, in most cases, be discarded in the processing. The thermal noise is an always-present factor and does not introduce any phase bias, while the processing noise can, in some cases, introduce either noise or phase variance (such as the Doppler-centroid noise) (Just and Bamler 1994). The misregistration noise can contribute to the noise in the cross-correlation index amplitude, increasing the interferogram noise contribution and degrading the absolute phase reconstruction. A misregistration of a little as $1/20^{th}$ of a resolution cell will generate a standard deviation of the interferometric phase of as much as 10° (Franceschetti and Lanari 1999). However, as long as the SAR images have the phase preserved and detailed orbital information available, these error sources are negligible.

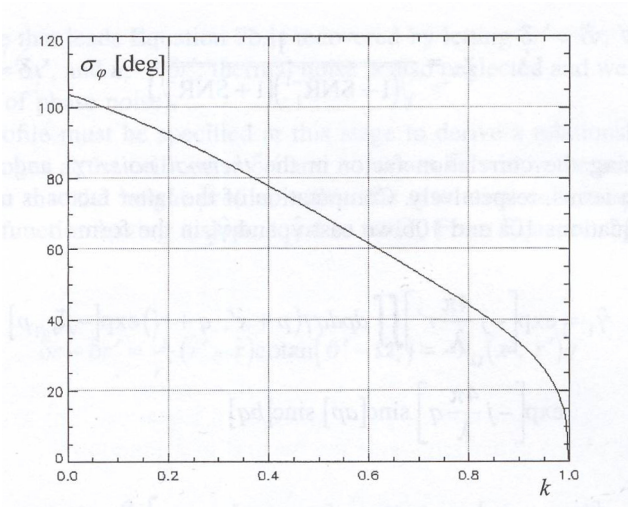

Figure 2.9: The coherence estimate plotted against the phase noise standard derivation. From Franceschetti and Lanari (1999).

In the following, the temporal-, geometric- and Doppler centroid-decorrelation will be discussed.

2.2.4.1 Geometrical decorrelation

The geometrical decorrelation is related to the baseline and the shift between the point scatterers in the image because of this. The larger the incidence angle, the larger the baseline and thus the phase ramp between the scatterers can become too large due to the varying aspect angle. Eq. 2.22 gives the critical baseline, showing the dependency on local slope, α. If the slope tilts away from the sensor the critical baseline increases, and the opposite is true if the slope tilts toward the sensor. However, decorrelation increases with an increasing baseline as shown in eq. 2.24.

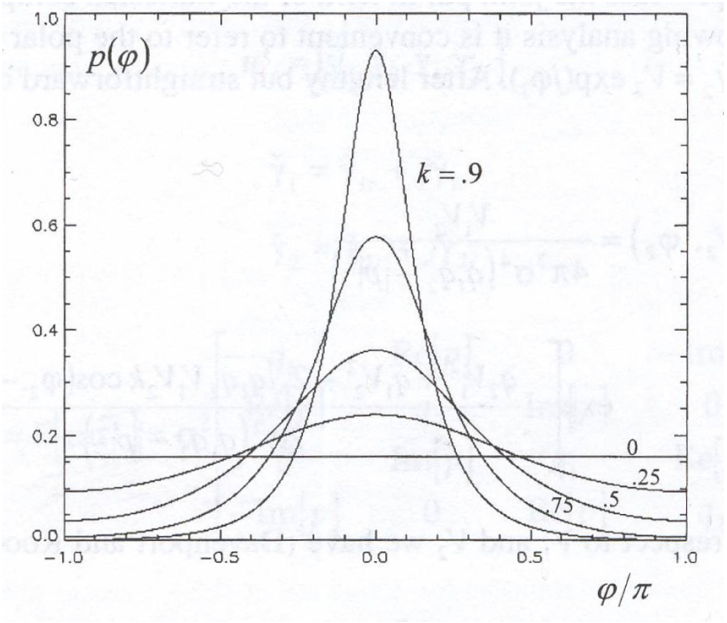

Figure 2.10: SAR images can be described by Gaussian pdfs. From Franceschetti and Lanari (1999).

This geometric decorrelation can be avoided if the radar signals have a slightly different frequency. Most radar systems have a constant frequency, thus the processing filters have to be tuned to different frequencies, a procedure called wavenumber shift filtering. This is given as (Bamler and Hartl 1998):

$$\Delta f_R = \frac{2B_\perp}{\lambda R_S \tan(\theta - \alpha)} \tag{2.30}$$

The spectral shift is identical to the local fringe frequency in range f_Φ. Dependency on the local slope α means that the fringe frequency has to be computed with a slope-adaptive spectral shift filtering, and if this is optimized, interferogram quality can be improved (Bamler and Hartl 1998, Rosen et al. 2000). Spectral shift increases with terrain slope (as seen in eq. 2.30), and is limited by the system bandwidth to values smaller than the critical baseline. Where the spectral shift is zero, the transition to radar shadow is found. This is at grazing incidence, i.e., $\alpha = \theta - 90°$ and the azimuth frequency shift plus half a wavelength is almost equal to the Fourier domain f_y plane. The spectral shift dependency on slope α means that as the slope increases, so does the spectral shift, until it equals the range system bandwidth. At larger slopes, no common bands are available for interferometric use. Layover is reached at values beyond $\alpha = \theta$, and the spectral shift is negative (Bamler and Hartl 1998).

2.2.4.2 Temporal decorrelation

Temporal decorrelation is specific to repeat pass SAR interferometry; the scene backscattering property function becomes time dependent and additional phase changes are present. The scatterers in the scenes are randomly rearranged with time and the speckle patterns of the image resolution elements differ, imparting a strong limitation on repeat-pass data (Rosen et al. 2000). Arid regions and vegetated areas are, to some extent, at variance, where arid regions display less temporal decorrelation (Franceschetti and Lanari 1999). This decorrelation is heavily dependent on the system wavelength, as well as the time interval and the terrain.

Several factors impart this time-dependent decorrelation of the signal: moisture levels, vegetation, deformation, erosion and anthropogenic changes (Bamler and Hartl 1998). Decorrelation due to volume scattering is included here, and, it can be argued, belong to temporal decorrelation. Strong wind ruffling/moving through vegetation or the presence of tree canopies (an inhomogeneous material) in C- or X-band SAR scenes can introduce a strong volume scattering (Elachi and van Zyl 2006). This is expanded on in chapter 2.2.10.

2.2.4.3 Processing decorrelation

The processing decorrelation is any error due to coregistration, resampling and orbit parameters. According to Weydahl (2001), coregistration errors are so small as to be considered negligible due to the accuracy of the fast Fourier transformation used to coregister the scenes. In *Gamma* software, the coregistration provides registration accuracy better than 0.2 pixels, i.e., less than 5% reduction in the interferometric correlation (*Gamma* manual 2008). The coregistration is usually performed on the amplitude image with a moving reference window, employing intensity cross-correlation to find the coherence maximum. A Least Squares polynomial (biquadratic) fit is calculated from the offsets, and a complex sinc interpolator resamples the second scene to the first (*Gamma* manual 2008).

2.2.4.4 Doppler centroid decorrelation

A difference in squint angles and look angles between the repeat-passes of the SAR sensor can give a decorrelation. The look angle difference gives a decorrelation in the range direction, the geometrical decorrelation discussed in 2.2.4.1. The squint angle difference can give a decorrelation in azimuth direction; this is the Doppler centroid decorrelation (Franceschetti and Lanari 1999). The ALOS PALSAR has yaw steering mode, i.e., azimuth image shift due to non-zero Doppler centroid is for the most part avoided (Shimada et al. 2005).

2.2.5 Filtering

Filtering the interferogram has the objective to reduce phase noise and thus the number of residues. This, in turn, makes the phase unwrapping simpler and more robust. A way of filtering the interferogram is to multi-look it, i.e., average the complex samples, reducing the standard deviation of the interferometric phase (*Gamma* manual 2008). This multi-looking is a way of estimating the coherence, giving a measure of the local interferogram quality as well as being a crucial part of the signal processing. Additionally, information about the scatterers can be extracted from temporal decorrelation (repeat-pass only), while single-pass configurations can provide information on the thickness of the scattering layer (Bamler and Hartl 1998). The estimate is, unfortunately, biased, and tends to overestimate low coherence. A suitable, quick alternative is the Cramér-Rao bound for unbiased coherence estimation of the (*Gamma* manual 2008: Bamler and Hartl 1998):

$$var(|\hat{\gamma}|)_{CR} = \frac{(1 - |\gamma|^2)^2}{2L} \tag{2.31}$$

Another common filter is the Goldstein filter, an adaptive filter used on the convoluted power spectrum, and this non-linear frequency domain filter is written as (Goldstein and Werner 1998):

$$Z(u,v) = \left[\hat{S}(u,v)\right]^{\alpha} \tag{2.32}$$

Where Z(u,v) is the direct filter response from the variance of the estimate $\hat{S}$ (u,v), and α is the exponent in the range of [0, 1]. If the exponent α = 0, no filtering occurs, while for α = 1 the filtering is strong. The filter algorithm is, as mentioned over, adaptive, and matches the local (non-stationary) fringe spectrum to separate the narrow band component from the surface backscatter and the noise component. According to Goldstein and Werner (1998), the phase noise in the interferogram gives an error equal to:

$$\sigma_r = \frac{\lambda}{4\pi}\sigma_\Phi \tag{2.33}$$

σ_r is the standard deviation for the deformation in the radar LOS, λ is the wavelength and σ_Φ is the phase noise. This is what the adaptive filter aims to remove from the interferogram, but the filter has to be used with caution; a too low exponent and the noise is still present, but similarly, a too high exponent risks creating fringes in areas with a total decorrelation.

2.2.6 Atmospherical distortions

SAR sensors are all-weather active sensors, meaning that they, in theory, are independent of weather and atmospherical conditions (see fig. 2.1, showing the electromagnetic spectrum). However, in reality, this is not true. The different wavelengths in SAR systems are impacted by the presence of topography and local atmospheric conditions in the troposphere; shorter wavelengths are more impacted, but only to a certain extent. The tropospheric delays are nondispersive, and they cannot be removed without supplementary data (Rosen et al. 2000). Topographic/orographic disturbances due to water vapour and/or turbulence in areas with a coarse relief make interferometric analyses difficult and cannot be modelled (Massonet and Feigl 1998). Zebker et al. (1997) found that temporal and spatial variation in air humidity of 20% could cause errors in the deformation calculation of up to 10 cm for SIR-C/X-SAR wavelengths, but that the L-band measurements in general performed better than C-band.

For spaceborne SAR image sensors, path delays due to ionospheric disturbances can be quite severe, depending on the frequency. L-band SAR can have greater than 50 m ionospheric path delay (Rosen et al. 2000). Generally, three types of ionospheric disturbances can be found to impact InSAR products. First, a group of effects including group delay, dispersion and Faraday rotation; second, clutter resulting from backscattering by electron density irregularities on the finest scales; and third, scintillation, a family of effects relating to spatial and temporal fluctuations in the signal parameters such as amplitude, phase and polarization. The ionosphere can affect the signal delay proportionally to λ^2 - for medium ionospherical conditions, a slant range error of 22.5 m can be expected for L-band SAR with a look angle of 23° (Xu et al. 2004).

Ionospheric path delay effects can be removed if enough images are available – due to the random nature of these disturbances the phase noise in the interferograms can be averaged through stacking and calibrated by removal of the phase delay through atmospheric data from an independent source (GNSS networks) (Williams et al. 1998). This, however, is time- and resource consuming, and neither GNSS data nor enough SAR scenes are necessarily available for the area being analysed. *Gamma* user manual (2008) mention linear atmospheric models to relate the unwrapped phase (due to path delays) to elevation as a solution, in combination with stacking.

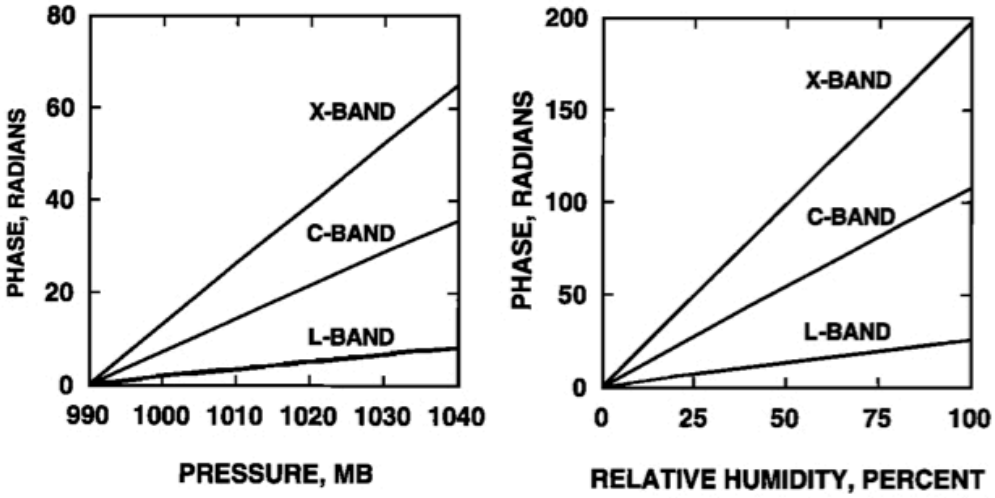

a)

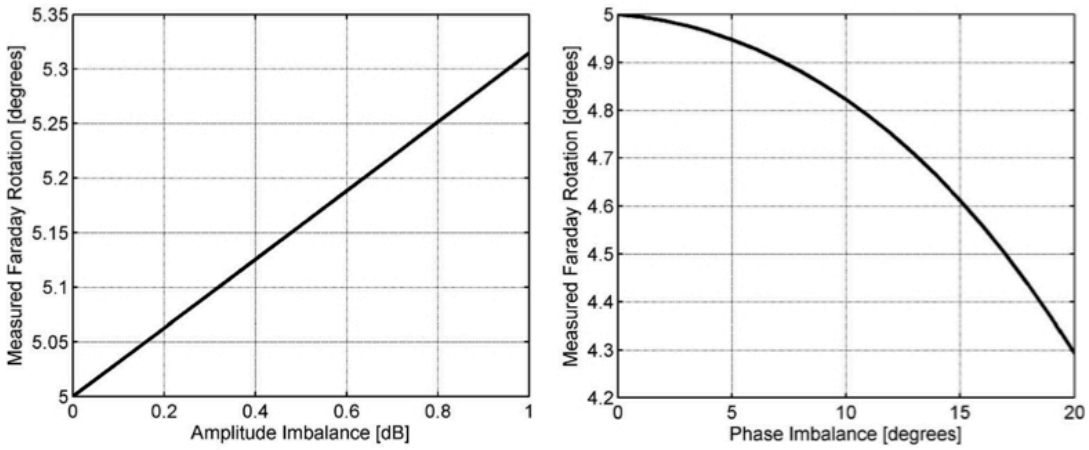

b)

Figure 2.11 a) Path delays due to pressure and humidity variations in the troposphere. From Zebker et al. (1997). b) Faraday Rotation biases due to amplitude and phase imbalances, one of several types of ionospheric effects on radar. From Meyer et al. (2008).

2.2.7 Phase unwrapping

Much research has gone into phase unwrapping algorithms. The underlying assumption is that any interferometric phase is wrapped modulo 2π (]-π, π], or one fringe equals half a wavelength) and that an integer number of 2π has to be added to the interferometric phase for each pixel to achieve sequential phase values across the entire image. If the interferogram is from a scene with relatively flat topography and little noise, the unwrapping is relatively easy. If, for any reason, there is a jump in the unwrapped phase, the algorithm has to take this into account. Herein lies the problem. Phase jumps could occur from any of these reasons (*Gamma* manual 2008):

- Phase noise: temporal decorrelation, baseline decorrelation, different Doppler centroids, shadow or low SNR
- Phase undersampling: steep slopes causing phase gradients > π.
- Phase discontinuities: layover, discontinuous surface deformation – both leading to phase jumps of multiples of 2π.

A phase jump is expressed as (Franceschetti and Lanari 1999):

$$|\Phi(P_1P_2)| = |\Phi(P_2) - \Phi(P_1)| < \pi \qquad (2.34)$$

Where P_1 and P_2 are neighbouring pixels. The jump between the pixels has to be less than π if the integration is to be successful.

Unwrapping of an interferogram can be done via local or global unwrapping methods. Two standard algorithms are in use: the branch-cut method (local) and the least squares (LS) fitting (global) (Rosen et al. 2000; Franceschetti and Lanari 1999), but there are hybrid approaches as well as other algorithms in use.

The branch-cut method tries to isolate sources of error prior to integration of the derivative of the first difference of the phase. This is done through trying to choose only paths of integration that lead to self-consistent solutions. Under the assumption that the integral of the differenced phase about a closed path is zero, any residues in the four pixels forming a neighbouring set are classified as negatively or positively charged. Integration paths encircling a net charge must be avoided, and this is where the branch cuts are created, connections between opposite charged residues that cannot be crossed by the path of integration. The selection of the branch-cuts is the most challenging part of any branch-cut algorithm, where natural phase shears should be kept discontinuous (Rosen et al. 2000).

Algorithms using LS fitting are based on minimizing the difference between the gradients of the solution and the wrapped phase in an LS sense (Rosen et al. 2000). Usually, a weighted LS method is used, even though it is computationally heavier, and choosing the weighting coefficient is as challenging as selecting branch-cuts.

The *Gamma* software uses two methods of phase unwrapping: the branch-cut region-growing algorithm (as described over) with additional masking of low coherence areas and improvement of the phase unwrapping in regions with high phase noise. The second algorithm uses Minimum Cost Flow (MCF) techniques in combination with a triangular irregular network (TIN). This is a global optimization technique, enabling unwrapping of large interferograms as well as enabling consideration of areas with very low coherence in the unwrapping (*Gamma* manual 2008).

More thorough treatment of the unwrapping algorithms are outside the scope of this thesis, but interested parties are directed to Franceschetti and Lanari (1999), Massonet and Feigl (1998) and Rosen et al. (2000) for a thorough discussion on the unwrapping of phase in interferograms.

2.2.8 L-band interferometry versus X-/C-band interferometry

The optimal wavelength for InSAR is dependent on many factors, mainly the available datasets in the area and time period of interest. If images from several SAR sensors are available from the same time period, over the same area, some factors have to be considered:

- The magnitude of the displacement of interest (for DInSAR).
- The terrain in the area of interest.
- The climate in the area (wet/dry).

The interaction of the surface being imaged and the radar waves is the basis in any InSAR application. Spaceborne SAR sensor systems have been designed with different end products in mind, such as interferometry, topographic mapping, polarimetry and sea level monitoring. Depending on the end product, different wavelengths have been used for SAR sensors. The most common wavelengths are the L-, C- and X-band sensors. K_u-band and P-band spaceborne SAR sensors are still in development (Elachi and van Zyl 2006), having wavelengths of respectively 2.17 cm and 86 cm.

SAR sensors (in action at present or in the recent past) with C-band sensors are the ERS-1 and -2 satellites, SIR-C/X-SAR satellite, RADARSAT-1, JERS-1 and ASAR Envisat

satellites. SIR-C/X-SAR also carry an X-band sensor. ALOS PALSAR, SIR-A and -B and SEASAT-A acquired scenes in L-band wavelengths (Franceschetti and Lanari 1999; Elachi and van Zyl 2006). The most common bands in spaceborne SARs are the C- and L-bands, and thus comparisons of these are apt.

In the literature, L-band radars are found to be very useful particularly for InSAR and DInSAR (Zebker et al. 1996). However, few satellites are launched with only interferometric SAR as the research and data acquisition goal; most satellites acquire several types of images with different sensors mounted on the satellite. ALOS PALSAR acquires images in Fine Beam Single and Dual, as well as polarimetric SAR images and experimental ScanSAR images (Rosenqvist et al. 2004), but the ALOS satellite also carries the AVNIR-2 and PRISM sensors (Jaxa 2012). Longer wavelengths have the advantage of having longer critical baselines, as well as better correlation over time, but the DInSAR measurements should be less precise as well as heavily impacted by ionospheric refraction (up to 16 times more) (Sandwell et al. 2008).

Not one wavelength can satisfy all observation desires – objects at roughly the same size as the wavelength give the best backscatter in SAR images. In addition, choosing frequency for a SAR sensor meant for interferometry/differential interferometry is complicated, where the need for fringe/deformation resolution needs to be balanced with the time span between images (Rosen et al. 2000). The SNR and backscattered power in the image are strong functions of wavelength, where similar surfaces can look rough in X-band but smooth in P-band. Depending on the wavelength, the incident waves are scattered differently by objects in nature: L-band wavelengths penetrate canopies and are scattered from the soil with double-bounce from trunks; C-band is scattered from leaves and branches while X-band scatters at the canopy boundary (Bamler and Hartl 1998). Deformation detected by InSAR is only significant if it produces a range change larger than the measurement uncertainty. The “small gradient limit” restricts interpretation to signals with a magnitude of the better part of a fringe. Resolving phase differences smaller than $^{1}/_{10^{th}}$ of a cycle is difficult: C-band interferometry is restricted to some millimetres; L-band has a threshold that is four times larger (Massonet and Feigl 1998).

Other challenges are the presence or absence of water in the scene being imaged; the different radar wavelengths have different scattering and penetrating behaviours in surfaces with or without water/moisture. If the surface is pure ice, dry soil or permafrost there is a volumetric loss tangent ≤ 10^{-2} (i.e., the tangent of the dielectric constant in a material, $\tan\delta = \frac{\varepsilon''}{\varepsilon'}$, where ε' is the real part and ε'' is the imaginary part corresponding to the medium's ability to absorb and transform the incoming wave's energy), while wet soil, sea ice and vegetation has a loss tangent ≈ 10^{-1}. The loss tangent increases with the amount of liquid water present in the propagation medium (Elachi and van Zyl 2006). If there is an absence of water, such as dry soil or snow, frequencies of 1.2 GHz or lower penetrates the medium. For dry soil, L-band radar can penetrate deeper than 1 m, while dry snow is transparent to this wavelength (Elachi and van Zyl 2006). In arctic and desert remote sensing, this can become a problem if the actual surface limit is of interest. This particular quality is, however, useful if subsurface features are of interest; for example, paleo river courses in the desert have been mapped through L-band interferometry (Richards 2009). Remote sensing of ground subsidence or elevation in the winter could be possible, as well as detection of the topmost ice layer in glaciers and glaciated areas.

Zebker et al. (1996) found that longer wavelengths gave better correlation for longer time gaps between the SAR interferograms. In wet and humid areas L-band also had better correlation than C-band, indicating that the tropospheric phase disturbances are less prominent in L-band InSAR. Sandwell et al. (2008) found the same, but showed that path delays caused by water vapour in the troposphere are independent of wavelength, so the distortion will affect both systems equally. From the wavelength, L-band interferometry should be four times worse than C-band. Surprisingly, Sandwell et al. find that ALOS LOS range precision is only 1.5 times worse than ERS range precision. In addition, they found an rms deviation of LOS vectors compared to GPS vectors of only 14 mm, and an azimuth offset standard deviation of 71 mm, only 2% of azimuth pixel size. This indicates that L-band interferometry can provide precise measurements of displacements, provided that the image pairs are chosen wisely, with baselines well within the critical baseline limit.

3 Study area and data

Differential interferometry in Iceland and Norway with ALOS PALSAR images may not work particularly well in all instances. This is due to difficult topography with steep mountainsides, deep fjords and valleys, ionospheric disturbances and tropospheric disturbances due to coarse topography. The climate in Iceland can be difficult, due to a maritime, temperate cool climate in the southern and western lowlands and the northern areas and the high mountains belong to an arctic climate. The climate along the western Norwegian coast is maritime and temperate, which could introduce tropospheric disturbances in valleys and mountainous areas. The limited scene-acquisition plan across Iceland and Norway (and other, similar areas) for the ALOS PALSAR mission is also a complicating factor. With steep mountain slopes and deep valley floors, all covered with vegetation, and some areas with exposed bedrock in higher elevations, the terrain is less than ideal for differential interferometry. The same can be said for Norway. Selected areas in Northern and Eastern Iceland and Western Norway are presented here, chosen for their geoscientific areas of interest, such as periglacial landforms, slow-moving landslides and challenging topography.

3.1 Tröllaskagi, North Iceland

3.1.1 Processed areas

In the southern part of the peninsula, the Hóladalur and Fremri-Grjótárdalur areas are chosen as being particularly interesting, due to the thoroughly investigated rock glaciers at the site (e.g., Wangensteen et al. 2006; Kellerer-Pirklbauer et al. 2008), as well as Svarfaðardalur, Kvarnardalur and Lambardalsöxl.

Almenningsnöf and Torfnavík/Höðnuvík in the north are found to be the most interesting parts, due to the large areas with displacement (Wangensteen et al. 2006; Jónsson 2009). Another interesting area lies just south of Torfnavík/Höðnuvík is Lambanesás, where a hitherto unknown landslide is detected.

3.1.2 Location

The Tröllaskagi area is in the north of Iceland, a peninsula situated between the Eyjafjörður in the east and Skagafjörður in the west. The main city in this area is Akureyri, found in the Eyjafjörður. Tröllaskagi is a mountainous peninsula, with high peaks and deep glacial fjords and valleys, including the Kerling mountain at 1538 m a.s.l.

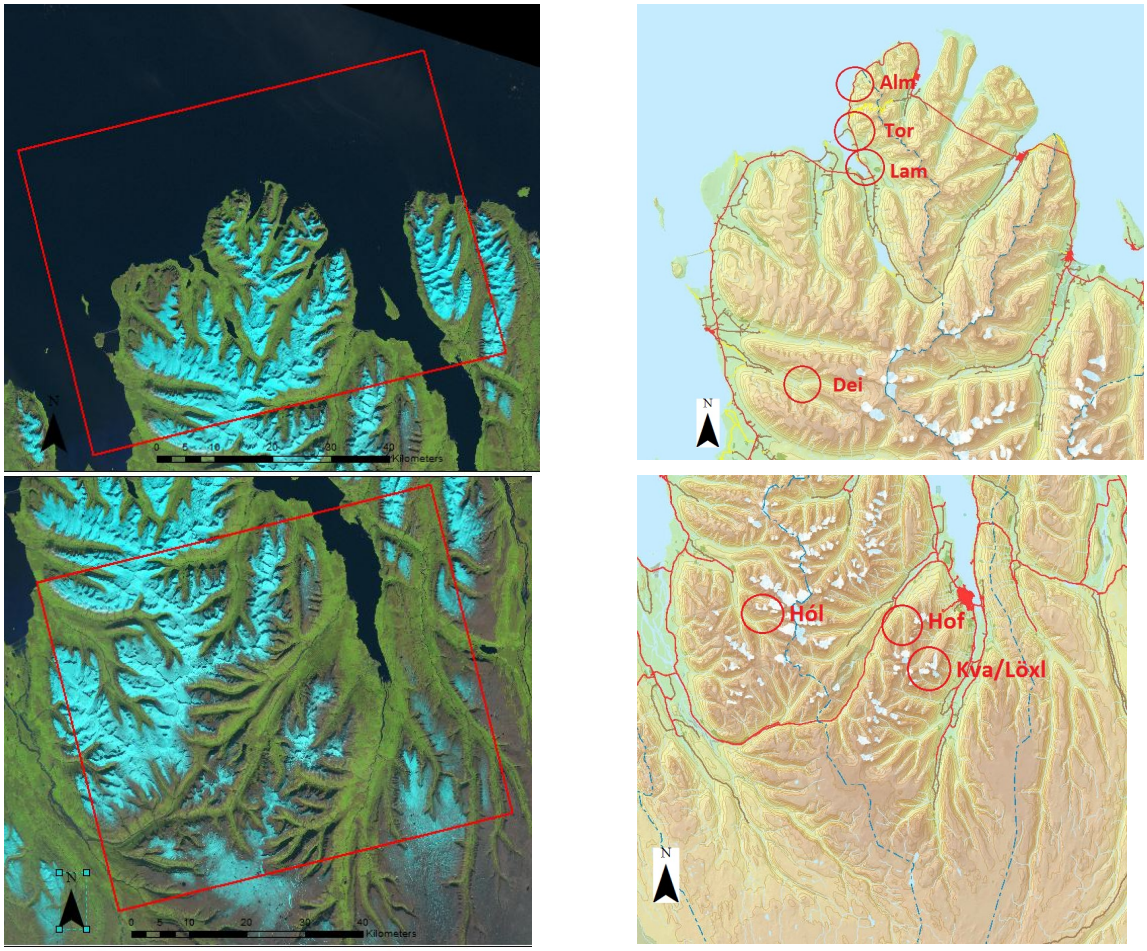

Figure 3.1: The extent of the SAR scenes used from Tröllaskagi (top left, bottom left). The location of the areas of interest (top right, below right). North: *Alm* = Almenningsnöf, *Tor* = Torfnavík, *Lam* = Lambanesás, *Dei* = Deildardalur. South: *Hól* = Hóladalur and Fremri-Grjótárdalur, *Hof* = Hofsárdalur and *Kva/Löxl* = Kvarnardalur and Lambardalsöxl. Background images: Landsat image downloaded 25.09.2012, map image from lmi.is, downloaded on 25.09.2012.

3.1.3 Geology and structures

Tröllaskagi lies in an area with Upper Tertiary age rocks, where some northern areas are up to 12 Ma. These rocks are basaltic piles of variable lithologies, and in the Hóladalur and Fremri-Grjótárdalur areas, the basalt is aged at around 7 Ma (Sigmundsson and Sæmundsson 2008; Thordarson and Hoskuldsson 2002). The northwestern part of the peninsula belongs to the Skagi volcanic belt, where Plio-Pleistocene, Upper Pleistocene and Holocene lava formations are found (Thordarson

and Hoskuldsson 2002). The landscape can be characterized as alpine, with high peaks and deep valleys. Some small glaciers are still found in the area, and the geomorphology is categorized by periglacial and fluvial landforms, particularly in higher elevations. Lilleøren (2012) characterizes the permafrost regions in Iceland as maritime and warm, with associated landforms differing from the corresponding in the European Alps. Equilibrium line altitudes (ELA) for the area are found approx. at 800m a.s.l. in coastal areas to around 1200 m a.s.l. in the interior (Caseldine and Stötter 1993). Permafrost is seen as a marginal phenomenon, only found in areas with favourable conditions (Etzelmüller et al. 2007; Farbrot et al. 2007b).

3.1.4 Former investigations

Several authors have investigated the Hóladalur and Fremri-Grjótárdalur periglacial landforms, with different results. Martin and Whalley (1987) and Whalley and Martin (1994) have defined the land forms in Tröllaskagi as rock glaciers developed during the Little Ice Age (LIA), decoupled from permafrost, whereas Barsch and Haeberli (Barsch 1996; Haeberli 2000) have found the opposite. Wangensteen et al. (2006) studied the rock glaciers close to Hólar through cross-correlation matching of multi-temporal orthophotos, and estimated the ages as pre-LIA and displacement velocities of the complexes at 0.10-0.84 m a^{-1}. Similar results were found by Kellerer-Pirklbauer et al. (2008) through Schmidt-hammer rebound values and photogrammetric measurements of surface displacement. The area lies in the lower boundaries of mountain permafrost in Iceland (Etzelmüller et al. 2007), further supporting the notion of presently active rock glaciers in the Hóladalur. Farbrot et al. (2007a) found rock wall retreat rates of 0.4-1.2mm a^{-1}, governed by frost shattering. This, combined with temperature measurements indicating extensive permafrost occurrences in the area, is a further suggestion of permafrost features. Lilleøren and Etzelmüller (2011) made an inventory of the landforms found at Tröllaskagi, and identified 265 rock glaciers, 205 interpreted as intact landforms and 60 as relict. Jónsson (2009) and Jónsson and Ágústsson (2007) find displacements spread over the Tröllaskagi peninsula by using ERS-1/2 differential interferograms.

At Almenningsnöf in the north, displacements are estimated at an average of 0.57 m a^{-1}, but parts of the displacement body are moving independently from the rest

(Wangensteen et al. 2006). Jónsson (2009) finds the same by using ERS-1/2 differential interferometry (without unwrapping, so no estimates of displacement magnitude in LOS are given).

3.1.5 SAR-recordings used

The ALOS PALSAR scenes are from an ascending orbit, track 13, frame 1320. The ALOS PALSAR data are courtesy of ESA under AOALO.3579.

Area	Image pairs	Baseline $B_{\perp}$ (m)
Tröllaskagi S	20070816_20071001	607,19
	20070816_20080818	-5209,95
	20070816_20081003	-5333,77
	20070816_20100709	1599,53
	20071001_20080818	-6909,69
	20071001_20081003	-5941,86
	20071001_20100709	995,73
	20080818_20081003	965,31
	20080818_20100709	7973,6
Tröllaskagi N	20070816_20071001	607,69
	20070816_20100709	1605,79
	20071001_20100709	999,16

Table 3.1: SAR scenes used for Differential InSAR in the Tröllaskagi peninsula. Two different frames are used to cover the entire area.

3.1.6 DEM

The DEM used for the Differential InSAR processing is taken from Troels Petersen's master thesis (2007). The accuracy is unknown, and only validated through visual inspection of the DEM. The DEM appears to be underestimating both high peaks and low valleys, and some residual topographic phase can be expected in images with a larger baseline.

3.1.7 Background data

A Landsat 7 image is used as background image, as well as an image from the topographic map service from Landmælingar Íslands, downloaded 25.09.2012.

3.2 Northern Austurland, Iceland

3.2.1 Processed areas

In the southern part, Seyðisfjörður, Reyðarfjarður and Hólarfjáll are of interest. The slope just west of Seyðisfjörður (the settlement) is susceptible to landslides after heavy rainfall (Wangensteen et al. 2006), but due to its north-eastern aspect, it is not optimally placed for the ascending SAR images.

In the north, two areas are of interest: the Smjörfjöll location, where a slow-moving landslide is known, and Lambardalur.

3.2.2 Location

The area covered by the ALOS PALSAR scenes is found between the Reyðarfjörður and just north of Héraðsflói in eastern Iceland. Egilsstaðir is the largest town in the area, located on the banks of Lagarfljót river. This area is also characterized by fjords, deep valleys and steep peaks, an alpine landscape formed by glacial and periglacial processes.

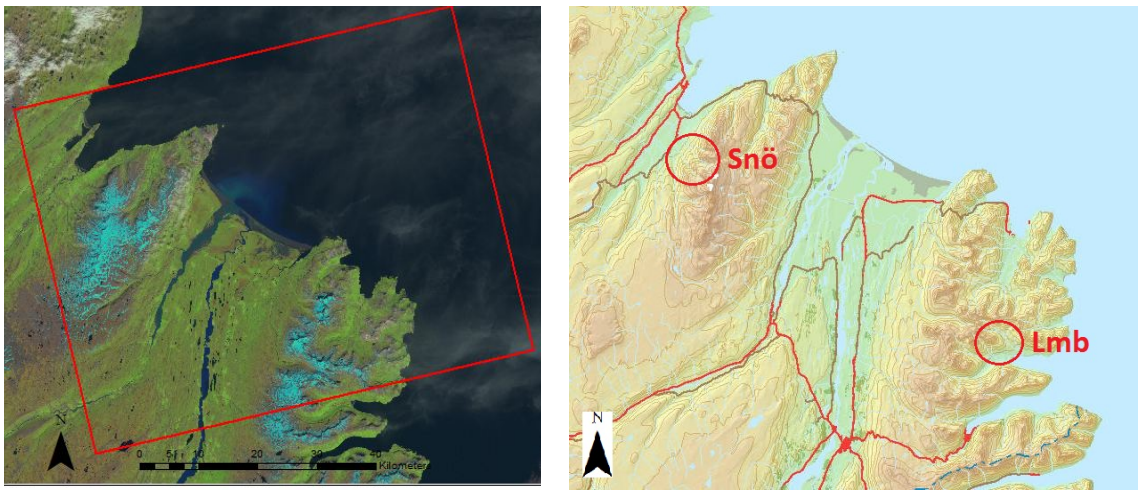

Figure 3.2a: SAR scenes from Austurland (left) and the areas of interest (right). *Snö* = Smjörfjöll and *Lmb* = Lambardalur. Background images: Landsat image downloaded 25.09.2012, map image from lmi.is, downloaded on 25.09.2012.

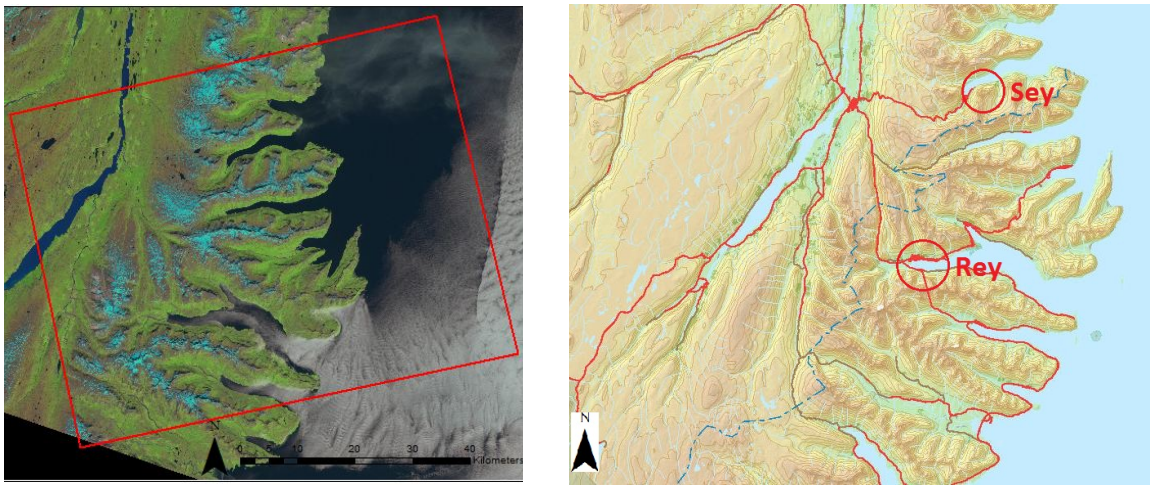

Figure 3.2b: SAR scenes from Austurland (left) and the areas of interest (right). *Sey* = Seyðisfjörður and *Rey* = Reyðarfjörður and Hólafjall. Background images: Landsat image downloaded 25.09.2012, map image from lmi.is, downloaded on 25.09.2012.

3.2.3 Geology and structures

Geologically, eastern Iceland consists of a Tertiary Basalt formation, with some rhyolite intrusions in areas with extinct volcanic systems (Thordarson and Hoskuldsson 2002). Héraðsflói, an area with extensive Holocene sandur deposits (Thordarson and Hoskuldsson 2002), stands out from the surrounding basaltic formations.

3.2.4 Former investigations

Few investigations of displacements have been made in this area, but Wangensteen et al. (2006) found some displacements close to Seyðisfjörður town. Jónsson and Ágústsson (2007) detected the same landslide with ERS-1/2 images, as well as detecting new, active slope creep in 30 locations with the largest landslides found in Vopnafjörður and Loðmundarfjörður.

3.2.5 SAR-recordings used

ALOS PALSAR scenes from ascending orbit, track 5, frames 1300 (south) and 1310 (north). The ALOS PALSAR data are courtesy of ESA under AOALO.3579.

Area	Image pairs	Baseline $B_{\perp}$ (m)
Austurland N	20070818_20071003	532,42
	20070818_20100826	2137,04
	20070818_20101011	2737,46
	20090823_20091008	448,01
	20100826_20101011	601,13
	20070818_20090823	-1666,5
	20071003_20090823	-2199,18
	20070818_20091008	-1217,88
	20071003_20091008	-1750,08
	20071003_20100826	1605,7
	20071003_20101011	2206,31
	20090823_20100826	3801,94
	20090823_20101011	4400,04
	20091008_20100826	3353,84
	20091008_20101011	3954,4
Austurland S	20070818_20071003	525,05
	20070818_20100826	2127,54
	20070818_20101011	2738,82
	20071003_20100826	1606,7
	20071003_20101011	2206,75
	20090823_20091008	444,5
	20100826_20101011	602,64
	20070818_20090823	-1663,82
	20070818_20091008	-1218,09
	20071003_20090823	-2190,13
	20071003_20091008	-1743,63
	20090823_20100826	3808,65
	20090823_20101011	4406,98
	20091008_20100826	3352,98
	20091008_20101011	3957,01

Table 3.2: SAR scenes used for Differential InSAR in north-eastern Iceland.

3.2.6 DEM

The DEM used for the Differential InSAR processing is taken from Troels Petersen's master thesis (2007). The accuracy is unknown, and only validated through visual inspection of the DEM. The DEM appears to be underestimating both high peaks and low valleys, and some residual topographic phase can be expected in images with a larger baseline.

3.2.7 Background data

A Landsat 7 image is used as background image, as well as an image from the topographic map service from Landmælingar Íslands, downloaded 25.09.2012.

3.3 Tafjord, Western Norway

3.3.1 Processed areas

Of particular interest in this area is the Åknesfjellet rockslide, one of the most investigated and monitored rockslides in the world (Oppikofer et al. 2009). This rockslide is being monitored by GPS, ground-based SAR, terrestrial laser scanning, piezometers and extensometers, all contributing to a thorough estimate of annual displacements in the mountainside. However, the entire Storfjord area is at risk for rockslides (Henderson et al. 2006).

3.3.2 Location

Tafjord is located south in the county of Møre og Romsdal in western Norway. Molde is the largest city in the county, but the Åknesfjelletfjellet rockslide threatens mainly the Geiranger and Tafjord fjords with associated small towns and settlements. The area has had fatal rockslides happen before: the Tafjord event in 1934, where 2-3 million m^3 of mountainside plunged into the fjord, leading to a tsunami with run-up height of more than 60 m (Oppikofer et al. 2009), as well as the Loen events in 1905 and 1936 in Nordfjord, Sogn og Fjordane (Ramberg et al. 2008). Other areas of interest are the Hegguraksla mountain and the Norddal valley.

3.3.3 Geology and structures

Autochthonous rock types from the Precambrian period were deformed and altered during the development of the Caledonian orogeny, and cover the whole of the area of Storfjorden (Henderson et al. 2006). The Tafjord and surrounding fjords all have substantial fan-like submarine rock avalanche deposits, probably triggered by weak rocks, steep cliff formations and/or earthquakes (Braathen et al. 2004). The rockslide area at Åknesfjellet is well-documented and consists of a back scarp, a basal shear zone at about 50 m depth and an interpreted toe zone where the sliding surface daylights the

surface (Ganerød et al. 2008). However, the entire area is, as mentioned over, susceptible to rockslides.

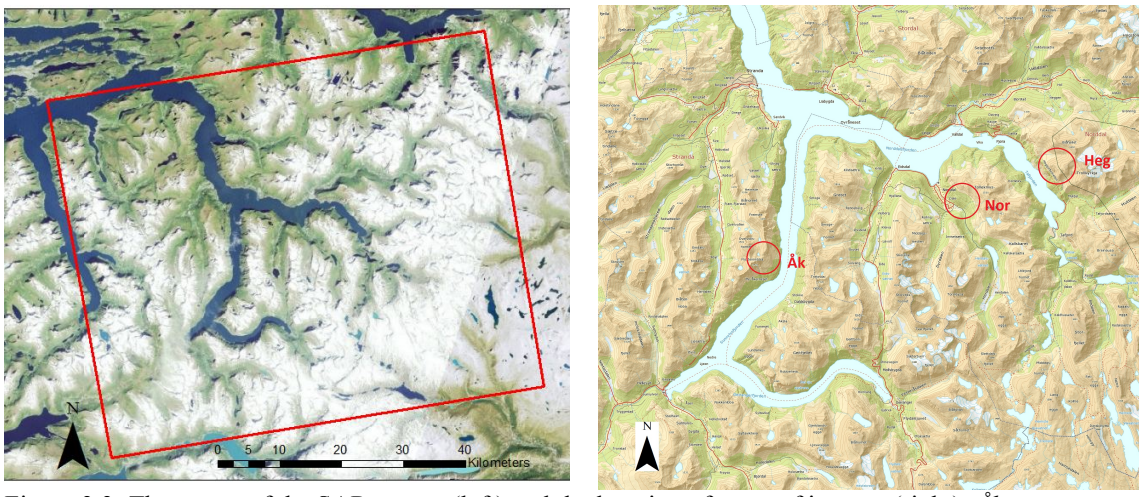

Figure 3.3: The extent of the SAR scenes (left) and the location of areas of interest (right). *Åk* = Åknesfjellet, *Nor* = Norddal, *Heg* = Hegguraksla. Norgedigitalt (Norge i Bilder, Statkart) and norgeskart.no as background images, downloaded 25.09.2012.

3.3.4 Former investigations

Particularly the Åknesfjellet rockslide area is well-documented throughout the last decade, and thorough discussion of the rockslide is found in, amongst many, Henderson et al. (2006), Braathen et al. (2004), Ganerød et al. (2008) and Derron et al. (2005).

3.3.5 SAR-recordings used

ALOS PALSAR scenes from ascending orbit, track 639, frame 1240. The ALOS PALSAR data are courtesy of ESA under AOALO.3579.

Area	Image pairs	Baseline $B_{\perp}$ (m)
Tafjord	20070902_20080904	-6044,85
	20070902_20090907	-1896,73
	20080904_20090907	4150,35

Table 3.3: SAR scenes used for Differential InSAR in Tafjord, western Norway.

3.3.6 DEM

The Norwegian Mapping Authority (Statens Kartverk) offers a DEM with 10 m resolution. This was resampled to 30 m, to fit with the SAR image resolution. The

precision of the DEM is given as 3-4 m in mountainous areas and 2-3 m otherwise, but could, particularly in areas with coarse topography and high elevations, be worse.

3.3.7 Background data

Norge i Bilder is used as a background image, as well as a topographic map image from norgeskart.no.

4 Processing the data

Processing has been done on the jern.uio.no server, where *Gamma* has been run through Shell in 64 bit RedHat enterprise Linux 5, 16 Xeon 2133 MHz processors and 98989 MB RAM. *Gamma* software ISP 1.1 and DIFF&GEO 1.2.

4.1 Co-registration and data preparation

Gamma software cannot use the original file formats of the ALOS PALSAR images. Therefore, some pre-processing steps have to be made. First, the images from ALOS PALSAR have to be transcribed into a format understood by *Gamma*. For most satellite images, the orbit state vectors have to be improved (ERS and Envisat vector products can be downloaded; while for some, such as JERS-1 and RADARSAT-1, no precise orbit data are available), but PALSAR data come with high-precision vectors and can be transcribed without any extra data (*Gamma* manual 2008). Precision orbit data is necessary for interferogram flattening and phase unwrapping, and should therefore be as precise as possible.

Before co-registering the single look complex (SLC) images, the PALSAR images can be oversampled into approximately square pixels by 1x4 for 15 m pixel spacing – a step *Gamma* mentions, but does not explicitly recommend (*Gamma* manual 2008). If an SLC is oversampled with a factor of 2, or more, prior to detection, aliasing due to increased bandwidth is eliminated and improves the sampling from the patch data (Werner et al. 2005).

Massonnet and Feigl (1998) recommend evaluating the geometric differences between the images, by correlating amplitude image patches. Modelling the geometric differences through a theoretical distortion grid and then resampling the slave to the master image. In *Gamma* (*Gamma* manual 2008), co-registering the scenes is done through computation of the offsets between the scenes, and then intensity tracking followed by coherence tracking provide offsets to be used in a Least Squares polynomial fit. The slave SLC is resampled to the master using a complex sinc interpolator. Images from areas with high contrast and/or fine topography are well suited for coregistration. The areas of interest in Iceland and Norway are anything but, with high mountainous

areas, challenging topography and, for Iceland, presence of sea in many images. This can prove challenging both for co-registering and further processing of the images.

In *Gamma*, the signal-to-noise ratio (SNR) is set to 7.0, meaning that only highly correlated areas through the scenes are used to compute the offsets used in the polynomial transformation between the slave and master scenes. By using 2D sinc interpolation, the slave SLC is resampled to the master SLC, and the sum of the residual offsets and the offset contribution determined from the polynomials during processing are the offsets used to resample the slave to the master SLC (*Gamma* manual 2008). A dense grid measuring the offsets between the slave images before and after resampling to the reference geometry can provide information on non-linear offset functions due to scene deformation (Massonnet and Feigl 1998), which is helpful if the topographic phase is the end result of the interferometric processing.

The final result of the processing is two segments from the original SLCs. These are used to create the differential interferograms.

4.2 Differential Interferometric SAR analysis

Depending on a DEM is available or not, 2-pass or 3-/4-pass differential interferometry is possible. If a DEM is available, 2-pass differential interferometry processing is possible, while 3- or 4-pass is necessary if a DEM is unavailable, or only DEMs of a too low quality can be accessed. 4-pass interferometry can also be used to process differential interferograms from two different image pairs, i.e., determining the relative displacement in LOS from time $period_1$ to time $period_2$. In this thesis, the 2-pass interferometric technique is used on the images; first, the differential interferograms from the different time periods are created, then the relative displacement in LOS from $period_1$ to $period_2$ is found. Removal of the displacement phase is done by combining the complex interferograms and reducing noise by scaling the baselines (*Gamma* manual 2008).

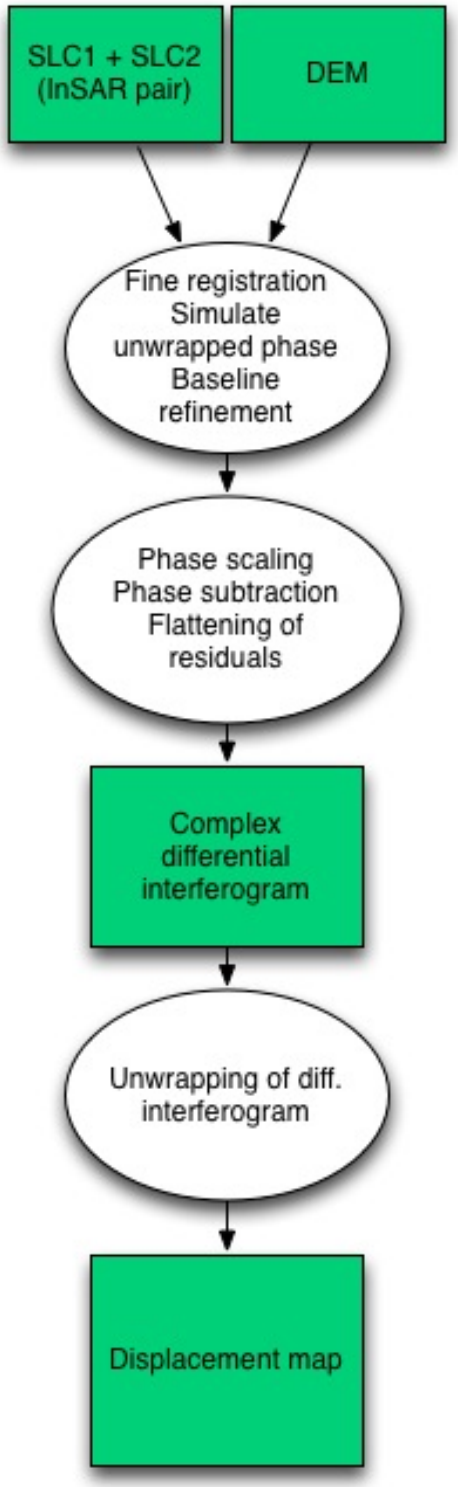

Figure 2.1: Flowchart describing the differential interferometric SAR processing in *Gamma*. Adapted from *Gamma* manual (2008).

Depending on the type of data available, the interferograms containing the differential phase effect can be wrapped or unwrapped before the formation of the differential

interferograms. If the interferogram is wrapped, some extra steps are necessary to get an unwrapped differential interferogram, but this can help if the orbital and/or baseline information is incorrect, through flattening and estimation of phase trends. If unwrapped, the phase trend can be removed through LS fitting techniques to adjust the scaling of the reference phase image (*Gamma* manual 2008).

Based on two SLCs and a DEM, the DEM is transformed into radar geometry and used as a simulated reference interferogram in the 2-pass differential interferometric technique. Based on this reference geometry, the interferometric baseline model and the height map in radar geometry the unwrapped interferometric phase corresponding to topography is calculated (i.e., the topographic phase). This topographic phase can either be subtracted from the unwrapped phase, or from the complex interferogram. In areas with relatively flat topography or little noise, subtraction of the topographic phase from the unwrapped phase is adequate, but for images with rugged topography and higher noise levels, subtracting the topographic phase from the complex interferogram (and following by unwrapping the differential phase) might be easier in stead of unwrapping of the phase image, due to the robustness of the complex interferogram. The drawback of this approach is that the scaling of the topographic phase (due to errors in the baseline model) cannot be improved through LS-fitting (*Gamma* manual 2008). ALOS PALSAR images, as used in this thesis, have very precise orbit metadata, and should display no errors due to errors in the baseline model.

The atmospheric phase contribution, as seen in eq. 2.29, is important, whether the interferograms are unwrapped post or prior to forming the differential interferograms. This could be mitigated through an estimated linear phase trend or through stacking of interferograms (*Gamma* manual 2008; Williams et al. 1998). When processing the data, estimation of linear phase trend was not incorporated, but a low-pass filter was used to remove atmospheric noise.

The DEM in simulated SAR phase is subtracted from the wrapped interferogram, the baseline parameters are refined and a refined differential interferogram is created based on the new parameters. Following this, a low-pass filtered version is produced and the differential interferogram has the low-pass filtered version removed to create a

high-pass filtered version, and displacement vectors in LOS are found. Depending on coherence thresholds, more or less of the differential interferogram is kept during unwrapping. This is also dependent on the unwrapping algorithm used (see subchapter 2.2.9); in this thesis the Minimum Cost Flow (MCF) technique in combination with a triangular irregular network (TIN) is used. The main advantage of this technique is the possibility of unwrapping large interferograms as well as enabling consideration of areas with very low coherence in the process. The results from the unwrapping are transformed from phase to deformation (cf. eq. 2.17). After this, the results are geocoded and exported to map geometry; this is to make the interpretation of the results easier also for the non-specialist. Binary float format is used for all the data in this thesis, meaning that they can be exported into programs like the ArcGIS program package.

5 Results

Here, the results from the DInSAR processing from the areas in chapter 3 are presented. Choices have been made as to which images are presented here, but all the processed images can be found in Appendix A, arranged according to area and the date the SLCs were acquired. The areas covered by the scenes are large, and a selection of relevant areas is discussed here to highlight both difficulties during processing and other sources of error. First, problems with coregistering, the atmosphere/troposphere, and the weather conditions are highlighted, and then the results of the processing are discussed.

5.1 SAR-scenes, coregistering, atmospherical conditions and weather conditions

Amplitude in SAR images is heavily dependent on the terrain aspect, the roughness of the terrain as well as the moisture levels on and in the ground. For differential interferometry, this is usually not an issue, unless there are factors affecting the ground quality, such as snow or heavy rain. In some of the images from north-eastern Iceland, snow cover is apparent in several images, particularly in the October 2009 images. See figure 5.1. Amplitude differences can be shown by using a colour composite image, "change-detection images", made from images acquired at different times from the same area, added to different channels in a composite image (RGB).

	Red	**Green**	**Blue**
Austurland S	18.08.2007	23.08.2007	26.08.2010
Austurland N	18.08.2007	23.08.2007	26.08.2010
Tröllaskagi S	01.10.2007	03.10.2008	09.07.2010
Tröllaskagi N	16.08.2007	01.10.2007	07.09.2010
Tafjord	02.09.2007	04.09.2008	07.09.2009

Table 5.1: The scenes used for composite images for change detection.

In figure 5.1, this type of image is shown for all areas, and the differently coloured areas show differing vegetation and moisture levels. Images acquired within the same month and season will have differing amplitude levels due to the differing moisture levels in

the ground and on the surface, while images from different seasons will have vegetation differences as well. Grey areas are areas with similar amplitude in all three scenes.

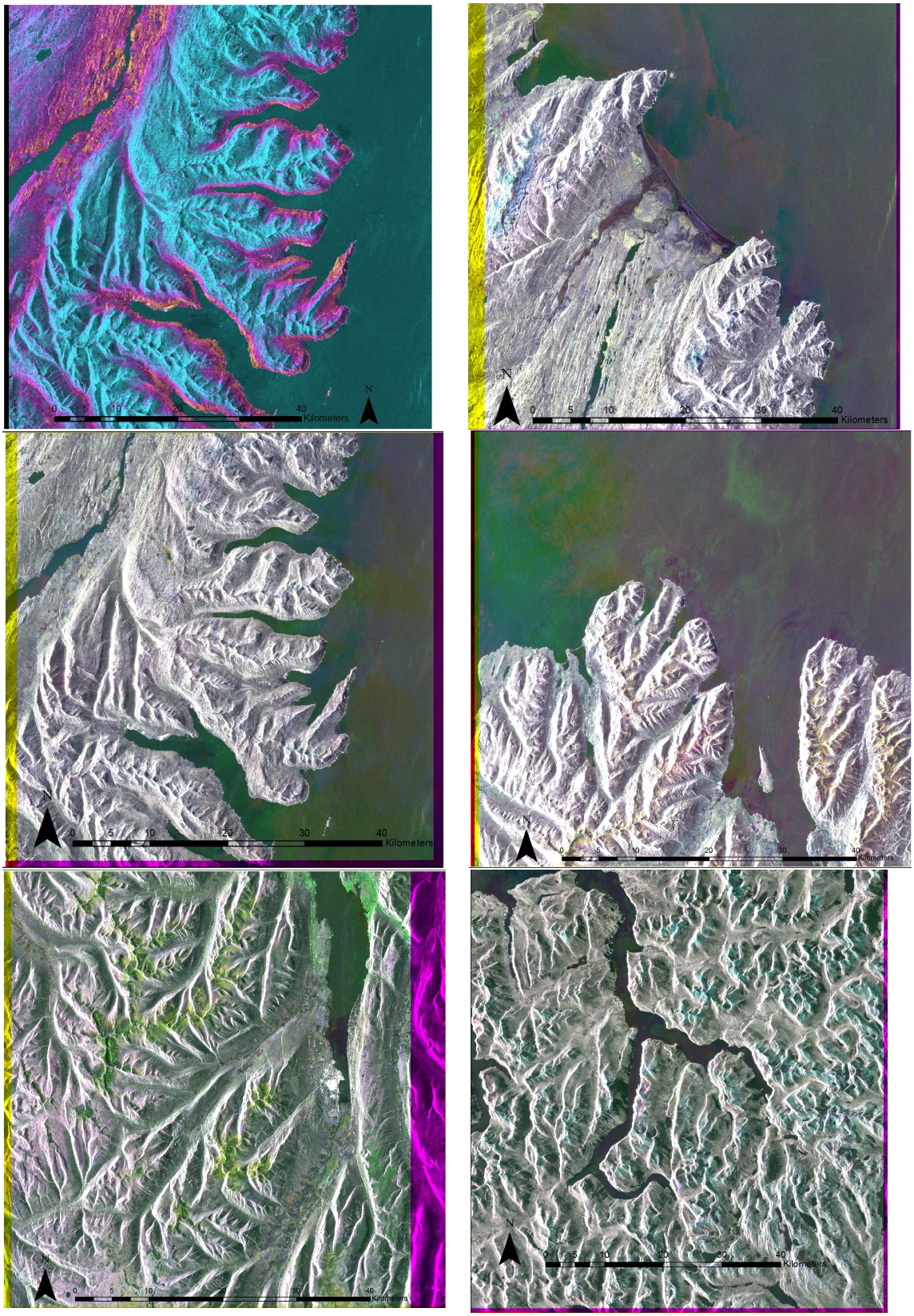

Figure 5.1: Coherence image from 23.08.2009-08.10.2009 (top l.). Composite images from Austurland N (top r.), Austurland S (middle l.), Tröllaskagi N (middle r.), Tröllaskagi S (bottom l.) and Tafjord (bottom r.) – see table 5.1 for images used.

The composite images from Austurland have a uniform grey colour, only with some blue in the mountains in the Austurland N image, in the northwest and the southeast. This could be an indication of more moisture in the 2007 and 2008 images, either due to rain or to other conditions, such as wet snow, in the 2007 and 2008 images. In the Austurland S image, large areas with green in the valleys are an indication of drier conditions in October 2008 than in October 2007 and July 2010. The Tafjord composite image has blue areas across the entire image, showing drier conditions in September 2009 than in the previous years.

The varying conditions in some of the images mean that some have to be discarded in the analysis, particularly images where wet snow cover in one of the images makes analysis difficult (ref. fig. 5.1). From tables 21, 30 and 39 in Appendix B, it can be seen that snow fell in north-eastern Iceland in the beginning of October 2009. The mean temperature was around 0°C, i.e., the snow present in the images is probably wet. Differential interferograms with large gaps lacking phase information and containing phase jumps, are difficult to unwrap, and might contain false displacement due to phase unwrapping problems. Long baselines will, in most cases, worsen the results even more. Even if the topographic phase is subtracted, residues of the topographic phase might still be contained in the signal and the displacement results thus reflect the topography in addition to or instead of displacement. If the DEM used contain large errors, such as over- and underestimation of the terrain, this will also influence the results of the interferometric processing. Some scenes were affected by processing errors, producing artefacts in the unwrapped differential interferograms (see for example fig. 5.21), such as sharp breaks in the unwrapped phase, “smears”, geometric shapes and blocky shapes. One image contains a large ionospheric disturbance, image 20070816 from Tröllaskagi S, see figure 5.2. The uneven band crossing the image in the south-eastern corner, stretching towards the west, is an ionospheric disturbance, but not the more common kidney-shaped type (Massonnet and Feigl 1998).

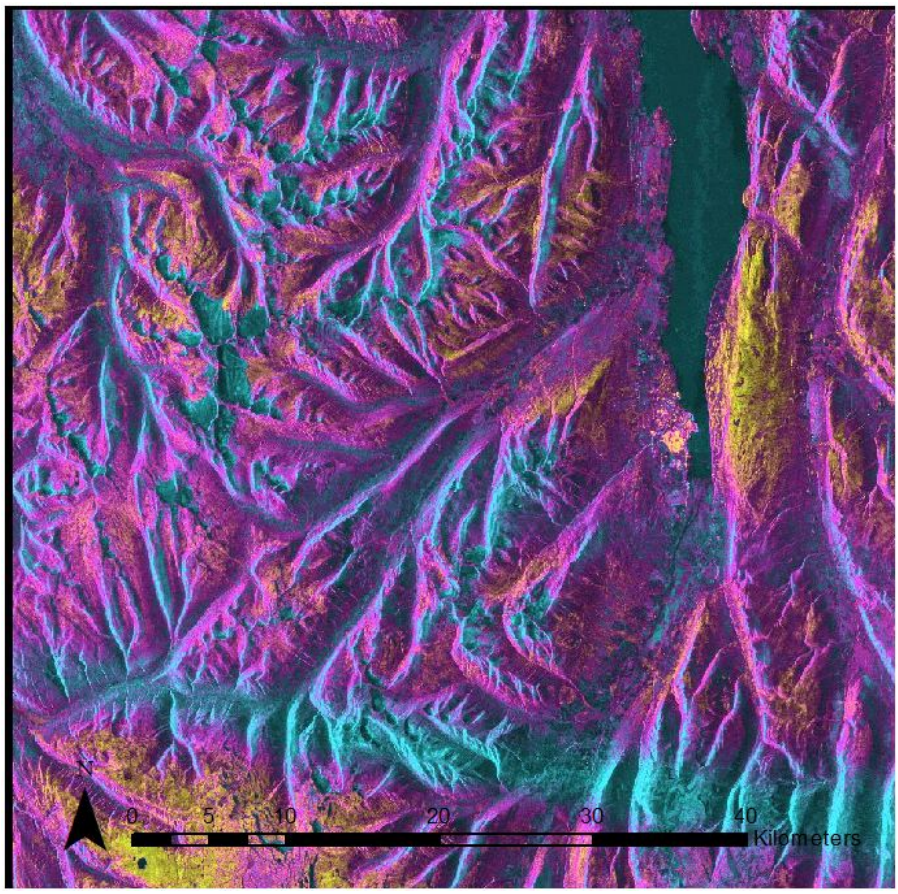

Figure 5.2: Coherence image from 16.08.2007-03.10.2007 images.

Meteorological data acquired from vedur.is show that heavy rain and/or snow fell between August and October in most years from 2007-2010. Particularly snowfall, but also heavy rainfall, change the surface properties recorded by the SAR sensor, resulting in decorrelation from $time_1$ to $time_2$. Meteorological data has to be taken into consideration (meteorological stations, locations of these and precipitation/temperature tables found in Appendix B), particularly precipitation in combination with temperatures close to 0°C such as station 425, Torfur, in Tröllaskagi October 2008. Here, a snowfall probably contributed to a lower coherence in differential interferograms containing the October 2008 image.

5.2 Results from the DInSAR analyses

In this chapter, results from the differential InSAR analyses are presented. The areas covered by ALOS PALSAR images are big, about 40x60 km in size, while the detected displacements are some meters to some hundreds of meters in cross-section. In order to meaningfully discuss the detected displacements, a selection of areas of interest has

been made. Simple statistics are presented in some cases to make the discussion of the results more meaningful.

Layover and shadowed areas are masked by *Gamma*; this is achieved through knowledge of the topography in the investigated areas and the geometry of the radar system. Areas in contact with layover are generalized and added to the layover mask due to its unsuitability for interferometric analyses. Layover for ALOS PALSAR SAR ascending images is found in slopes with south-eastern aspect and a slope angle exceeding 7.9° – 60.0° (image centre 34.4°) depending on near or far range. All images used in this thesis are from ascending orbits.

All coherence images are found in Appendix A, with their corresponding histograms showing the distribution of coherence in each image.

In general, the differential interferograms created from scenes acquired within the same year is of high quality. Coherence is good, and the differential interferograms are not influenced by any residue topographic phase. Some DEM errors are apparent, such as in the 16.08.2007-03.10.2007 unwrapped differential interferogram (see fig. 5.3). The line crossing the Dalsmynni peninsula to the east of Tröllaskagi is a DEM segmentation error, and clearly produces an error in the differential interferogram. Other DEM errors might not be as clear as this, producing erroneous displacement or, in combination with a large baseline, large residues of the topographic phase across the differential interferogram. Images with a small baseline perform better in the differential interferograms than images with a large baseline, despite a large temporal separation. See for example the unwrapped differential interferograms from Tröllaskagi (fig. 5.3), where the 16.08.2007-03.10.2008 scenes have a baseline of 5333.77m, low coherence and only patches of unwrapped phase in the differential interferogram, whereas the 16.08.2007-09.07.2010 scenes have a baseline of 1599.53 m, high coherence in parts of the scenes and the differential interferogram contain large, continuous areas with unwrapped phase. Other sources of error over entire differential interferograms are unwrapping errors, where particularly phase jumps, in areas with steep slopes, and other types of large gaps can introduce errors across parts of the differential interferogram. Both Norway and Iceland have challenging topography and

climate for differential interferometry, and this introduces some error sources in the images, as noted over. In the 16.08.2007-09.07.2010 differential interferogram from Tröllaskagi south, some interesting effects can be seen (fig. 5.3). The baseline between the images is 995.73 m, but the quality of the unwrapped image is not particularly good, with apparent displacement over parts of the image, particularly in valleys to the south. This is probably due to tropospherical differences from October 2007 to July 2010 in addition to temporal decorrelation and DEM errors.

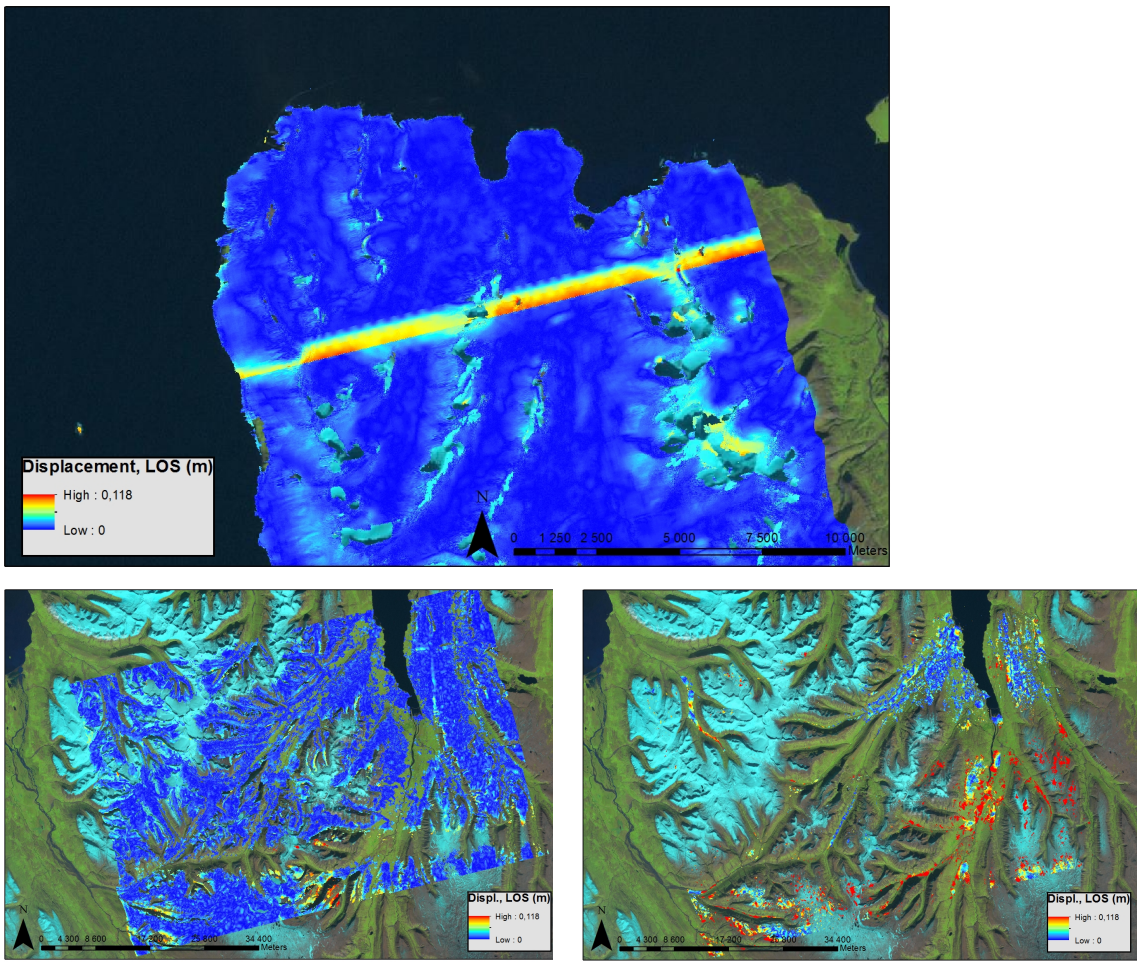

Figure 5.3: DEM error on Dalsmynni peninsula, northern Tröllaskagi from 16.08.2007-01.10.2007 unwrapped differential interferogram (top), 16.08.2007-09.07.2010 unwrapped differential interferogram (bottom left) and 16.08.2007-03.10.2008 unwrapped differential interferogram (bottom right). Landsat background image, downloaded 25.09.2012.

5.2.1 Tröllaskagi, Iceland

5.2.1.1 South: Svarfaðardalur, Fremri-Grjótárdalur & Hóladalur

The locations of the areas of interest are shown in fig. 5.4.

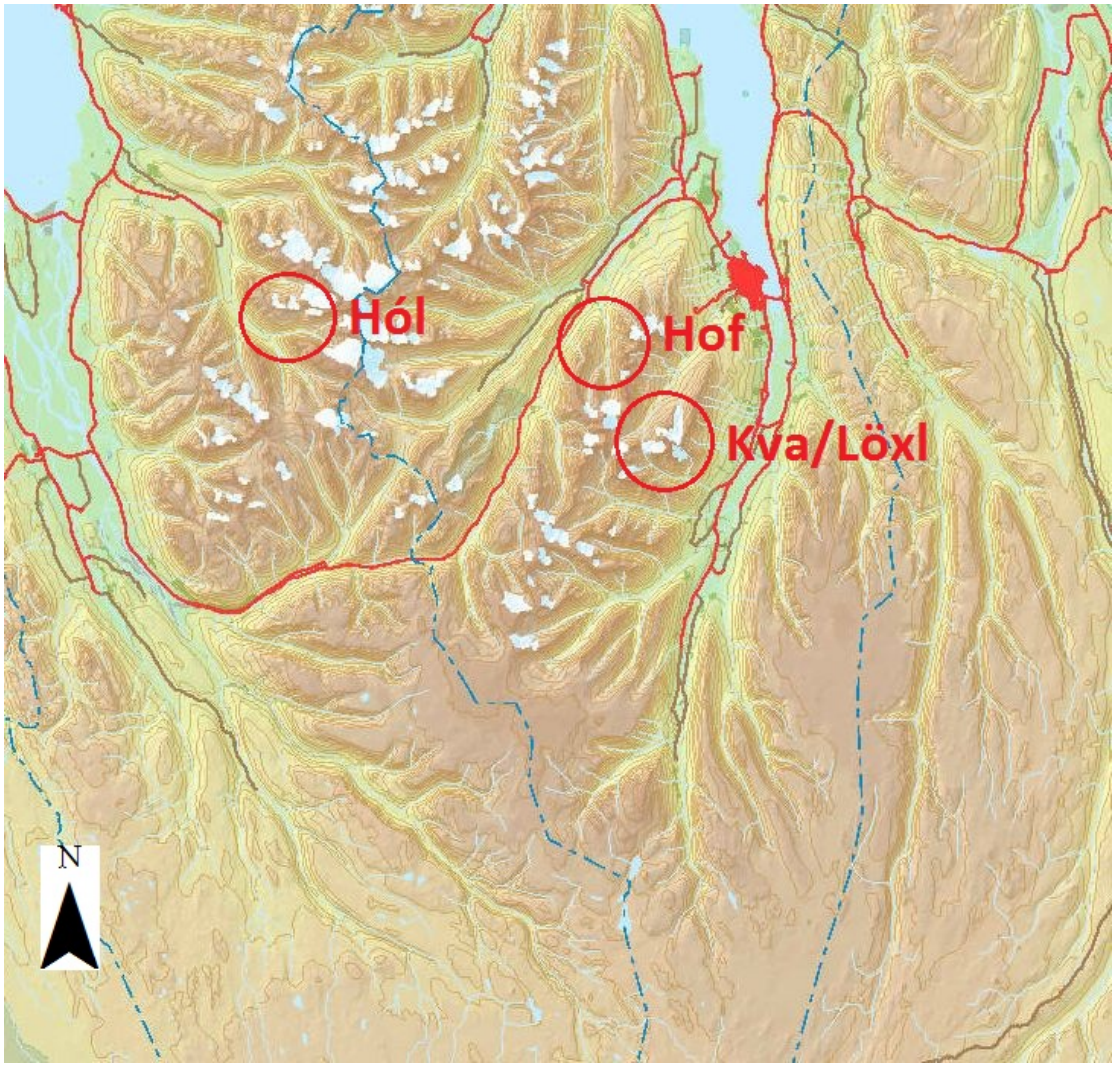

Figure 5.4: Locations of displacements discussed in 5.2.1.1. *Hól* for Hóladalur and Fremri-Grjótárdalur, *Hof* for Hofsárdalur and *Kva/Löxl* for Kvarnardalur and Lambardalsöxl. Map image downloaded from lmi.is, 25.09.2012.

In Hofsárdalur, a tributary valley to Svarfaðardalur, a valley extending to the south from the Svarfaðardalur in Eyjafjörður, a displacement of up to 9 cm in radar LOS can be seen in the 01.10.2007-09.07.2010 unwrapped differential interferogram, but just barely in the 16.08.2007-01.10.2007 unwrapped differential interferogram, up to 2-3 cm (fig. 5.5). The upper part of the area is masked, probably due to decorrelation from wet snow or temporal decorrelation. The images were acquired in October 2007 and July 2010 – i.e., in different seasons. Temperatures, humidity and air pressure is usually significantly different in July and October in Iceland, and added to this is the large temporal difference between the images. The detected displacement is in a valley with steep sides, something that can introduce height dependent tropospherical effects. Temporal, seasonal and height dependent tropospheric decorrelation all contribute to

the apparent, probably erroneous, displacement found here. Jónsson (2009) found displacements in the same area in his investigation, on a scale of 1-2 cm from July to August 2004, see fig. 5.6. His differential interferograms are wrapped, and show the same amount of displacement as the 2007 image pair from ALOS PALSAR.

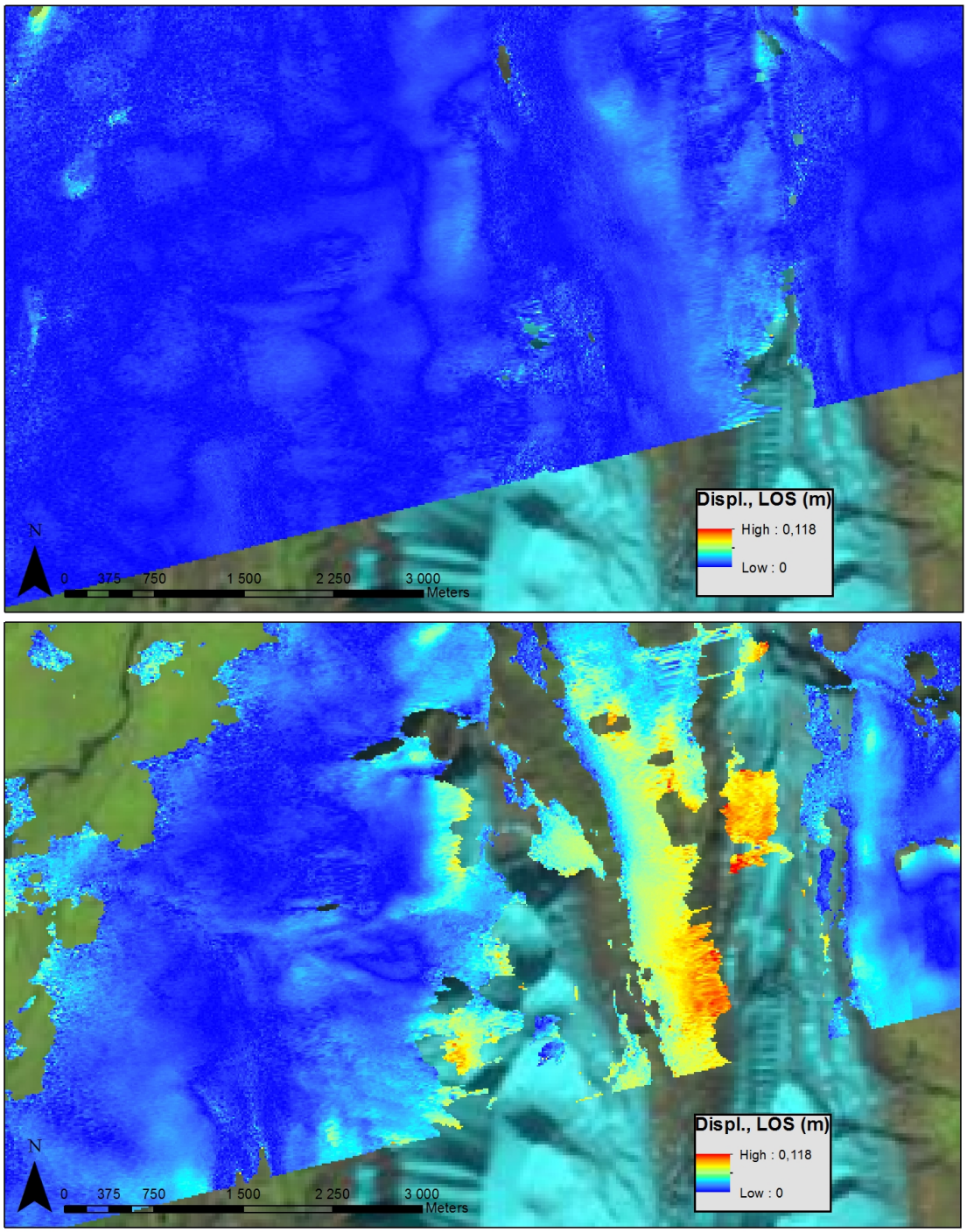

Figure 5.5: Displacement in Hofsárdalur. The unwrapped differential interferograms were created with the 16.08.2007-01.10.2007 (top) and 01.10.2007-09.07.2010 (bottom) image pairs. Landsat background image, downloaded 25.09.2012.

Fremri-Grjótárdalur and Hóladalur are two neighbouring valleys in south-western Tröllaskagi ("Hól" in fig. 5.4). Steep valleys, high plateaus and vegetated valley bottoms characterize this area, and some small glaciers are found in the area. Permafrost is probably present in the plateaus and valleys (Etzelmüller et al. 2007). Figure 5.7 shows the detected displacement in radar LOS for the dates 16.08.2007-01.10.2007, 18.08.2008-03.10.2008 and 16.08.2007-09.07.2010. A minimum detected displacement of 4 cm in radar LOS close to the toe of the rock glacier is detected at both locations in the 16.08.2007.01.10.2007 differential interferogram, with an increasing speed towards the rock glacier head at 11.8 cm at the most. This translates into a displacement parallel to the slope of 2.8 – 8.5 cm, assuming a 34° look angle. The heads of the rock glaciers are masked, probably due to accumulation of talus and snow, which has decorrelated the radar signal. In the 2008 image pair, the coherence is low, probably due to snowfall, and thus only parts of the image have a coherence of more than 0.7 (see Appendix A for statistics). The 2007-2010 unwrapped differential interferogram show decorrelation over the rock glaciers due to displacement (in radar LOS) greater than 11.8 cm, while the surrounding areas indicate little, if any displacement.

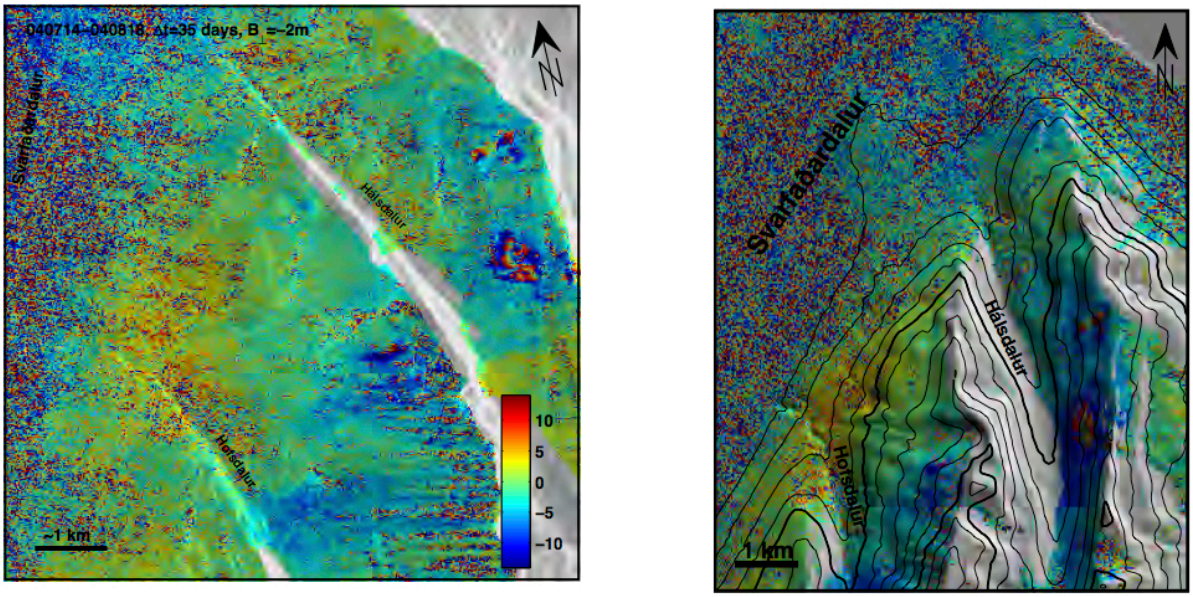

Figure 5.6: Hofsárdalur displacement from Jónsson (2009). Envisat images, displacement of up to 1 cm shown in the wrapped differential interferogram.

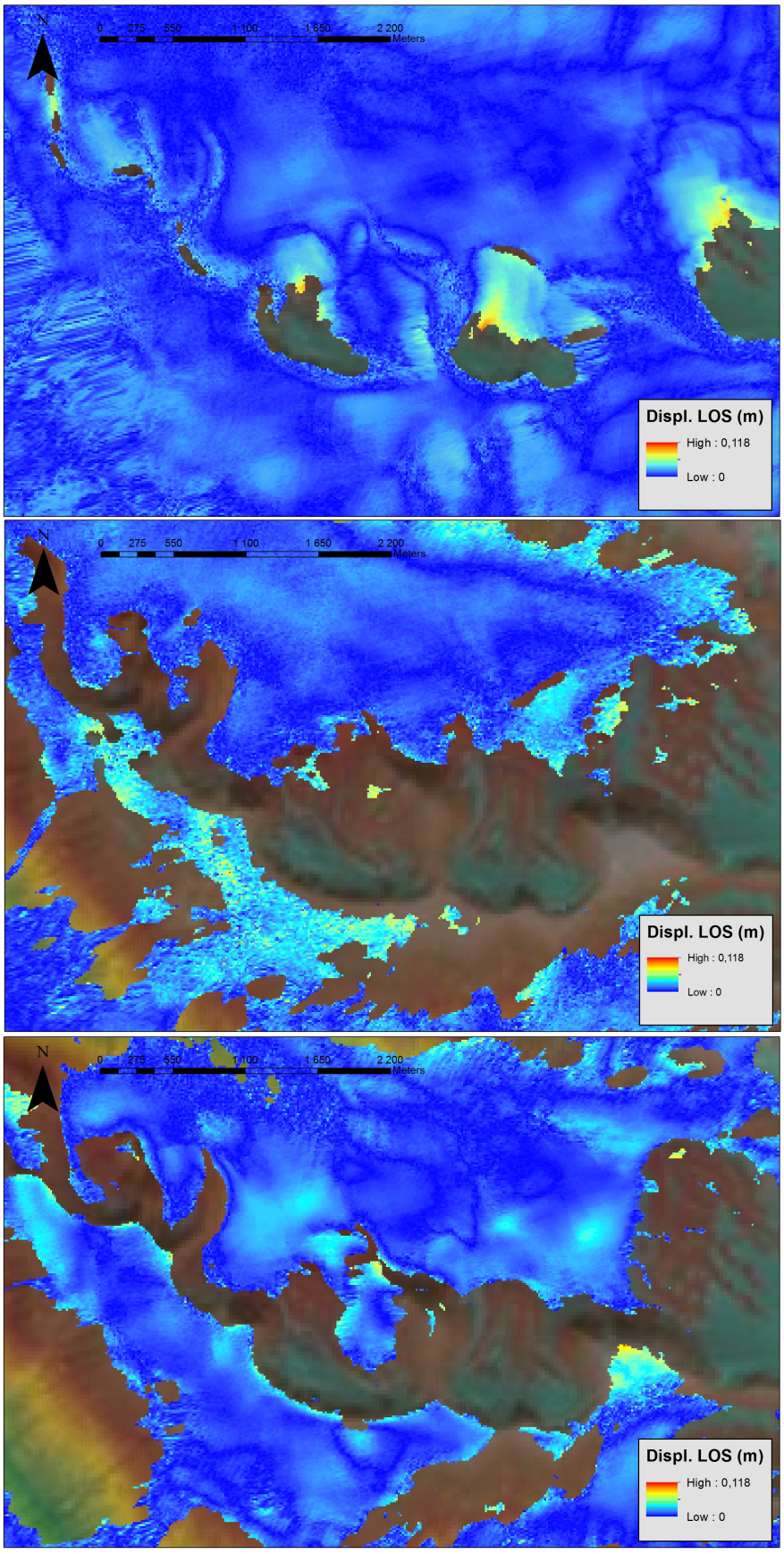

Figure 5.7: Unwrapped differential interferograms (in radar LOS) for 16.08.2007-03.10.2007 (top) and 19.08.2008-06.10.2008 (middle) and 16.08.2007-09.07.2010 (bottom). Landsat background image, downloaded 25.09.2012.

5.2.1.2 North: Almenningsnöf, Torfnavík and Höðnuvík

Locations of the areas with displacement are shown in fig. 5.8.

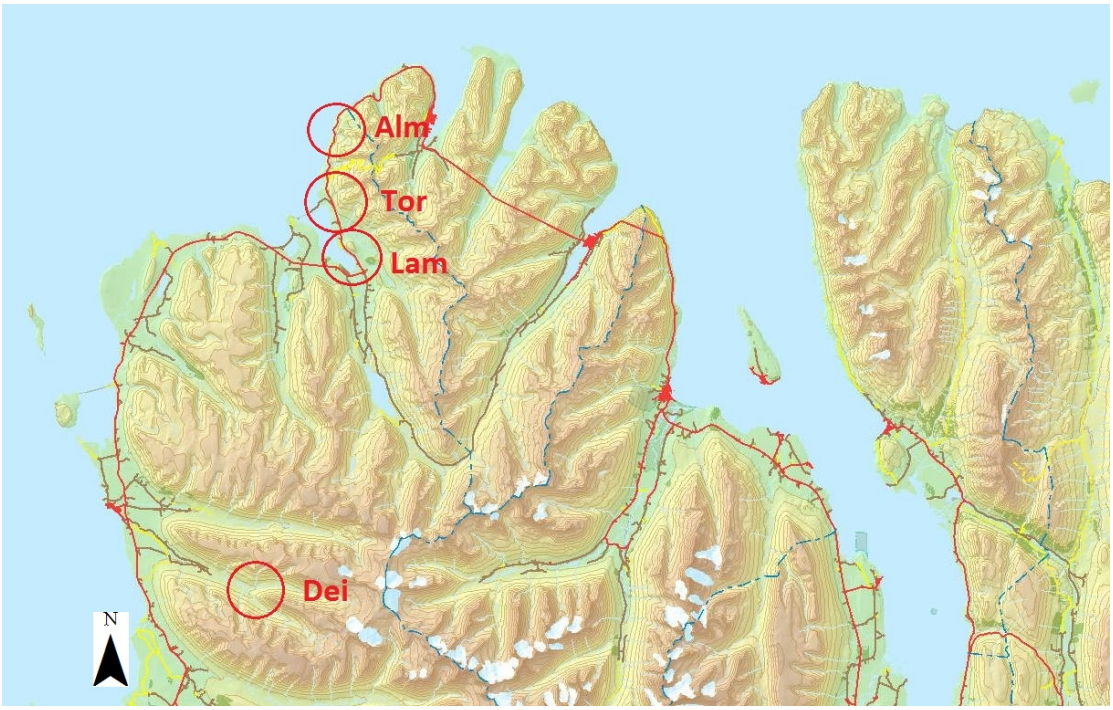

Figure 5.8: Locations of displacements discussed in 5.2.1.2. *Alm* for Almenningsnöf, *Tor* for Torfnavík and Höðnuvík, *Lam* for Lambanesás and *Dei* for Deildardalur. Map image downloaded from lmi.is, 25.09.2012.

Almenningsnöf is a well-known slow-moving landslide at the north-western tip of Tröllaskagi peninsula. The area is sparsely vegetated, and the area shows signs of moving masses, with transverse ridges and cracks criss-crossing the area. In figure 5.9 the radar LOS displacement for the area is presented, from image pairs 16.08.2007-01.10.2007, 16.08.2007-09.07.2010 and 01.10.2007-09.07.2010. All display displacement from t_1 to t_2, but the landslide is moving at a low velocity. From August to October 2007, parts of the landslide move only about 2-3 cm (in radar LOS) while the front has a displacement of about 9 cm in the same time period. The landslide has moved fast enough to become decorrelated in some areas from 2007-2010, but the general displacement for the entire area is close to 11.8 cm, and shows the full extent of the landslide. Wangensteen et al. (2006) found differing velocities in the landslide, bisected by a fault; the lower part had a lower velocity (see fig. 5.10). This is not discernible in the LOS displacement seen here. Jónsson (2009) found displacement on a magnitude of 1-2 cm in wrapped phase LOS in the lower part of the landslide with ERS and Envisat images from 1995 and 2004 (fig. 5.11).

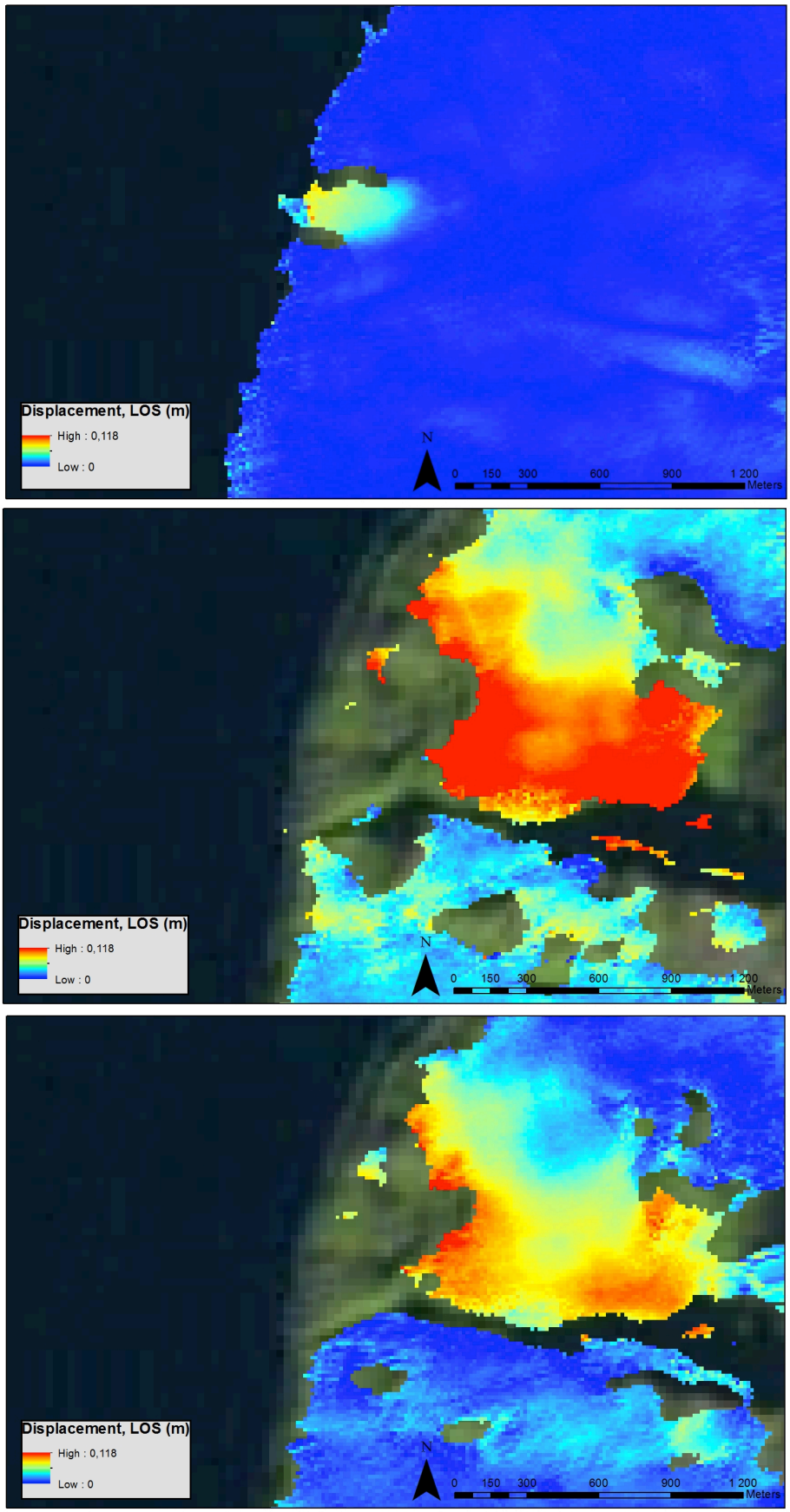

Figure 5.9: Unwrapped differential interferograms from Almenningsnöf. 16.08.2007-01.10.2007 top, 16.08.2007-09.07.2010 middle and 01.10.2007-09.07.2010 bottom. Landsat background image, downloaded 25.09.2012.

South of this location, in Höðnuvík and Torfnavík, larger, slower displacements seem to be active. In the 2007-results, the displacements are not visible from August to October (see fig. 5.12). However, the results from 2007-2010 show larger displacements, close to 9-12 cm (radar LOS) in some areas, while other parts of the areas are masked, probably due to large displacement rates over the 3-year period. These landslides are known from former investigations, both Jónsson (2009) and Guðmundsson (2000) have found similar results. A presumed landslide is present in Lambanesás, where a large displacement seems to be active, but this needs to be confirmed by either in situ examinations or by other remote sensing methods such as airborne or optical satellite image matching.

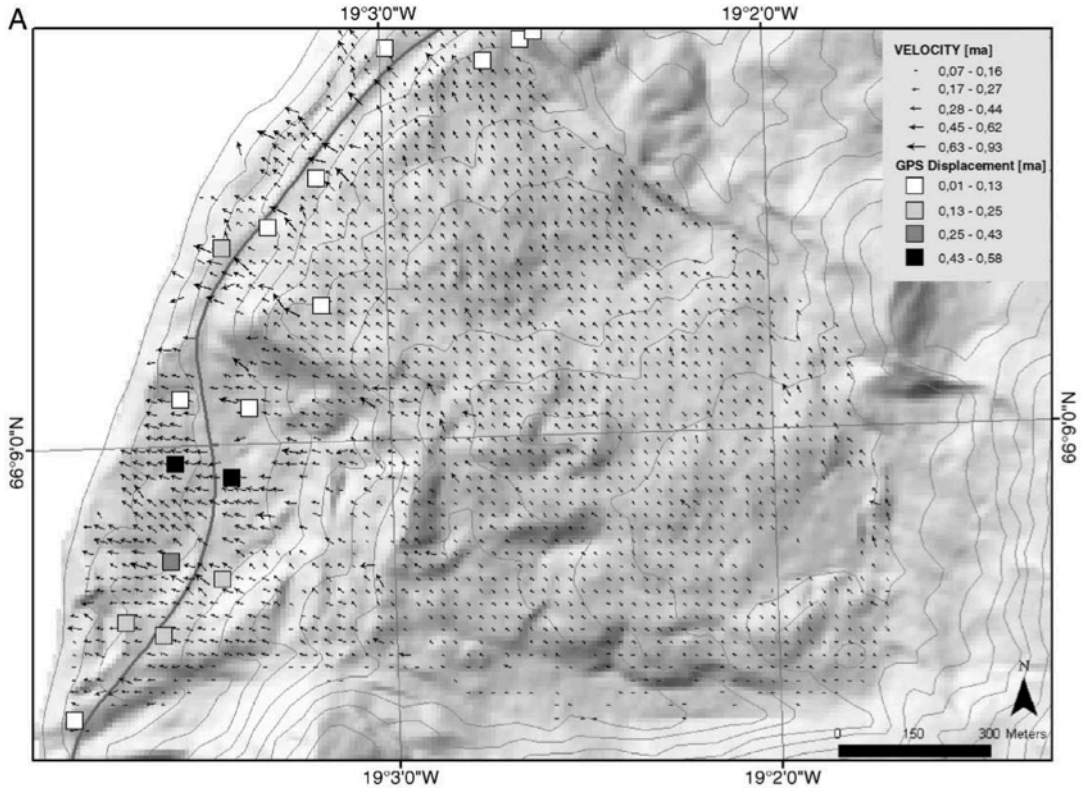

Figure 5.10: Displacement measured by Wangensteen et al. (2006) based on air photos from 1985 and 1994 compared with GPS measurements from Vegagerðin (Icelandic Road Authorities).

If the displacement in the direction of steepest descent is calculated, assuming a 34° look angle, displacement velocities close to 5.0-8.5 cm is found for Almenningsnöf in the 16.08.2007-01.10.2007 period (from the upper to the lower part), while the 01.10.2007-09.07.2010 period has velocities of 6.5-8.5 cm across the upper landslide area. Wangensteen et al. (2006) found an average velocity of 0.13-0.58 m a^{-1} for the different parts of Almenningsnöf for the years 1985 to 1994, and 0.15-0.38 m a^{-1} for the

years 1977-1985. Velocities vary within the landslide itself, with average velocities of 0.57 m a^{-1} in the south-western part, 0.33 m a^{-1} in the mid section and 0.13 m a^{-1} in the upper part of the body. The north-western part has an average velocity of 0.17 m a^{-1}.

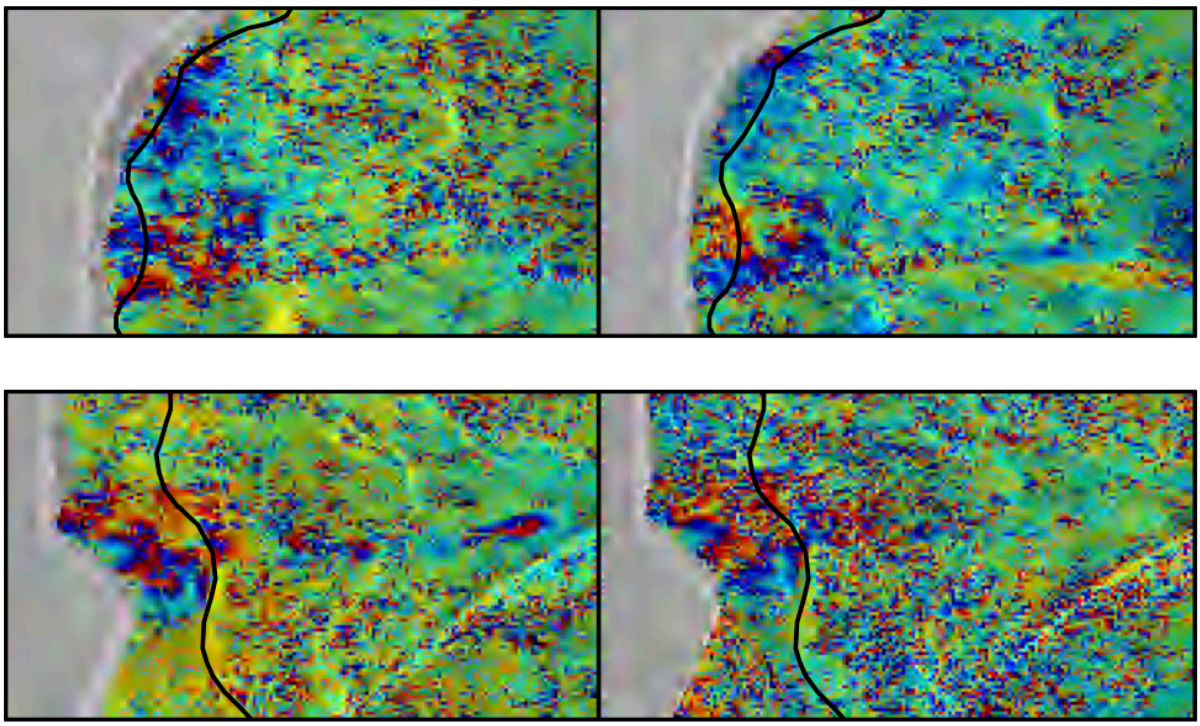

Figure 5.11: Almenningsnöf and Torfnavík from Jonsson (2009). Wrapped differential interferograms from ERS July-September 1995 (left, top and bottom) and Envisat June-July 2004 (right, top and bottom). Displacement detected only in the lower part of the landslide.

5.2.1.3 Other areas: Deildardalur, Kvarnardalur and Lambárdalsöxl

Other areas where displacement is detected are the Deildardalsjökull area, east of Höfðaströnd in Skagafjörður, and Kvarnardalur and Lambardalsöxl, south of Akureyri in Eyjafjörður. Here, at higher elevations, displacements similar to Hóladalur and Fremri-Grjótárdalur are found in the unwrapped differential interferograms. These displacements are probably some sort of permafrost creep, either rock glaciers or debris covered glaciers. In figure 5.13, these areas are presented (from the unwrapped differential interferogram from 16.08.2007-01.10.2007), and the lobate morphology, combined with transverse ridges on the surface of the landforms further indicate an active, permafrost-related surface creep. All three locations are in the vicinity of small glaciers, further indicating debris covered glaciers.

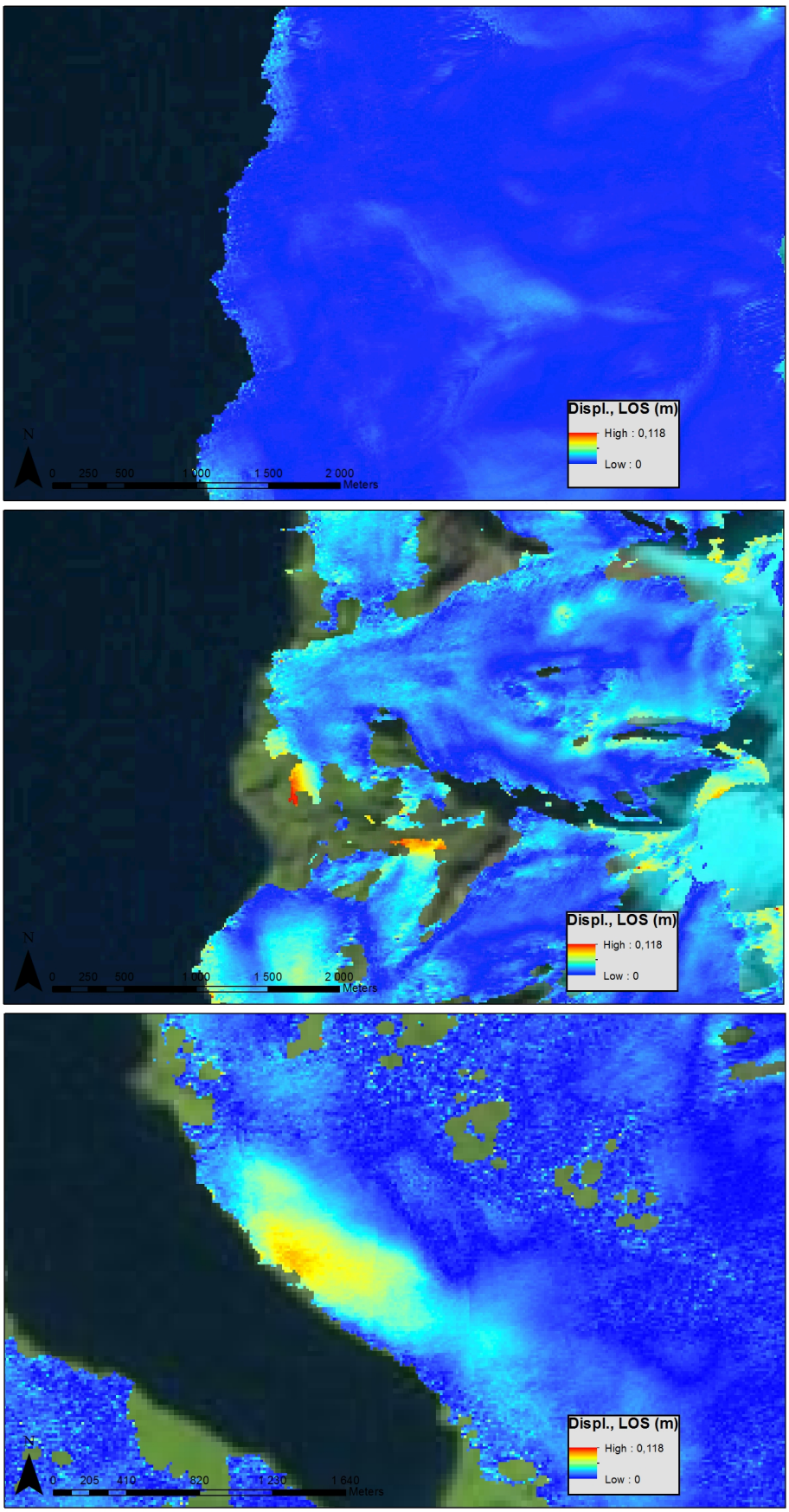

Figure 5.12: Unwrapped differential interferograms from Torfnavík (top), Höðnuvík (middle) and Lambanesás (bottom). T: 16.08.2007-03.10.2007 and 16.08.2007-09.07.2010; L: 16.08.2007-09.07.2010. Landsat background image, downloaded 25.09.2012.

The Deildardalur displacement is probably not a physical displacement of the ground. The size of the erroneous displacement is too small to be an ionospheric disturbance. When the shape of the apparent displacement is considered, as well as its placement in a slope with a north-northeastern aspect, it is probable that this is a combination of unwrapping errors and perhaps a DEM error. The baseline for the 16.08.2007-01.10.2007 differential interferogram is 607.69 m, one of the smaller baselines in this thesis. This makes the kidney-shaped displacement an indication of an unwrapping error or an atmospherical error of some sort. When looking at the wrapped differential interferograms in figure 5.13, it seems probable that the displacement is due to either a local, ionospheric or atmospherical effect or a DEM error, since the shape is present in the wrapped interferogram as well.

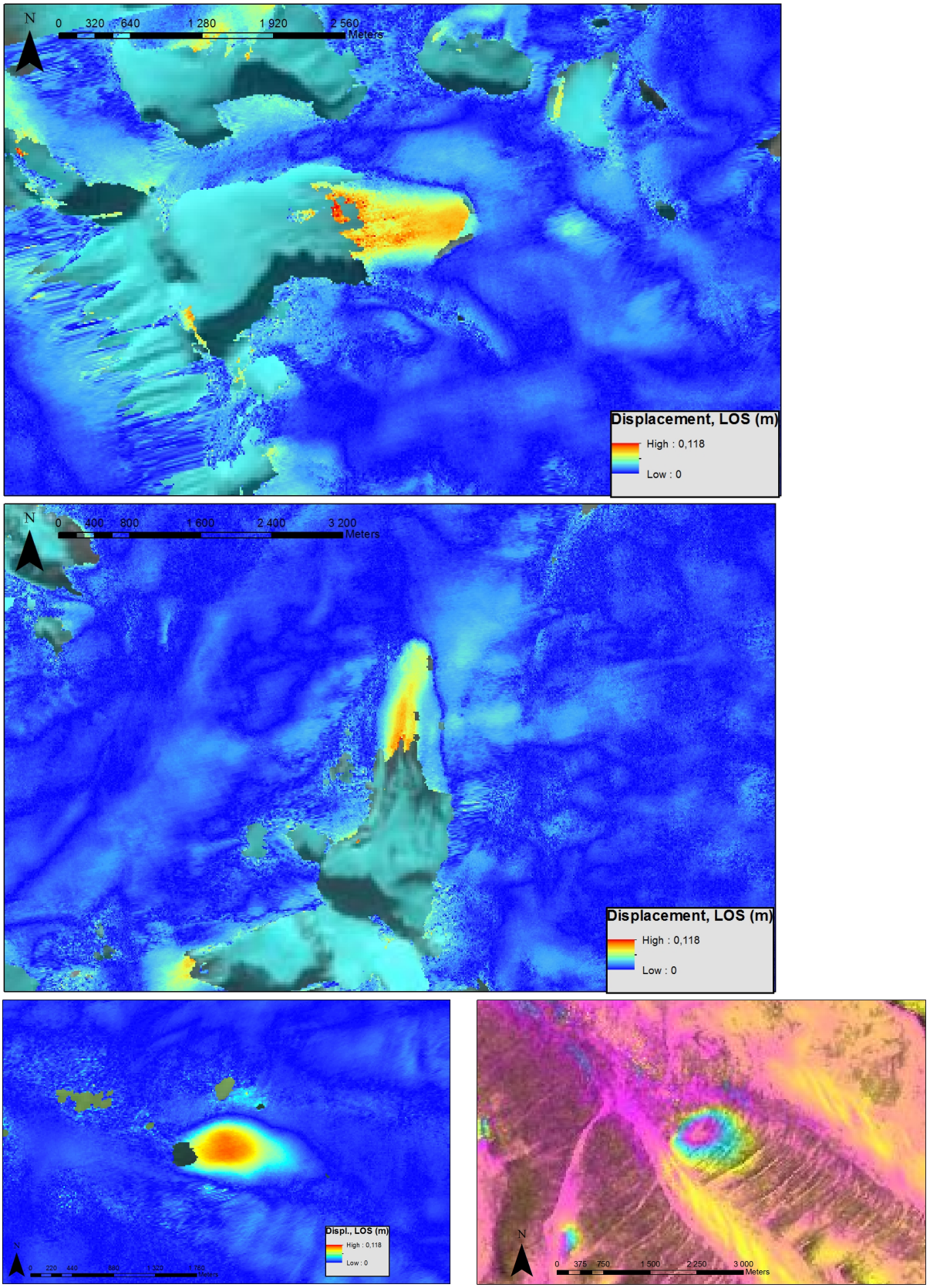

Figure 5.13: Kvarnardalur (top), Lambardalsöxl (middle), Deildardalur unwrapped and wrapped (bottom left and right), all from 16.08.2007-01.10.2007. Landsat background image, downloaded 25.09.2012.

5.2.2 Austurland, Iceland

5.2.2.1 South: Seyðisfjörður, Reyðarfjarður and Hólafjall

The discussed locations are presented in figure 5.14.

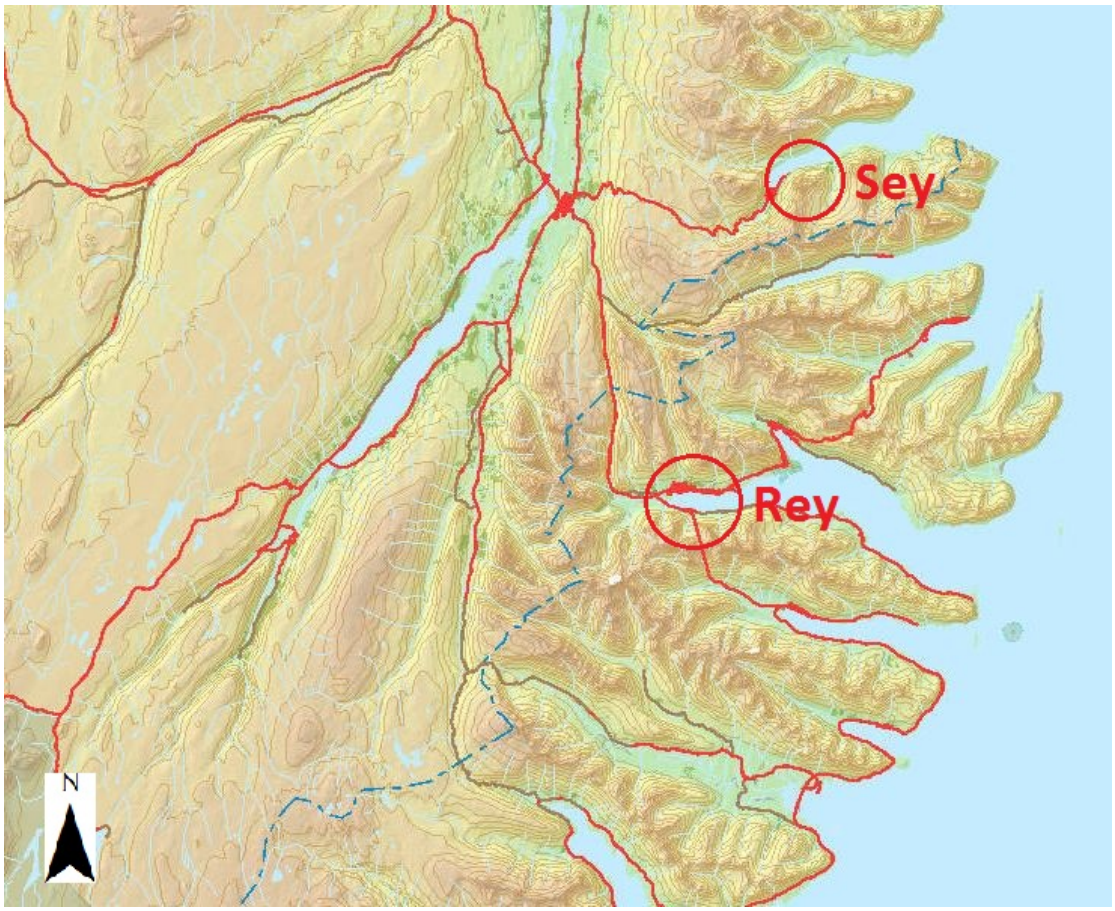

Figure 5.14: The locations of discussed areas in 5.2.2.1. *Sey* is Seydisfjordur and *Rey* is Reyðarfjörður and Hólafjall. Background map image downloaded from lmi.is, 25.09.2012.

The Seyðisfjörður landslide is well known, but does not display any specific landform in connection to the surface displacement. The landslide is placed in a slope above the Seyðisfjörður community, facing west. The slope is debris-covered, with little to no vegetation, and should have a high coherence (fig. 5.15). The size of the landslide area is found to be 400 x 250 m^2 (Jónsson 2007). Differential interferometric analyses show no significant displacement in the slope in 2007, 2009 and 2010, but from 18.08.2007 to 23.08.2009, there is an indication of displacement (fig. 5.15). However, there are large areas masked due to lack of coherence, this originating from signal decorrelation due to temporal or geometrical decorrelation. When comparing the unwrapped with the wrapped differential interferogram, it is apparent that the displacement is close to an area with layover and shadow, introducing a possibility of phase jumps in the unwrapping algorithm. Baseline for the 18.08.2007-23.08.2009 differential

interferogram is 1663.82 m, well below the critical length. Due to the geometry of the radar sensors, the sensor will not register any displacement or mass movement in azimuth direction. The Seyðisfjörður landslide moves in a north-north-eastern direction and the sensor will not pick up any displacement due to the parallel movement of the sensor to the landslide movement. If descending images were available, the landslide could possibly be detected. If there is any detected displacement in the interferograms, it is on a scale of less than some centimetres per year. Jónsson (2007) found displacement in some differential interferograms, and none in some (fig. 5.16). Episodic displacement is not unknown behaviour for this landslide, with displacement rates varying from ≥ 30 cm a^{-1} to almost 0 cm a^{-1}.

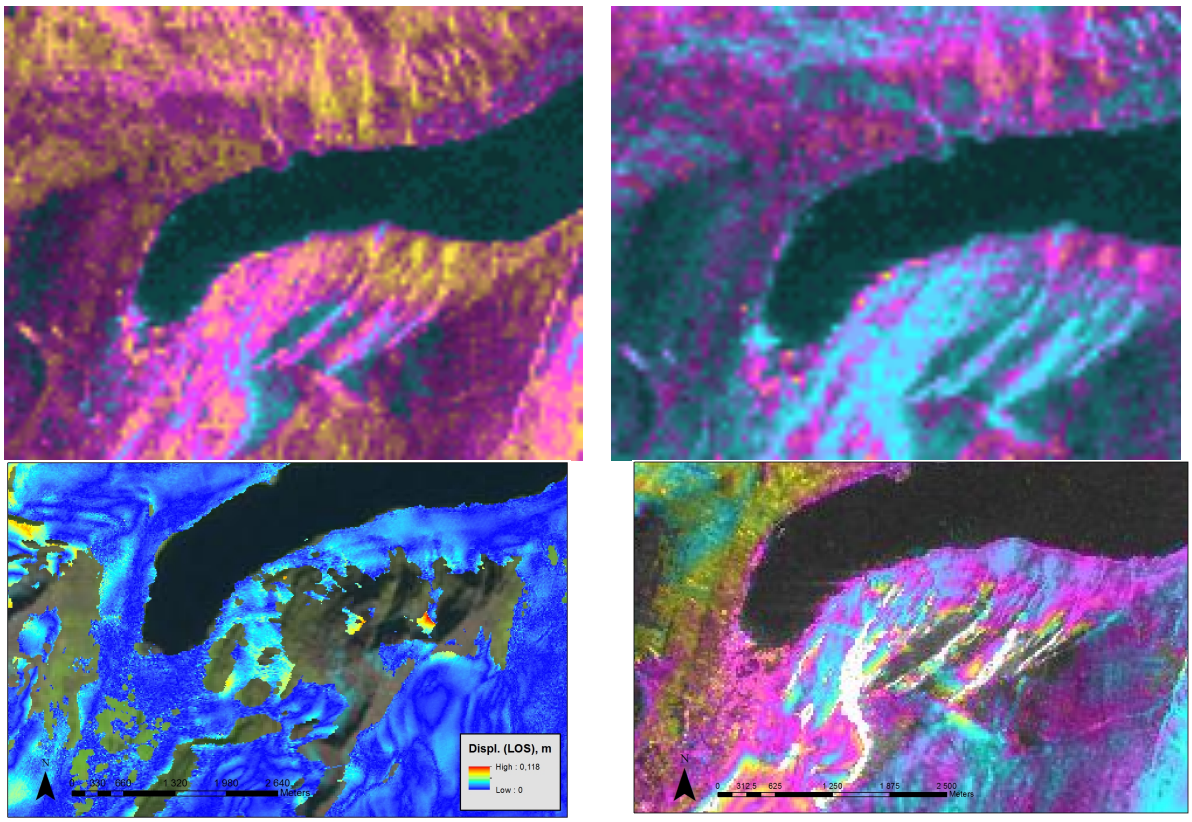

Figure 5.15: Coherence between the Seydisfjordur images 16.08.2007-03.10.2007 (top left) and 16.08.2007-23.09.3009 (top right), detected displacement (radar LOS) from 18.08.2007-23.08.2009 unwrapped differential interferogram (bottom left) and wrapped differential interferogram from 18.08.2007-23.08.2009 (bottom right). Landsat background image, downloaded 25.09.2012.

In Reyðarfjörður, another error in the DEM in combination with a north-north-eastern aspect shows up clearly (see fig. 5.17 for comparison of wrapped and unwrapped differential interferograms). When the results from 18.08.2007-03.10.2007 and 26.08.2010-11.10.2010 are compared, the half moon shaped mask is the same, but an

apparent phase jump is present in the 2007-image, this is due to an unwrapping error. Another area of interest is the area called Jökulbotnar on the south side of the fjord, where displacements of some centimetres are detected. Jónsson (2007) found displacement in the same area, but characterized it as "speculative", due to the area being snow-covered most of the year. In the unwrapped differential interferogram based on the 18.08.2007-23.08.2009 image pair (figure 5.17) there is detected displacement. However, it is detached from the surrounding phase, and is connected to areas masked due to shadow and layover. Displacement at this location could be plausible, but needs to be confirmed by in situ field investigations.

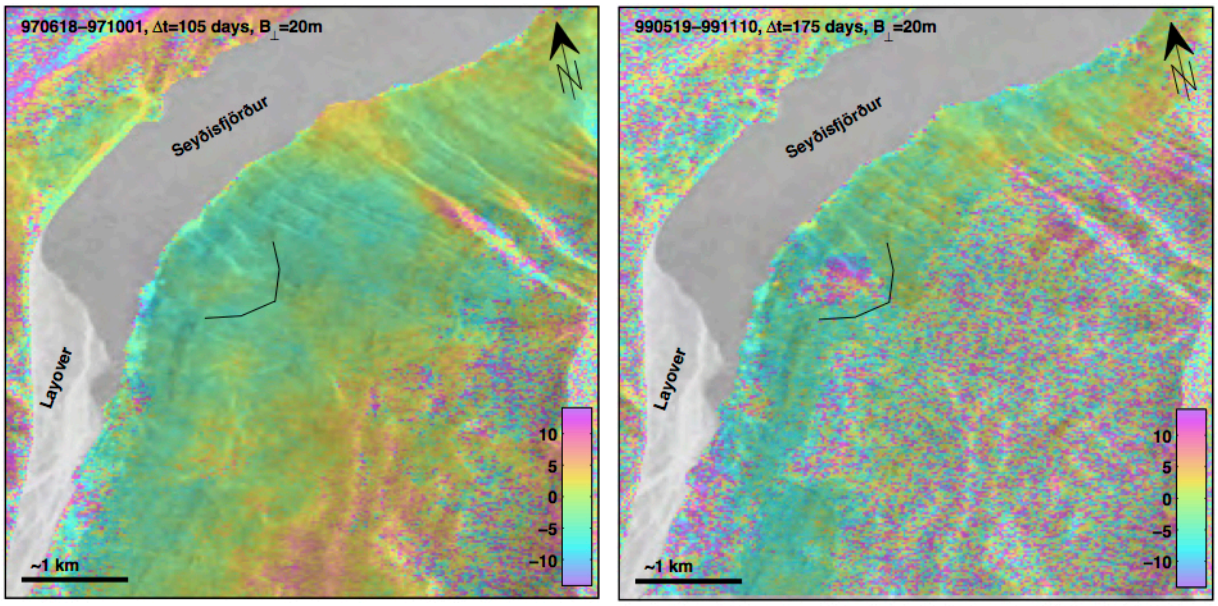

Figure 5.16: The landslide at Seyðisfjörður, from Jónsson (2007). ERS wrapped differential interferograms from descending orbits, showing displacement from May-November 1999 (right), but none from June-October 1997 (left).

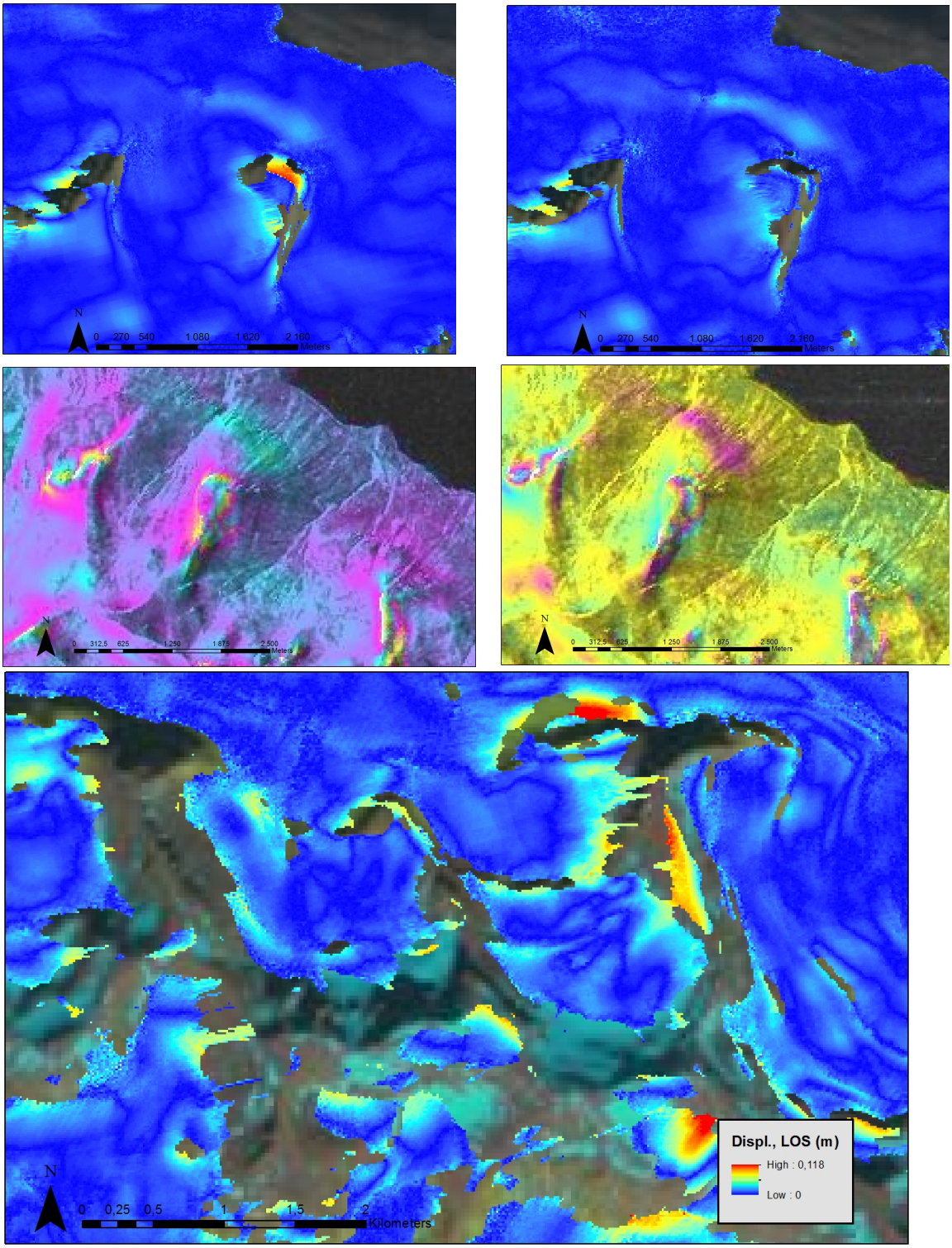

Figure 5.17: Unwrapping error in Reyðarfjörður, 2007 image pair to the top left, 2010 image pair to the top right, wrapped interferogram from 2007 (middle left) and 2010 (middle right). Jökulbotnar location (bottom image), unwrapped differential interferogram from 18.08.2007-23.08.2009. Landsat background image, downloaded 25.09.2012.

In the Hólafjall area there is a kidney-shaped displacement in a south-east facing rockwall, present both in the 2007-images and the 2010-images (fig. 5.18). The baselines between the images are 525.05m for the 2007 image pair and 602.64m for the

2010 pair, reducing any errors from the DEM. The shape and size of the displacement is too small to be an ionospheric disturbance, but it could be due to a combination of a small DEM error and southeast-facing slope, leading to an erroneous displacement signal. The wrapped differential interferogram (fig. 5.18) contain the same type of kidney shaped displacement signal, making a DEM error more probable.

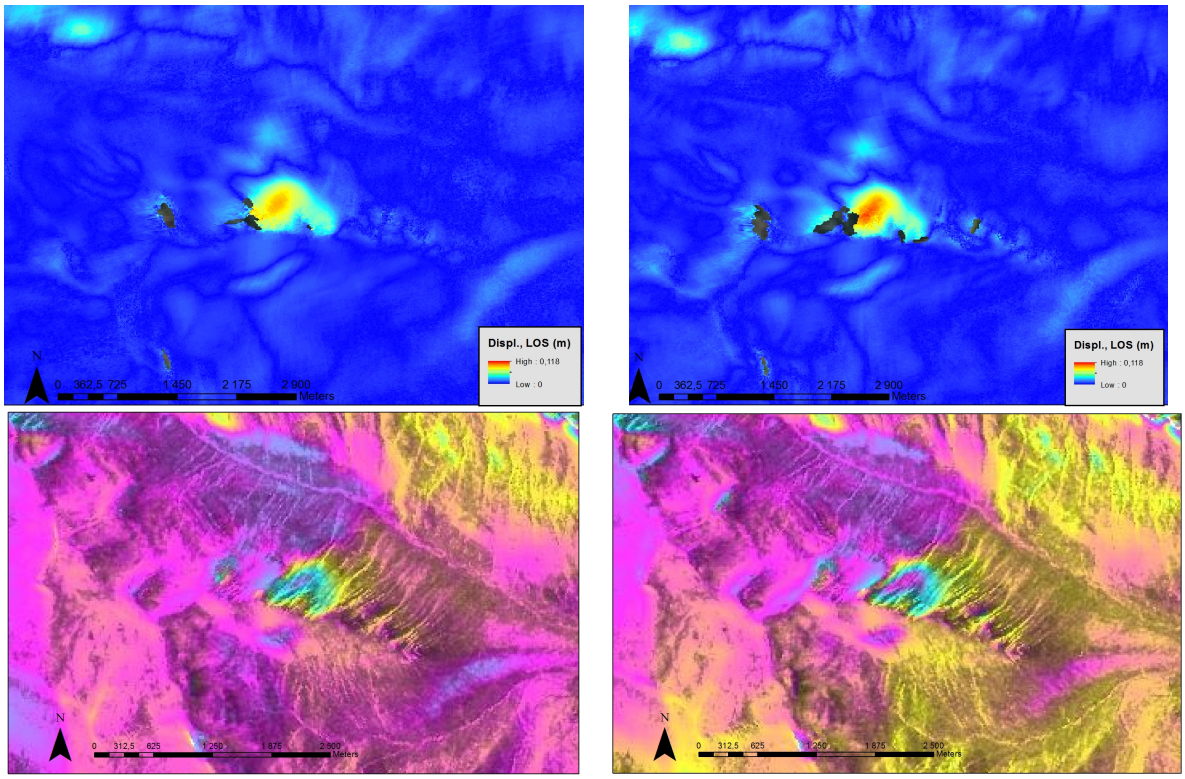

Figure 5.18: Hólafjall unwrapped differential interferograms: 18.08.2007-03.10.2007 (top left), 26.08.2010-11.10.2010 (top right). Wrapped differential interferograms: 18.08.2007-03.10.2007 (below left) and 26.08.2010-11.10.2010 (below right).

5.2.2.2 North: Lambardalur, Vopnafjörður

Locations of the discussed displacements are shown in figure 5.19.

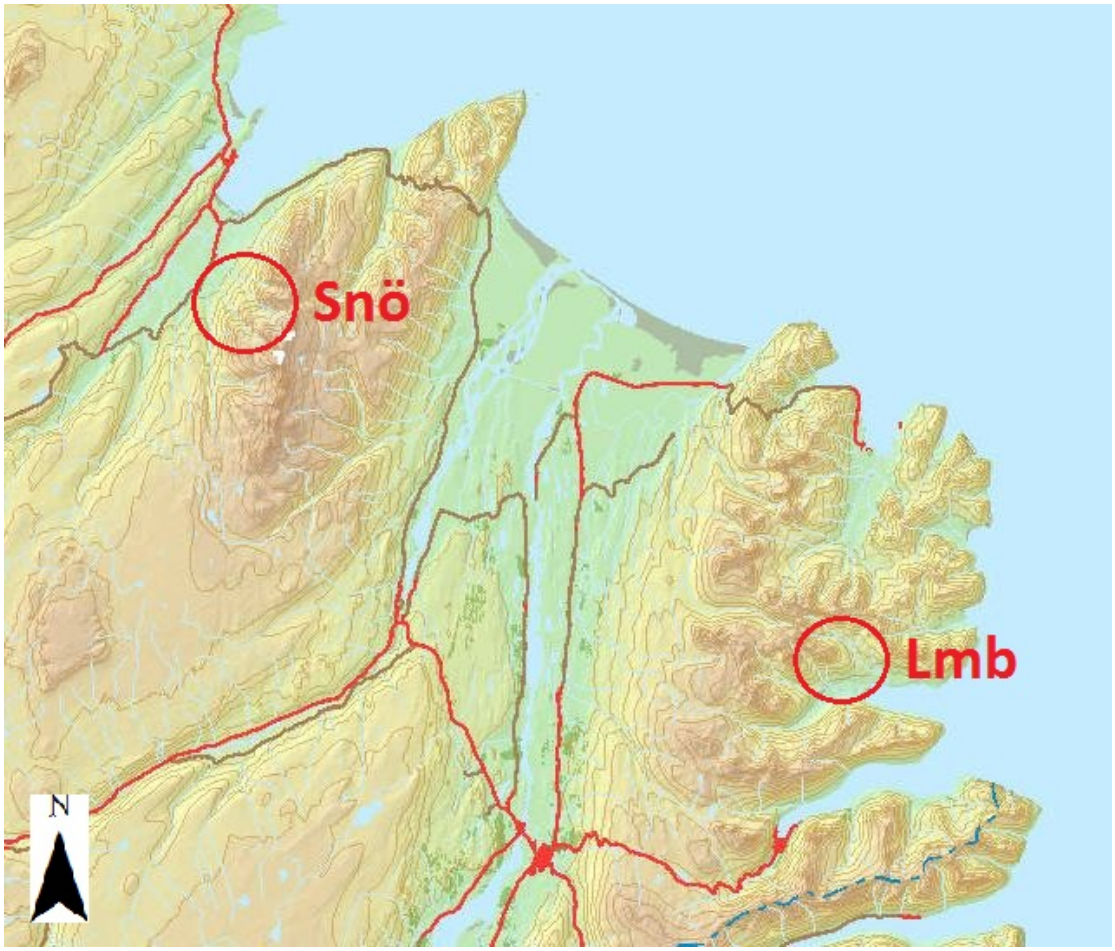

Figure 5.19: Locations of areas discussed in 5.2.2.2. *Snö* is Smjörfjöll and *Lmb* is Lambardalur. Map image downloaded from lmi.is, 25.09.2012.

Fewer apparent displacements are present in the northern part of Austurland. At the Nattmálafjall location in Lambardalur the unwrapped differential interferograms register apparent displacements. This corresponds well with the landforms present in satellite optical images, where landforms with a lobate morphology and patches of snow at the head of the landform are found. From Guðmundsson's thesis (Guðmundsson 2000, unpubl. MSc thesis), periglacial landforms are common in this area. Permafrost is present in the north-eastern part of Iceland, but active permafrost features are found at elevations ≥ 900 m (Etzelmüller et al. 2007; Farbrot et al. 2007b). These landforms lie at 700 m a.s.l., some hundred meters below the theoretical permafrost limit in the area. In fig. 5.20, the results from the unwrapped differential interferograms over this area are presented. Some small displacement seems to be present in the unwrapped differential interferogram based on the 2007 and 2010 image pairs. However, the

16.08.2007-11.10.2010 unwrapped differential interferogram indicate a large displacement, but large areas are decorrelated and masked due to temporal decorrelation. The aspect of the area is northern, and only the east-facing sidewall of the cirque valleys is masked, probably due to shadow. Jónsson (2007) found displacement of 1-2 cm in wrapped radar LOS phase in the same area, probably corresponding with two known landslides called "Innri- and Ytri-Þverhryggir" (fig. 5.21). His scenes are from Envisat and ERS, and span a year (July 2004-July 2005), and are both descending (ERS) and ascending (Envisat). Both sensors detect displacement in this area.

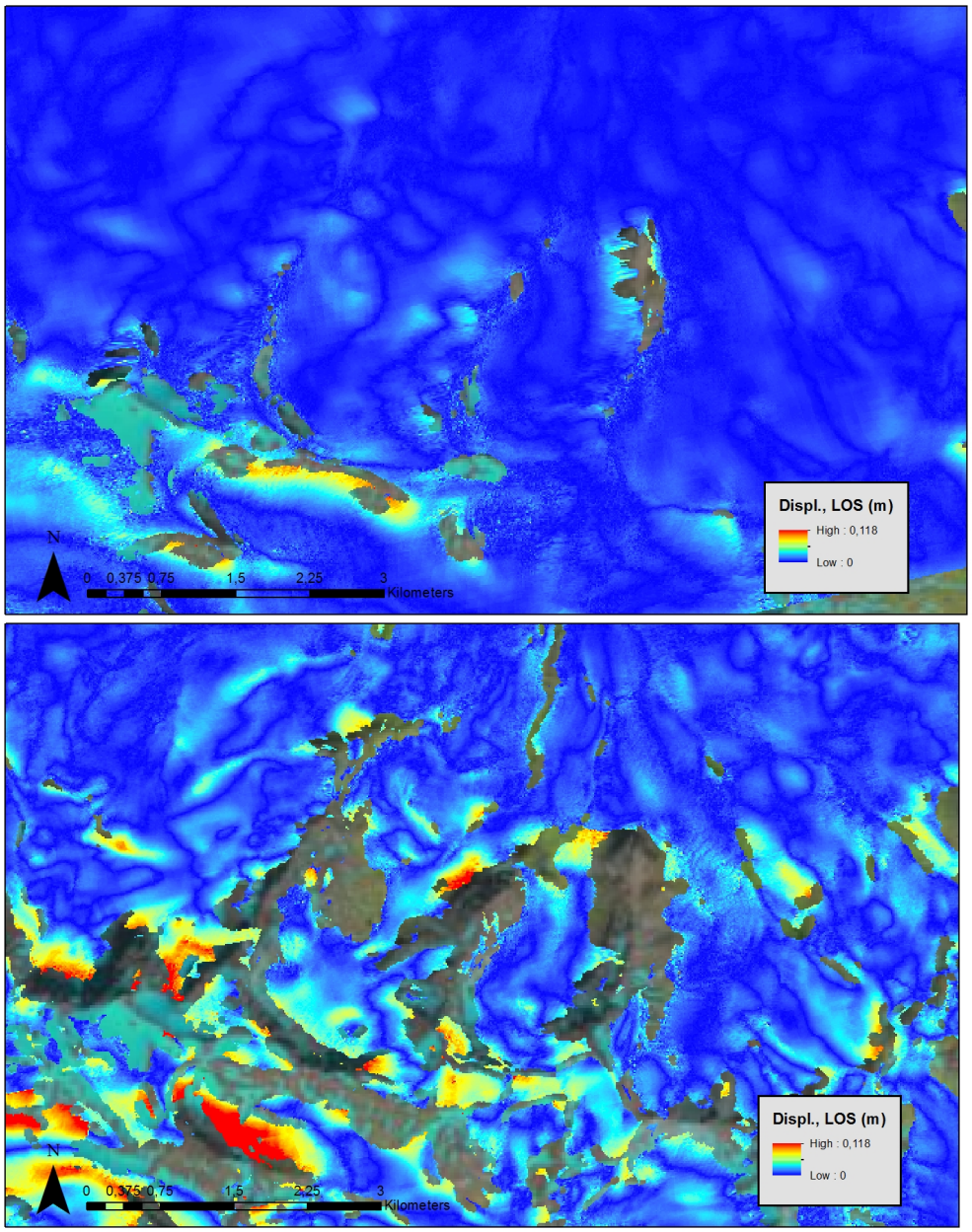

Figure 5.20: Innri- and Ytri-Þverhryggir, 18.08.2007-03.10.2007 (top) and 18.08.2007-11.10.2010 (bottom) unwrapped differential interferograms, radar LOS. Landsat background image, downloaded 25.09.2012.

The peninsula between the Vopnafjörður and Héraðsflói has an alpine topography with steep peaks and deep valleys. In this area, the differential interferometric analyses indicate displacement in some areas. Farbrot et al. (2007b) and Etzelmüller et al. (2007) found no indications of permafrost in this area. On the north-western side of Smjörfjöll, a landslide is detected (moving towards the west), between the Haugsá and Skjaldþingsstaðaá rivers. In the image pairs from 2007 and 2009 no certain displacement is present, but in the 18.08.2007-23.08.2009 unwrapped differential interferogram, a distinct wedge shape is discernible, and movements in radar LOS up to 9 cm are found, see figure 5.22. However, large areas are masked, and any DEM or unwrapping errors could contribute to create an erroneous result.

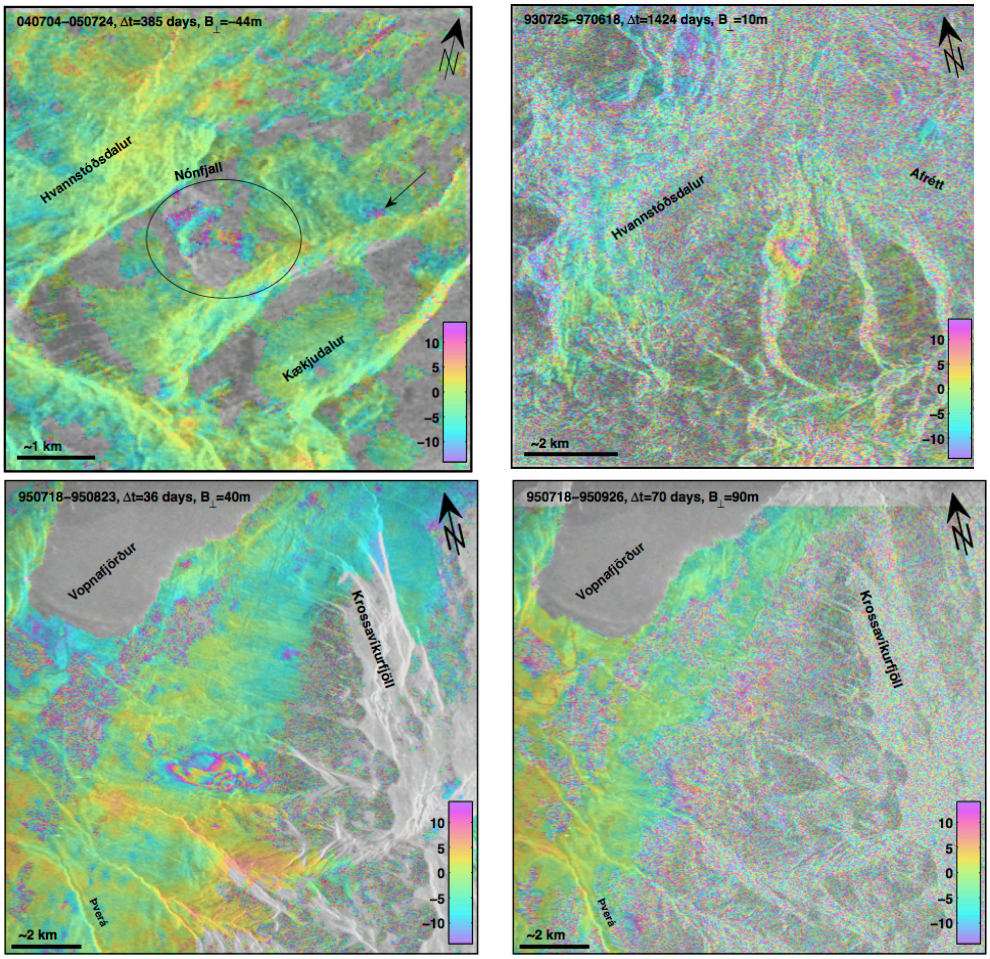

Figure 5.21: Lambardalur Envisat July 2004-July 2005 (ascending, top left) and ERS July 1993-June 1997 (descending, top right) and Vopnafjörður ERS July 1995-August 1995 and July 1995-September 1995 (both descending, bottom left and right) from Jónsson (2007).

The wrapped images show that much of the displacement is centred around the layover in the mountainsides, as can be seen in fig. 5.22. This is an indication of phase jumps as well as unwrapping errors. The baseline for the 18.08.2007-03.10.2007 differential interferogram is 532.42 m, while the 18.08.2007-23.08.2009 baseline is 1666.50 m, thus making DEM errors more pronounced in the 18.08.2007-23.08.2009 differential interferogram in addition to phase jumps and unwrapping errors. Jónsson (2007) found a similar displacement in the ERS wrapped differential interferograms from July 1995-August 1995 and July 1995-September 1995, from descending orbits (fig. 5.21, bottom). From July to September, the landslide has a large enough displacement to cause decorrelation (i.e., more than 1.4 cm displacement in radar LOS in Jónsson's differential interferograms), in difference to the July to August wrapped differential interferogram from the same year. In the 18.08.2007-03.10.2007 differential interferograms from ALOS PALSAR, the displacement is close to 9 cm in radar LOS, possibly indicating an increased velocity in the landslide from 1995 to 2007-2009.

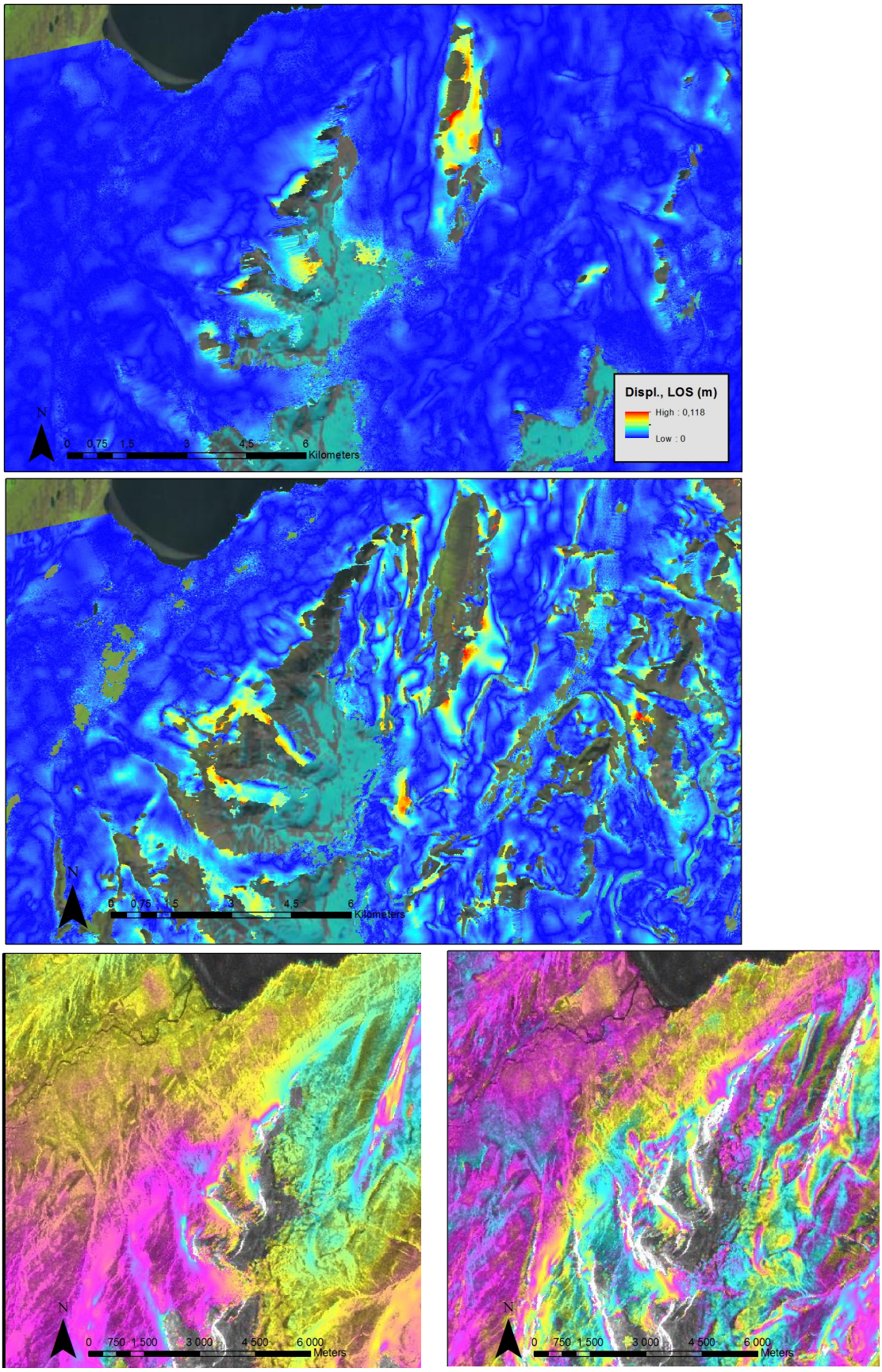

Figure 5.22: Unwrapped differential interferograms from Smjörfjöll area, Vopnafjörður: 18.08.2007-03.10.2007 (top) and 18.08.2007-23.08.2009 (middle). Wrapped differential interferograms from 18.08.2007-03.10.2007 (bottom left) and 18.08.2007-23.08.2009 (bottom right). Landsat background image, downloaded 25.09.2012.

5.2.3 Tafjord, Western Norway

5.2.3.1 Åknesfjellet and Hegguraksla

The locations of the discussed displacements are shown in figure 5.23.

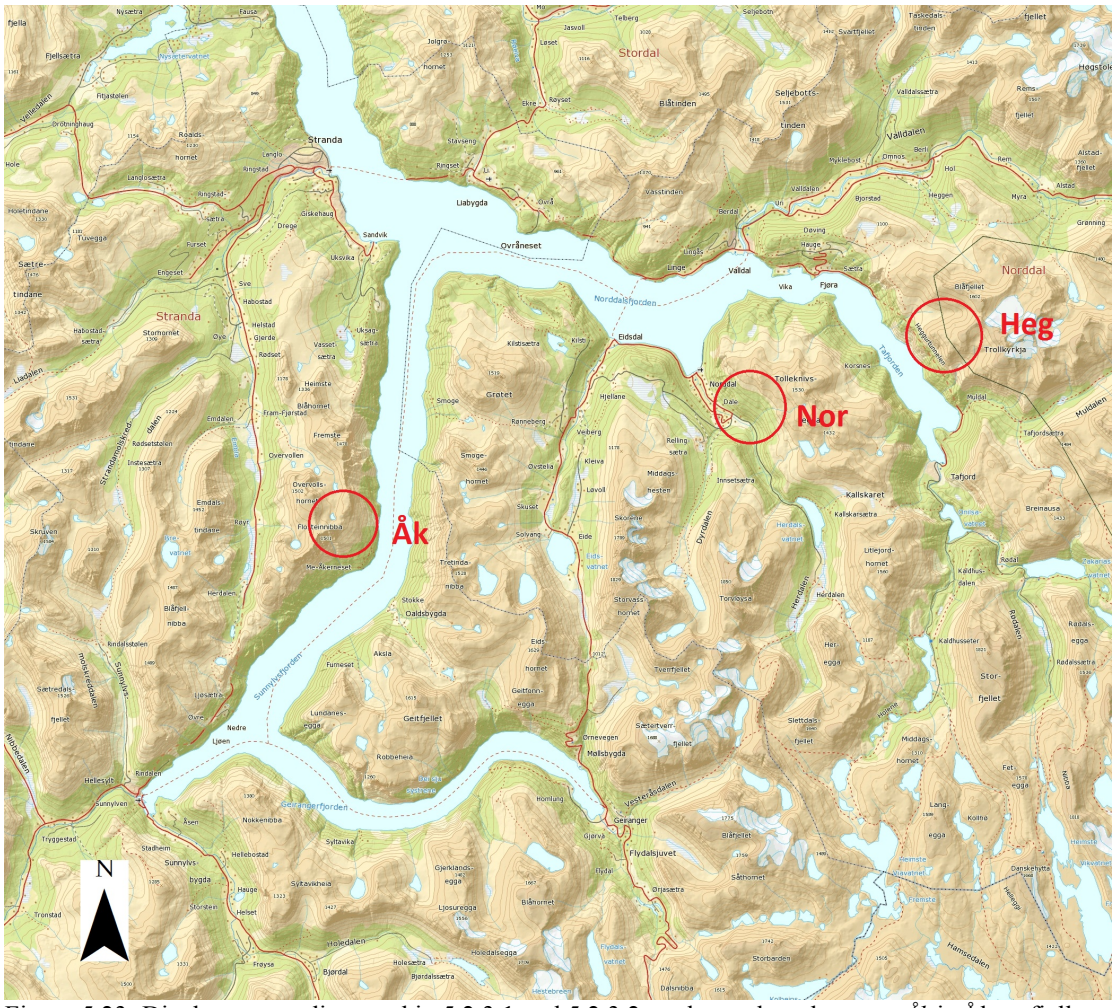

Figure 5.23: Displacements discussed in 5.2.3.1 and 5.2.3.2 are located on the map. *Åk* is Åknesfjellet, *Heg* is Hegguraksla and *Nor* is Norddalen. Map image downloaded from norgeskart.no, 25.09.2012.

Åknesfjellet is the best-investigated unstable mountainside in Norway. Located in Sunnylvsfjorden, in one of the most popular tourist areas in the country, a collapse here is a threat to several thousands of human lives. The area consists of deformed slopes where Åknesfjellet is one of several unstable blocks with a weaker zone acting as a sliding surface (Braathen et al. 2004). Hegguraksla is located in Norddalsfjorden, and shares the same geological features as Åknesfjellet, an unstable block with a weaker zone (Kristensen and Blikra 2010). The mountainside has a western aspect, and is, therefore, only partially visible in the radar images due to layover. Both mountainsides are closely monitored at present.

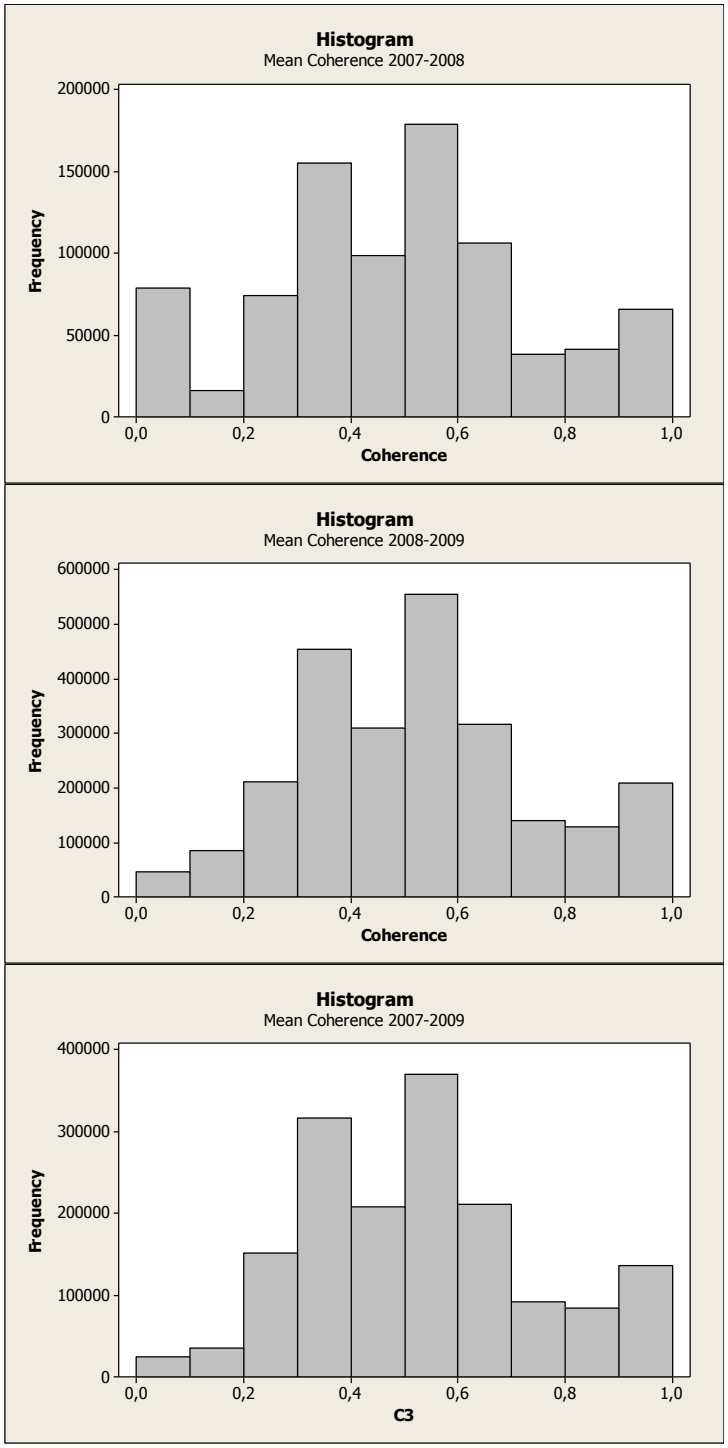

Figure 5.24: Coherence histograms for the Tafjord radar images. Baseline for 2007-2008 is 6044.85 m, 2008-2009 is 4150.35 m and for 2007-2009 it is 1896.73 m.

Three images were available for analysis, acquired 02.09.2007, 04.09.2008 and 07.09.2009, and the unwrapped differential interferograms are presented in fig. 5.25. Only the interferogram based on the 02.09.2007-07.09.2009 images are adequate for use, and even these images are influenced by a low coherence in large areas. Comparing the coherence of the three image pairs, they have the same distribution (fig. 5.24), but

the 2007-2008 image pair has a higher frequency of null coherence. The 2007-2009 image pair has a smaller baseline than the other image pairs, making a more favourable image pair for successful differential interferometric analysis.

In figure 5.25, the unwrapped differential interferograms from Åknesfjellet is presented. Due to challenging topography, a long time interval between the acquired images and unstable weather conditions, as well as layover and shadowing all make unwrapping errors common in the interferograms (see fig. 5.25 for comparison of a multilook-image and unwrapped radar LOS displacement). However, some areas do produce a signal coherent enough to be unwrapped. The baseline for the 2007-2009 differential interferogram is 1896.73 m, well within the critical baseline, but not optimal for differential interferometry. The other differential interferograms have baselines close to or larger than the critical baseline, making any DEM errors or other processing errors more apparent. The displacement in the 2007-2009 differential interferogram is not limited to the location of the rockslide, but is also found in the vicinity. This could be due to unwrapping errors, a DEM error and a suboptimal baseline length or local, height dependent tropospherical effects.

The displacement at Åknesfjellet is of a magnitude of 6-7 cm in radar LOS from 02.09.2007 to 04.09.2009. If this is translated to movement following the steepest descent, assuming a 34° look angle, the displacement is on a magnitude of 5.3 cm for the time period, indicating a displacement of ~2.7 cm a^{-1}. The Åknes/Tafjord Beredskap has measured the displacement velocity since 2004/2005, and the measured mean annual displacement velocity is 6-8 cm a^{-1} (with seasonal variations) in the upper part of the mountainside (Blikra 2012). The results from ALOS PALSAR are much smaller and very inaccurate, compared with the Åknes/Tafjord Beredskap's results.

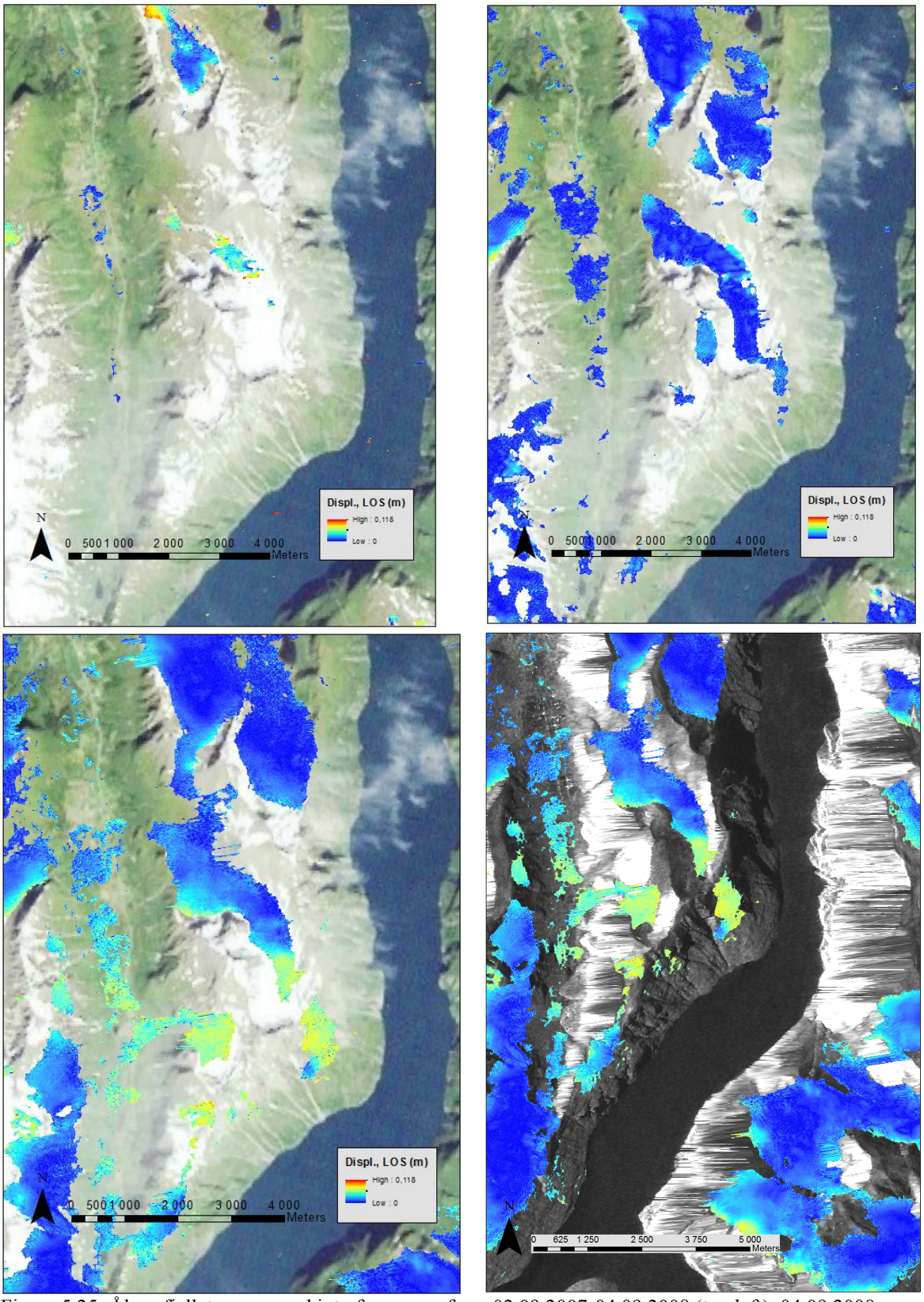

Figure 5.25: Åknesfjellet unwrapped interferograms from 02.09.2007-04.09.2008 (top left), 04.09.2008-07.09.2009 (top right), 02.09.2007-07.09.2009 (bottom left), and unwrapped interferogram from 02.09.2007-07.09.2009 over MLI from 02.09.2007-07.09.2009 image pair. Notice layover in the mountainsides with a western aspect and shadow in those with an eastern aspect. Background image from Norge i bilder, norgedigitalt.no.

Hegguraksla, the other mountainside under close surveillance, is not considered as a risk of the same proportions as Åknesfjellet (Blikra 2012). Due to layover, only the upper part of the area with registered displacements is in the radar's line of sight. In figure 5.27, the results from the unwrapped differential interferograms are presented. Most of the displacement is not at the main Hegguraksla site, but at a site some hundred meters south of Hegguraksla. In this area, bathymetry has identified a large, submarine talus cone (Henderson et al. 2006) Here, some apparent displacement is detected, but the results are found in isolated patches due to the layover from the west-facing mountainsides. The results are, therefore, not entirely unambiguous. The baselines are, as mentioned over, large, and any DEM errors and unwrapping errors will be largely influential on the end results. When figure 5.26 is considered, the wrapped versions show, in comparison to the unwrapped versions, that the errors can be attributed to the DEM in combination with the large baseline. No apparent unwrapping errors can be seen, but for the phase jumps common in differential interferograms with phase residue due to displacement scattered across the image.

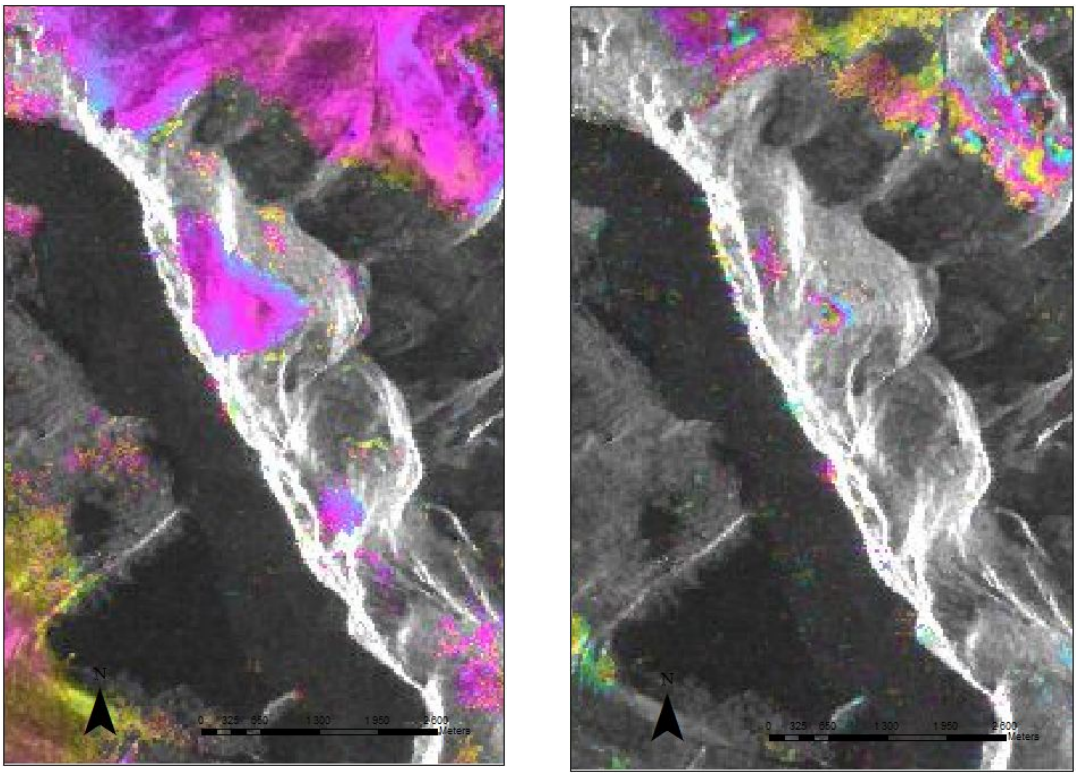

Figure 5.26: Hegguraksla, Tafjord. Wrapped differential interferograms from 02.09.2007-07.09.2009 (left) and 02.09.2007-04.09.2008 (right). Notice how the phase follows the terrain in the 2008-2009 differential interferogram.

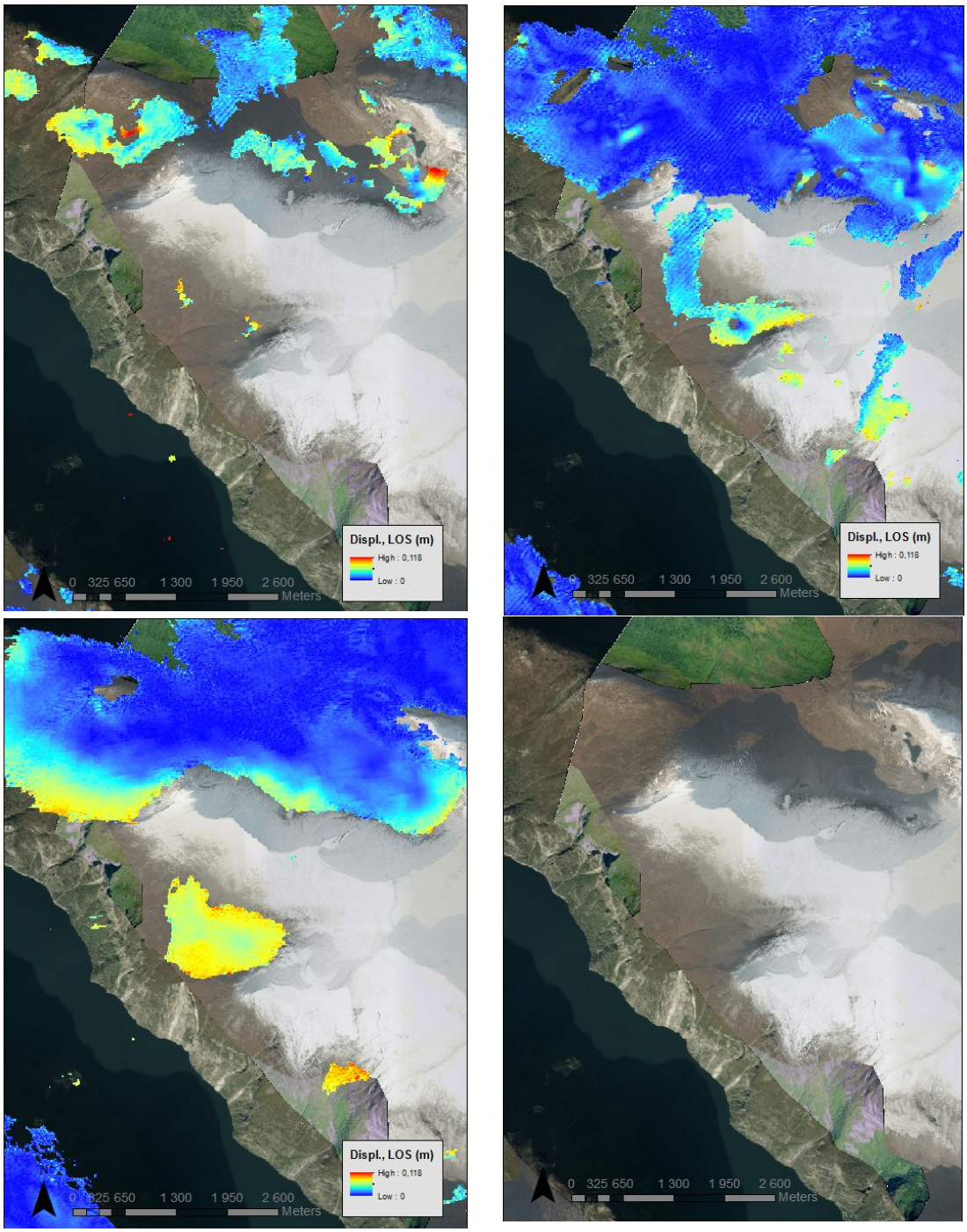

Figure 5.27: Hegguraksla, Tafjord. Displacement 02.09.2007-04.09.2008 (top left), 04.09.2008-07.09.2009 (top right), 02.09.2007-07.09.2009 (middle left), Hegguraksla itself (middle right), wrapped differential interferograms from 02.09.2007-07.09.2009 (bottom left) and 02.09.2007-04.09.2008 (bottom right). Background image downloaded from Norge i bilder, norgedigitalt.no, 25.09.2012.

5.2.3.2 Other areas of interest: Norddal

Norddal is a small valley running south-east from Norddalsfjorden. The topography is coarse, with steep mountainsides and a vegetated valley floor, and shares the same geological characteristics as Åknesfjellet and Hegguraksla. In the unwrapped

differential interferograms, some displacement is detected in the west-facing mountainside. This displacement is, as with Åknesfjellet and Hegguraksla, only found in isolated patches, and could be attributed to unwrapping errors and layover as much as to any physical displacement in the area. The area was examined by Henderson et al. (2006), and deemed unstable. GPS surveillance was initiated in the summer 2006, due to its proximity to the village and its recently developed, impressive talus cone (Henderson et al. 2006). The displacement in the unwrapped differential interferogram amounts to up 6-9 cm in radar LOS, a large displacement in 2 years (fig. 5.28). However, due to the large uncertainty this needs to be confirmed by other methods, either in situ or otherwise. The wrapped images show the dependency on topography in this area. The apparent displacement follows the terrain, indicating a DEM error. Any displacement is due to this, as well as the errors in the unwrapping due to isolated patches of coherent phase.

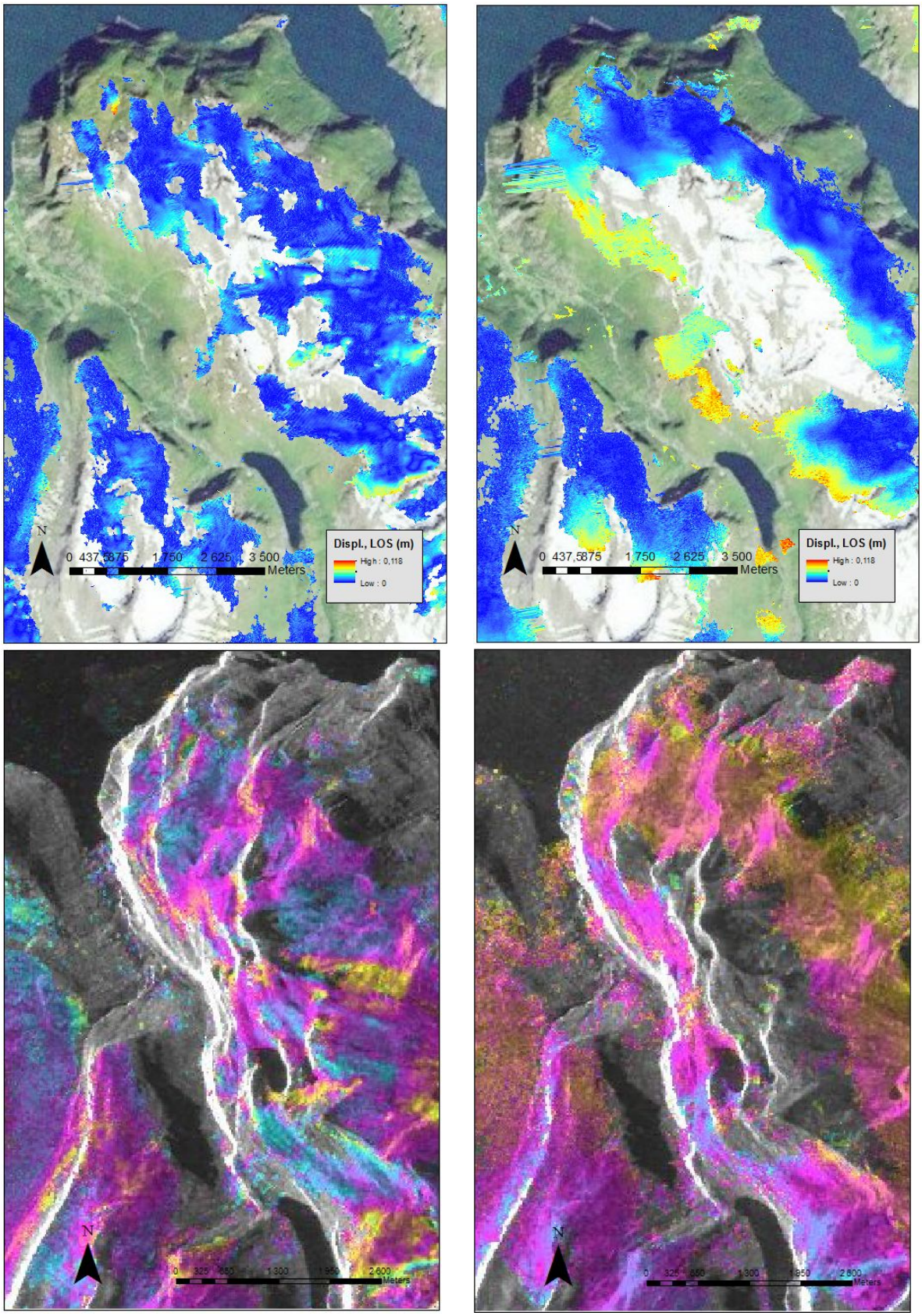

Figure 5.28: Unwrapped differential interferogram over Norddal. 04.09.2008-07.09.2009 left, 02.09.2007-07.09.2009 right. Notice unwrapping error in north-west both in the 04.09.2008-07.09.2009 and 02.09.2007-07.09.2009 images. Background image downloaded from Norge i bilder, norgedigitalt.no, 25.09.2012.

6 Discussion

Differential interferometry is a useful remote sensing method, but has its limitations. Particularly ionospheric/atmospheric conditions influence the results, as well as any displacements exceeding the radar's wavelength. Both Iceland and Norway are areas where DInSAR is difficult and challenging due to topography and geometrical and temporal limitations, as well as humidity and wet snow. L-band SAR is more robust than C-and X-band, particularly in areas with high moisture levels/precipitation or vegetation, but it is, at the same time, more susceptible to ionospheric disturbances. The atmospheric component is, to some extent, removed by high pass filtering as described in chapter 2.2.5, but without an atmospheric model based on either GNSS networks or local meteorological measurements, this is only partially compensated in the differential interferograms.

The 2007 image pairs have, in general, performed the best, while the 2010 images come in at a close second. This is due to favourable conditions for interferometry, a small baseline and short time intervals between the images, as well as little snow and heavy rain. Precipitation and temperatures around freezing can influence coherence measures to such a degree that temporal decorrelation is limiting even for 1-day C-band Tandem data sets (Weydahl 2001). However, even if the conditions are favourable, the measured displacement is not necessarily trustworthy. Several error sources are present in the images and could produce erroneous displacement, but are difficult to verify due to few available sources for verification, particularly in Iceland. Any error estimates are therefore difficult to produce, but an error of at least 1.5 cm in radar LOS displacement has to be expected (Strozzi et al 2010).

The areas studied in this thesis are either in periglacial areas or in areas susceptible to landslides and rockfalls. These events are, in some cases, slow moving, while some move periodically/episodic or with high velocities during short time periods. The differential interferometric results can only provide information from the time interval between the acquired/used images, and this does not provide any information on the type of mass movement, only indicating the total displacement from $time_1$ to $time_2$. The satellite radar images used for DInSAR analyses are able to access difficult to reach

areas, and this is what makes satellite differential interferometry well suited to surveillance over large areas, but as a tool for long-term surveillance there are other options that are better suited. Metternicht et al. (2005) find the same, with three main stages of landslide related studies: detection and identification, monitoring, and spatial analysis and hazard prediction. Differential interferometry is useful for detection and identification as well as monitoring any mass movements. Strozzi et al. (2004) utilised in situ indicators/rock glacier inventories, space-borne radar interferometry and digital photogrammetry/DEM analysis to detect permafrost creep. The radar interferometry was found to be suitable to quantify activity over large areas, as well as detecting small movements in relict/inactive rock glaciers, as well as being a compliment to the traditional methods. DInSAR has been used to monitor deep-seated rock mass movement (Strozzi et al. 2010), where an acceleration of/in the landslide was detected from the mid-1990s to 2008. Other methods were also used in the study, showing the potential in multi-method, multi-temporal analyses of permafrost and landslide hazards. The multi-method, multi-temporal approach is particularly useful in areas with mountainous terrain, where different look angles and repeat orbits/passes supply complementary information.

Even if the areas processed in this thesis are difficult, due to geometrical and temporal restraints, some results were obtained. Some well known mass movements were detected, particularly Almenningsnöf (Tröllaskagi, Iceland), Hóladalur and Fremri-Grjótárdalur (Tröllaskagi, Iceland), and Åknesfjellet/Hegguraksla/Norddal (Tafjord, Norway). On the Tröllaskagi peninsula, several areas with rock glaciers/debris covered glaciers had detected displacements. Due to the periglacial/paraglacial areas within the study areas, some mass movements and instabilities are expected; particularly in steep slopes and mountainsides where slope erosion and build-up of debris cones is related to the paraglacial and, in some cases, renewed paraglacial response (Benn and Evans 2010). Due to the difficult conditions in the radar images, any displacement in slopes with layover and foreshortening or in connection with radar shadow and other masked areas needs to be considered uncertain at best. Detected displacement in areas with previously known displacement can be validated from other types of measurement, but should still be seen as a supplement to on-going, in situ measurements, not as freestanding confirmations of displacement. The available DEMs over Tröllaskagi and

Austurland are large contributions to any erroneous results, particularly in the differential interferograms with a large baseline. Failing to remove the topographic phase contribution will result in erroneous displacement and difficulties extracting any displacement from $time_1$ to $time_2$ as shown in several differential interferograms in this thesis. The smaller the baseline, the less topographic phase is present in the differential interferograms, and these images, in general, produce better differential interferograms for detection of mass movement. Breaks in the DEM and under- and overestimation of peaks and valleys can result in mass movements being registered as non-existing, or the opposite due to its contribution in both the removal of topographic phase in the interferogram processing as well as in the unwrapping of the differential interferogram. Added to these errors, are the other topography-induced errors (layover, shadow, and foreshortening), as discussed over.

Even in differential interferograms with high coherence, the radar's LOS limits results due to its inability to register any displacement/movement in the same direction as the sensor's orbital track. The Seyðisfjörður landslide is an example of this, where the sensor is incapable of registering any displacement (if present). The sensor may not register areas with on-going mass movements, particularly if the available datasets are from either ascending or descending orbits only. By acquiring images from both ascending and descending orbits, it is also theoretically possible to extract the three-dimensional displacement vector from the registered mass movement. The atmospheric and tropospheric contributions are, as mentioned over, difficult to quantify and eliminate from the differential interferograms. Some disturbances are easy to identify, such as the large ionospheric disturbance found in the 16.08.2007 scene, but other disturbances such as tropospheric water vapour and turbulence or differences in temperatures and air pressure can also contribute to artificial fringes or decorrelation of the signal. In some differential interferograms this can be seen as decorrelation and erroneous displacement, such as in Hofsárdalur, where the 2007-2010 differential interferogram contains a large, unexpected displacement. L-band DInSAR is less sensitive to vegetation and changes in the vegetation than C- and X-band DInSAR. However, decorrelation in vegetated areas is probable for a large temporal separation between images, and added to this is any precipitation and/or changes in ground conditions due to moisture and freezing conditions. Jónsson (2007; 2009) used

ascending and descending scenes from ERS-1 and 2 and from Envisat in Tröllaskagi and Austurland, Iceland. His results contain more detected displacement, in several areas, such as Seyðisfjörður, due to using scenes from descending orbits and having a shorter time span between the acquired scenes. However, the results are not necessarily more precise, due to temporal and geometrical decorrelation in the C-band wavelengths.

Differential interferometry with L-band SAR images has a large potential, even under difficult conditions. Considering the uncertainties and error sources, it is a tool well suited to remote sensing of mass movements in remote, hard-to-reach areas. Despite the geometrical and temporal limitations, image pairs with a small baseline produced differential interferograms of high quality and are as such useful for discovery and, for hard-to-reach areas, monitoring of active landslides/mass movements. Image pairs with temporal separation over 900 days still have a high coherence and produce differential interferograms with areas of coherent mass movement. Jónsson (2007; 2009) used ERS-1 and 2 and Envisat scenes separated by up to four years, but encountered problems with decorrelation in the scenes with a large baseline, but also in scenes acquired in difficult weather conditions and in different seasons. Rough topography is a large problem particularly with ERS-1 and 2 images, due to large layover from the 23° look angle. Feasible improvements to the DInSAR method are, first of all, higher temporal resolution, and secondly, better spatial resolution. Another area benefiting from improvement is the processing software, particularly the unwrapping algorithms, reducing ambiguities in the wrapped phase and producing better displacement estimates. ALOS PALSAR L-band SAR data is not available in large enough quantities to facilitate the SBAS or PS techniques, making deformation estimates over large areas and long time series difficult to produce. The L-band data, if available in large quantities and long time series, would probably have a higher coherence over a longer time period, enabling more robust estimates than is possible with C- and X-band today. DInSAR is used today to discover potentially unstable mountainsides in both western and northern Norway, and the robustness of the L-band SAR data make these somewhat suited to this task, however, good results are dependent on several factors. The reliability of the results is dependent on the size of the baseline combined with the quality of the DEM as well as the influence of atmospherical, topographic and temporal

factors on the differential interferograms. If these perform optimally, the differential interferograms can provide useful data on unstable mass movements.

7 Conclusion

The premise for this thesis was the potential of L-band differential interferometry to detect slope instabilities and mass movements under difficult topographic and climatic conditions. The longer wavelength and, thusly, a relatively good coherence over time, result in a potential to detect new mass movements and displacements in the chosen areas.

Differential interferometry *can* be useful in these areas, despite the difficult topography and climate. The difficulties lie, for the most part, in the topography and available DEMs, where geometrical restraints in the data analysis create erroneous results, or no results at all. When these constraints are considered, the method produces results that are somewhat useful as a way of detecting displacements and mass movements, but they would have to be monitored in situ or be part of a continuous remote sensing monitoring program for hard to reach areas. Displacement was detected both in Iceland and Norway, at previously known sites, and at one unknown site in Iceland. In Iceland, rock glaciers and large, slow moving mass movements/landslides were detected by the method. In Norway, unstable mountainsides were detected, but also showing the limited possibilities of the DInSAR even in the challenging topography of the Norwegian fjords, where displacement was detected at sites with no known displacement, close to heavily monitored areas such as Åkerneset.

Only ascending images were available for interferometric analysis, no descending images had a baseline within the critical limit for ALOS PALSAR. If the descending images were available for analysis, an analysis of the LOS components in displacements found in both image sets could provide the full displacement vector. This is a helpful tool, particularly in areas that are hard to reach. The results are, to some degree, difficult to interpret. False displacement is present in almost all differential interferograms, and the DEM quality impacts the results to a large degree as well. Some areas with previously known landslides/mass movements had no detected displacement in the differential interferograms, either due to geometrical problems with the images/DEM and/or lack of coherence, or due to the landslide's displacement pattern. The ionospheric and tropospheric disturbances in the differential

interferograms were not as prominent as could be expected, due to either favourable conditions when the scenes were acquired or due to the time of year the images were acquired.

Further studies of L-band differential interferometry will benefit from new satellites, with high-resolution sensors and orbits designed for interferometry. More images would also enable techniques such as PS or SBAS to be used, which could produce interesting results for detection of both mass movements and deformations in the terrain. Regarding differential interferometry, better unwrapping algorithms would further enhance the estimation of detected displacement and contribute to results with less uncertainty. High quality DEMs are requisite to achieve useful results; as this thesis has shown, a low quality DEM will cause false displacements and results of low quality.

As the climate changes, there will be more unstable slopes and mountainsides due to heavier precipitation and, in some areas, the disappearance of permafrost. Surveillance of large areas is possible through differential interferometry, and large-scale, automated surveillance could be possible in the future if sensors with geometry and repeat orbits designed for interferometry were launched. The biggest drawback of ALOS PALSAR is the lack of useful image pairs for interferometry, but as this thesis has shown, by carefully selecting the image pairs, some useful results are obtainable, even in challenging topography and climates.

Literature

Atzori, S., Hunstad, I., Chini, M., Salvi, S., Tolomei, C., Bignami, C., . . . Boschi, E. (2009). Finite fault inversion of DInSAR coseismic displacement of the 2009 L'Aquila earthquake (central Italy). *Geophysical Research Letters, 36*(15), L15305.

Bamler, R., & Hartl, P. (1998). Synthetic aperture radar interferometry. *Inverse Problems, 14*(4), R1-R54.

Barsch, D. (1996). Rockglaciers: indicators for the present and former geoecology in high mountain environments.

Benn, D. I., & Evans, D. J. A. (2010). *Glaciers and glaciation*: Hodder Education.

Blikra, L. (2012). Evaluering av drenering som risikoreduserende tiltak ved Åknes. *Åknesrapport* (Vol. 07-2012, pp. 24). Norway: Åknes/Tafjord Beredskap IKS.

Braathen, A., Lars Harald Blikra, Silje S. Berg, Frode Karlsen. (2004). Rock-slope failures in Norway; type, geometry, deformation mechanisms and stability. *Norwegian Journal of Geology, 84*, 21.

Bürgmann, R., Rosen, P. A., & Fielding, E. J. (2000). Synthetic aperture radar interferometry to measure Earth's surface topography and its deformation. *Annual Review of Earth and Planetary Sciences, 28*(1), 169-209.

Cascini, L., Fornaro, G., & Peduto, D. (2010). Advanced low- and full-resolution DInSAR map generation for slow-moving landslide analysis at different scales. *Engineering Geology, 112*(1–4), 29-42. doi: 10.1016/j.enggeo.2010.01.003

Caseldine, C., & Stötter, J. (1993). 'Little Ice Age'glaciation of Tröllaskagi peninsula, northern Iceland: climatic implications for reconstructed equilibrium line altitudes (ELAS). *The Holocene, 3*(4), 357-366.

CCRS. (2007). Fundamentals of Remote Sensing (pp. 258): Canada Centre of Remote Sensing.

Chini, M., Pierdicca, N., & Emery, W. J. (2009). Exploiting SAR and VHR optical images to quantify damage caused by the 2003 Bam earthquake. *Geoscience and Remote Sensing, IEEE Transactions on, 47*(1), 145-152.

Cumming, I. G., & Wong, F. H. (2005). *Digital processing of synthetic aperture radar data : algorithms and implementation*. Boston, MA: Artech House.

Curlander, J. C., & McDonough, R. N. (1991). *Synthetic aperture radar - Systems and signal processing*. New York: Wiley.

Derron, M., Blikra, L., & Jaboyedoff, M. (2005). High resolution digital elevation model analysis for landslide hazard assessment (Åkerneset, Norway). *Landslides and avalanches: ICFL*, 101-106.

Elachi, C., & Van Zyl, J. J. (2006). *Introduction to the physics and techniques of remote sensing* (Vol. 28): Wiley-Interscience.

EORC, JAXA (2012). About ALOS. Retrieved 13.08.2012, 2012, from http://www.eorc.jaxa.jp/ALOS/en/about/palsar.htm

Etzelmüller, B., Farbrot, H., Guðmundsson, Á., Humlum, O., Tveito, O. E., & Björnsson, H. (2007). The regional distribution of mountain permafrost in Iceland. *Permafrost and Periglacial Processes, 18*(2), 185-199.

Farbrot, H., Etzelmüller, B., Guðmundsson, Á., Humlum, O., Kellerer-Pirklbauer, A., Eiken, T., & Wangensteen, B. (2007a). Rock glaciers and permafrost in Tröllaskagi, northern Iceland. *Zeitschrift für Geomorphologie, Supplementary Issues, 51*(2), 1-16.

Farbrot, H., Etzelmüller, B., Schuler, T. V., Guðmundsson, Á., Eiken, T., Humlum, O., & Björnsson, H. (2007b). Thermal characteristics and impact of climate change on mountain permafrost in Iceland. *Journal of Geophysical Research, 112*(F3).

Franceschetti, G., & Lanari, R. (1999). *Synthetic aperture radar processing*: CRC.

Gamma. (2008). Documentation - User's Guide. Gamma Software. Gümligen, Switzerland: Gamma Remote Sensing AG.

Ganerød, G. V., Grøneng, G., Rønning, J. S., Dalsegg, E., Elvebakk, H., Tønnesen, J. F., . . . Braathen, A. (2008). Geological model of the Åknes rockslide, western Norway. *Engineering Geology, 102*(1), 1-18.

Gens, R., & Van Genderen, J. L. (1996). Review Article SAR interferometry—issues, techniques, applications. *International Journal of Remote Sensing, 17*(10), 1803-1835. doi: 10.1080/01431169608948741

Goldstein, R. M., & Werner, C. L. (1998). Radar interferogram filtering for geophysical applications. *Geophysical Research Letters, 25*(21), 4035-4038.

Guðmundsson, Á. (2000). *Frerafjöll, urðarbingir á Tröllaskaga.* (MSc.), University of Iceland, Iceland.

Haeberli, W. (2000). Modern research perspectives relating to permafrost creep and rock glaciers: a discussion. *Permafrost and Periglacial Processes, 11*(4), 290-293.

Henderson, I. H. C., Saintot, A., & Derron, M. H. (2006). Structural mapping of potential rockslide sites in the Storfjorden area, western Norway: the influence of bedrock geology on hazard analysis *NGU Report* (Vol. 2006.052, pp. 83). Trondheim: NGU.

Hernandez, B., Cotton, F., Campillo, M., & Massonnet, D. (1997). A Comparison between short term (co-seismic) and long-term (one year) slip for the Landers earthquake: Measurements from strong motion and SAR interferometry. *Geophysical Research Letters, 24*, 1579-1582.

Jónsson, S. (2007). A survey of active landslide movement in east Iceland from satellite radar interferometry. (Vol. VÍ-VS-03, pp. 81): Veðurstofa Íslands.

Jónsson, S. (2009). A survey of active slope movements in central-north Iceland from satellite radar interferometry. (Vol. VÍ 2009-002, pp. 78): Icelandic Meteorological Office.

Jónsson, S., & Ágústsson, K. (2007). *A Survey of active Landslide Movement in Iceland from SAR Interferometry.* Paper presented at the Geophysical Research Abstracts.

Just, D., & Bamler, R. (1994). Phase statistics of interferograms with applications to synthetic aperture radar. *Appl. Opt., 33*(20), 4361-4368.

Kellerer-Pirklbauer, A., Wangensteen, B., Farbrot, H., & Etzelmüller, B. (2008). Relative surface age-dating of rock glacier systems near Hólar in Hjaltadalur, northern Iceland. *Journal of Quaternary Science, 23*(2), 137-151.

Kenyi, L., & Kaufmann, V. (2003). *Measuring rock glacier surface deformation using SAR interferometry.* Paper presented at the Eighth International Conference on Permafrost.

Kristensen, L., & Blikra, L. (2010). Hegguraksla in Tafjorden: Monitoring and data analyses. *Åknesrapport* (Vol. 04-2010, pp. 11). Norway: Åknes/Tafjord Beredskap IKS.

Lilleøren, K. S. (2012). *Late-Pleistocene and Holocene mountain permafrost geomorphology of Norway and Iceland.* (Ph.D.), University of Oslo.

Lilleøren, K. S., & Etzelmüller, B. (2011). A regional inventory of rock glaciers and ice-cored moraines in Norway. *Geografiska Annaler: Series A, Physical Geography, 93*(3), 175-191.

Lopez-Martinez, C., & Pottier, E. (2007). On the extension of multidimensional speckle noise model from single-look to multilook SAR imagery. *Geoscience and Remote Sensing, IEEE Transactions on, 45*(2), 305-320.

Martin, H. E., & Whalley, W. B. (1987). Rock glaciers: part 1: rock glacier morphology: classification and distribution. *Progress in Physical Geography, 11*(2), 260-282.

Massonnet, D., & Feigl, K. L. (1998). Radar interferometry and its application to changes in the Earth's surface. *Rev. Geophys., 36*(4), 441-500. doi: 10.1029/97rg03139

Metternicht, G., Hurni, L., & Gogu, R. (2005). Remote sensing of landslides: An analysis of the potential contribution to geo-spatial systems for hazard assessment in mountainous environments. *Remote Sensing of Environment, 98*(2–3), 284-303. doi: 10.1016/j.rse.2005.08.004

Meyer, F. J., & Nicoll, J. (2008). *The impact of the ionosphere on interferometric SAR processing.* Paper presented at the Geoscience and Remote Sensing Symposium, 2008. IGARSS 2008. IEEE International.

Oppikofer, T., Jaboyedoff, M., Blikra, L., Derron, M. H., & Metzger, R. (2009). Characterization and monitoring of the Aknes rockslide using terrestrial laser scanning. *Natural Hazards and Earth System Sciences, 9*(3), 1003-1019.

Petersen, T. (2007). *Generation and comparison of digital elevation models for two regions in the northern Iceland.* (MSc), University of Oslo, Oslo.

Ramberg, I. B., Solli, A., & Nordgulen, Ø. (2008). *The Making of a land : geology of Norway*. Trondheim: The Norwegian Geological Association.

Richards, J. A. (2009). *Remote sensing with imaging radar*: Springer.

Rosen, P. A., Hensley, S., Joughin, I. R., Li, F. K., Madsen, S. N., Rodriguez, E., & Goldstein, R. M. (2000). Synthetic aperture radar interferometry. *Proceedings of the IEEE, 88*(3), 333-382.

Rosenqvist, A., Shimada, M., Ito, N., & Watanabe, M. (2007). ALOS PALSAR: A pathfinder mission for global-scale monitoring of the environment. *Geoscience and Remote Sensing, IEEE Transactions on, 45*(11), 3307-3316.

Rott, H., & Nagler, T. (2006). The contribution of radar interferometry to the assessment of landslide hazards. *Advances in Space Research, 37*(4), 710-719. doi: 10.1016/j.asr.2005.06.059

Sandwell, D. T., Myer, D., Mellors, R., Shimada, M., Brooks, B., & Foster, J. (2008). Accuracy and resolution of ALOS interferometry: Vector deformation maps of the Father's Day intrusion at Kilauea. *Geoscience and Remote Sensing, IEEE Transactions on, 46*(11), 3524-3534.

Shimada, M., Rosenqvist, A., Watanabe, M., & Tadono, T. (2005). *The polarimetric and interferometric potential of ALOS PALSAR.* Paper presented at the Proceedings of the 2nd International Workshop POLINSAR 2005 (ESA SP-586). 17-21 January 2005, ESRIN, Frascati, Italy. Editor: H. Lacoste. ISBN: 92-9092-897-2., p. 41.

Sigmundsson, F., & Sæmundsson, K. (2008). Iceland: a window on North-Atlantic divergent plate tectonics and geologic processes. *EPISODES, 31*(1), 92-97.

Strozzi, T., Delaloye, R., Kääb, A., Ambrosi, C., Perruchoud, E., & Wegmüller, U. (2010). Combined observations of rock mass movements using satellite SAR interferometry, differential GPS, airborne digital photogrammetry, and airborne photography interpretation. *Journal of Geophysical Research, 115*(F1), F01014.

Strozzi, T., Farina, P., Corsini, A., Ambrosi, C., Thüring, M., Zilger, J., . . . Werner, C. (2005). Survey and monitoring of landslide displacements by means of L-band satellite SAR interferometry. *Landslides, 2*(3), 193-201. doi: 10.1007/s10346-005-0003-2

Strozzi, T., Kääb, A., & Frauenfelder, R. (2004). Detecting and quantifying mountain permafrost creep from in situ inventory, space-borne radar interferometry and airborne digital photogrammetry. *International Journal of Remote Sensing, 25*(15), 2919-2931. doi: 10.1080/0143116042000192330

Thordarson, T., & Hoskuldsson, A. (2002). *Iceland.* (Vol. 3). Harpenden, England: Terra.

Wangensteen, B., Guðmundsson, Á., Eiken, T., Kääb, A., Farbrot, H., & Etzelmüller, B. (2006). Surface displacements and surface age estimates for creeping slope landforms in Northern and Eastern Iceland using digital photogrammetry. *Geomorphology, 80*(1), 59-79.

Werner, C., Wegmuller, U., Strozzi, T., & Wiesmann, A. (2005). *Precision estimation of local offsets between pairs of SAR SLCs and detected SAR images.* Paper presented at the

Geoscience and Remote Sensing Symposium, 2005. IGARSS'05. Proceedings. 2005 IEEE International.

Weydahl, D. J. (2001). Analysis of ERS Tandem SAR coherence from glaciers, valleys, and fjord ice on Svalbard. *Geoscience and Remote Sensing, IEEE Transactions on, 39*(9), 2029-2039.

Whalley, W., & Martin, H. (1994). Rock Glaciers in Tröllaskagi: their origin and climatic significance. *Münchener Geographische Arbeiten B, 12*, 289-308.

Williams, S., Bock, Y., & Fang, P. (1998). Integrated satellite interferometry: Tropospheric noise, GPS estimates and implications for interferometric synthetic aperture radar products. *Journal of Geophysical Research, 103*(B11), 27051-27067.

Xu, Z. W., Wu, J., & Wu, Z. S. (2004). A survey of ionospheric effects on space-based radar. *Waves in Random Media, 14*(2), 189-273.

Zebker, H. A. (2000). Studying the Earth with interferometric radar. *Computing in Science & Engineering, 2*(3), 52-60. doi: 10.1109/5992.841796

Zebker, H. A., Rosen, P., Hensley, S., & Mouginis-Mark, P. J. (1996). Analysis of active lava flows on Kilauea volcano, Hawaii, using SIR-C radar correlation measurements. *Geology, 24*(6), 495-498.

Zebker, H. A., Rosen, P. A., & Hensley, S. (1997). Atmospheric effects in interferometric synthetic aperture radar surface deformation and topographic maps. *J. Geophys. Res., 102*(B4), 7547-7563. doi: 10.1029/96JB03804

Appendix A

Tröllaskagi, northern Iceland. North.

Background images for the North and Eastern Iceland results are from Landsat, downloaded 25.09.2012. Background images for the Tafjord images are from norgedigitalt.no/Norge i Bilder, downloaded 25.09.2012.

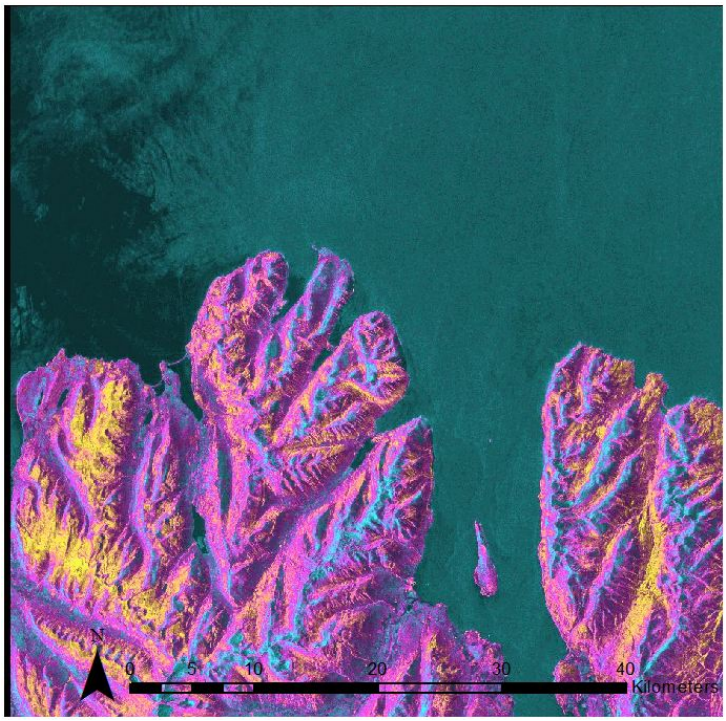

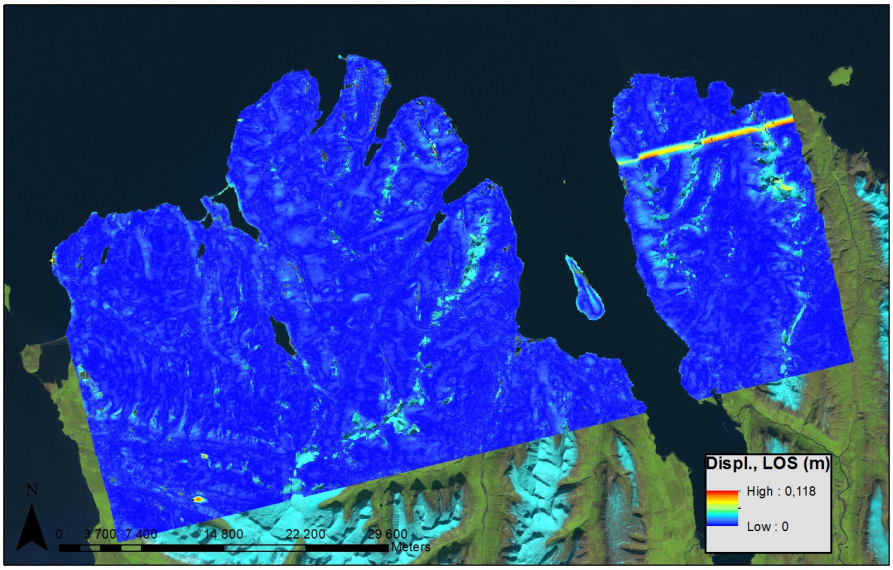

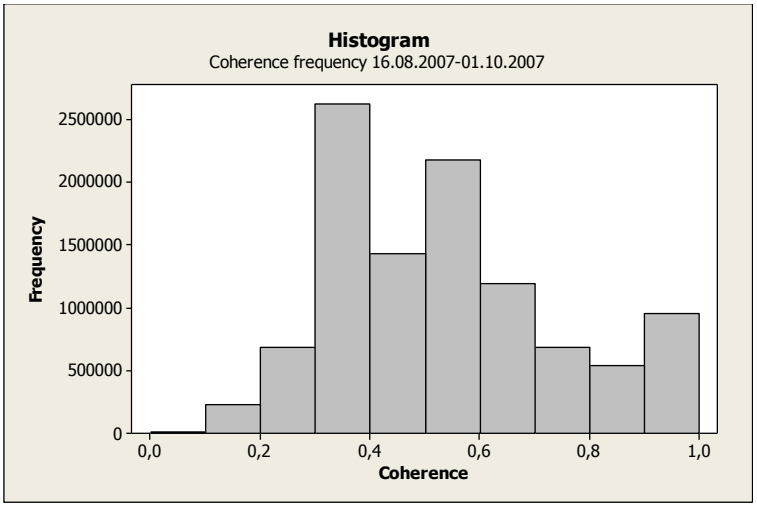

Figure 1: Coherence (top), Unwrapped differential interferogram (middle) and histogram (bottom) from 16.08.2007-01.10.2007.

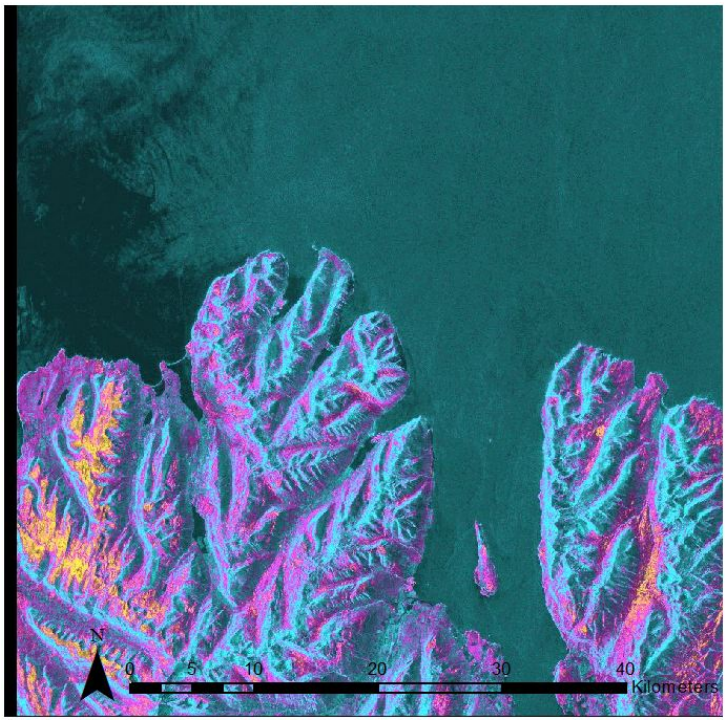

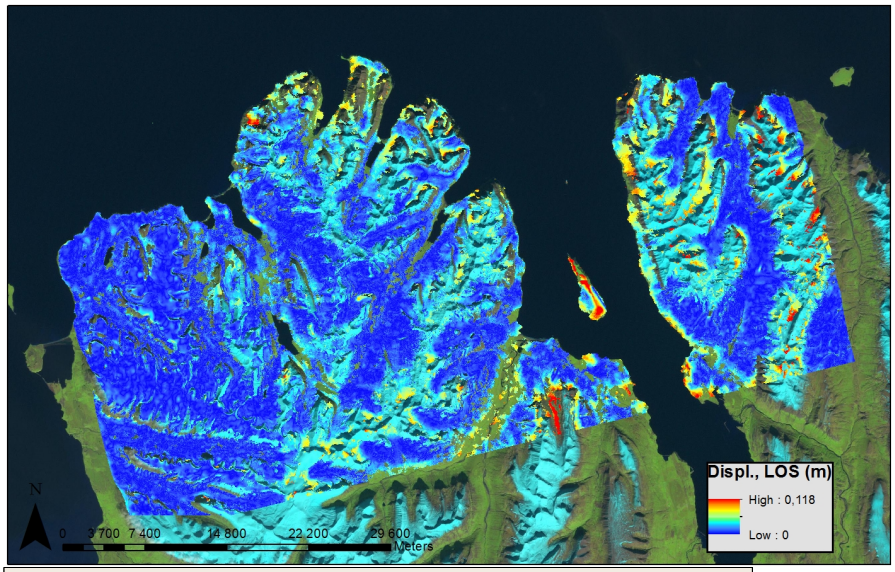

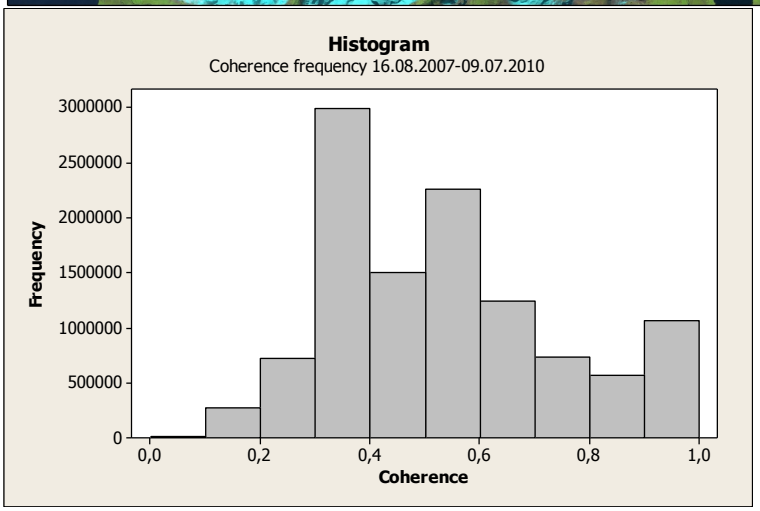

Figure 2: Coherence (top), Unwrapped differential interferogram (middle) and histogram (bottom) from 16.08.2007-09.07.2010.

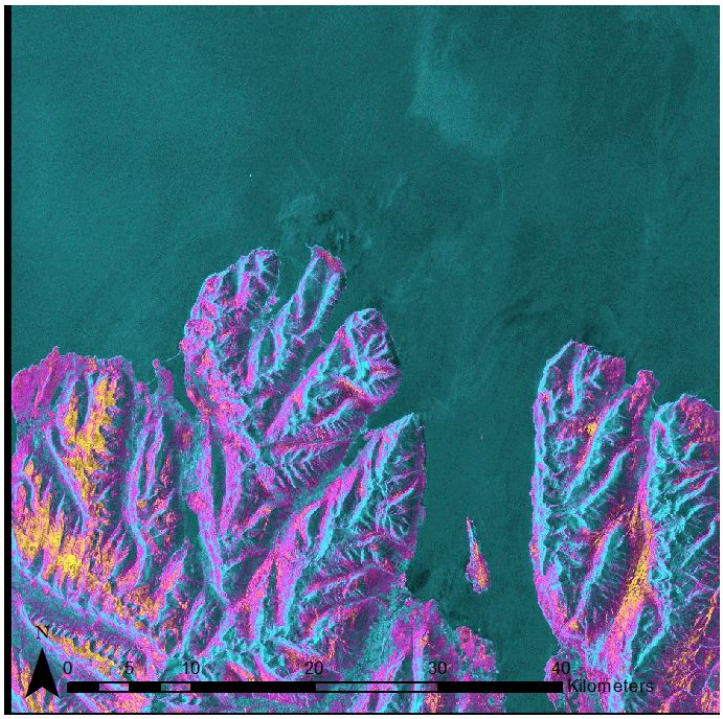

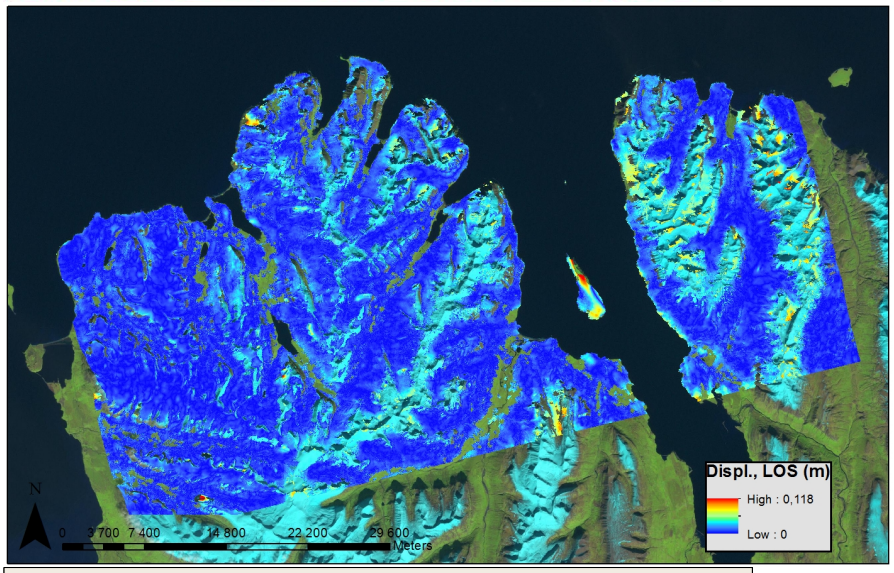

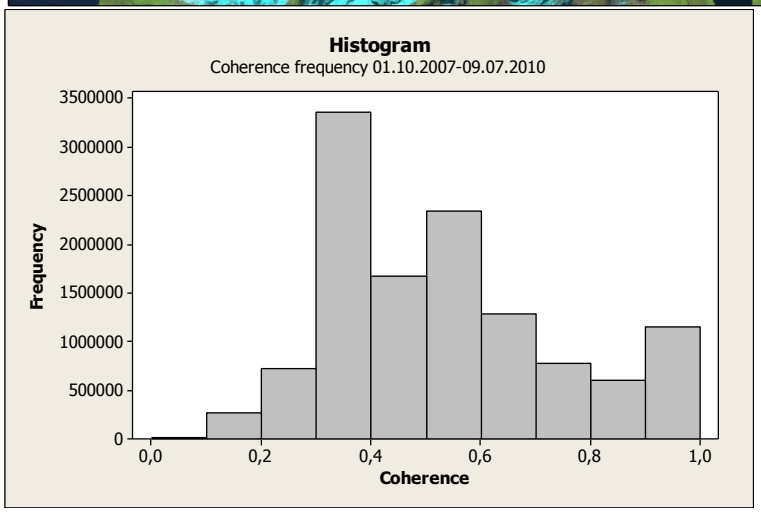

Figure 3: Coherence (top), Unwrapped differential interferogram (middle) and histogram (bottom) from 01.10.2007-09.07.2010.

Tröllaskagi, northern Iceland. South.

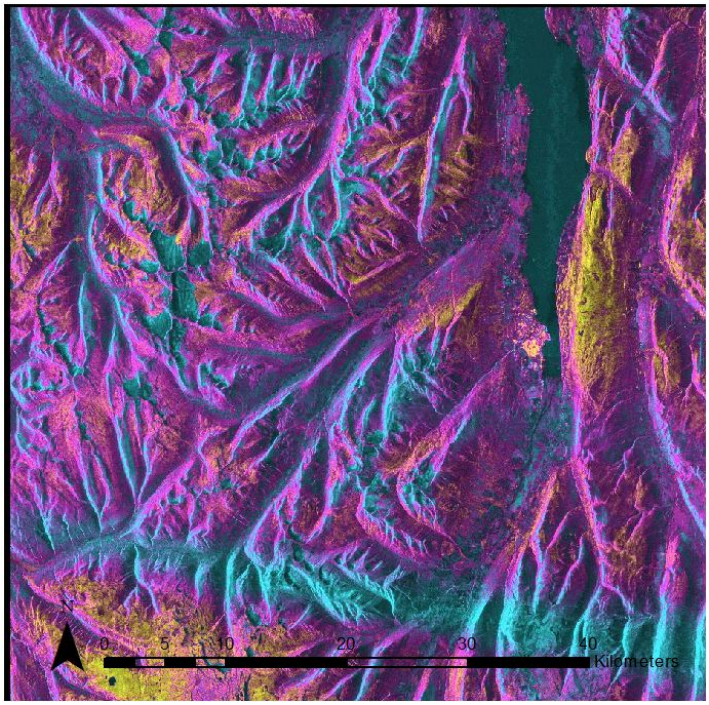

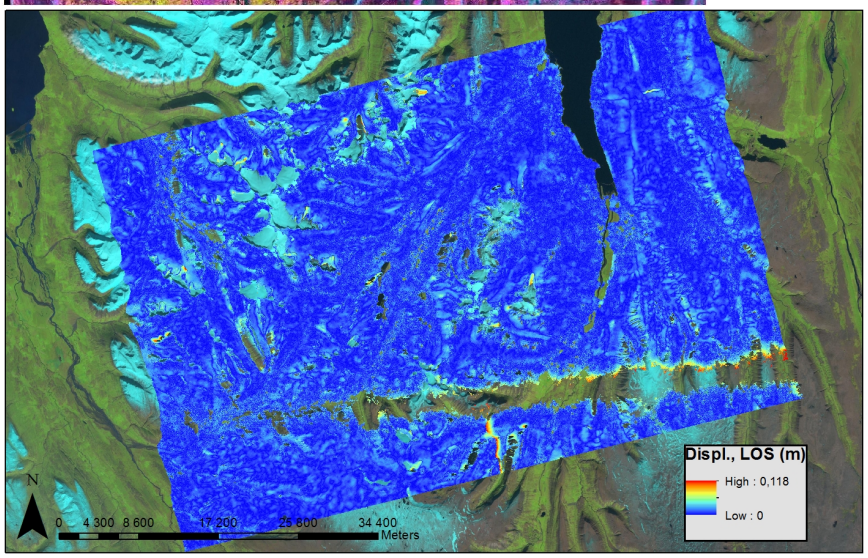

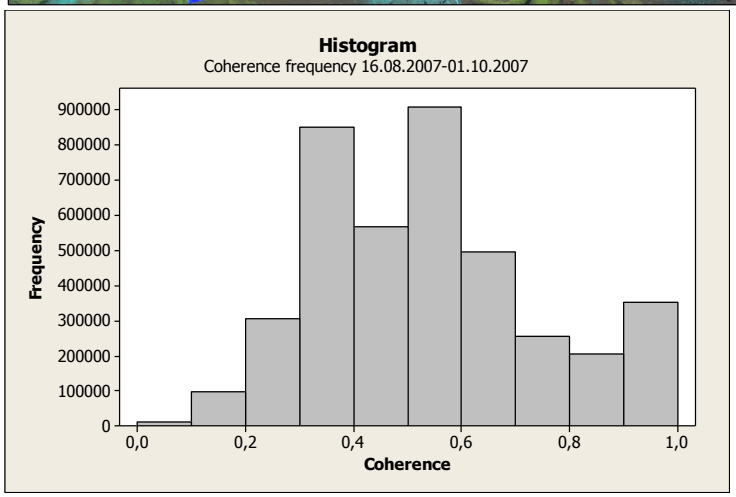

Figure 4: Coherence (top), Unwrapped differential interferogram (middle) and histogram (bottom) from 16.08.2007-01.10.2007.

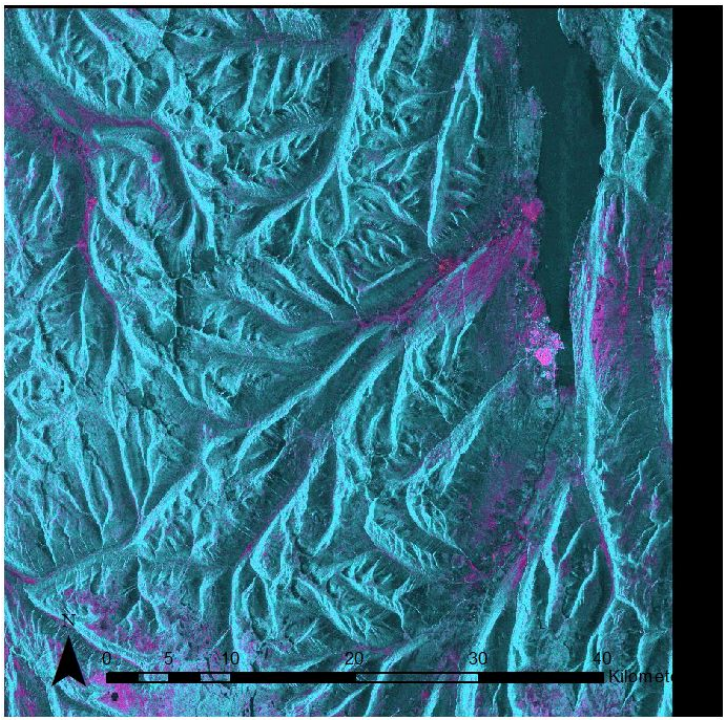

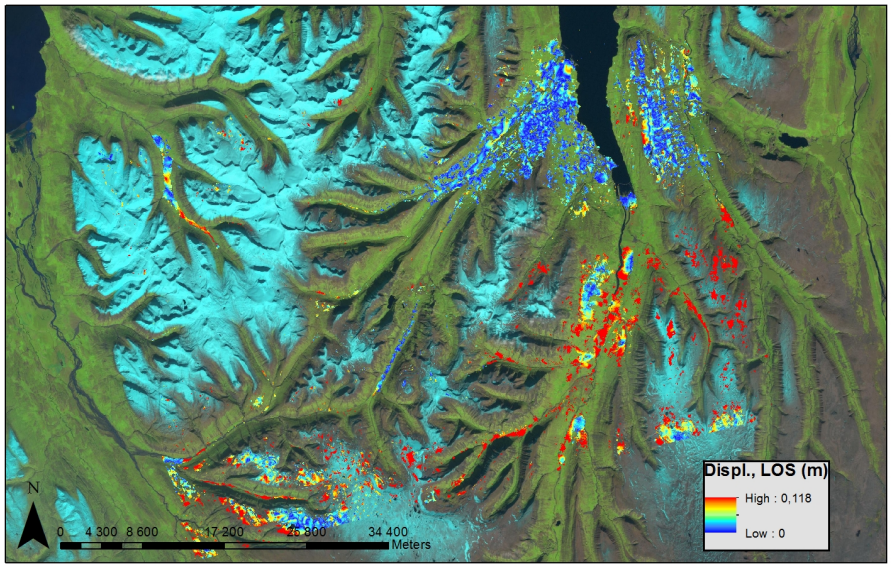

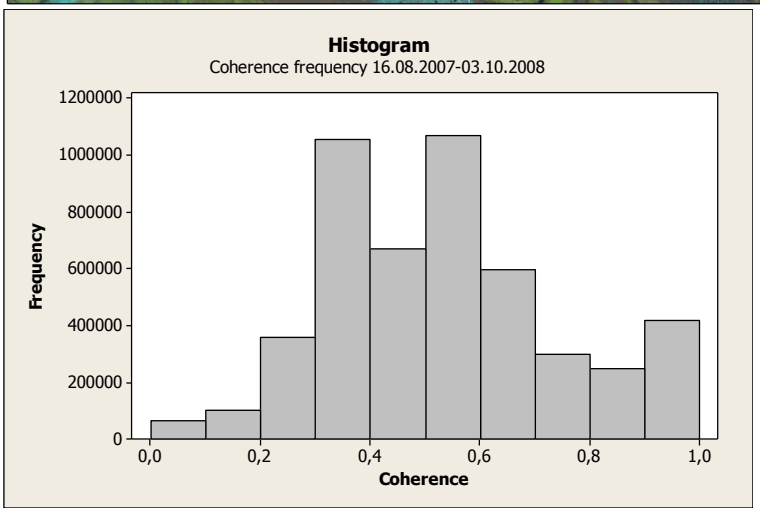

Figure 5: Coherence (top), Unwrapped differential interferogram (middle) and histogram (bottom) from 16.08.2007-03.10.2008.

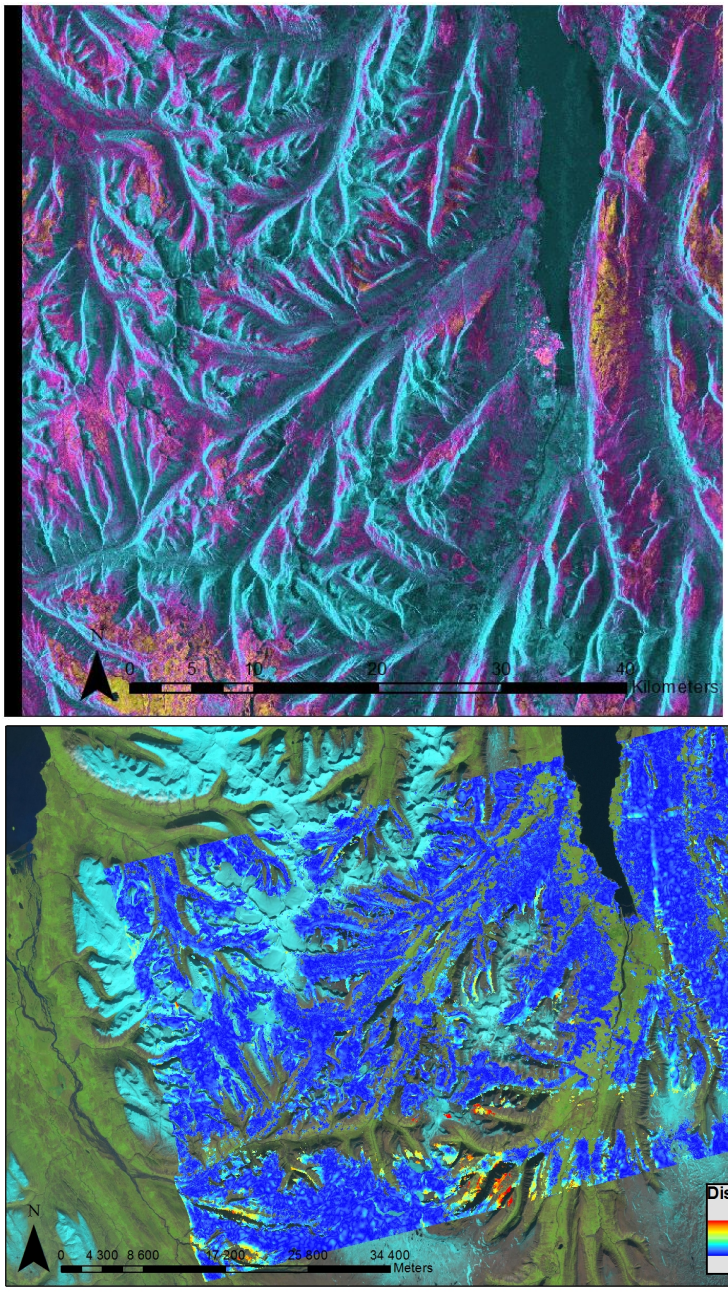

Figure 6: Coherence (top), Unwrapped differential interferogram (middle) and histogram (bottom) from 16.08.2007-09.07.2010.

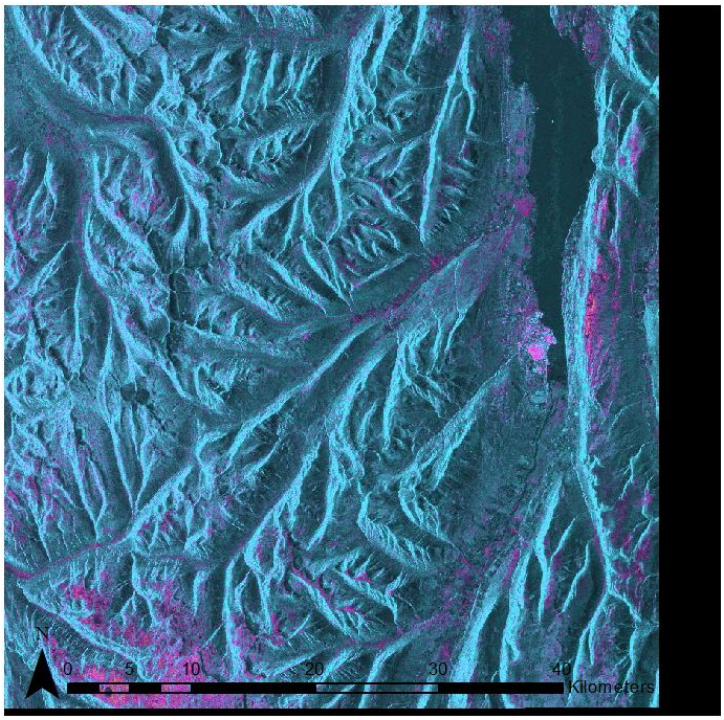

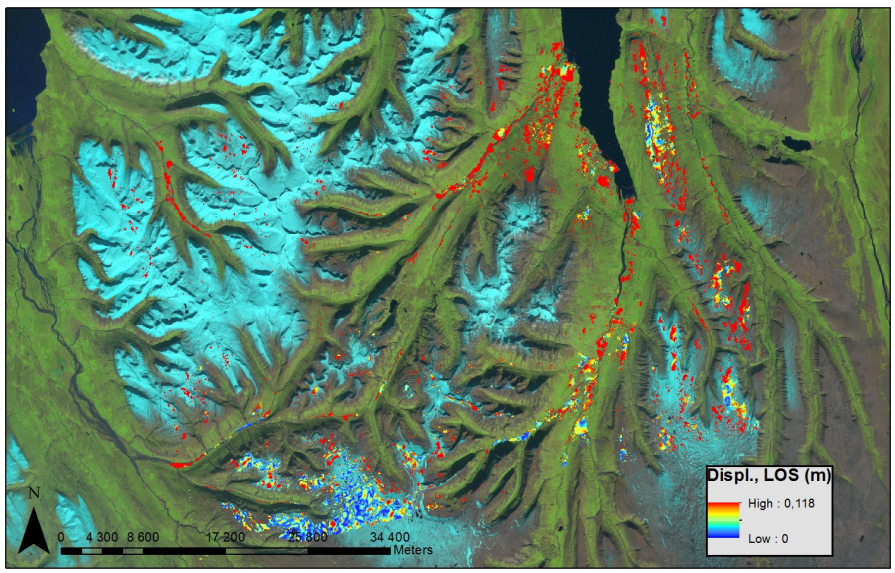

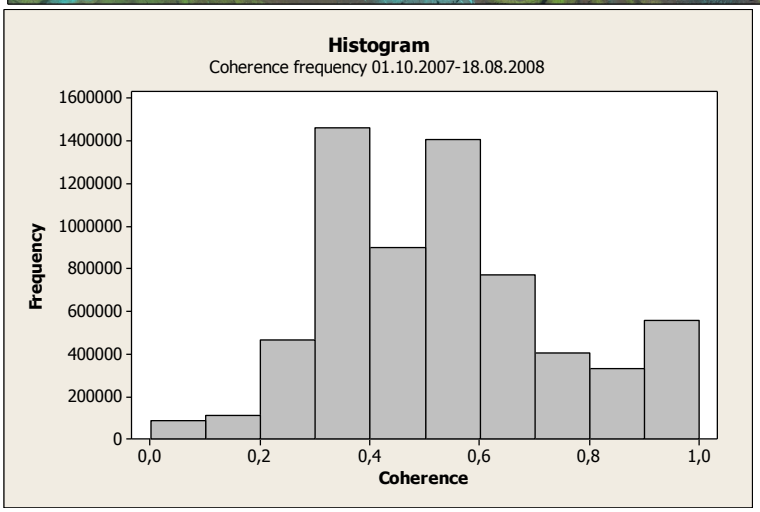

Figure 7: Coherence (top), Unwrapped differential interferogram (middle) and histogram (bottom) from 01.10.2007-18.08.2008.

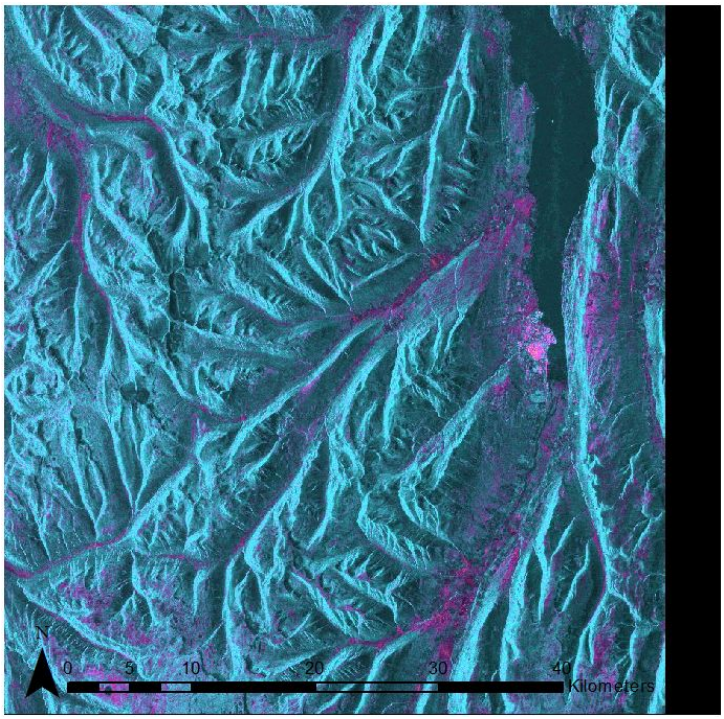

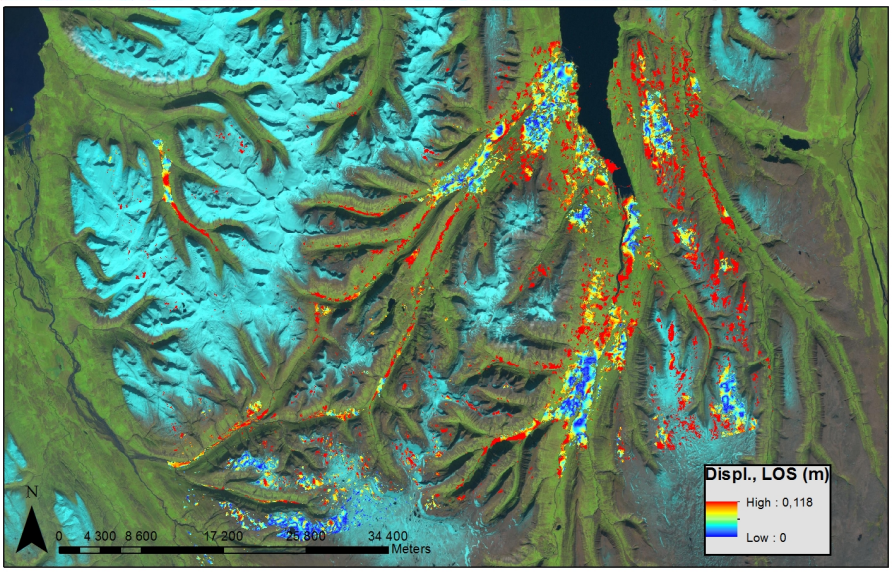

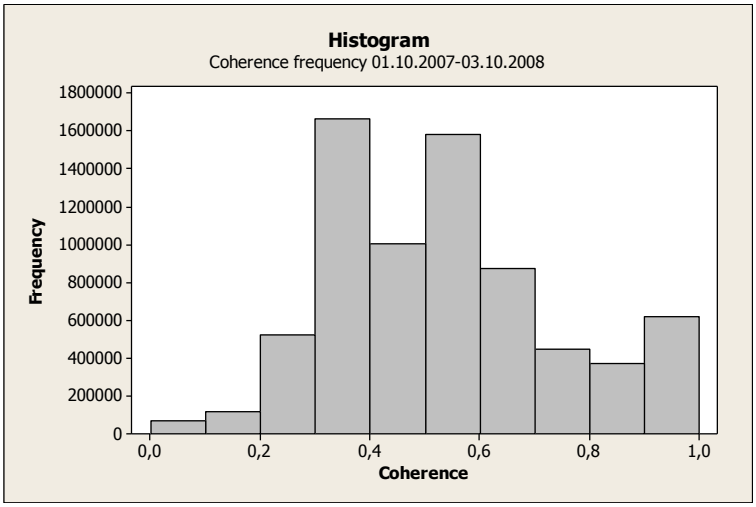

Figure 8: Coherence (top), Unwrapped differential interferogram (middle) and histogram (bottom) from 01.10.2007-03.10.2008.

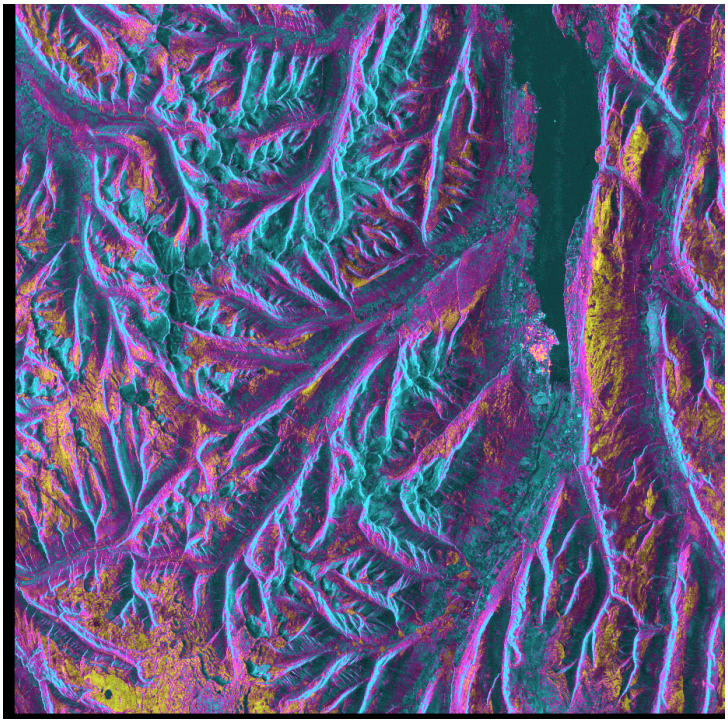

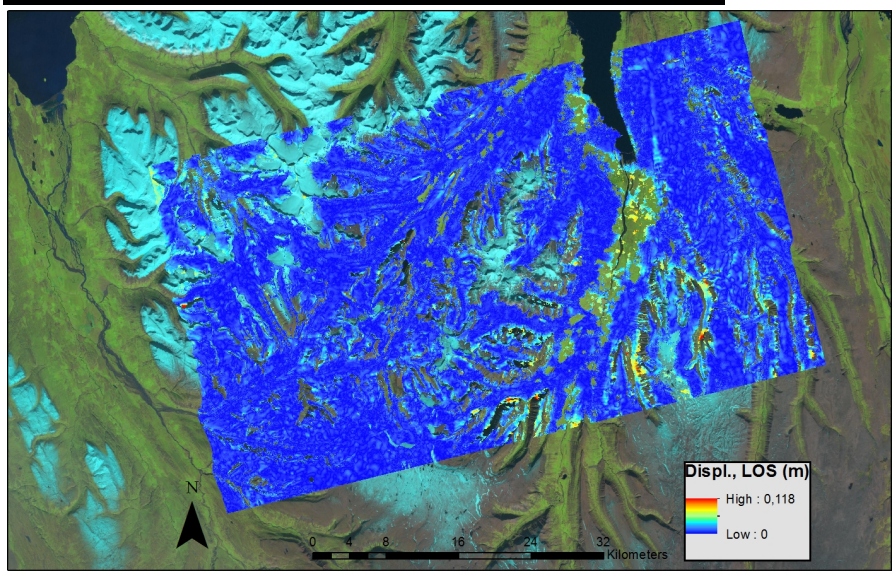

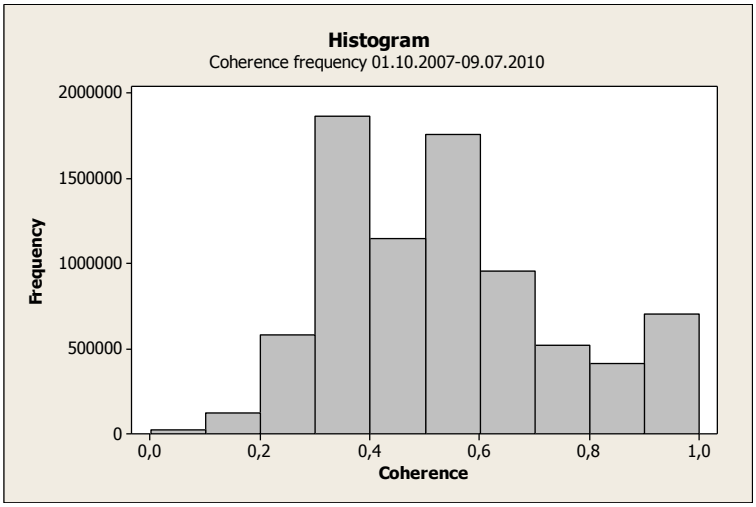

Figure 9: Coherence (top), Unwrapped differential interferogram (middle) and histogram (bottom) from 01.10.2007-09.07.2010.

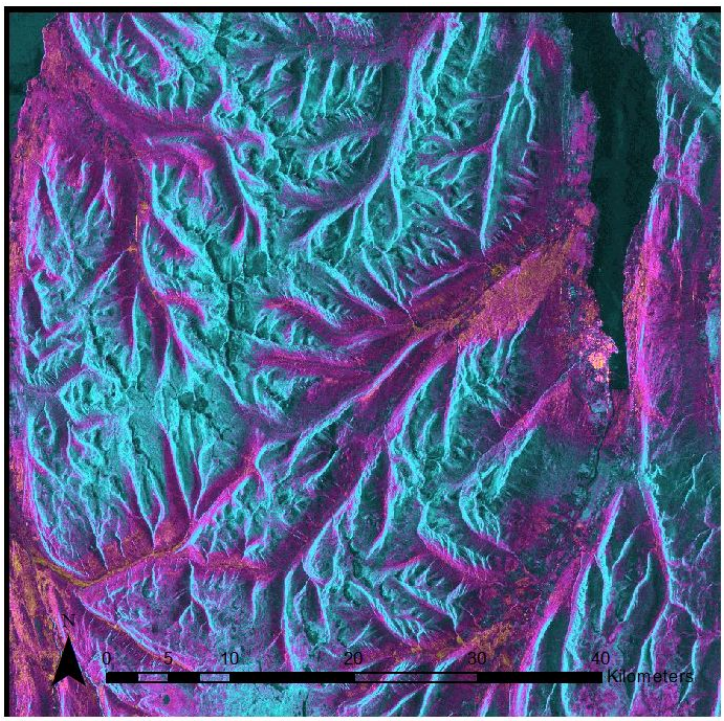

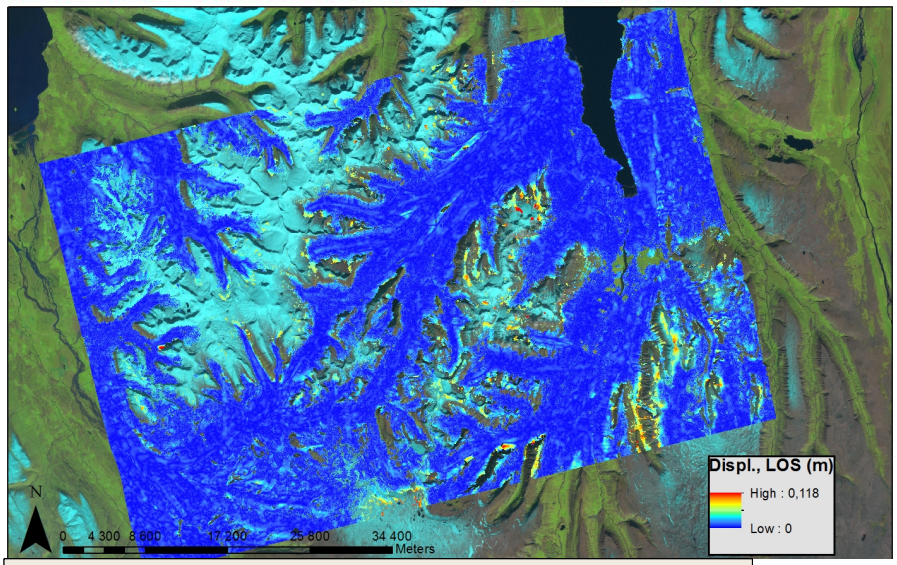

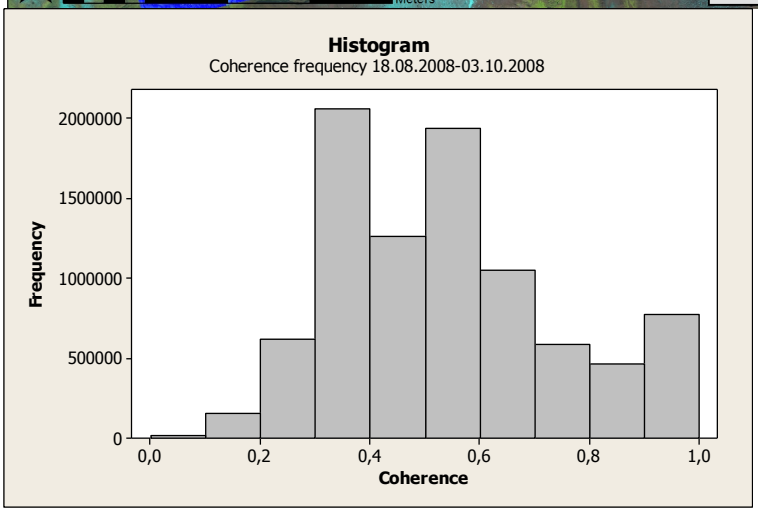

Figure 10: Coherence (top), Unwrapped differential interferogram (middle) and histogram (bottom) from 18.08.2008-03.10.2008.

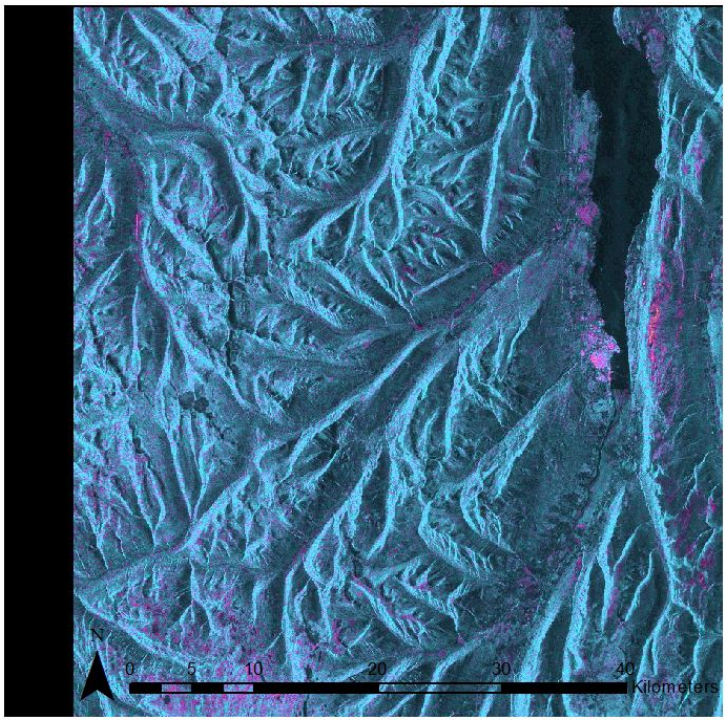

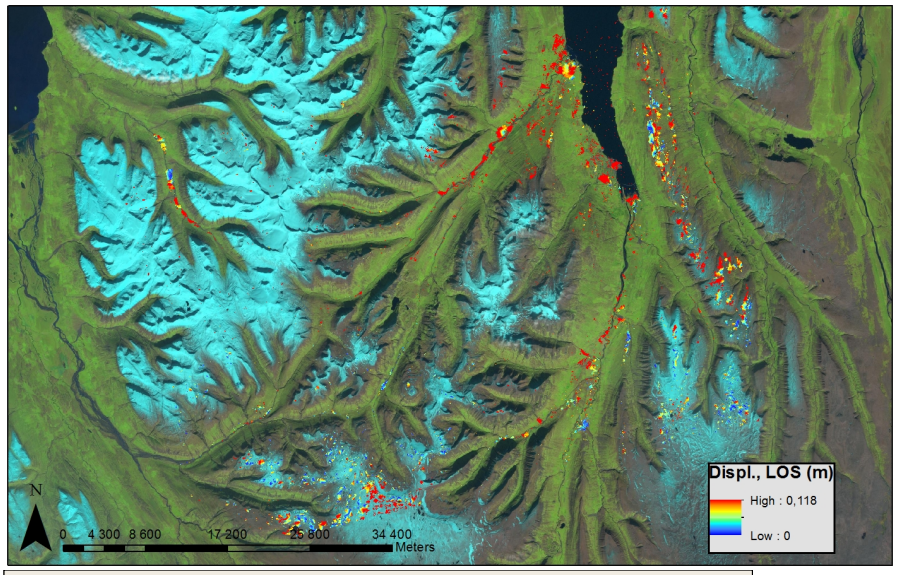

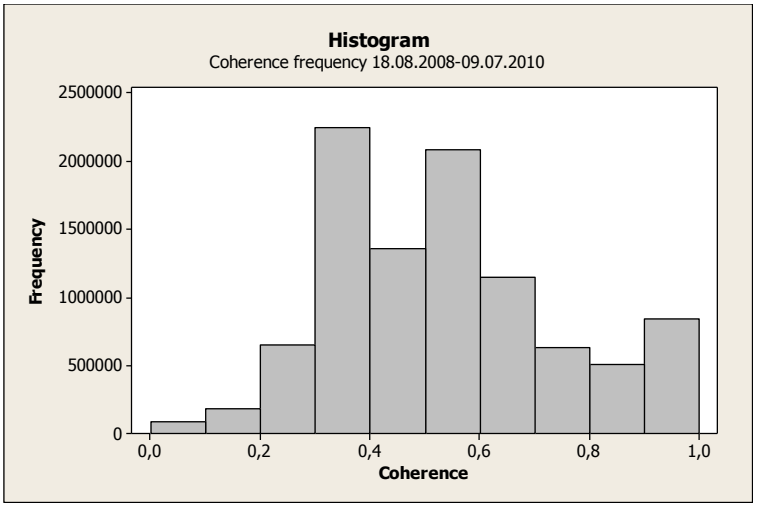

Figure 11: Coherence (top), Unwrapped differential interferogram (middle) and histogram (bottom) from 18.08.2008-09.07.2010.

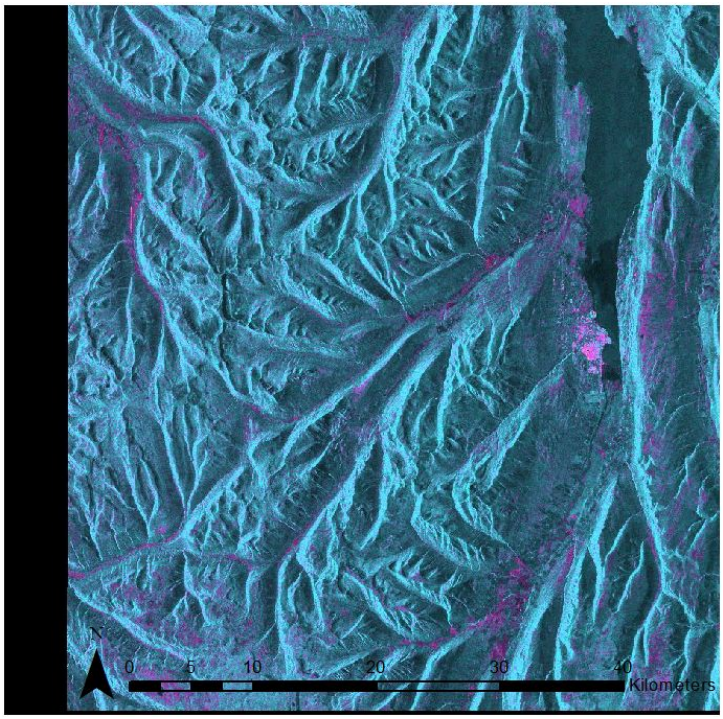

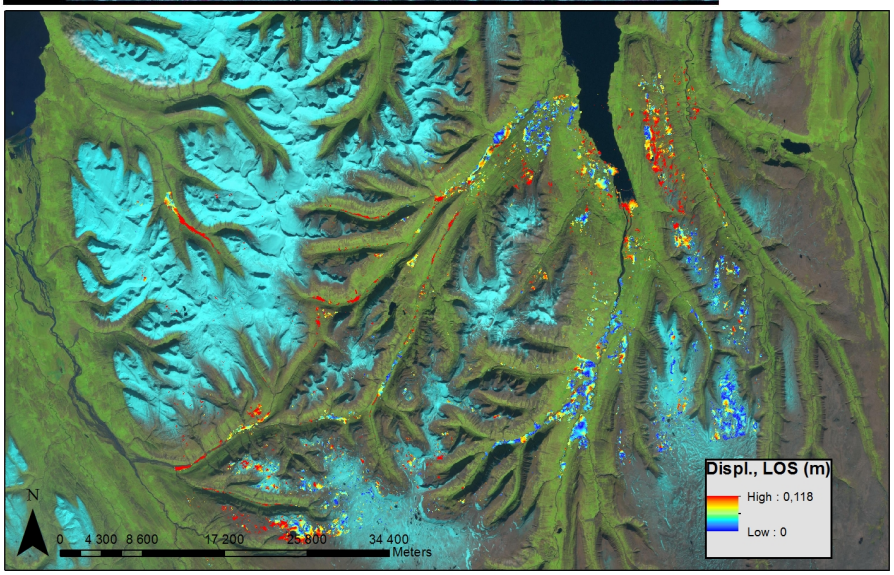

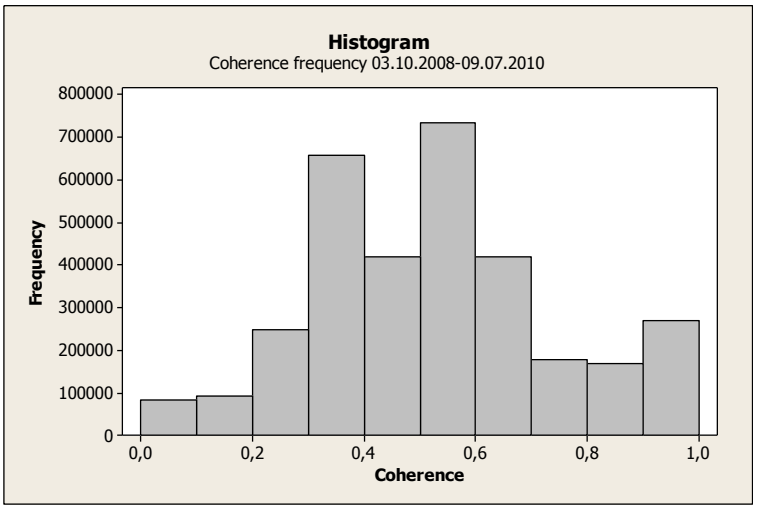

Figure 12: Coherence (top), Unwrapped differential interferogram (middle) and histogram (bottom) from 03.10.2008-09.07.2010.

Austurland, eastern Iceland. North.

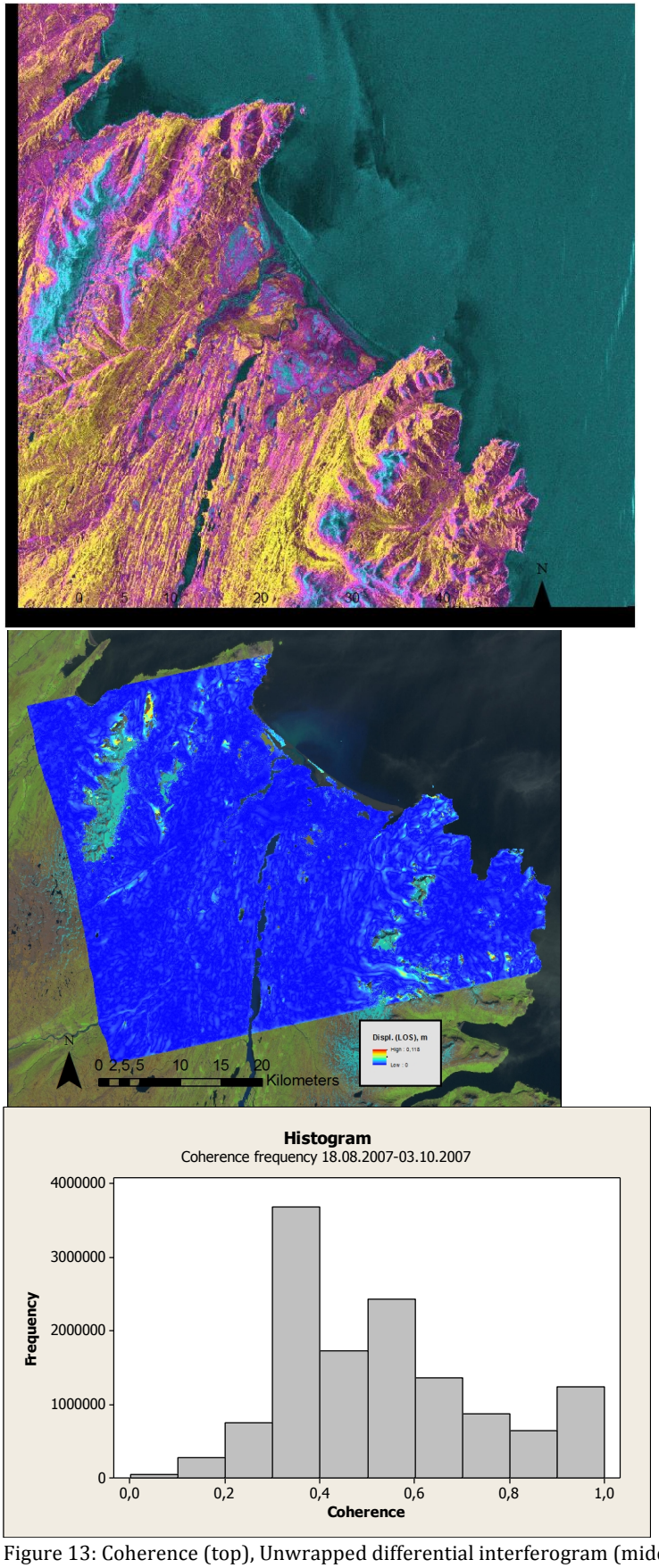

Figure 13: Coherence (top), Unwrapped differential interferogram (middle) and histogram (bottom) from 18.08.2007-03.10.2007.

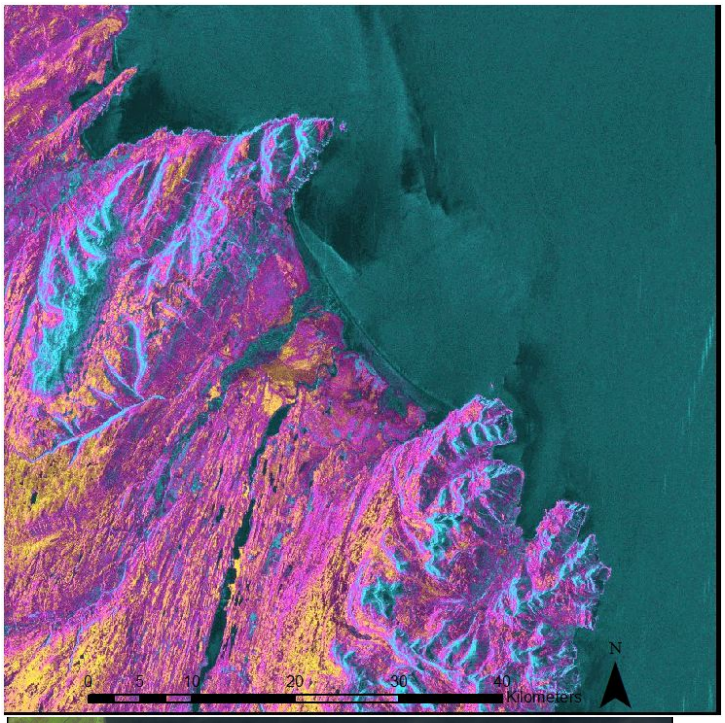

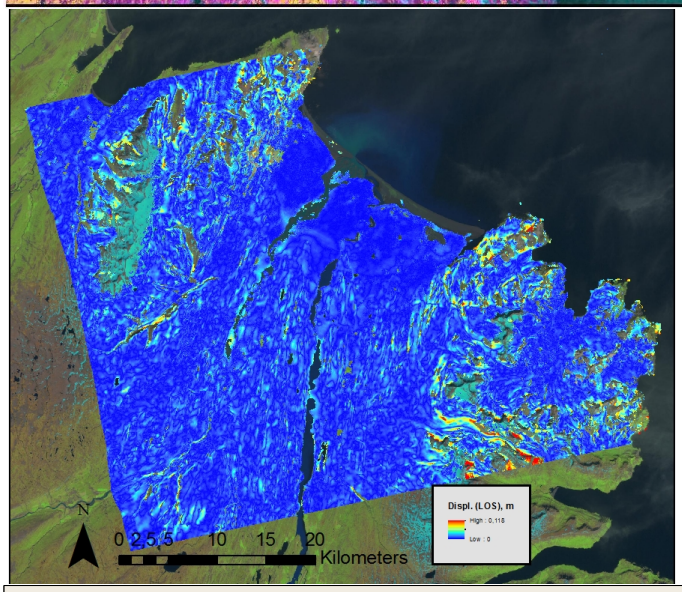

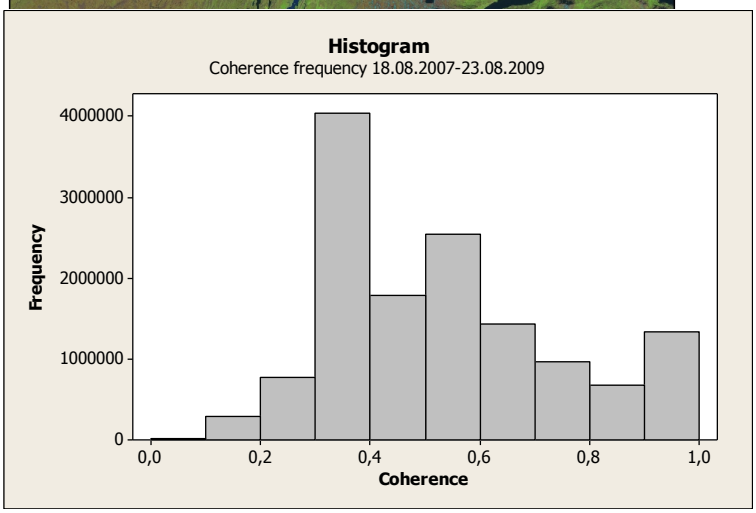

Figure 14: Coherence (top), Unwrapped differential interferogram (middle) and histogram (bottom) from 18.08.2007-23.08.2009.

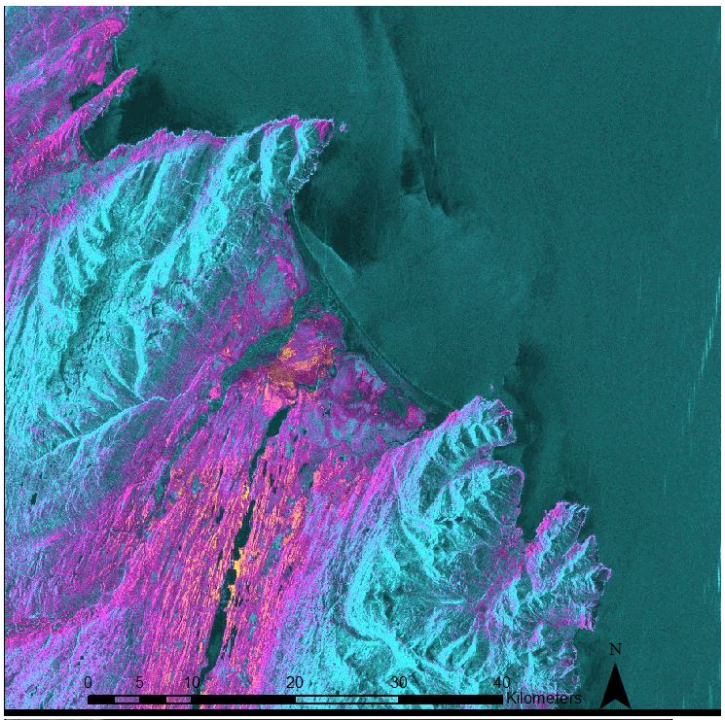

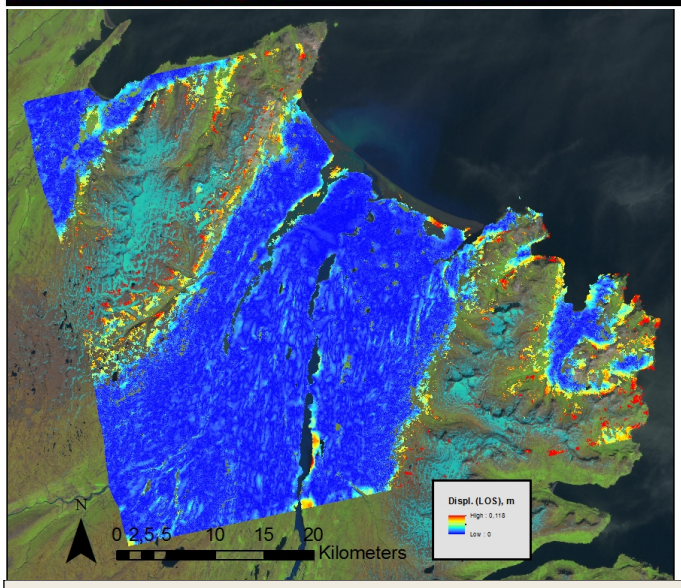

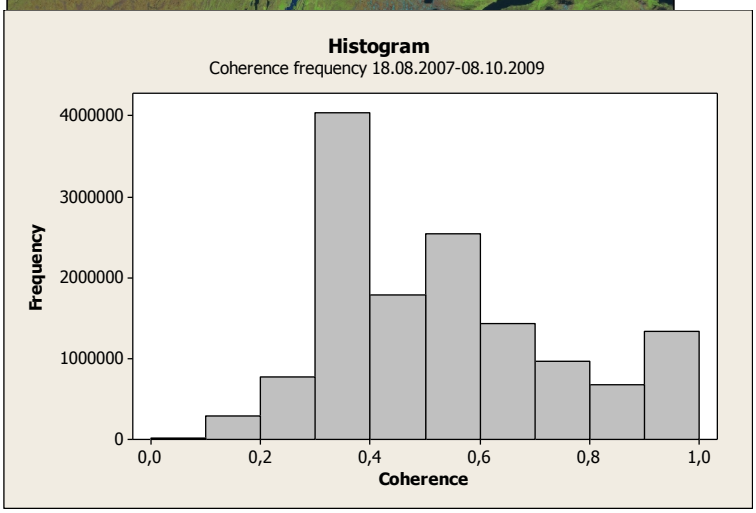

Figure 15: Coherence (top), Unwrapped differential interferogram (middle) and histogram (bottom) from 18.08.2007-08.10.2009.

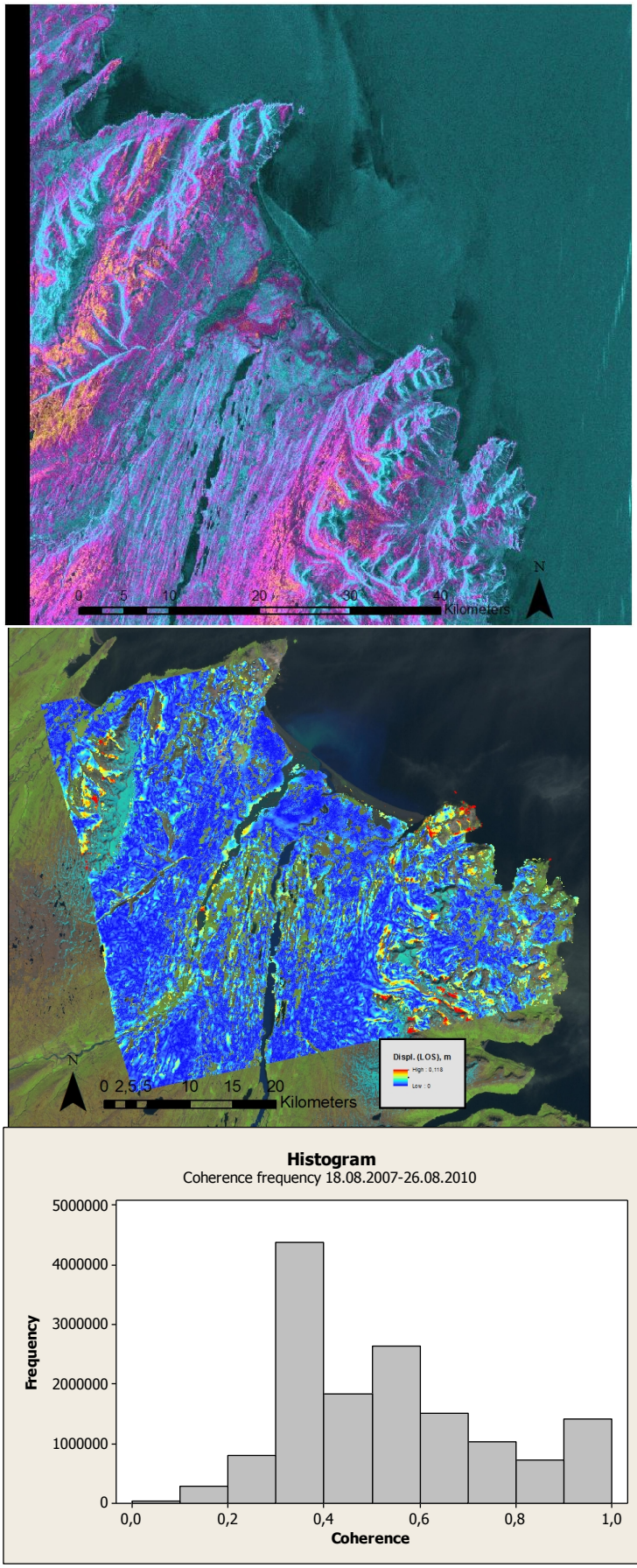

Figure 16: Coherence (top), Unwrapped differential interferogram (middle) and histogram (bottom) from 18.08.2007-26.08.2010.

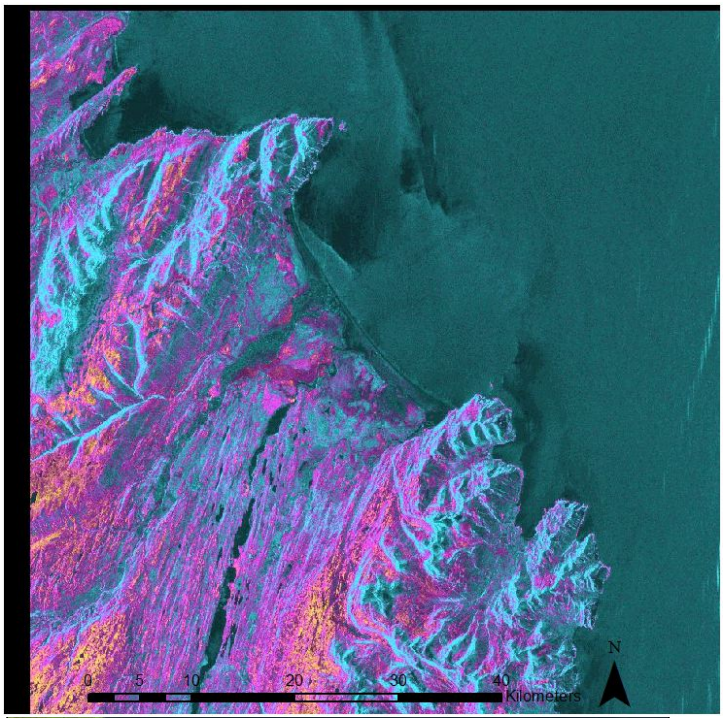

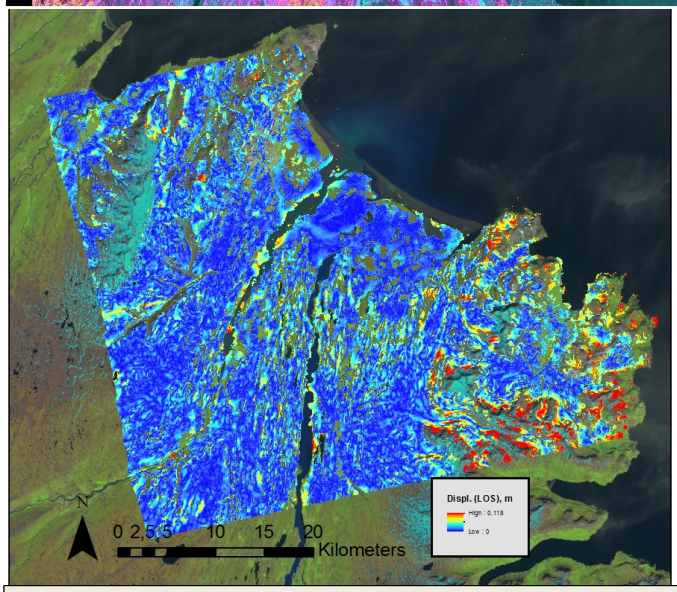

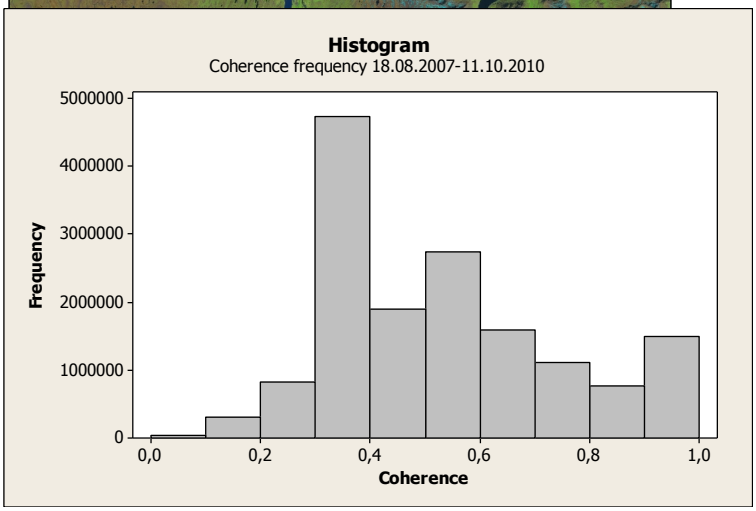

Figure 17: Coherence (top), Unwrapped differential interferogram (middle) and histogram (bottom) from 18.08.2007-11.10.2010.

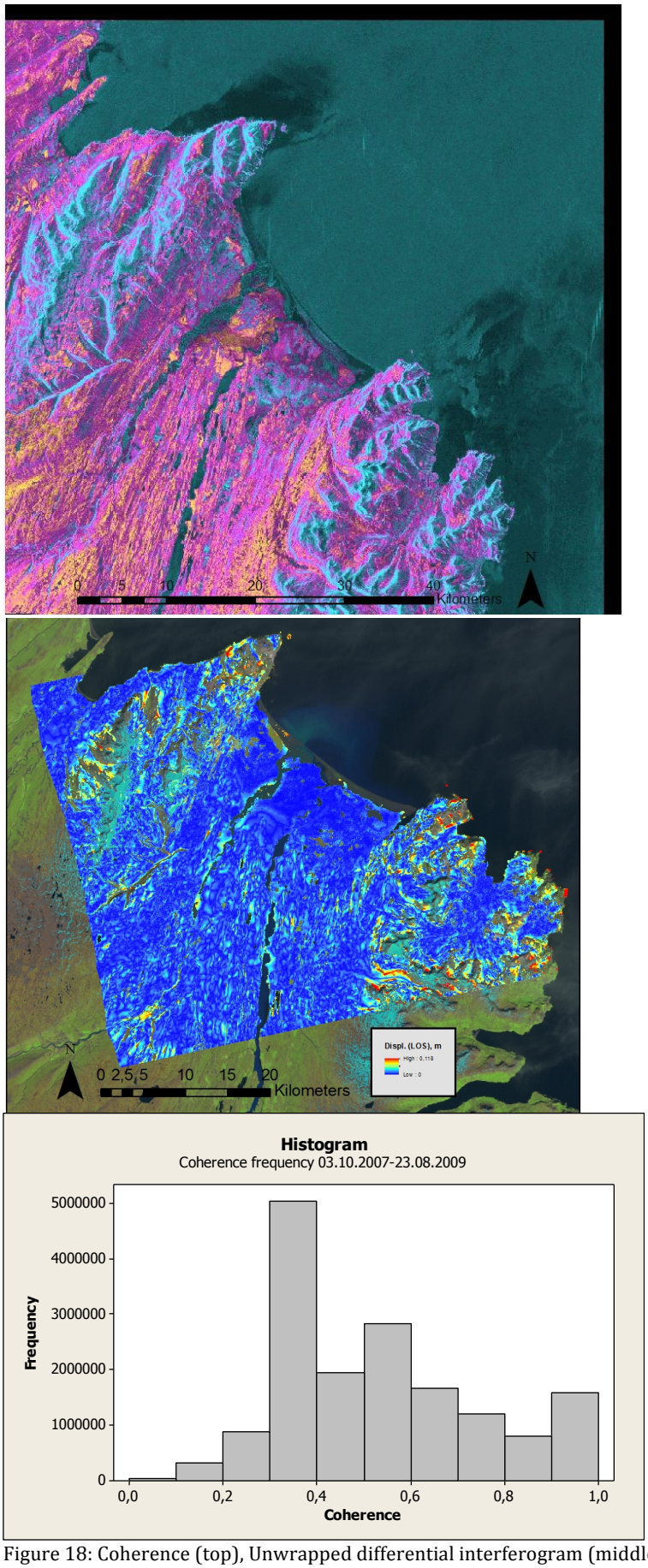

Figure 18: Coherence (top), Unwrapped differential interferogram (middle) and histogram (bottom) from 03.10.2007-23.08.2009.

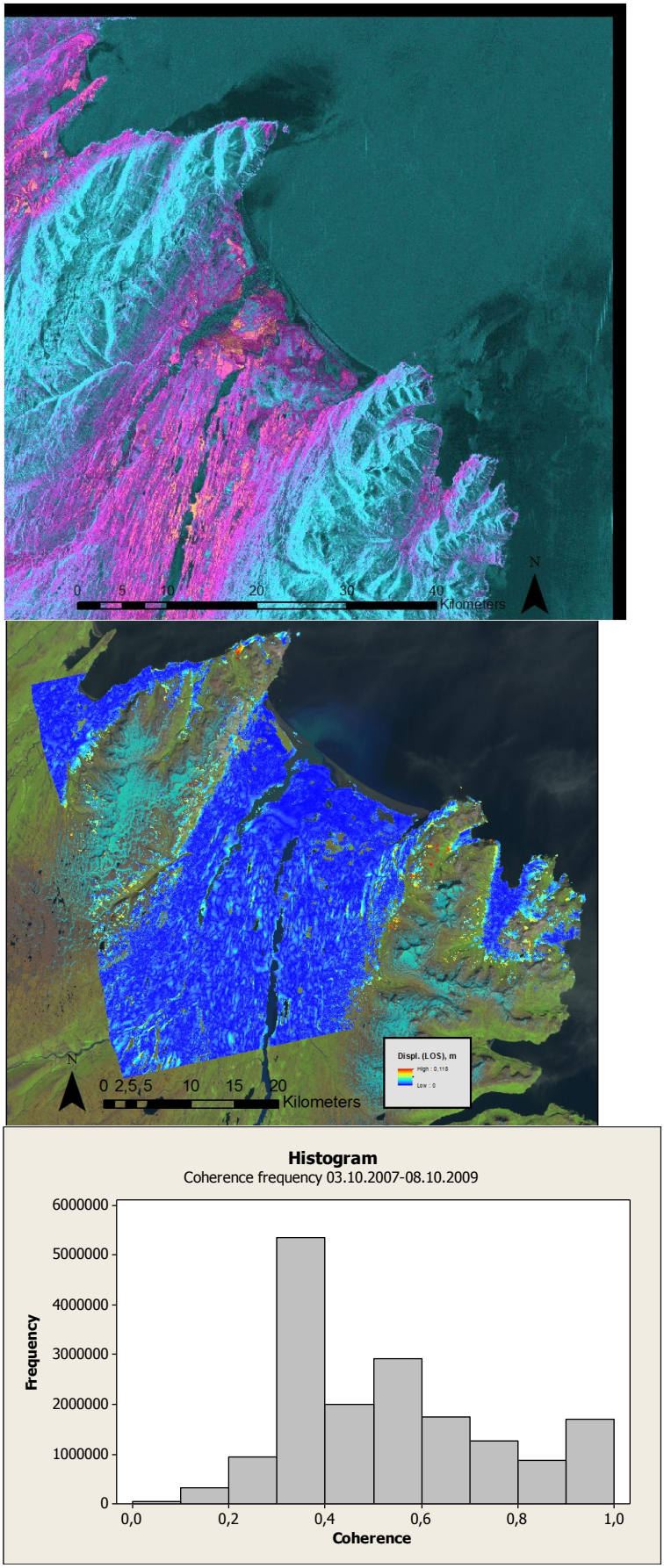

Figure 19: Coherence (top), Unwrapped differential interferogram (middle) and histogram (bottom) from 03.10.2007-08.10.2009.

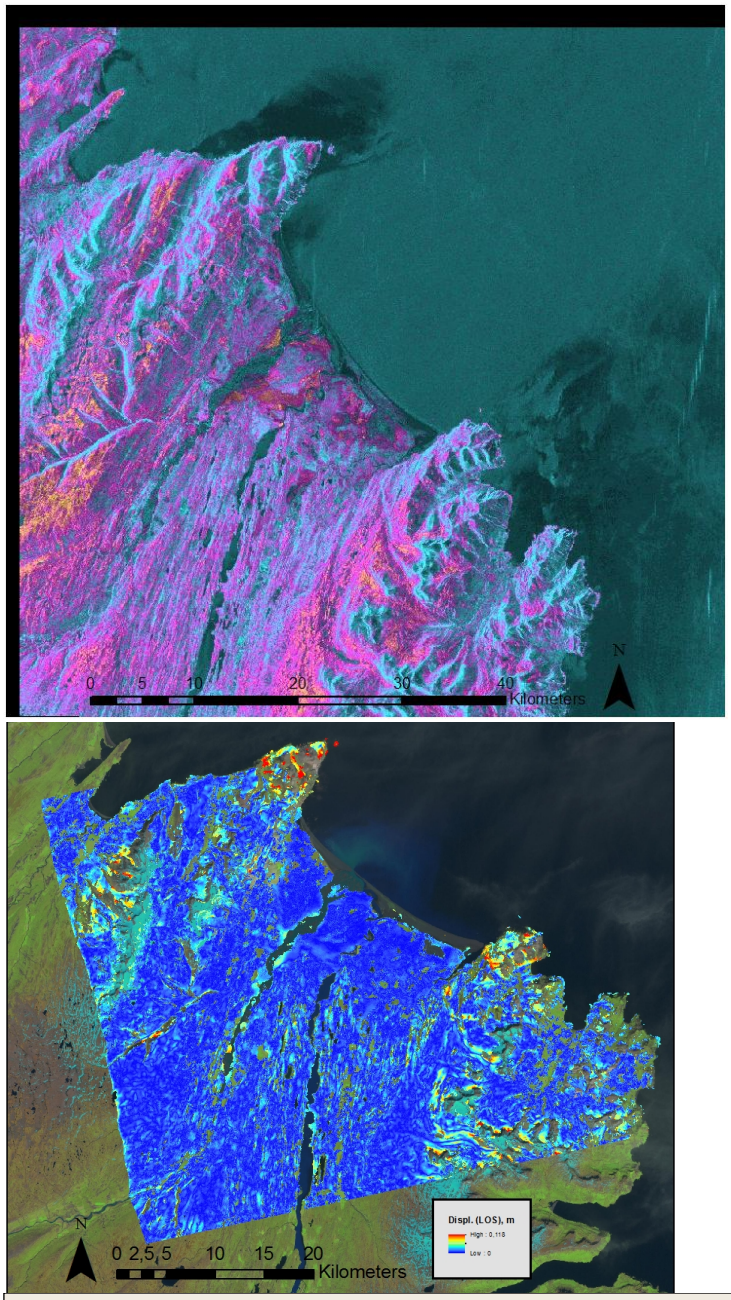

Figure 20: Coherence (top), Unwrapped differential interferogram (middle) and histogram (bottom) from 03.10.2007-26.08.2010.

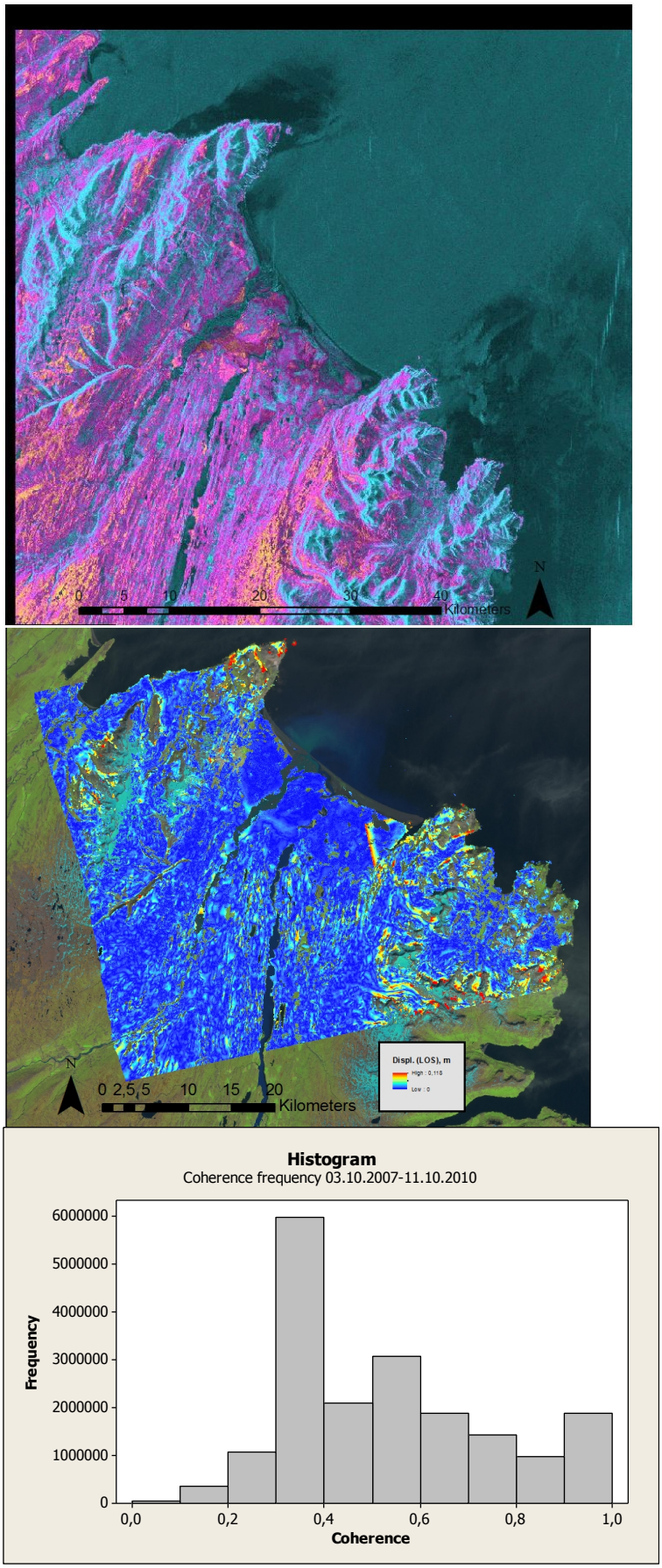

Figure 21: Coherence (top), Unwrapped differential interferogram (middle) and histogram (bottom) from 03.10.2007-11.10.2010.

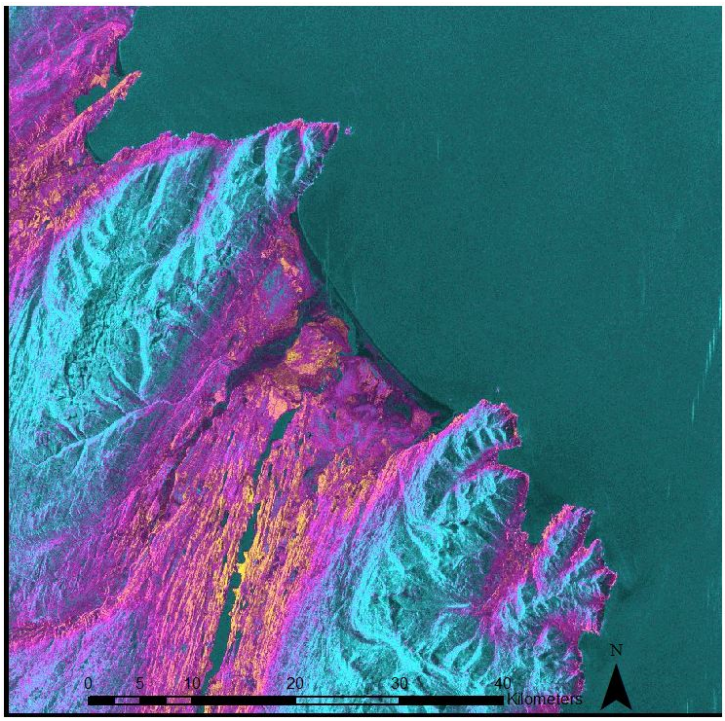

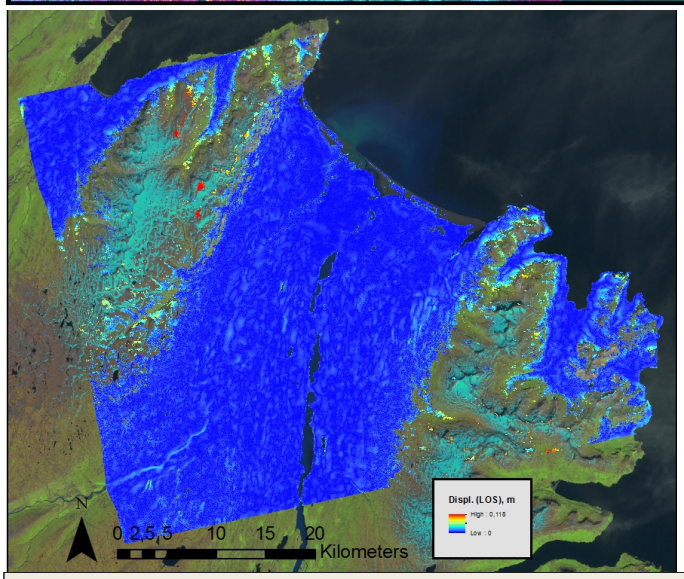

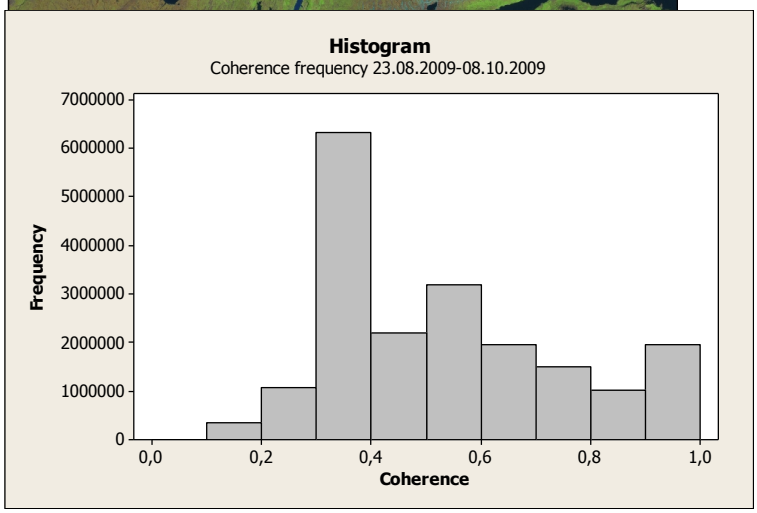

Figure 22: Coherence (top), Unwrapped differential interferogram (middle) and histogram (bottom) from 23.08.2009-08.10.2009.

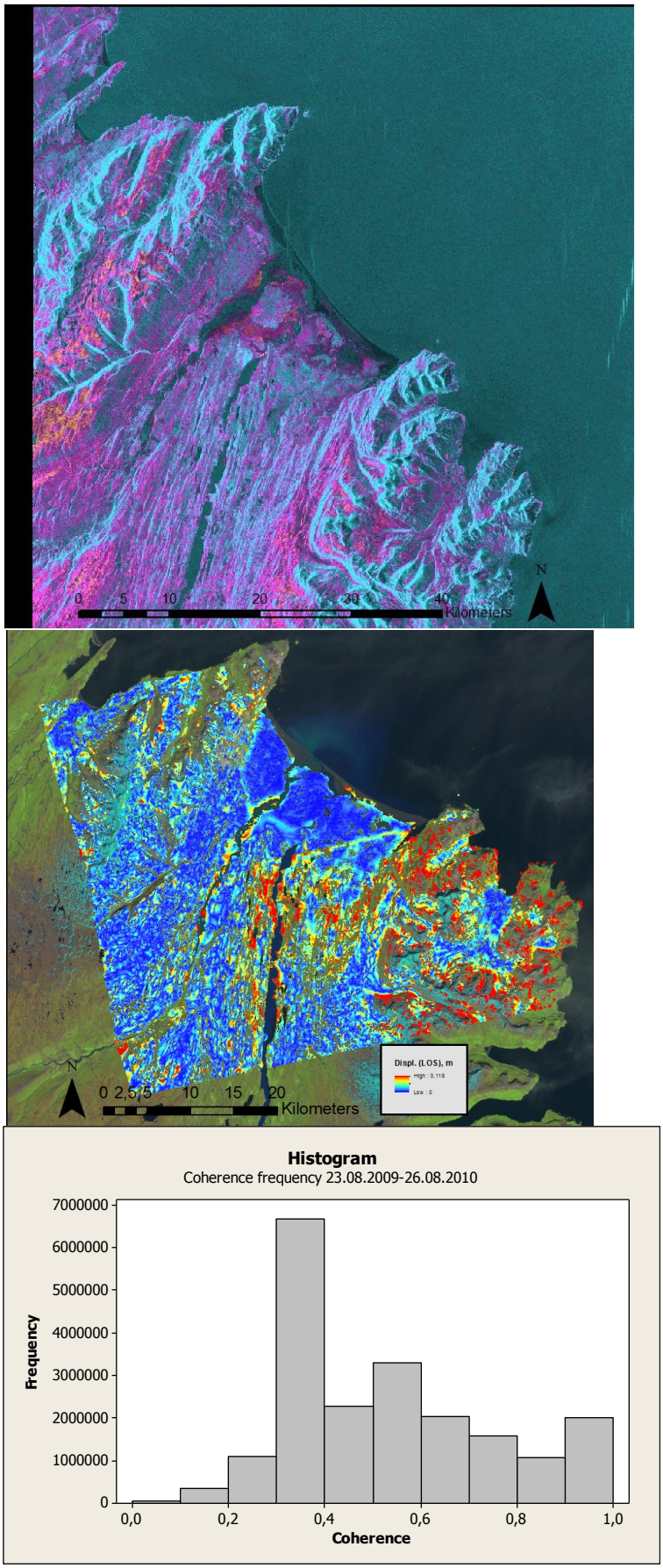

Figure 23: Coherence (top), Unwrapped differential interferogram (middle) and histogram (bottom) from 23.08.2009-26.08.2010.

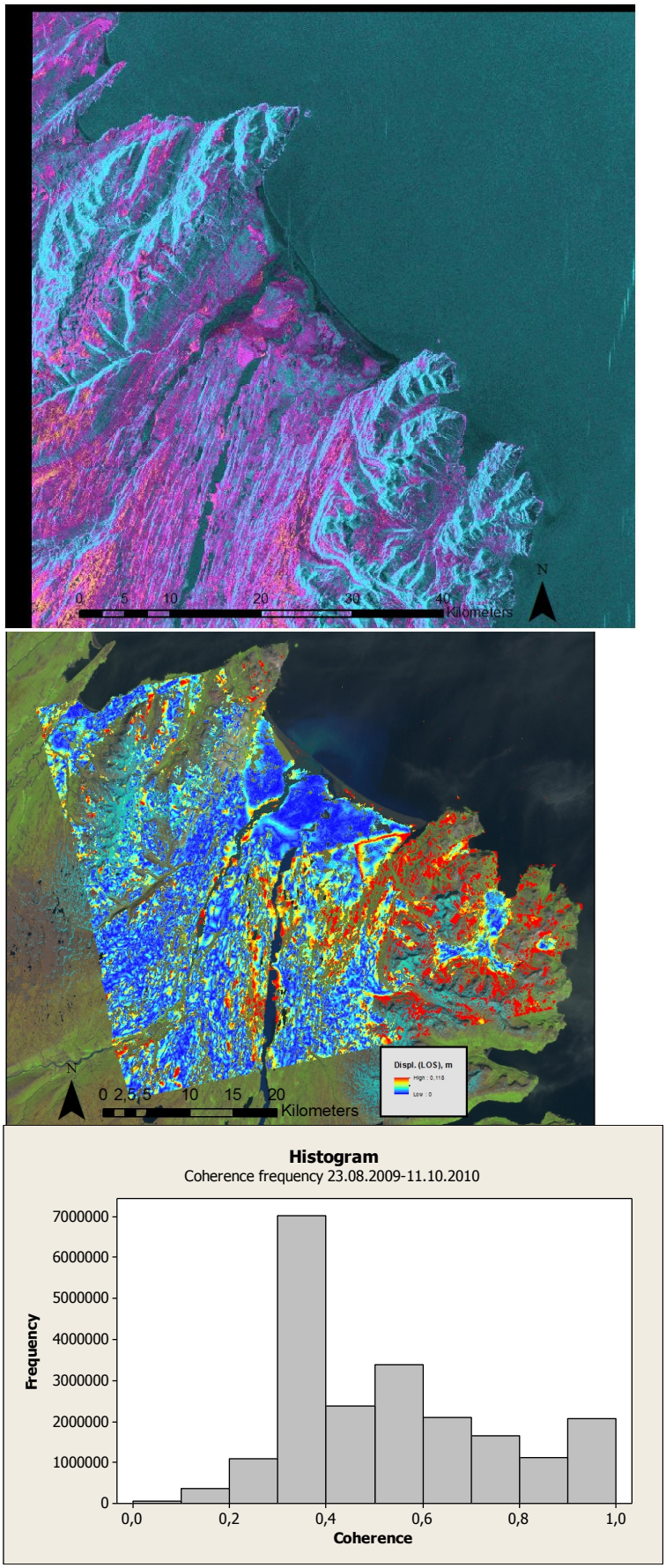

Figure 24: Coherence (top), Unwrapped differential interferogram (middle) and histogram (bottom) from 23.08.2009-11.10.2010.

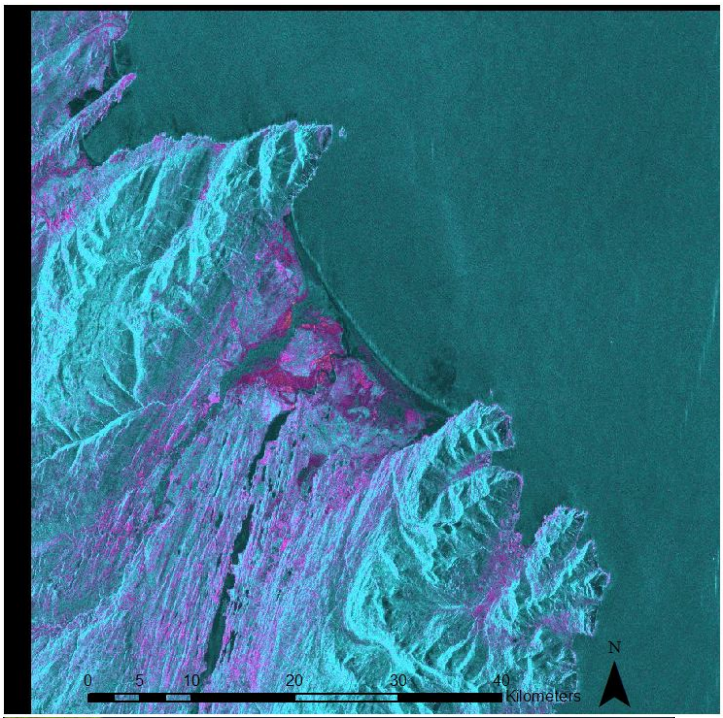

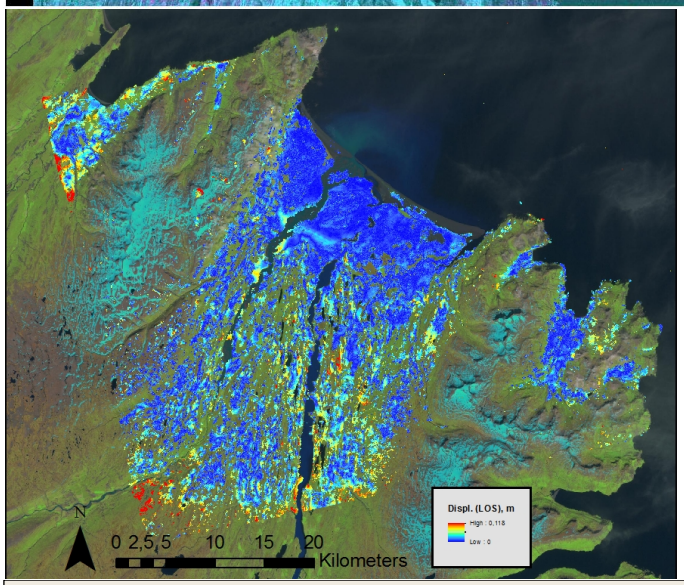

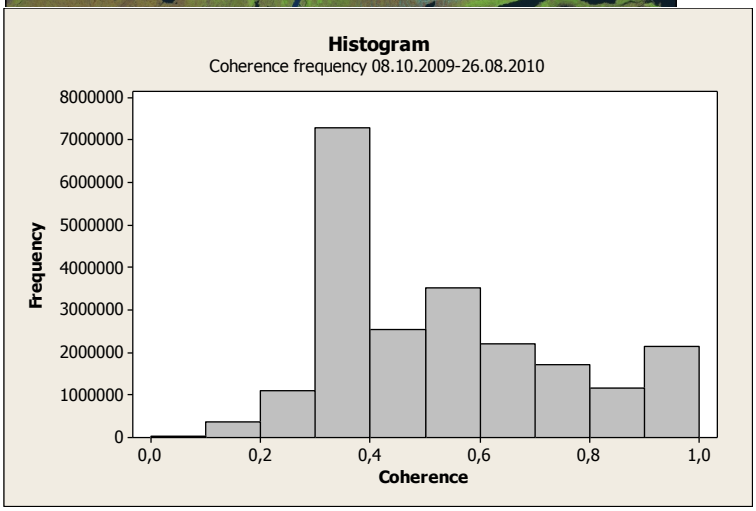

Figure 25: Coherence (top), Unwrapped differential interferogram (middle) and histogram (bottom) from 08.10.2009-26.08.2010.

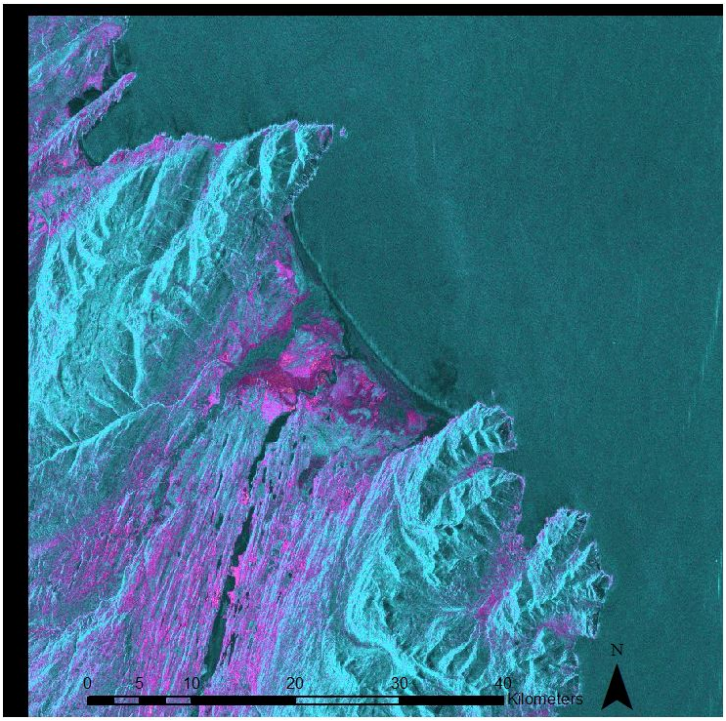

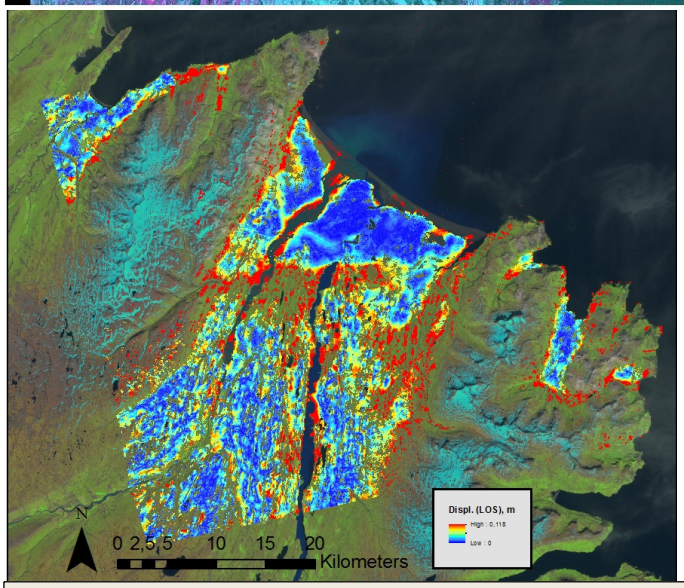

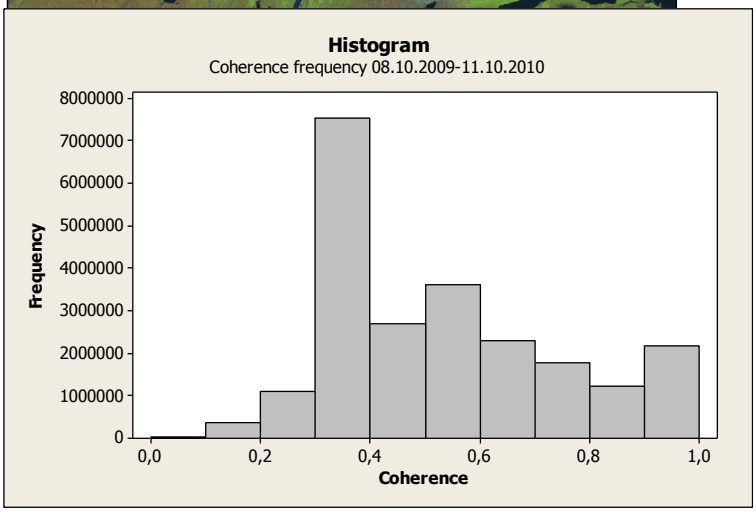

Figure 26: Coherence (top), Unwrapped differential interferogram (middle) and histogram (bottom) from 08.10.2009-11.10.2010.

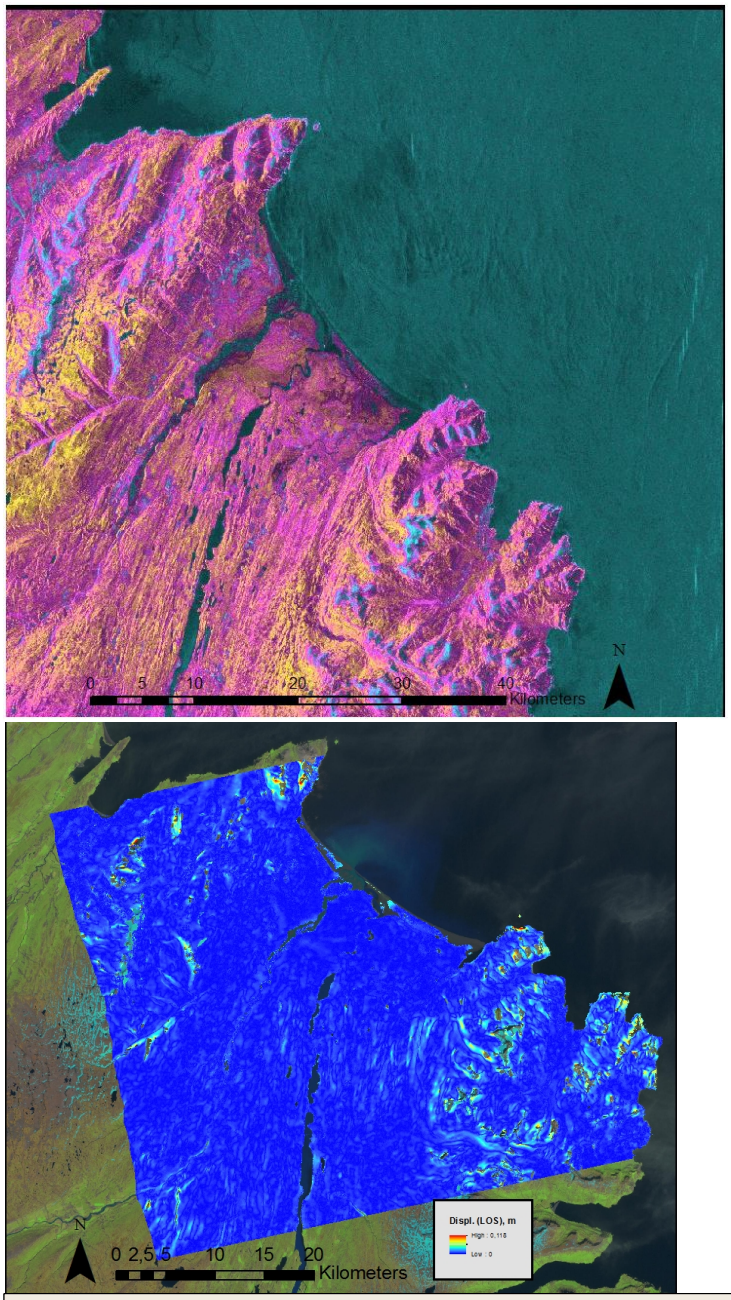

Figure 27: Coherence (top), Unwrapped differential interferogram (middle) and histogram (bottom) from 26.08.2010-11.10.2010.

Austurland, eastern Iceland. South.

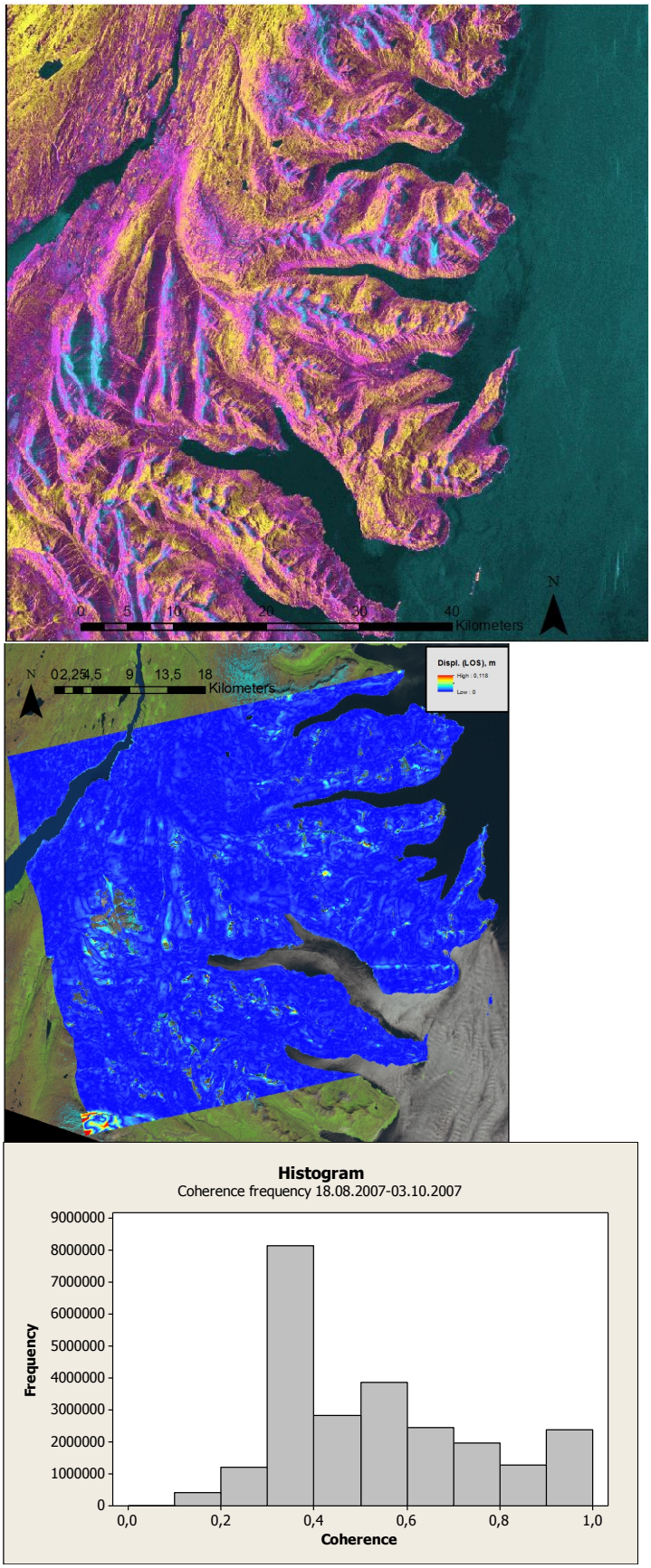

Figure 28: Coherence (top), Unwrapped differential interferogram (middle) and histogram (bottom) from 18.08.2007-03.10.2007.

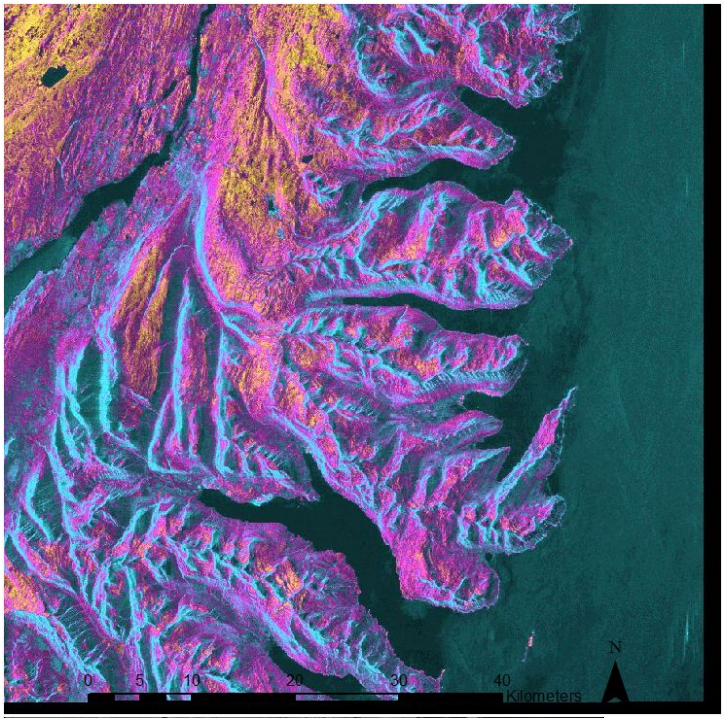

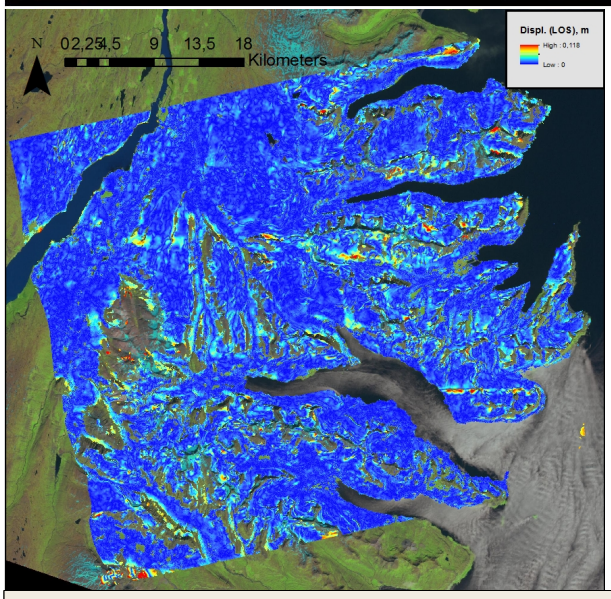

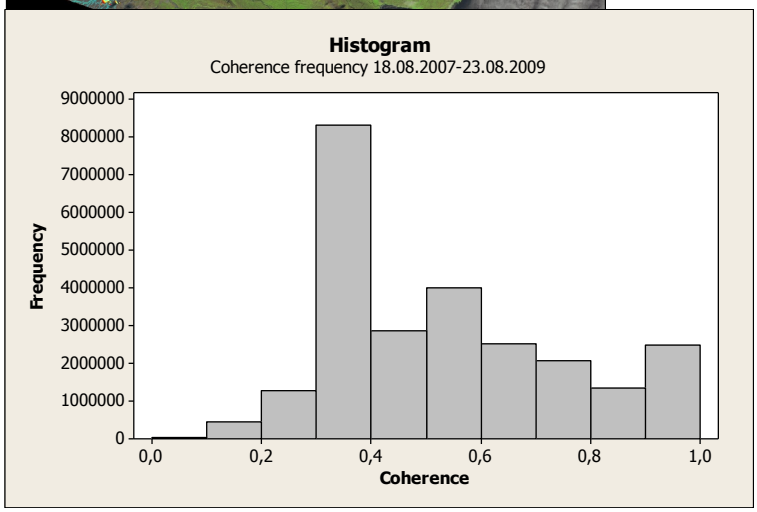

Figure 29: Coherence (top), Unwrapped differential interferogram (middle) and histogram (bottom) from 18.08.2007-23.08.2009.

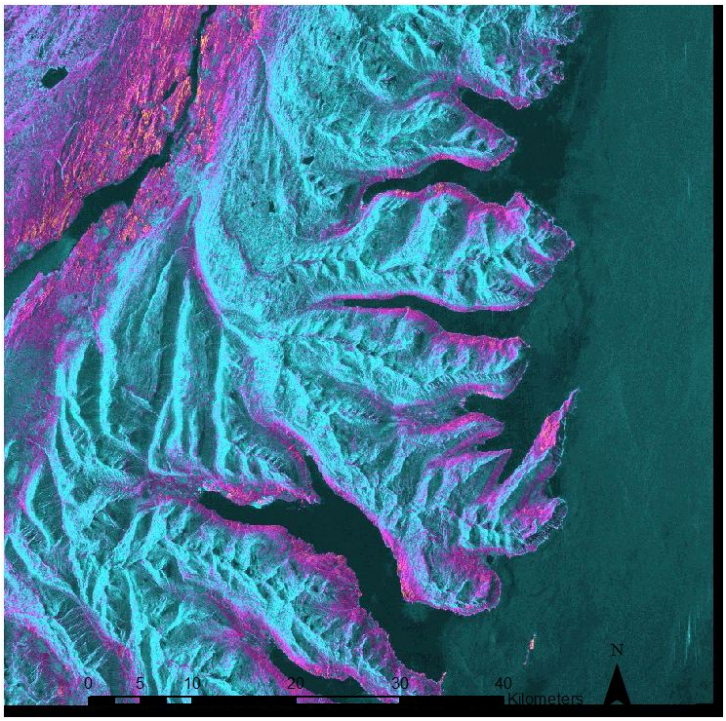

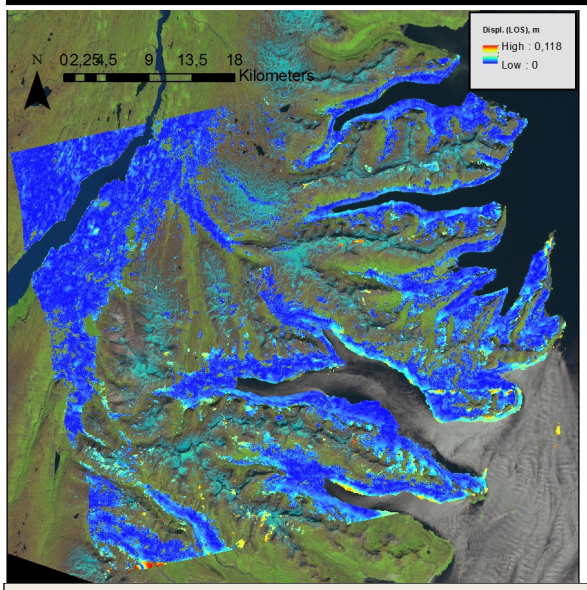

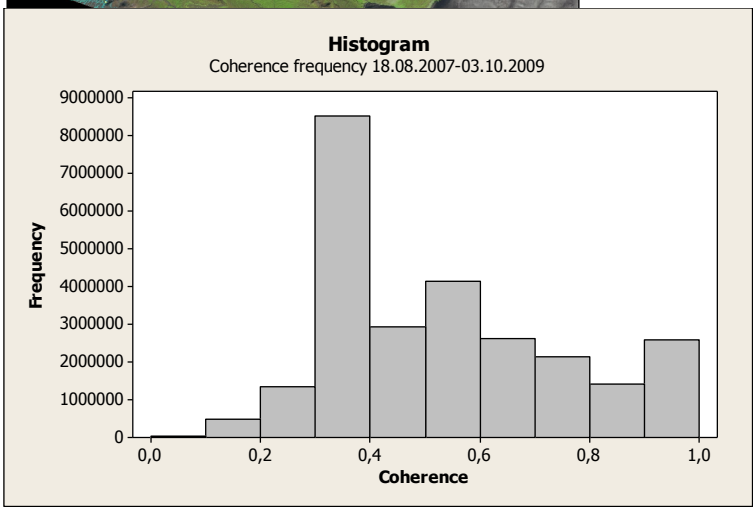

Figure 30: Coherence (top), Unwrapped differential interferogram (middle) and histogram (bottom) from 18.08.2007-08.10.2009.

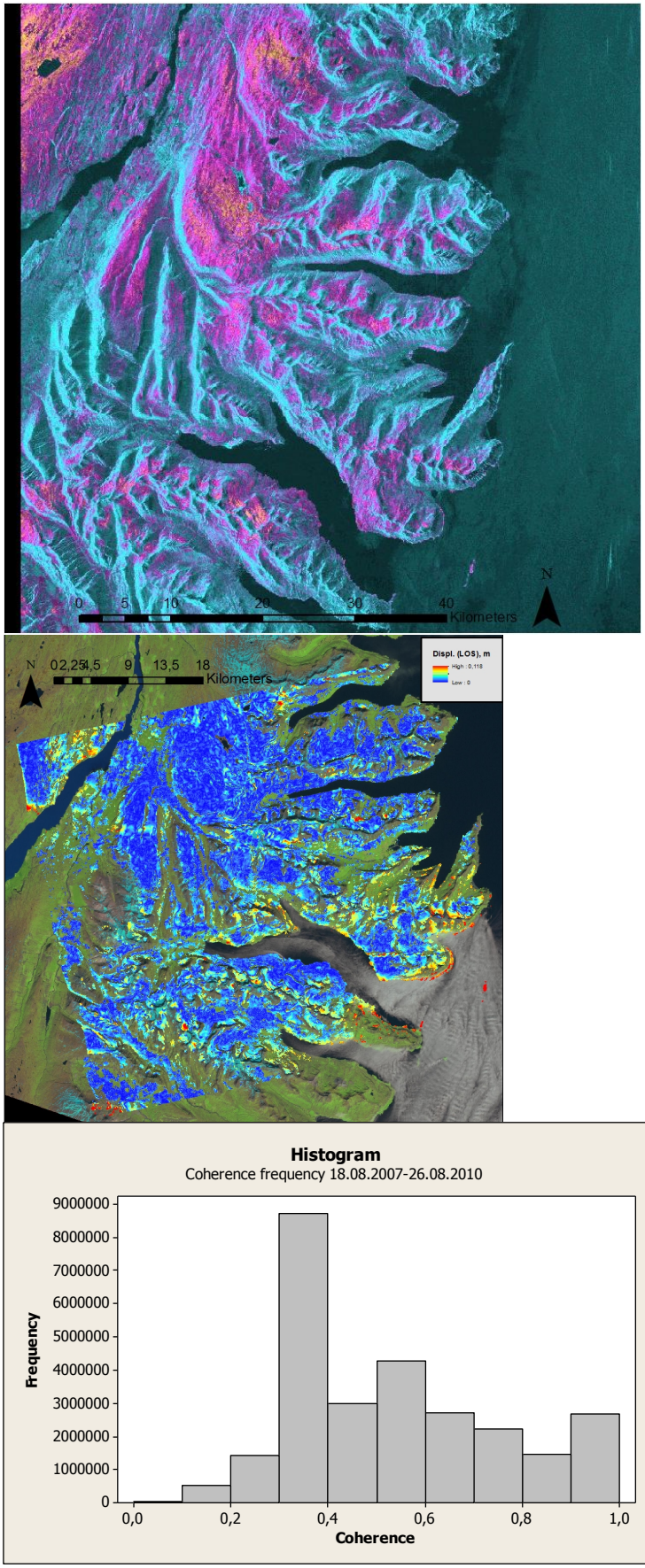

Figure 31: Coherence (top), Unwrapped differential interferogram (middle) and histogram (bottom) from 18.08.2007-26.08.2010.

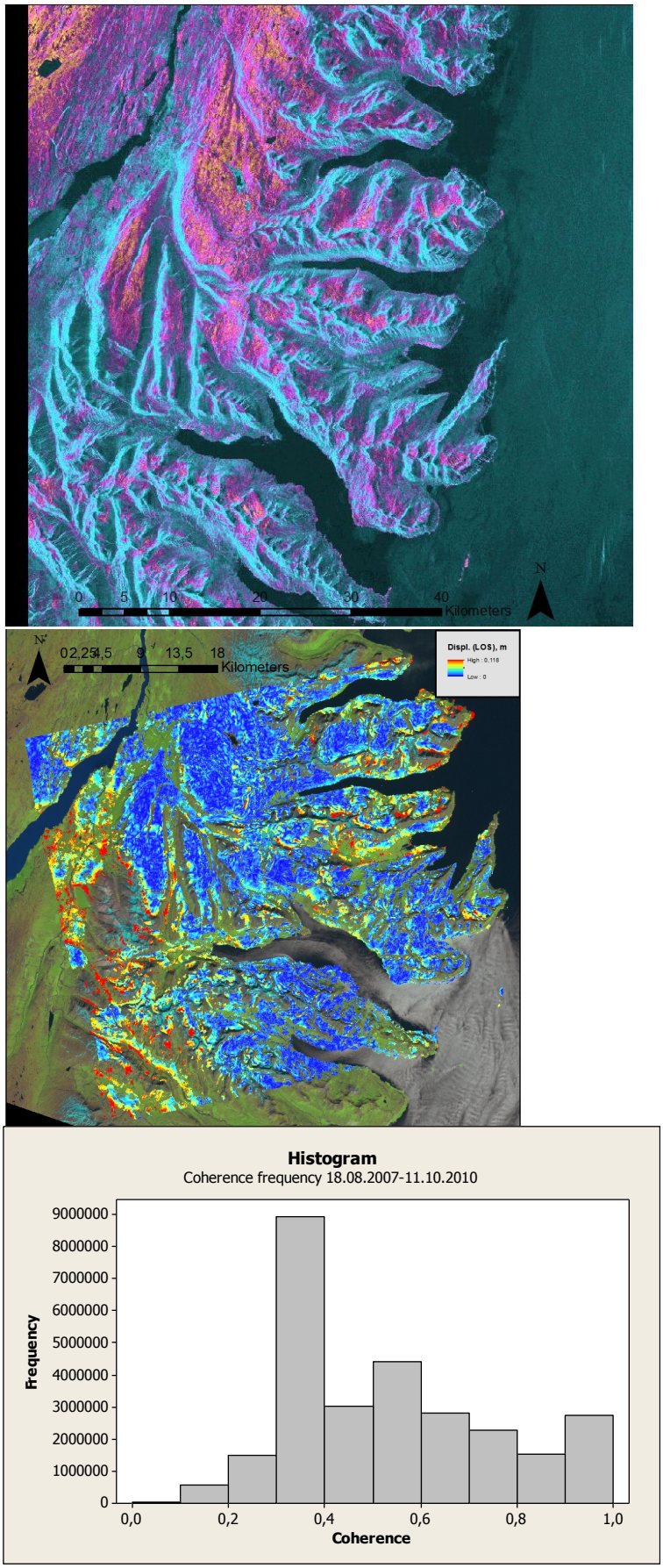

Figure 32: Coherence (top), Unwrapped differential interferogram (middle) and histogram (bottom) from 18.08.2007-11.10.2010.

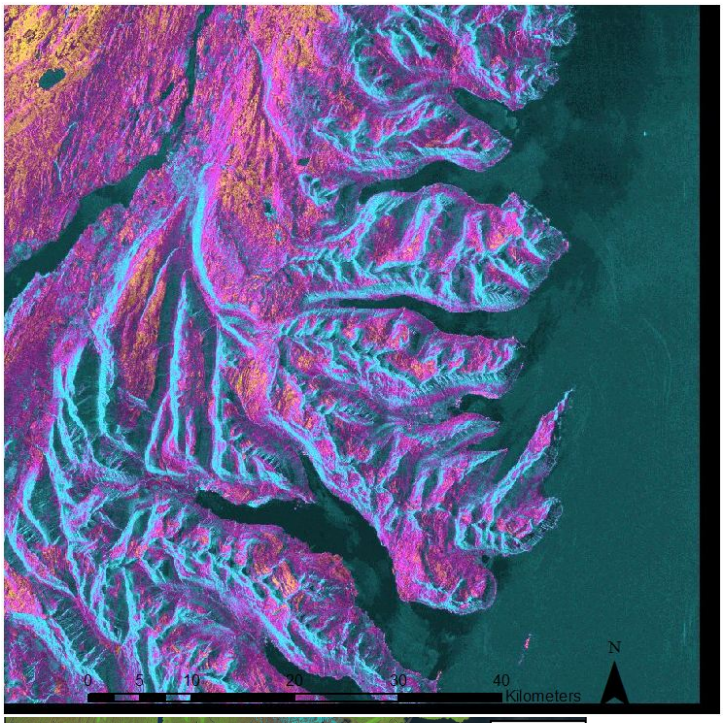

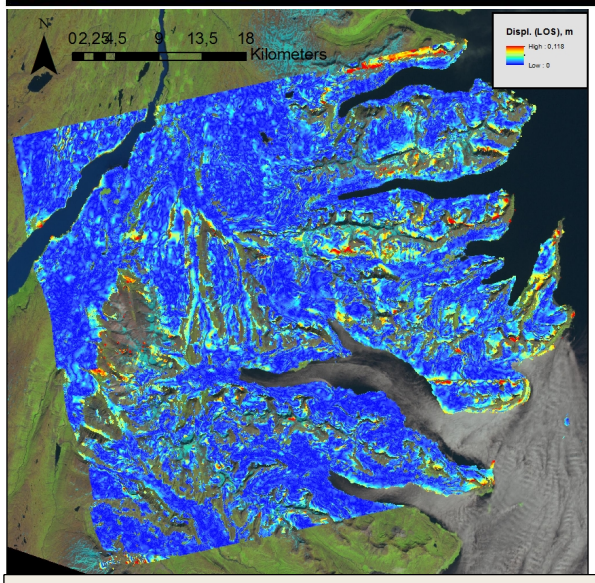

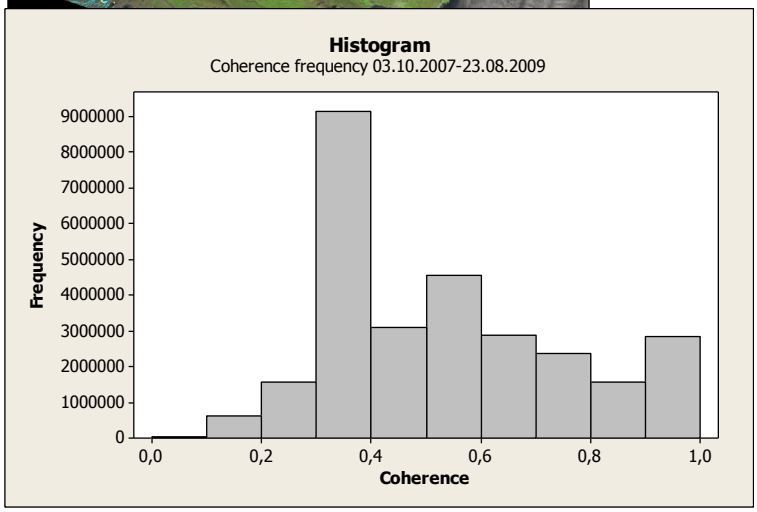

Figure 33: Coherence (top), Unwrapped differential interferogram (middle) and histogram (bottom) from 03.10.2007-23.08.2009.

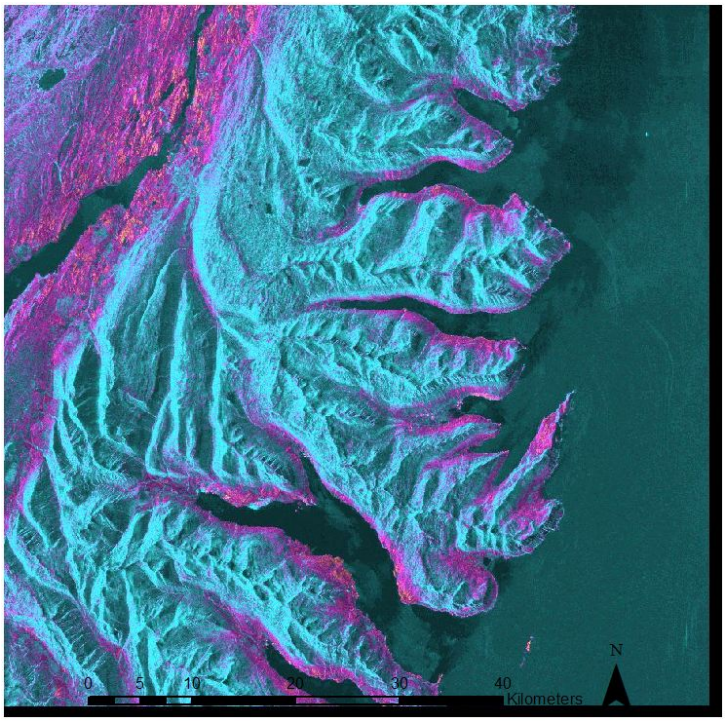

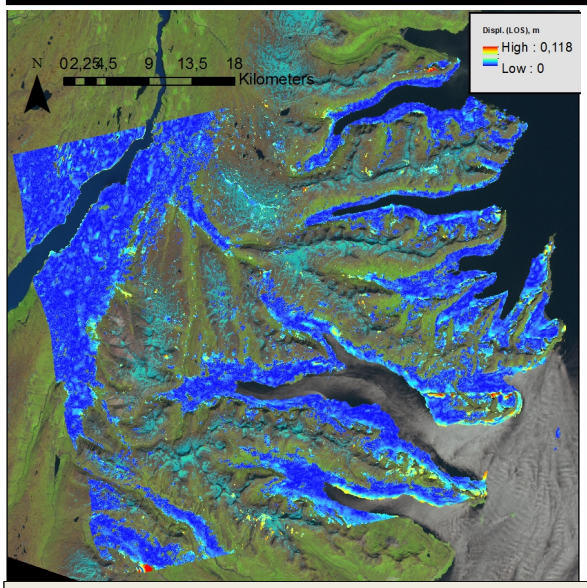

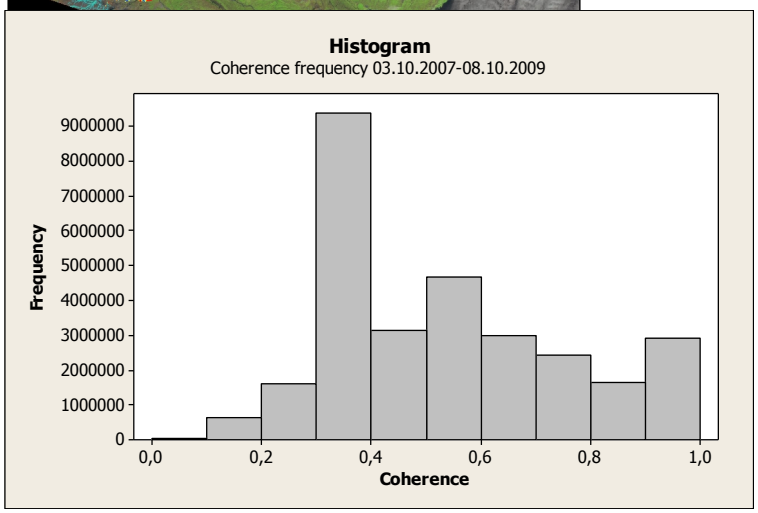

Figure 34: Coherence (top), Unwrapped differential interferogram (middle) and histogram (bottom) from 03.10.2007-08.10.2009.

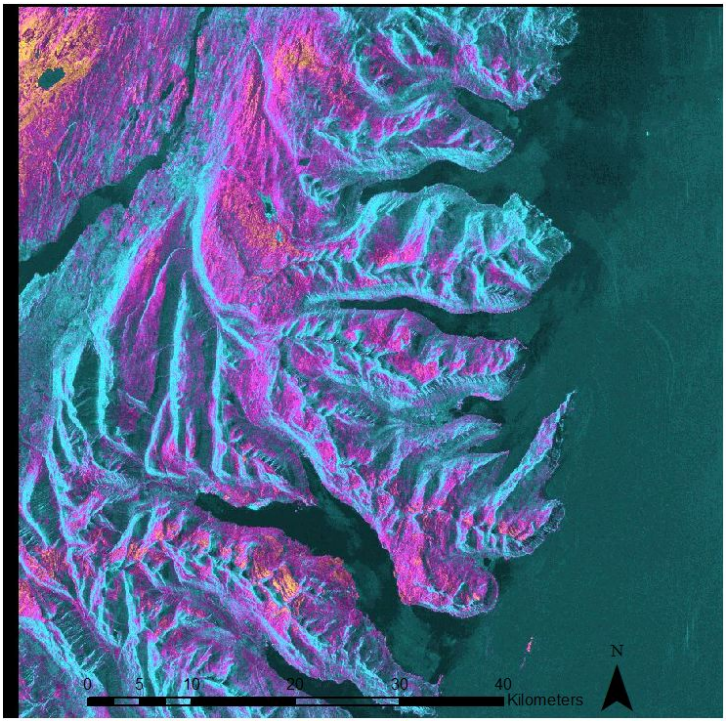

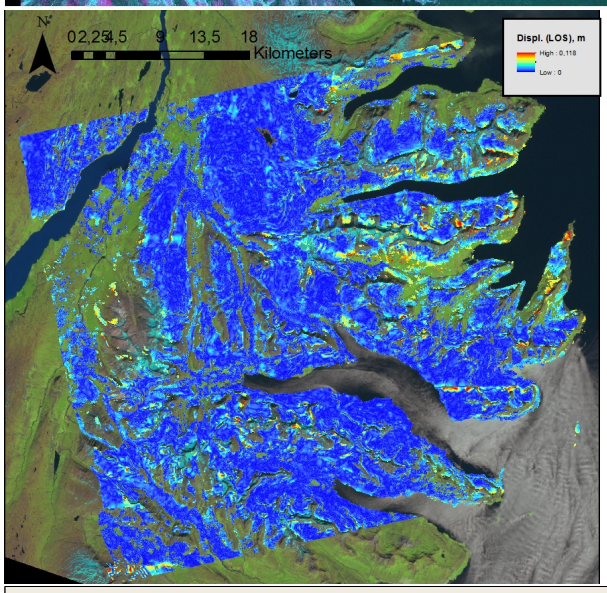

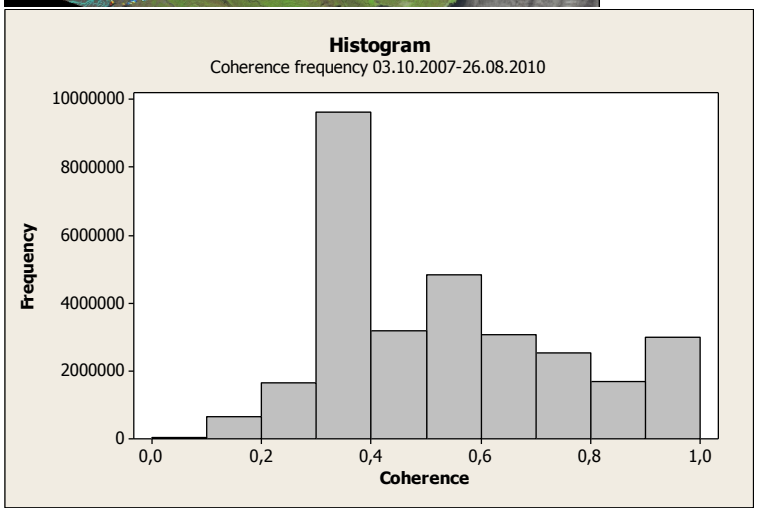

Figure 35: Coherence (top), Unwrapped differential interferogram (middle) and histogram (bottom) from 03.10.2007-26.08.2010.

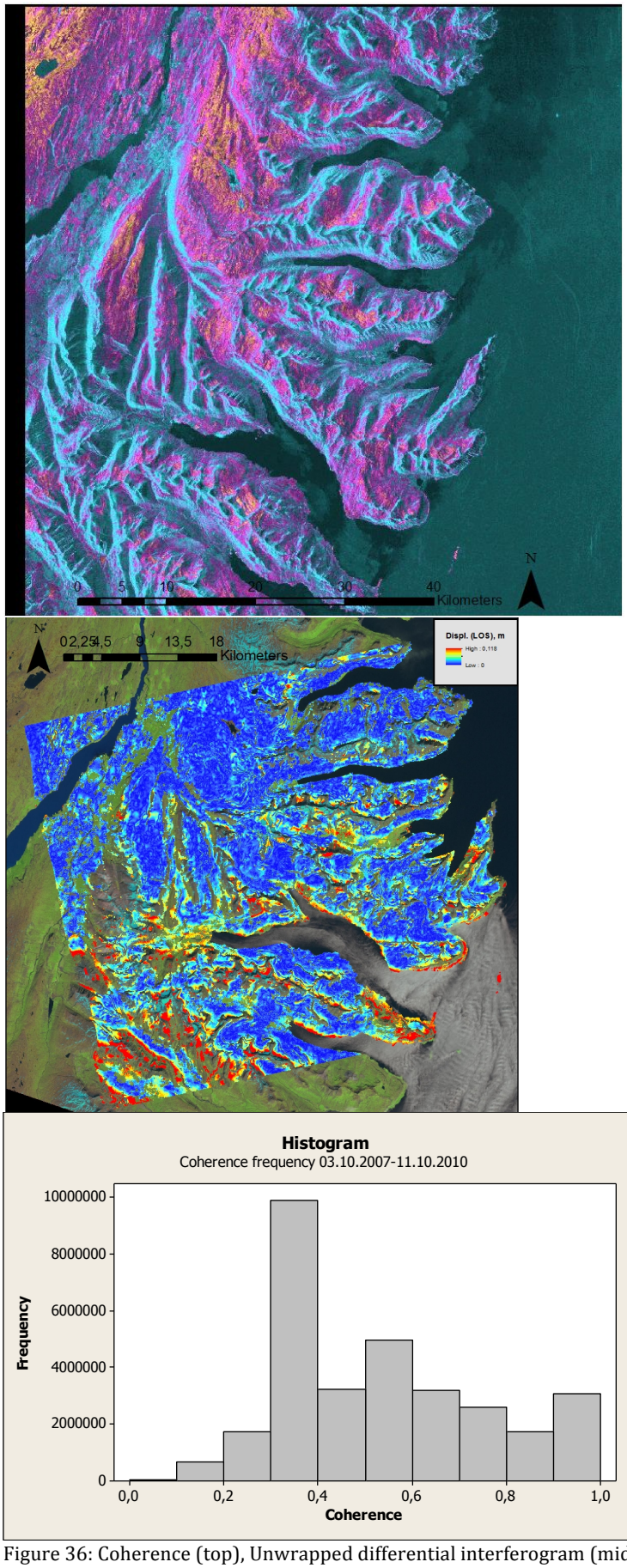

Figure 36: Coherence (top), Unwrapped differential interferogram (middle) and histogram (bottom) from 03.10.2007-11.10.2010.

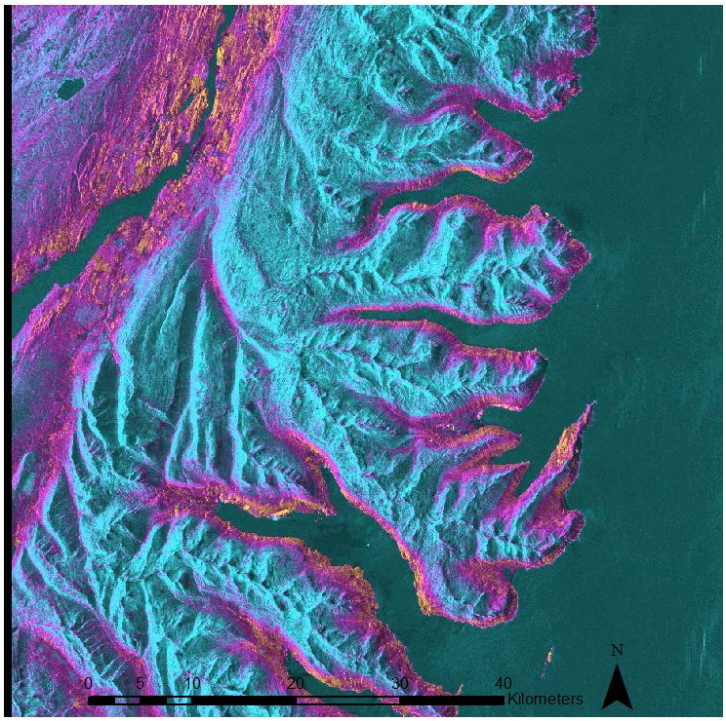

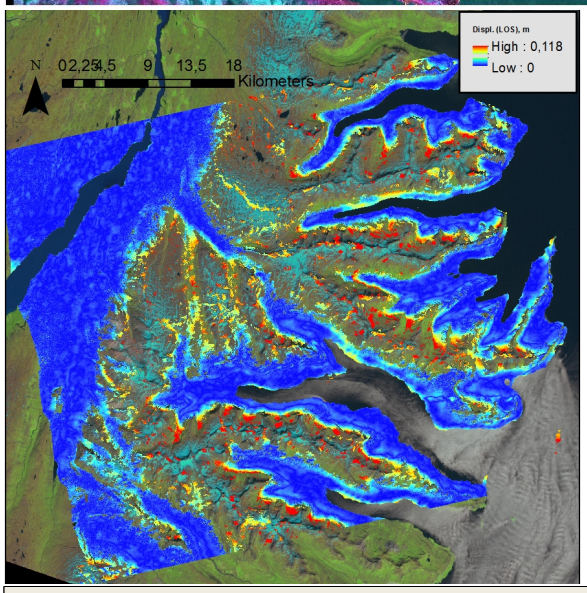

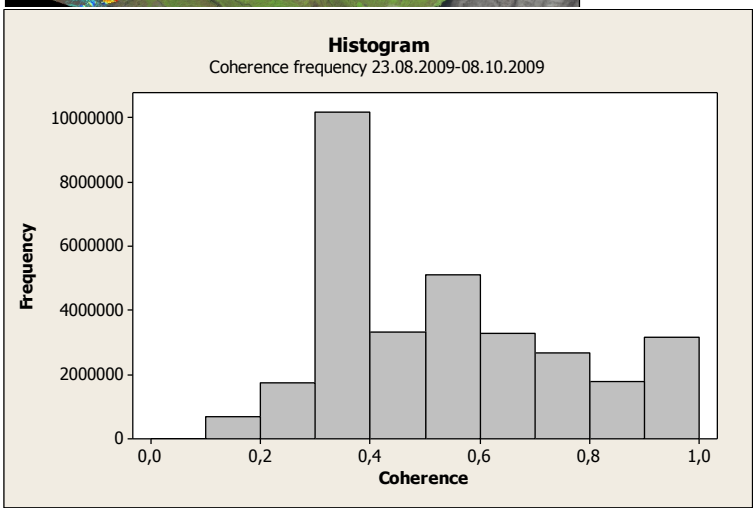

Figure 37: Coherence (top), Unwrapped differential interferogram (middle) and histogram (bottom) from 23.08.2009-08.10.2009.

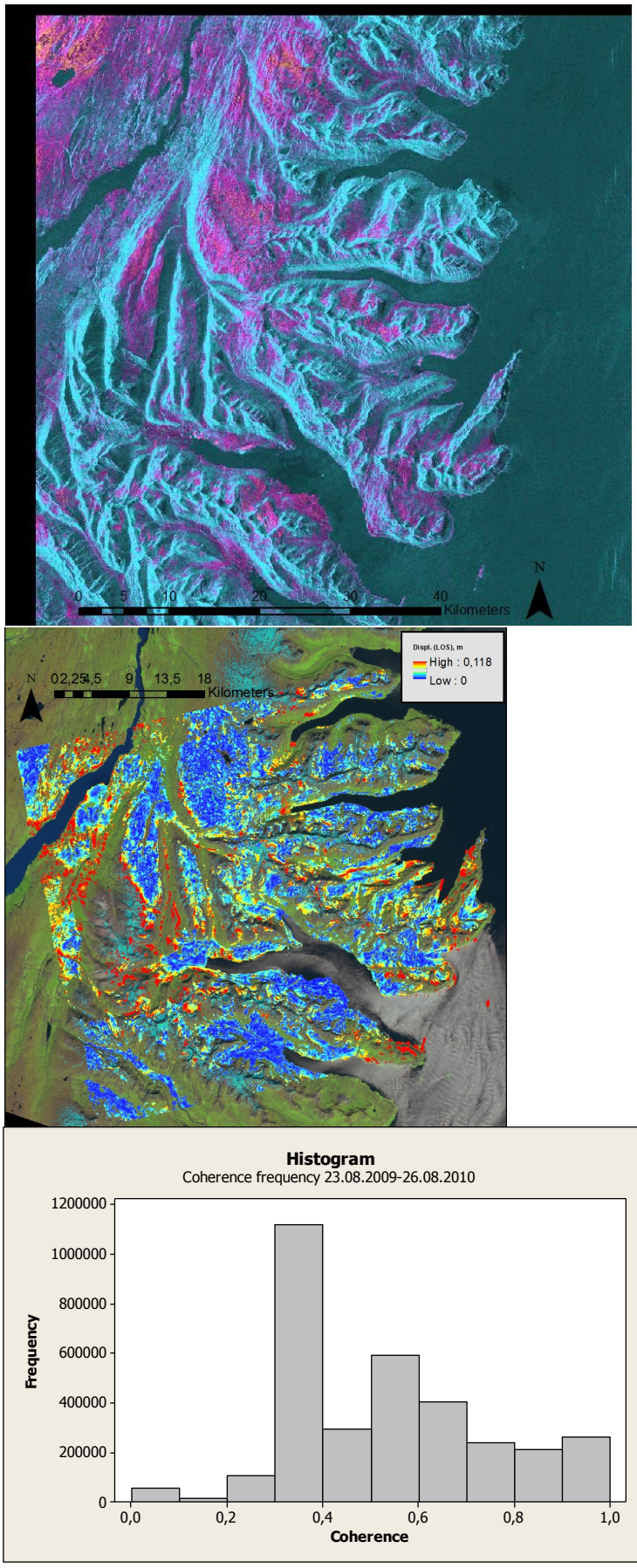

Figure 38: Coherence (top), Unwrapped differential interferogram (middle) and histogram (bottom) from 23.08.2009-26.08.2010.

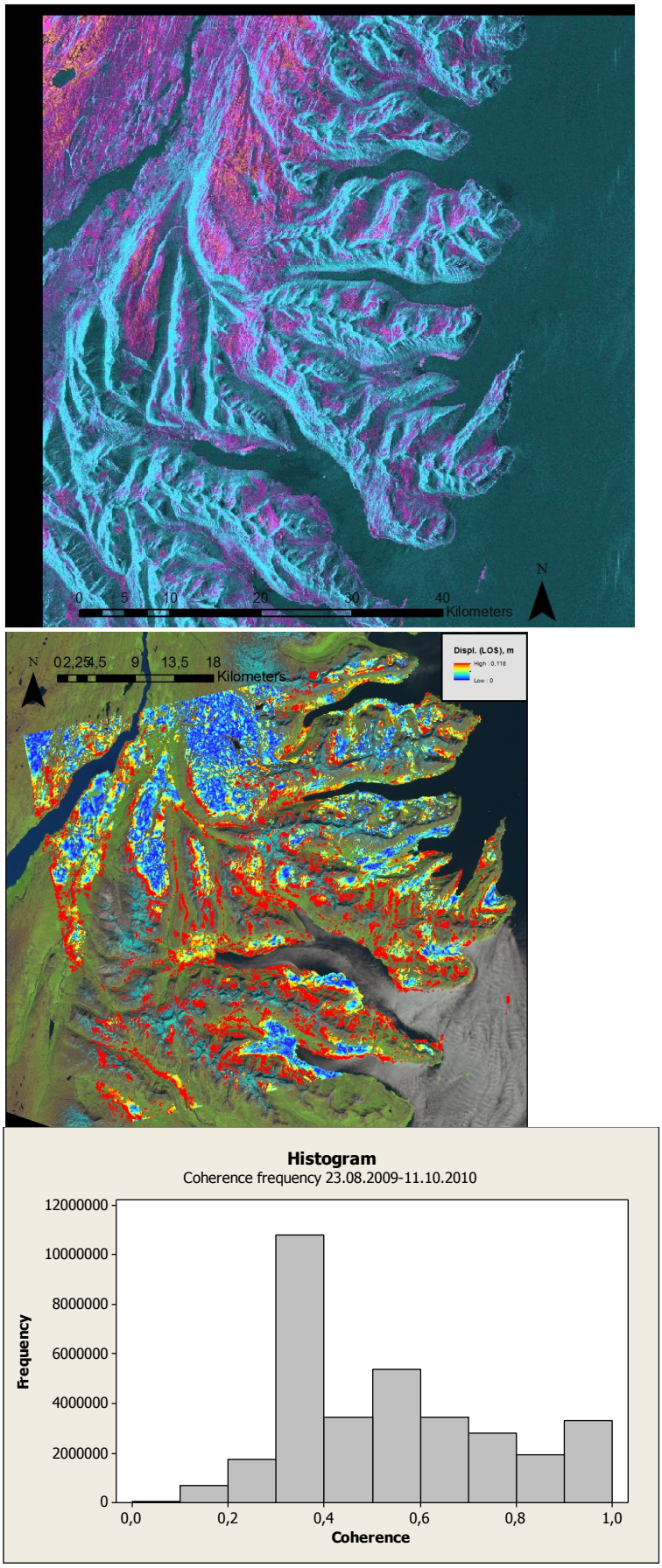

Figure 39: Coherence (top), Unwrapped differential interferogram (middle) and histogram (bottom) from 23.08.2009-11.10.2010.

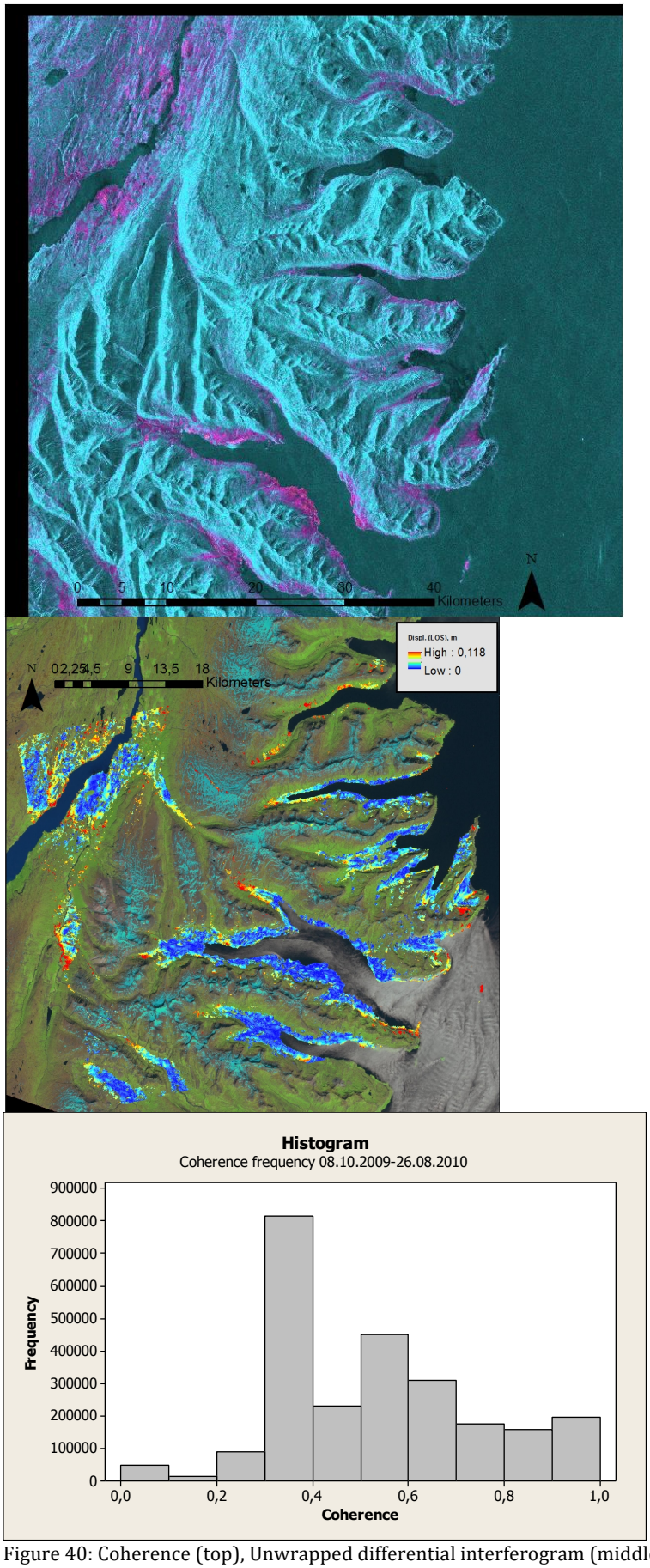

Figure 40: Coherence (top), Unwrapped differential interferogram (middle) and histogram (bottom) from 08.10.2009-26.08.2010.

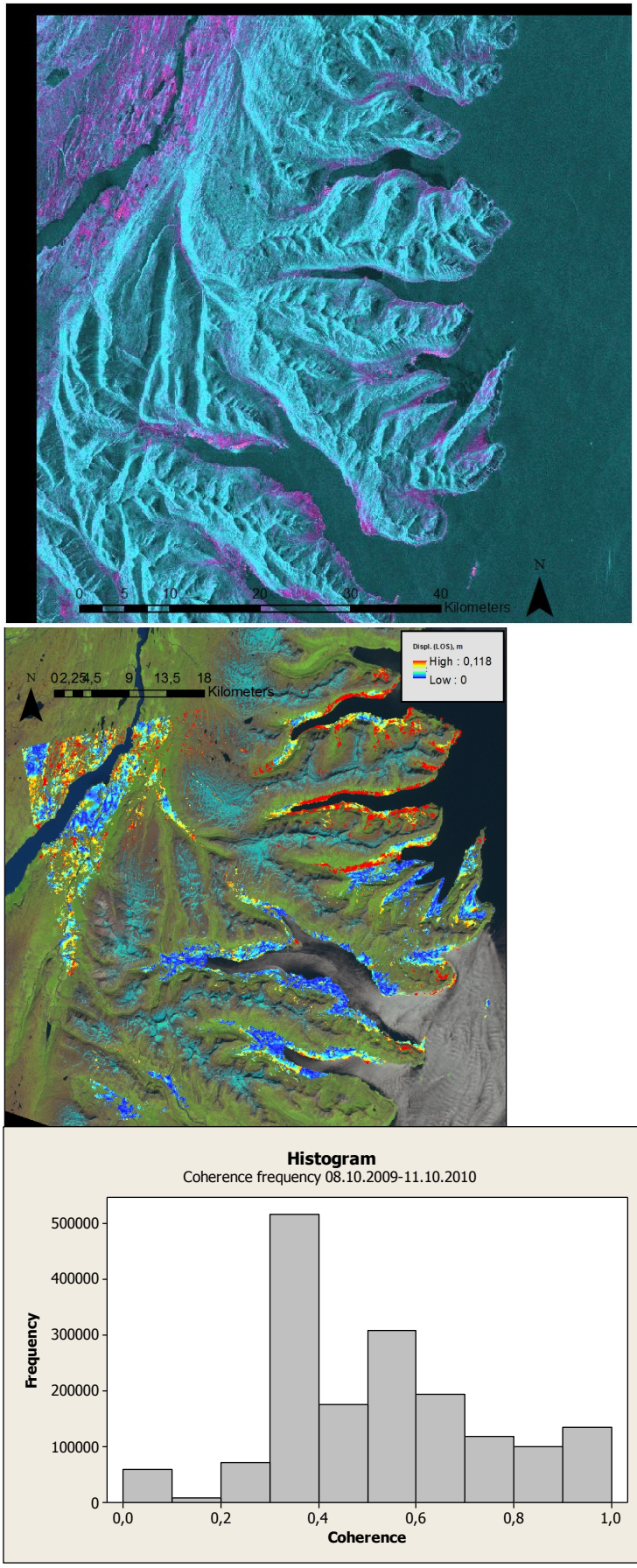

Figure 41: Coherence (top), Unwrapped differential interferogram (middle) and histogram (bottom) from 08.10.2009-11.10.2010.

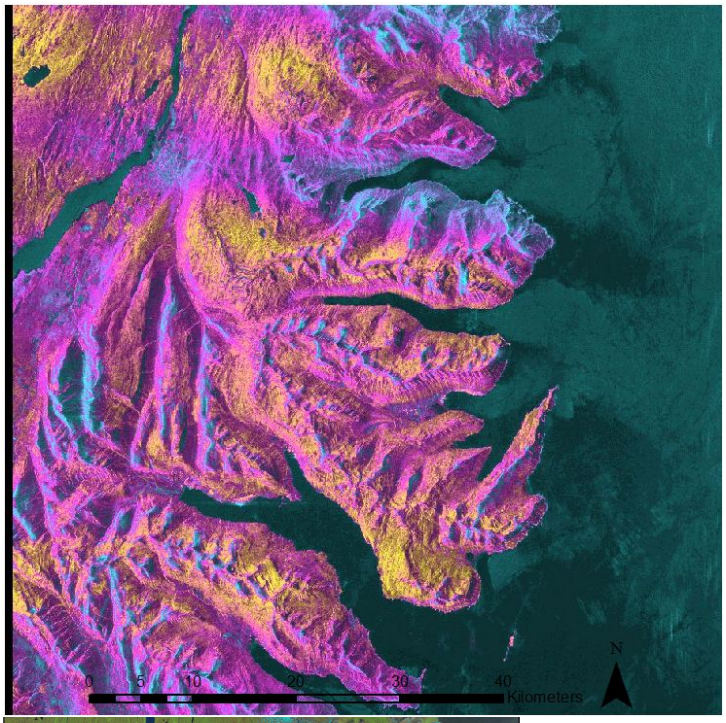

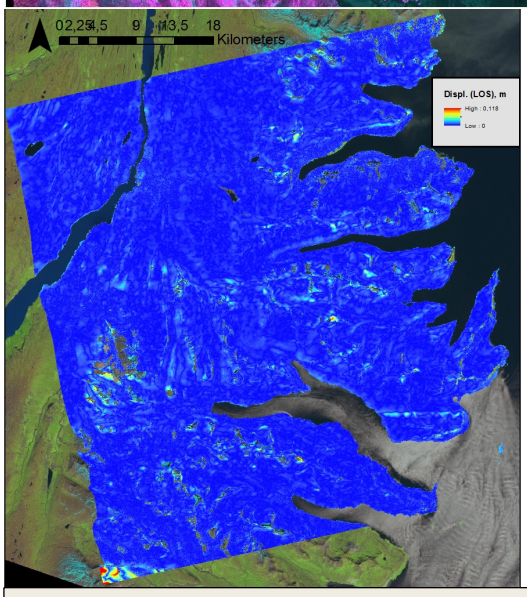

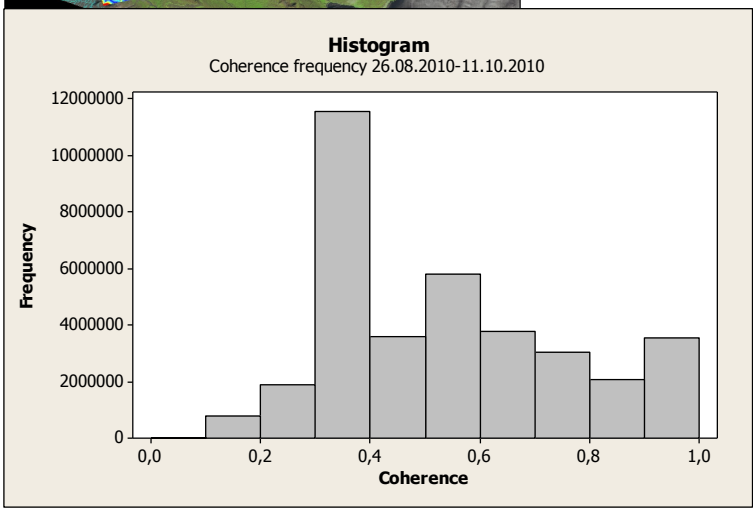

Figure 42: Coherence (top), Unwrapped differential interferogram (middle) and histogram (bottom) from 26.08.2010-11.10.2010.

Tafjord, western Norway.

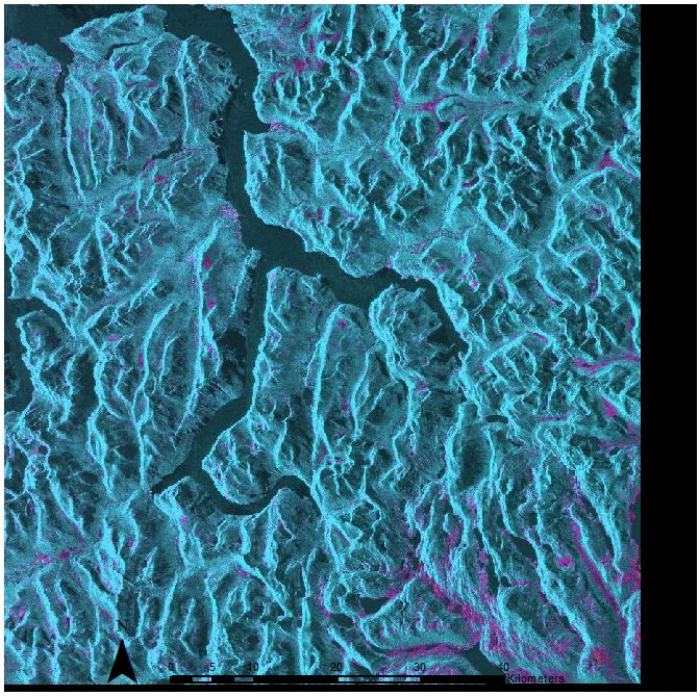

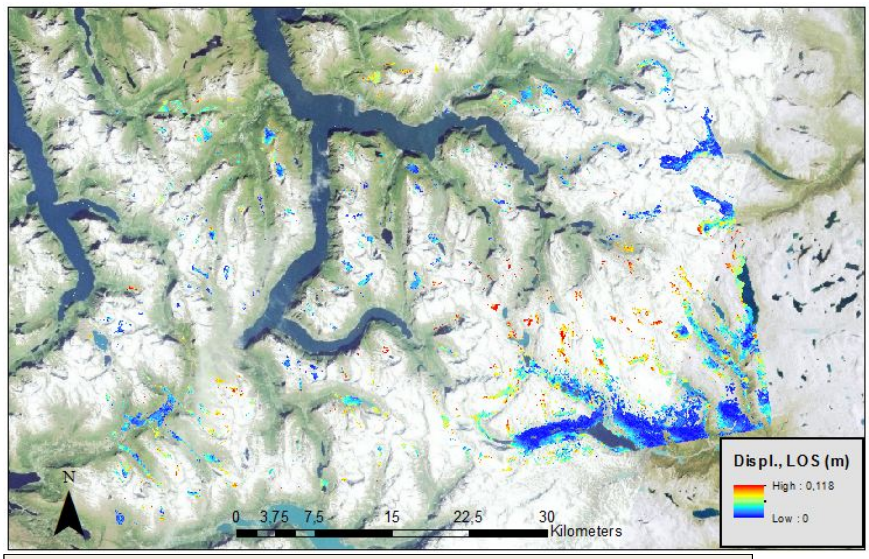

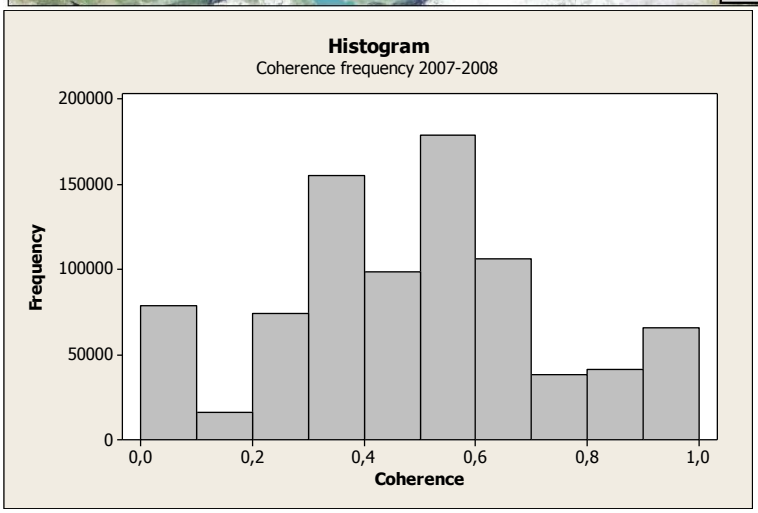

Figure 43: Coherence (top), Unwrapped differential interferogram (middle) and histogram (bottom) from 02.09.2007-04.09.2008.

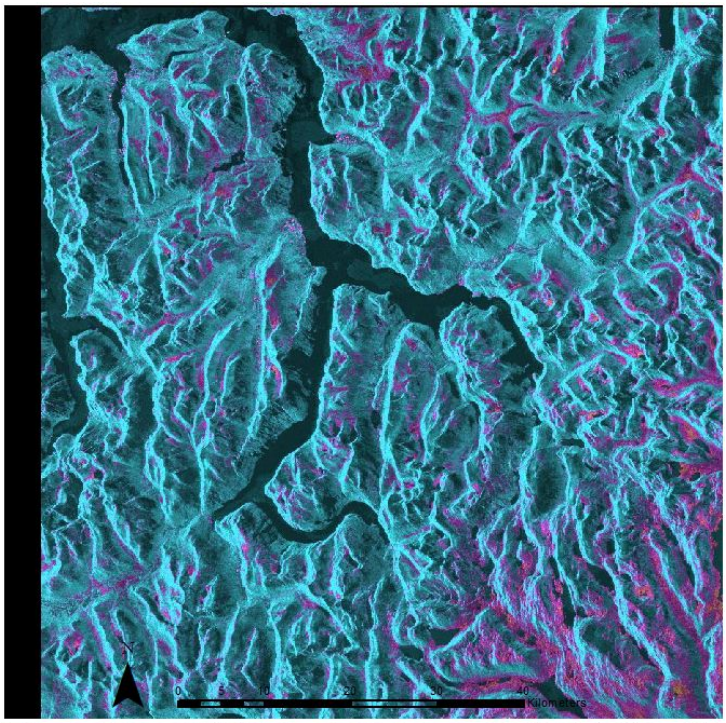

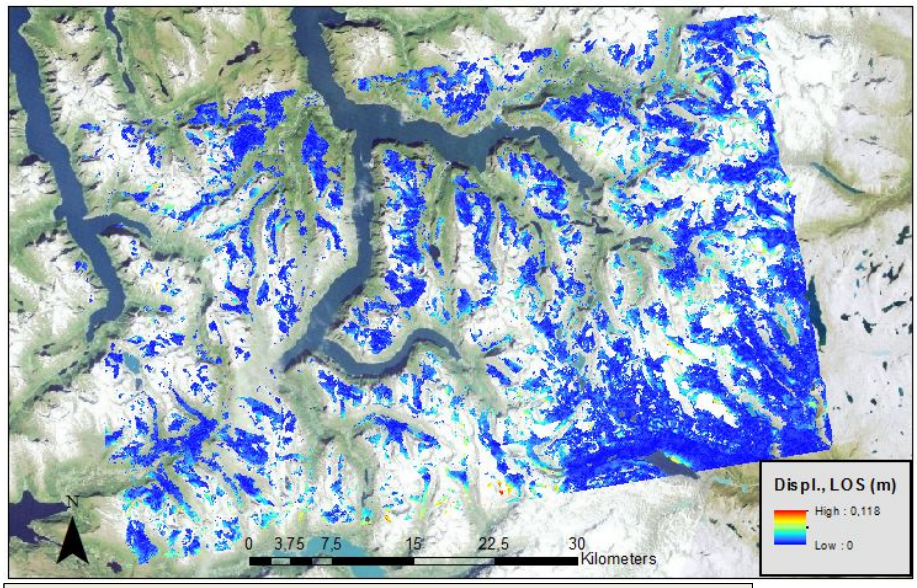

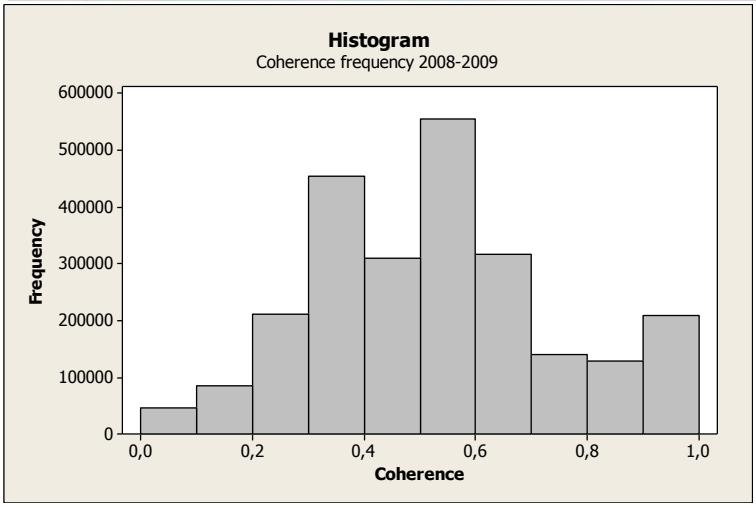

Figure 44: Coherence (top), Unwrapped differential interferogram (middle) and histogram (bottom) from 04.09.2008-07.09.2009.

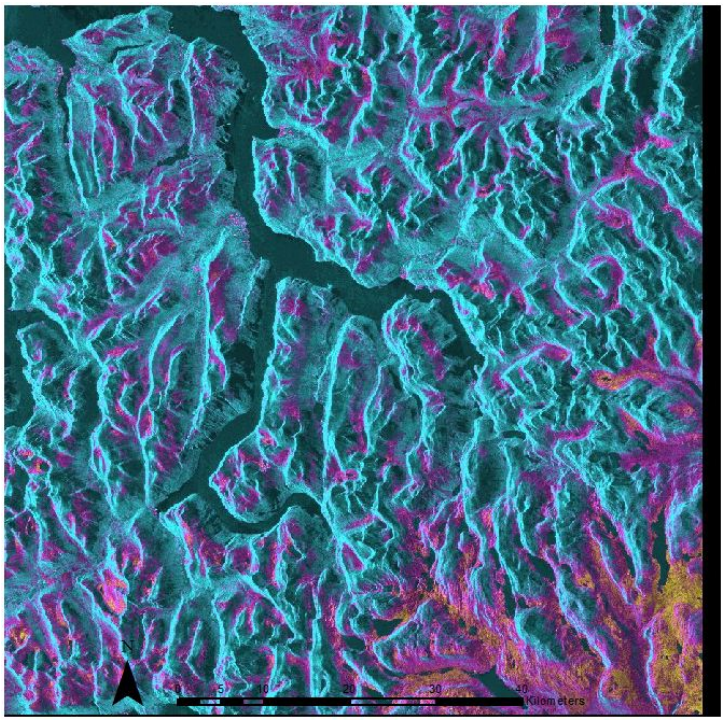

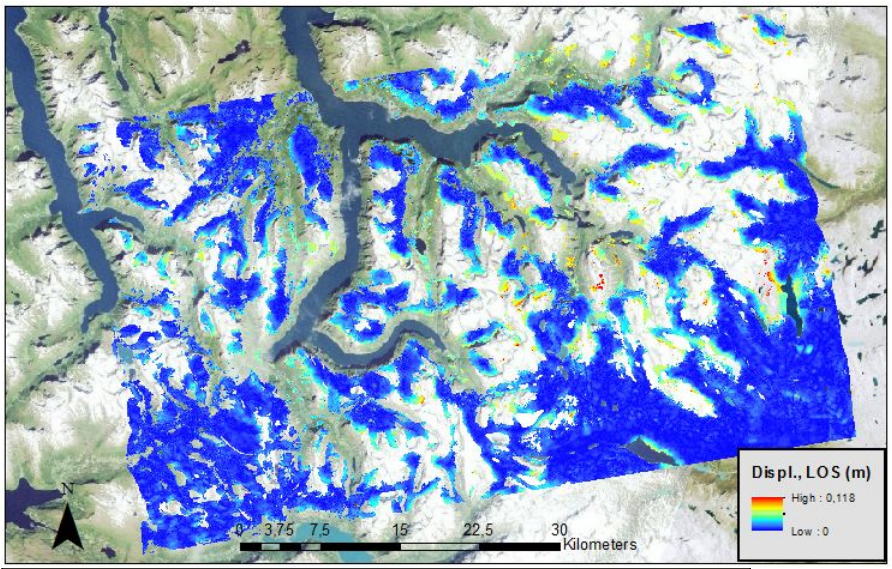

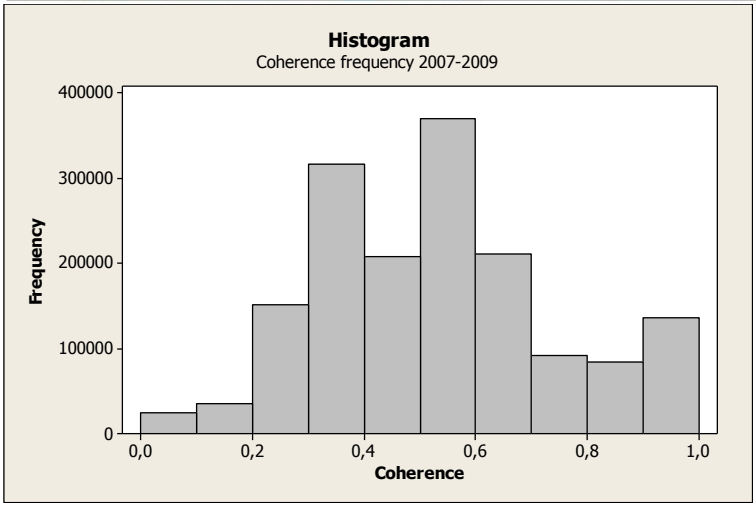

Figure 45: Coherence (top), Unwrapped differential interferogram (middle) and histogram (bottom) from 02.09.2007-07.09.2009.

Appendix B

Precipitation and temperatures, Iceland

Austurland

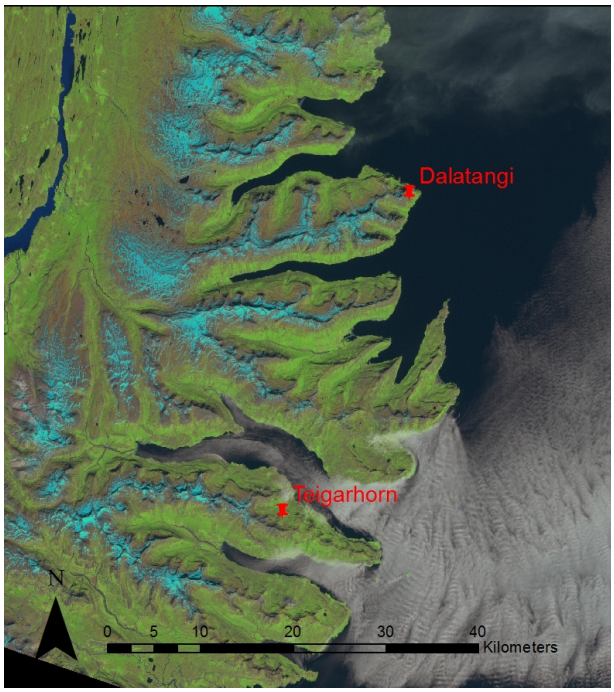

Figure 1: Location of the weather stations in Austurland. Landsat background image, 25.09.2012.

Dalatangi

2007:

Station number	Year	Month	Day	Temperature (°C)	Precipitation (mm)
620	2007	8	1	6,8	53,7
620	2007	8	2	7,4	3,1
620	2007	8	3	5,9	
620	2007	8	4	7,4	8,3
620	2007	8	5	8,0	0,3
620	2007	8	6	7,4	0,1
620	2007	8	7	6,9	0,1
620	2007	8	8	5,4	0,0
620	2007	8	9	9,0	
620	2007	8	10	8,7	0,2
620	2007	8	11	7,6	3,5
620	2007	8	12	7,2	3,6
620	2007	8	13	7,1	2,9
620	2007	8	14	5,7	0,6
620	2007	8	15	6,8	0,2

620	2007	8	16	6,8	0,2
620	2007	8	17	6,8	0,2
620	2007	8	18	6,4	
620	2007	8	19	5,7	0,1
620	2007	8	20	6,7	0,1
620	2007	8	21	5,6	0,2
620	2007	8	22	10,7	0,6
620	2007	8	23	7,5	
620	2007	8	24	8,5	
620	2007	8	25	7,2	
620	2007	8	26	5,3	
620	2007	8	27	5,0	
620	2007	8	28	6,5	
620	2007	8	29	6,8	
620	2007	8	30	6,4	4,8
620	2007	8	31	6,9	21,5

Table 1: Temperature and precipitation in August 2007, Dalantangi. Eastern Iceland.

Station number	Year	Month	Day	Temperature (°C)	Precipitation (mm)
620	2007	9	1	7,5	2,3
620	2007	9	2	5,5	7,5
620	2007	9	3	3,3	0,4
620	2007	9	4	8,0	1,2
620	2007	9	5	7,3	0,0
620	2007	9	6	5,9	2,7
620	2007	9	7	6,8	4,2
620	2007	9	8	7,3	0,1
620	2007	9	9	7,5	3,7
620	2007	9	10	6,1	0,1
620	2007	9	11	8,5	0,1
620	2007	9	12	5,1	1,3
620	2007	9	13	4,1	44,3
620	2007	9	14	2,5	13,4
620	2007	9	15	0,3	0,1
620	2007	9	16	1,9	0,8
620	2007	9	17	1,0	6,5
620	2007	9	18	3,5	1,6
620	2007	9	19	4,4	1,9
620	2007	9	20	5,7	15,0
620	2007	9	21	5,3	14,0
620	2007	9	22	2,4	0,5
620	2007	9	23	4,1	23,2

620	2007	9	24	3,4	101,3
620	2007	9	25	1,9	4,1
620	2007	9	26	1,9	0,1
620	2007	9	27	7,4	0,2
620	2007	9	28	8,5	0,1
620	2007	9	29	6,9	0,1
620	2007	9	30	6,6	0,4

Table 2: Temperature and precipitation in September 2007, Dalantangi. Eastern Iceland.

Station number	Year	Month	Day	Temperature (°C)	Precipitation (mm)
620	2007	10	1	4,9	1,1
620	2007	10	2	8,2	
620	2007	10	3	3,9	0,1
620	2007	10	4	5,3	0,1
620	2007	10	5	6,8	3,8
620	2007	10	6	3,8	11,8
620	2007	10	7	4,1	0,6
620	2007	10	8	2,7	
620	2007	10	9	2,3	0,5
620	2007	10	10	1,3	4,6
620	2007	10	11	2,4	56,8
620	2007	10	12	4,6	6,4
620	2007	10	13	6,9	0,2
620	2007	10	14	5,7	0,3
620	2007	10	15	4,4	4,4
620	2007	10	16	1,8	0,4
620	2007	10	17	-0,5	0,5
620	2007	10	18	-0,4	
620	2007	10	19	7,7	0,7
620	2007	10	20	8,4	
620	2007	10	21	7,5	0,1
620	2007	10	22	5,0	2,9
620	2007	10	23	7,3	4,4
620	2007	10	24	6,1	0,2
620	2007	10	25	7,7	0,4
620	2007	10	26	5,4	13,7
620	2007	10	27	3,9	
620	2007	10	28	1,9	
620	2007	10	29	0,4	
620	2007	10	30	-1,6	0,3

620	2007	10	31	0,3	13,9

Table 3: Temperature and precipitation in October 2007, Dalantangi. Eastern Iceland.

2009:

Station number	Year	Month	Day	Temperature (°C)	Precipitation (mm)
620	2009	8	1	8,5	0,1
620	2009	8	2	8,8	20,5
620	2009	8	3	10,0	50,1
620	2009	8	4	8,9	0,5
620	2009	8	5	9,1	138,2
620	2009	8	6	9,0	17,0
620	2009	8	7	9,0	2,9
620	2009	8	8	9,0	0,2
620	2009	8	9	8,9	
620	2009	8	10	6,1	
620	2009	8	11	8,2	1,5
620	2009	8	12	8,5	
620	2009	8	13	7,1	2,9
620	2009	8	14	8,4	3,4
620	2009	8	15	7,6	
620	2009	8	16	7,8	3,4
620	2009	8	17	7,6	0,1
620	2009	8	18	8,2	0,1
620	2009	8	19	9,1	41,1
620	2009	8	20	8,3	17,3
620	2009	8	21	8,2	
620	2009	8	22	6,7	
620	2009	8	23	5,6	
620	2009	8	24	9,5	17,9
620	2009	8	25	8,2	0,4
620	2009	8	26	7,8	0,3
620	2009	8	27	8,6	1,8
620	2009	8	28	9,4	21,5
620	2009	8	29	8,4	5,6
620	2009	8	30	8,8	
620	2009	8	31	7,6	0,1

Table 4: Temperature and precipitation in August 2009, Dalantangi. Eastern Iceland.

Station number	Year	Month	Day	Temperature (°C)	Precipitation (mm)
620	2009	9	1	6,4	10,7
620	2009	9	2	5,7	0,2
620	2009	9	3	3,9	

620	2009	9	4	5,2	0,2
620	2009	9	5	5,3	0,1
620	2009	9	6	6,2	0,2
620	2009	9	7	8,5	13,8
620	2009	9	8	5,5	5,2
620	2009	9	9	9,0	1,3
620	2009	9	10	8,4	
620	2009	9	11	8,7	
620	2009	9	12	6,6	0,2
620	2009	9	13	8,6	
620	2009	9	14	10,3	0,2
620	2009	9	15	7,8	0,2
620	2009	9	16	6,6	
620	2009	9	17	8,1	0,7
620	2009	9	18	9,2	
620	2009	9	19	7,5	5,8
620	2009	9	20	5,4	0,1
620	2009	9	21	7,5	12,5
620	2009	9	22	4,6	0,1
620	2009	9	23	2,8	1,5
620	2009	9	24	4,6	1,1
620	2009	9	25	6,3	0,3
620	2009	9	26	5,5	
620	2009	9	27	4,7	0,1
620	2009	9	28	2,6	0,4
620	2009	9	29	1,0	
620	2009	9	30	3,1	0,0

Table 5: Temperature and precipitation in September 2009, Dalantangi. Eastern Iceland.

Station number	Year	Month	Day	Temperature (°C)	Precipitation (mm)
620	2009	10	1	2,0	0,7
620	2009	10	2	1,6	2,5
620	2009	10	3	-1,5	4,5
620	2009	10	4	0,5	6,7
620	2009	10	5	0,0	2,4
620	2009	10	6	0,1	0,8
620	2009	10	7	0,2	1,5
620	2009	10	8	0,2	0,2
620	2009	10	9	0,0	
620	2009	10	10	1,6	15,5
620	2009	10	11	2,5	24,3
620	2009	10	12	1,7	0,2

620	2009	10	13	6,9	10,3
620	2009	10	14	6,9	0,1
620	2009	10	15	8,0	
620	2009	10	16	7,3	
620	2009	10	17	8,5	
620	2009	10	18	4,0	0,7
620	2009	10	19	-1,0	
620	2009	10	20	0,1	0,1
620	2009	10	21	1,6	8,2
620	2009	10	22	5,1	52,8
620	2009	10	23	6,5	14,1
620	2009	10	24	3,6	
620	2009	10	25	3,9	
620	2009	10	26	1,6	
620	2009	10	27	1,7	0,1
620	2009	10	28	1,7	1,3
620	2009	10	29	5,0	15,1
620	2009	10	30	7,0	0,9
620	2009	10	31	6,6	31,8

Table 6: Temperature and precipitation in October 2009, Dalantangi. Eastern Iceland.

2010:

Station number	Year	Month	Day	Temperature (°C)	Precipitation (mm)
620	2010	8	1	6,8	0,2
620	2010	8	2	5,3	
620	2010	8	3	8,0	12,8
620	2010	8	4	8,4	58,4
620	2010	8	5	7,3	28,1
620	2010	8	6	6,6	
620	2010	8	7	8,4	
620	2010	8	8	8,2	0,7
620	2010	8	9	7,2	0,1
620	2010	8	10	7,0	0,1
620	2010	8	11	7,9	1,2
620	2010	8	12	5,1	
620	2010	8	13	6,4	
620	2010	8	14	8,4	2,2
620	2010	8	15	7,7	0,1
620	2010	8	16	9,2	4,4
620	2010	8	17	7,5	0,1
620	2010	8	18	8,7	14,5
620	2010	8	19	7,6	13,4

620	2010	8	20	6,9	2,2
620	2010	8	21	6,2	4,1
620	2010	8	22	7,6	2,3
620	2010	8	23	8,5	23,0
620	2010	8	24	6,9	33,3
620	2010	8	25	7,4	3,8
620	2010	8	26	6,6	5,9
620	2010	8	27	5,0	0,5
620	2010	8	28	5,9	
620	2010	8	29	4,7	0,1
620	2010	8	30	9,0	
620	2010	8	31	9,4	0,1

Table 7: Temperature and precipitation in August 2010, Dalantangi. Eastern Iceland.

Station number	Year	Month	Day	Temperature (°C)	Precipitation (mm)
620	2010	9	1	8,1	1,1
620	2010	9	2	7,8	
620	2010	9	3	10,4	
620	2010	9	4	9,7	
620	2010	9	5	9,6	0,0
620	2010	9	6	8,7	0,2
620	2010	9	7	9,4	0,9
620	2010	9	8	9,6	0,1
620	2010	9	9	9,0	12,7
620	2010	9	10	8,9	11,6
620	2010	9	11	8,2	1,7
620	2010	9	12	7,6	0,6
620	2010	9	13	8,5	9,8
620	2010	9	14	6,5	0,3
620	2010	9	15	6,6	36,8
620	2010	9	16	5,3	3,9
620	2010	9	17	4,3	0,3
620	2010	9	18	3,0	
620	2010	9	19	3,6	0,1
620	2010	9	20	5,4	1,1
620	2010	9	21	4,8	0,7
620	2010	9	22	3,2	0,3
620	2010	9	23	3,2	0,1
620	2010	9	24	2,5	
620	2010	9	25	5,2	
620	2010	9	26	8,9	0,1
620	2010	9	27	8,0	2,2

620	2010	9	28	8,2	0,8
620	2010	9	29	8,7	16,9
620	2010	9	30	8,4	0,3

Table 8: Temperature and precipitation in September 2010, Dalantangi. Eastern Iceland.

Station number	Year	Month	Day	Temperature (°C)	Precipitation (mm)
620	2010	10	1	8,2	10,1
620	2010	10	2	8,2	10,1
620	2010	10	3	7,9	0,2
620	2010	10	4	7,3	12,9
620	2010	10	5	7,0	32,0
620	2010	10	6	8,3	12,9
620	2010	10	7	8,5	2,9
620	2010	10	8	7,5	
620	2010	10	9	5,2	
620	2010	10	10	4,1	
620	2010	10	11	4,0	0,1
620	2010	10	12	3,4	0,3
620	2010	10	13	5,2	0,2
620	2010	10	14	5,1	0,5
620	2010	10	15	6,2	
620	2010	10	16	6,3	
620	2010	10	17	6,9	0,1
620	2010	10	18	1,7	1,4
620	2010	10	19	-0,4	0,6
620	2010	10	20	0,6	0,1
620	2010	10	21	-0,6	9,6
620	2010	10	22	1,1	0,9
620	2010	10	23	0,4	4,2
620	2010	10	24	-0,7	0,3
620	2010	10	25	-2,3	
620	2010	10	26	2,0	34,5
620	2010	10	27	5,6	11,5
620	2010	10	28	2,7	65,8
620	2010	10	29	3,0	2,2
620	2010	10	30	1,0	11,0
620	2010	10	31	0,1	7,7

Table 9: Temperature and precipitation in October 2010, Dalantangi. Eastern Iceland.

Teigarhorn

2007:

Station number	Year	Month	Day	Temperature (°C)	Precipitation (mm))
675	2007	8	1	9,0	10,5
675	2007	8	2	8,0	
675	2007	8	3	7,4	1,1
675	2007	8	4	8,2	4,3
675	2007	8	5	10,1	
675	2007	8	6	3,9	
675	2007	8	7	2,5	
675	2007	8	8	4,6	0,2
675	2007	8	9	9,0	0,3
675	2007	8	10	8,4	3,5
675	2007	8	11	7,5	0,3
675	2007	8	12	6,9	1,8
675	2007	8	13	8,5	0,0
675	2007	8	14	7,6	
675	2007	8	15	7,2	
675	2007	8	16	7,7	
675	2007	8	17	5,9	
675	2007	8	18	6,3	
675	2007	8	19	5,7	0,0
675	2007	8	20	7,0	0,2
675	2007	8	21	6,9	
675	2007	8	22	11,5	0,0
675	2007	8	23	6,3	0,0
675	2007	8	24	5,0	
675	2007	8	25	6,7	2,0
675	2007	8	26	6,1	
675	2007	8	27	2,8	1,5
675	2007	8	28	4,3	
675	2007	8	29	7,4	1,3
675	2007	8	30	6,5	10,0
675	2007	8	31	7,3	4,3

Table 10: Temperature and precipitation in August 2007, Teigarhorn. Eastern Iceland.

Station number	Year	Month	Day	Temperature (°C)	Precipitation (mm))
675	2007	9	1	4,4	6,4
675	2007	9	2	5,5	

675	2007	9	3	1,5	
675	2007	9	4	8,8	22,0
675	2007	9	5	7,0	
675	2007	9	6	6,0	9,9
675	2007	9	7	6,9	2,9
675	2007	9	8	7,0	
675	2007	9	9	6,8	1,0
675	2007	9	10	6,5	2,1
675	2007	9	11	5,7	0,0
675	2007	9	12	4,4	8,0
675	2007	9	13	0,1	17,4
675	2007	9	14	-2,7	0,0
675	2007	9	15	-0,5	0,0
675	2007	9	16	1,3	0,0
675	2007	9	17	1,1	5,4
675	2007	9	18	2,4	3,4
675	2007	9	19	0,8	
675	2007	9	20	2,4	19,0
675	2007	9	21	4,3	1,0
675	2007	9	22	3,0	
675	2007	9	23	5,1	
675	2007	9	24	3,5	
675	2007	9	25	0,2	8,9
675	2007	9	26	0,0	
675	2007	9	27	7,4	1,3
675	2007	9	28	8,0	6,6
675	2007	9	29	7,1	0,1
675	2007	9	30	4,5	0,9

Table 11: Temperature and precipitation in September 2007, Teigarhorn. Eastern Iceland.

Station number	Year	Month	Day	Temperature (°C)	Precipitation (mm))
675	2007	10	1	5,0	1,3
675	2007	10	2	5,8	1,0
675	2007	10	3	2,8	0,0
675	2007	10	4	4,1	
675	2007	10	5	6,2	9,2
675	2007	10	6	-7,2	1,0
675	2007	10	7	0,1	
675	2007	10	8	0,3	
675	2007	10	9	1,5	
675	2007	10	10	2,3	1,5
675	2007	10	11	4,2	30,0

675	2007	10	12	4,0	17,7
675	2007	10	13	7,3	4,0
675	2007	10	14	6,8	3,5
675	2007	10	15	5,1	2,7
675	2007	10	16	2,3	
675	2007	10	17	-2,0	
675	2007	10	18	1,0	2,5
675	2007	10	19	8,0	11,6
675	2007	10	20	9,5	1,1
675	2007	10	21	6,8	13,9
675	2007	10	22	6,5	5,2
675	2007	10	23	7,4	80,0
675	2007	10	24	7,5	5,1
675	2007	10	25	6,3	49,0
675	2007	10	26	2,7	33,9
675	2007	10	27	2,1	3,0
675	2007	10	28	-0,9	
675	2007	10	29	-2,8	
675	2007	10	30	-3,2	
675	2007	10	31	-0,3	18,3

Table 12: Temperature and precipitation in August 2007, Teigarhorn. Eastern Iceland.

Tröllaskagi

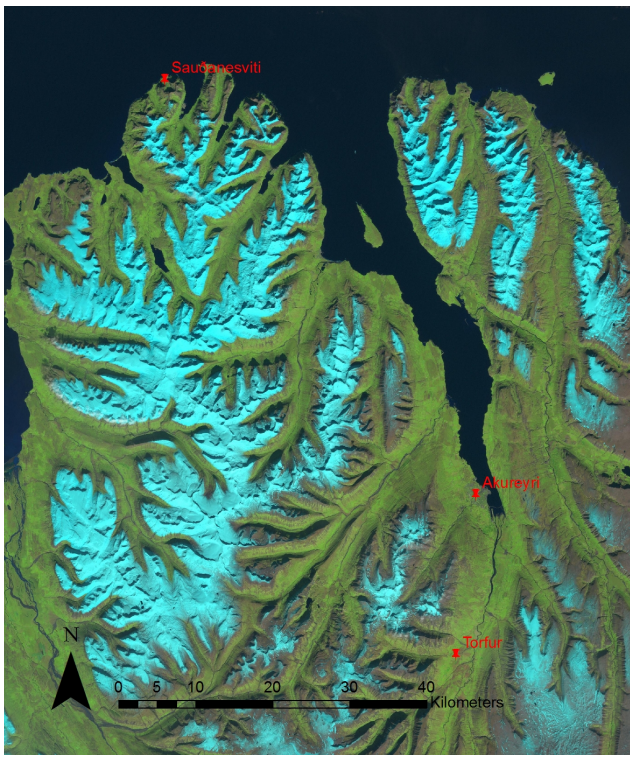

Figure 2: Location of the weather stations in Tröllaskagi area. Landsat background image, downloaded 25.09.2012.

Sauðanesviti

2007:

Station number	Year	Month	Day	Temperature (°C)	Precipitation (mm)
400	2007	8	1	6,2	1,2
400	2007	8	2	5,3	1,1
400	2007	8	3	6,0	0,0
400	2007	8	4	5,1	4,1
400	2007	8	5	5,8	10,7
400	2007	8	6	9,2	0,1
400	2007	8	7	7,9	
400	2007	8	8	9,4	
400	2007	8	9	9,0	0,2
400	2007	8	10	8,9	0,2
400	2007	8	11	7,0	0,9
400	2007	8	12	6,8	0,4
400	2007	8	13	5,9	3,4
400	2007	8	14	5,4	0,0
400	2007	8	15	5,4	1,3
400	2007	8	16	5,6	0,3
400	2007	8	17	4,7	

400	2007	8	18	6,9	
400	2007	8	19	6,2	
400	2007	8	20	6,1	1,6
400	2007	8	21	9,0	0,0
400	2007	8	22	8,5	14,2
400	2007	8	23	10,0	21,9
400	2007	8	24	9,0	4,7
400	2007	8	25	7,3	0,2
400	2007	8	26	5,9	2,7
400	2007	8	27	5,9	
400	2007	8	28	7,0	
400	2007	8	29	7,6	9,3
400	2007	8	30	7,9	15,0
400	2007	8	31	7,4	23,3

Table 13: Temperature and precipitation in August 2007, Sauðanesviti. Northern Iceland.

Station number	Year	Month	Day	Temperature (°C)	Precipitation (mm)
400	2007	9	1	6,3	28,1
400	2007	9	2	5,4	6,9
400	2007	9	3	5,0	
400	2007	9	4	8,7	2,5
400	2007	9	5	6,0	16,2
400	2007	9	6	7,9	3,9
400	2007	9	7	7,9	4,1
400	2007	9	8	5,9	11,3
400	2007	9	9	6,5	11,6
400	2007	9	10	6,4	3,2
400	2007	9	11	4,3	5,9
400	2007	9	12	4,9	0,0
400	2007	9	13	3,3	16,4
400	2007	9	14	2,4	3,1
400	2007	9	15	2,4	
400	2007	9	16	1,9	2,3
400	2007	9	17	1,4	1,9
400	2007	9	18	4,6	1,0
400	2007	9	19	5,0	0,2
400	2007	9	20	4,4	0,0
400	2007	9	21	3,1	7,9
400	2007	9	22	1,9	3,3
400	2007	9	23	3,3	2,9
400	2007	9	24	1,8	2,6
400	2007	9	25	0,3	1,7

400	2007	9	26	3,0	
400	2007	9	27	10,5	4,1
400	2007	9	28	9,9	
400	2007	9	29	8,7	
400	2007	9	30	2,6	8,7

Table 14: Temperature and precipitation in September 2007, Sauðanesviti. Northern Iceland.

Station number	Year	Month	Day	Temperature (°C)	Precipitation (mm)
400	2007	10	1	2,5	8,0
400	2007	10	2	4,0	2,3
400	2007	10	3	4,0	7,1
400	2007	10	4	7,2	0,0
400	2007	10	5	5,4	0,2
400	2007	10	6	-0,6	45,0
400	2007	10	7	1,6	4,1
400	2007	10	8	3,0	
400	2007	10	9	0,9	2,4
400	2007	10	10	2,4	2,2
400	2007	10	11	4,1	13,7
400	2007	10	12	4,3	2,7
400	2007	10	13	8,7	0,7
400	2007	10	14	3,2	0,3
400	2007	10	15	-0,1	7,6
400	2007	10	16	-1,0	3,5
400	2007	10	17	-2,5	
400	2007	10	18	-2,0	0,1
400	2007	10	19	5,7	3,7
400	2007	10	20	8,2	2,0
400	2007	10	21	1,1	1,7
400	2007	10	22	-0,4	40,3
400	2007	10	23	6,1	0,1
400	2007	10	24	6,0	0,2
400	2007	10	25	9,0	0,0
400	2007	10	26	2,4	0,0
400	2007	10	27	3,2	1,1
400	2007	10	28	-3,1	0,3
400	2007	10	29	-0,9	0,0
400	2007	10	30	-1,7	4,6
400	2007	10	31	-1,7	28,6

Table 15: Temperature and precipitation in October 2007, Sauðanesviti. Northern Iceland.

2008:

Station number	Year	Month	Day	Temperature (°C)	Precipitation (mm)
400	2008	8	1	11,9	
400	2008	8	2	10,0	
400	2008	8	3	8,8	0,0
400	2008	8	4	9,4	0,0
400	2008	8	5	9,2	0,0
400	2008	8	6	8,5	
400	2008	8	7	8,0	
400	2008	8	8	8,2	0,0
400	2008	8	9	9,6	
400	2008	8	10	10,0	
400	2008	8	11	9,3	
400	2008	8	12	8,9	
400	2008	8	13	9,7	
400	2008	8	14	12,1	
400	2008	8	15	13,3	0,1
400	2008	8	16	11,5	
400	2008	8	17	13,6	
400	2008	8	18	12,8	
400	2008	8	19	9,2	1,8
400	2008	8	20	9,3	0,9
400	2008	8	21	11,0	
400	2008	8	22	11,1	0,3
400	2008	8	23	11,5	4,7
400	2008	8	24	9,7	0,7
400	2008	8	25	10,6	0,0
400	2008	8	26	11,8	16,3
400	2008	8	27	10,0	0,1
400	2008	8	28	10,0	0,1
400	2008	8	29	11,5	9,6
400	2008	8	30	10,4	1,1
400	2008	8	31	10,0	0,0

Table 16: Temperature and precipitation in August 2008, Sauðanesviti. Northern Iceland.

Station number	Year	Month	Day	Temperature (°C)	Precipitation (mm)
400	2008	9	1	9,6	4,4
400	2008	9	2	9,4	3,3
400	2008	9	3	7,4	
400	2008	9	4	5,7	3,3
400	2008	9	5	9,8	0,3
400	2008	9	6	12,2	0,0

400	2008	9	7	10,4	0,0
400	2008	9	8	9,6	0,0
400	2008	9	9	12,5	
400	2008	9	10	12,5	0,0
400	2008	9	11	10,0	0,1
400	2008	9	12	10,5	8,8
400	2008	9	13	11,6	0,5
400	2008	9	14	12,6	0,0
400	2008	9	15	13,2	0,0
400	2008	9	16	14,8	0,9
400	2008	9	17	13,2	0,0
400	2008	9	18	8,5	3,7
400	2008	9	19	12,5	6,9
400	2008	9	20	8,6	11,0
400	2008	9	21	7,9	0,1
400	2008	9	22	9,7	11,2
400	2008	9	23	7,7	1,0
400	2008	9	24	11,4	2,3
400	2008	9	25	9,3	1,1
400	2008	9	26	7,2	0,0
400	2008	9	27	6,4	12,1
400	2008	9	28	7,5	0,0
400	2008	9	29	5,0	8,9
400	2008	9	30	3,2	5,2

Table 17: Temperature and precipitation in September 2008, Sauðanesviti. Northern Iceland.

Station number	Year	Month	Day	Temperature (°C)	Precipitation (mm)
400	2008	10	1	2,3	1,8
400	2008	10	2	-0,9	1,8
400	2008	10	3	0,1	4,1
400	2008	10	4	1,8	4,5
400	2008	10	5	3,9	
400	2008	10	6	8,1	
400	2008	10	7	7,7	0,8
400	2008	10	8	8,0	11,7
400	2008	10	9	8,0	0,0
400	2008	10	10	6,6	0,3
400	2008	10	11	4,1	14,2
400	2008	10	12	4,0	7,8
400	2008	10	13	4,9	2,7
400	2008	10	14	3,7	11,7
400	2008	10	15	3,9	3,7

400	2008	10	16	6,3	3,2
400	2008	10	17	6,6	0,4
400	2008	10	18	-0,1	7,9
400	2008	10	19	0,1	0,0
400	2008	10	20	1,0	1,2
400	2008	10	21	1,0	3,8
400	2008	10	22	-0,5	0,1
400	2008	10	23	3,0	16,4
400	2008	10	24	1,1	5,6
400	2008	10	25	0,6	6,7
400	2008	10	26	1,0	6,3
400	2008	10	27	-1,9	0,1
400	2008	10	28	0,3	0,3
400	2008	10	29	1,8	0,0
400	2008	10	30	1,5	2,6
400	2008	10	31	10,8	

Table 18: Temperature and precipitation in August 2008, Sauðanesviti. Northern Iceland.

2009:

Station number	Year	Month	Day	Temperature (°C)	Precipitation (mm)
400	2009	8	1	6,1	0,1
400	2009	8	2	7,6	3,7
400	2009	8	3	8,9	5,9
400	2009	8	4	6,9	6,3
400	2009	8	5	8,0	10,4
400	2009	8	6	11,0	0,0
400	2009	8	7	11,7	
400	2009	8	8	11,7	0,0
400	2009	8	9	10,0	
400	2009	8	10	8,0	0,4
400	2009	8	11	8,2	1,1
400	2009	8	12	8,4	0,0
400	2009	8	13	7,5	0,0
400	2009	8	14	7,9	2,1
400	2009	8	15	8,2	
400	2009	8	16	7,8	0,0
400	2009	8	17	7,0	
400	2009	8	18	7,8	
400	2009	8	19	6,9	0,0
400	2009	8	20	4,8	15,3
400	2009	8	21	3,9	16,9

400	2009	8	22	5,1	6,3
400	2009	8	23	7,1	
400	2009	8	24	8,2	6,9
400	2009	8	25	8,7	14,6
400	2009	8	26	9,4	
400	2009	8	27	7,3	
400	2009	8	28	6,1	5,1
400	2009	8	29	4,9	47,9
400	2009	8	30	5,0	7,8
400	2009	8	31	3,7	3,0

Table 19: Temperature and precipitation in August 2009, Sauðanesviti. Northern Iceland.

Station number	Year	Month	Day	Temperature (°C)	Precipitation (mm)
400	2009	9	1	4,6	3,7
400	2009	9	2	3,9	0,6
400	2009	9	3	5,7	0,0
400	2009	9	4	5,4	0,0
400	2009	9	5	2,9	0,0
400	2009	9	6	4,4	
400	2009	9	7	7,5	
400	2009	9	8	7,3	12,5
400	2009	9	9	6,1	7,7
400	2009	9	10	9,0	2,1
400	2009	9	11	7,1	1,9
400	2009	9	12	9,9	2,2
400	2009	9	13	10,7	0,0
400	2009	9	14	9,9	
400	2009	9	15	8,4	0,5
400	2009	9	16	4,9	0,5
400	2009	9	17	9,0	9,9
400	2009	9	18	7,3	1,8
400	2009	9	19	5,9	3,5
400	2009	9	20	5,1	
400	2009	9	21	4,6	1,9
400	2009	9	22	1,3	4,6
400	2009	9	23	1,7	0,1
400	2009	9	24	3,4	10,2
400	2009	9	25	2,9	26,5
400	2009	9	26	2,4	1,2
400	2009	9	27	1,4	10,4
400	2009	9	28	0,1	0,1
400	2009	9	29	0,5	

400	2009	9	30	1,4	5,2

Table 20: Temperature and precipitation in September 2009, Sauðanesviti. Northern Iceland.

Station number	Year	Month	Day	Temperature (°C)	Precipitation (mm)
400	2009	10	1	0,4	4,1
400	2009	10	2	-0,1	
400	2009	10	3	0,4	1,7
400	2009	10	4	-1,4	1,7
400	2009	10	5	-0,8	0,1
400	2009	10	6	0,5	
400	2009	10	7	-0,1	0,0
400	2009	10	8	-0,8	
400	2009	10	9	1,9	
400	2009	10	10	3,4	6,8
400	2009	10	11	1,1	0,0
400	2009	10	12	0,1	
400	2009	10	13	1,8	
400	2009	10	14	6,3	
400	2009	10	15	6,9	0,8
400	2009	10	16	8,0	
400	2009	10	17	4,0	10,4
400	2009	10	18	-1,3	28,6
400	2009	10	19	-2,1	0,9
400	2009	10	20	-1,6	0,0
400	2009	10	21	-2,0	
400	2009	10	22	3,7	1,6
400	2009	10	23	1,8	7,9
400	2009	10	24	1,8	5,8
400	2009	10	25	1,9	0,0
400	2009	10	26	1,1	1,0
400	2009	10	27	3,3	
400	2009	10	28	2,9	
400	2009	10	29	5,4	0,0
400	2009	10	30	6,0	
400	2009	10	31	7,0	3,3

Table 21: Temperature and precipitation in October 2009, Sauðanesviti. Northern Iceland.

Akureyri

2007:

Station number	Year	Month	Day	Temperature (°C)	Precipitation (mm)
422	2007	8	1	8,2	7,6
422	2007	8	2	7,0	0,0
422	2007	8	3	3,4	
422	2007	8	4	7,3	1,4
422	2007	8	5	6,8	1,1
422	2007	8	6	8,9	0,1
422	2007	8	7	4,9	
422	2007	8	8	10,7	
422	2007	8	9	9,8	0,9
422	2007	8	10	11,2	0,7
422	2007	8	11	9,2	1,9
422	2007	8	12	8,0	1,4
422	2007	8	13	6,6	2,1
422	2007	8	14	7,1	0,1
422	2007	8	15	6,0	0,1
422	2007	8	16	6,8	
422	2007	8	17	5,1	
422	2007	8	18	8,1	0,3
422	2007	8	19	5,6	0,0
422	2007	8	20	7,6	0,0
422	2007	8	21	10,5	0,0
422	2007	8	22	11,3	5,4
422	2007	8	23	11,1	0,8
422	2007	8	24	8,2	15,9
422	2007	8	25	8,4	0,8
422	2007	8	26	3,8	2,2
422	2007	8	27	2,5	
422	2007	8	28	4,5	
422	2007	8	29	8,3	7,2
422	2007	8	30	8,0	8,1
422	2007	8	31	8,6	0,0

Table 22: Temperature and precipitation in August 2007, Akureyri. Northern Iceland.

Station number	Year	Month	Day	Temperature (°C)	Precipitation (mm)
422	2007	9	1	8,3	0,3
422	2007	9	2	6,0	3,4
422	2007	9	3	2,4	0,0
422	2007	9	4	11,4	1,4

422	2007	9	5	10,2	0,0
422	2007	9	6	8,0	6,0
422	2007	9	7	8,5	2,2
422	2007	9	8	8,2	
422	2007	9	9	8,0	2,2
422	2007	9	10	5,5	0,2
422	2007	9	11	6,0	0,0
422	2007	9	12	3,7	0,1
422	2007	9	13	2,0	18,7
422	2007	9	14	0,8	8,4
422	2007	9	15	-1,0	
422	2007	9	16	1,2	0,1
422	2007	9	17	-1,5	0,6
422	2007	9	18	4,6	
422	2007	9	19	2,5	0,0
422	2007	9	20	4,5	1,8
422	2007	9	21	3,2	2,2
422	2007	9	22	0,6	0,9
422	2007	9	23	4,2	0,6
422	2007	9	24	2,0	6,0
422	2007	9	25	-0,6	0,8
422	2007	9	26	1,0	
422	2007	9	27	11,2	0,0
422	2007	9	28	10,9	
422	2007	9	29	9,3	
422	2007	9	30	5,0	4,5

Table 23: Temperature and precipitation in September 2007, Akureyri. Northern Iceland.

Station number	Year	Month	Day	Temperature (°C)	Precipitation (mm)
422	2007	10	1	3,6	3,4
422	2007	10	2	6,8	0,1
422	2007	10	3	4,1	0,5
422	2007	10	4	8,6	0,0
422	2007	10	5	5,0	0,7
422	2007	10	6	1,9	7,2
422	2007	10	7	-2,1	0,0
422	2007	10	8	-0,2	
422	2007	10	9	-0,7	
422	2007	10	10	1,0	1,9
422	2007	10	11	3,4	30,3
422	2007	10	12	4,8	4,3

422	2007	10	13	8,9	2,7
422	2007	10	14	4,5	0,0
422	2007	10	15	1,1	2,9
422	2007	10	16	-0,8	0,5
422	2007	10	17	-5,0	0,3
422	2007	10	18	-4,7	0,0
422	2007	10	19	11,0	0,4
422	2007	10	20	10,2	
422	2007	10	21	1,9	2,2
422	2007	10	22	1,0	19,2
422	2007	10	23	6,0	3,7
422	2007	10	24	5,2	0,1
422	2007	10	25	6,9	0,0
422	2007	10	26	1,6	0,2
422	2007	10	27	2,1	0,0
422	2007	10	28	-0,4	
422	2007	10	29	-5,0	
422	2007	10	30	-2,4	0,5
422	2007	10	31	-1,4	19,7

Table 24: Temperature and precipitation in August 2007, Akureyri. Northern Iceland.

2008:

Station number	Year	Month	Day	Temperature (°C)	Precipitation (mm)
422	2008	8	1	14,8	
422	2008	8	2	12,6	0,0
422	2008	8	3	11,3	0,0
422	2008	8	4	11,1	
422	2008	8	5	11,2	
422	2008	8	6	10,3	
422	2008	8	7	9,8	
422	2008	8	8	9,8	0,4
422	2008	8	9	10,9	0,0
422	2008	8	10	10,6	
422	2008	8	11	10,7	0,6
422	2008	8	12	9,7	
422	2008	8	13	10,7	
422	2008	8	14	13,0	
422	2008	8	15	14,1	
422	2008	8	16	13,2	
422	2008	8	17	14,8	
422	2008	8	18	12,8	
422	2008	8	19	10,8	0,5

422	2008	8	20	9,8	0,4
422	2008	8	21	11,4	
422	2008	8	22	13,6	
422	2008	8	23	14,2	0,2
422	2008	8	24	10,5	
422	2008	8	25	10,0	0,7
422	2008	8	26	11,6	5,0
422	2008	8	27	10,2	1,2
422	2008	8	28	10,4	0,6
422	2008	8	29	12,5	3,9
422	2008	8	30	10,8	0,0
422	2008	8	31	9,9	0,2

Table 25: Temperature and precipitation in August 2008, Akureyri. Northern Iceland.

Station number	Year	Month	Day	Temperature (°C)	Precipitation (mm)
422	2008	9	1	9,8	1,4
422	2008	9	2	10,8	5,5
422	2008	9	3	8,7	
422	2008	9	4	7,8	
422	2008	9	5	8,9	0,0
422	2008	9	6	10,9	
422	2008	9	7	11,5	
422	2008	9	8	12,0	
422	2008	9	9	10,8	
422	2008	9	10	12,9	0,0
422	2008	9	11	10,5	2,6
422	2008	9	12	12,4	10,5
422	2008	9	13	12,5	0,0
422	2008	9	14	12,4	0,0
422	2008	9	15	12,0	
422	2008	9	16	12,9	
422	2008	9	17	13,8	1,7
422	2008	9	18	9,2	0,5
422	2008	9	19	12,4	0,0
422	2008	9	20	9,5	1,4
422	2008	9	21	7,7	0,0
422	2008	9	22	9,5	2,7
422	2008	9	23	7,3	0,0
422	2008	9	24	11,9	2,3
422	2008	9	25	7,5	0,0
422	2008	9	26	6,2	1,4
422	2008	9	27	6,8	2,9

422	2008	9	28	8,0	0,0
422	2008	9	29	5,3	0,2
422	2008	9	30	2,1	0,2

Table 26: Temperature and precipitation in September 2008, Akureyri. Northern Iceland.

Station number	Year	Month	Day	Temperature (°C)	Precipitation (mm)
422	2008	10	1	1,5	2,8
422	2008	10	2	-1,6	5,5
422	2008	10	3	-2,8	0,3
422	2008	10	4	0,9	6,4
422	2008	10	5	1,8	
422	2008	10	6	6,2	
422	2008	10	7	6,2	0,4
422	2008	10	8	6,3	6,0
422	2008	10	9	3,8	0,0
422	2008	10	10	7,2	1,4
422	2008	10	11	4,4	1,1
422	2008	10	12	3,5	0,1
422	2008	10	13	3,6	0,1
422	2008	10	14	1,7	0,4
422	2008	10	15	0,5	
422	2008	10	16	3,4	0,0
422	2008	10	17	5,5	0,0
422	2008	10	18	0,0	1,9
422	2008	10	19	-1,9	0,0
422	2008	10	20	-0,5	3,5
422	2008	10	21	-1,0	2,6
422	2008	10	22	-4,5	0,0
422	2008	10	23	0,2	25,9
422	2008	10	24	-1,0	0,0
422	2008	10	25	-0,1	5,7
422	2008	10	26	-0,7	18,3
422	2008	10	27	-3,4	0,5
422	2008	10	28	-3,9	3,5
422	2008	10	29	-4,8	0,4
422	2008	10	30	-2,7	
422	2008	10	31	7,8	

Table 27: Temperature and precipitation in October 2008, Akureyri. Northern Iceland.

2009:

Station number	Year	Month	Day	Temperature (°C)	Precipitation (mm)
422	2009	8	1	7,3	0,7
422	2009	8	2	5,6	0,0
422	2009	8	3	9,8	2,5
422	2009	8	4	9,4	0,1
422	2009	8	5	12,0	12,6
422	2009	8	6	13,8	0,1
422	2009	8	7	8,7	
422	2009	8	8	12,2	
422	2009	8	9	9,4	
422	2009	8	10	9,2	0,0
422	2009	8	11	9,1	0,0
422	2009	8	12	10,2	0,5
422	2009	8	13	8,6	1,0
422	2009	8	14	5,1	0,2
422	2009	8	15	8,2	1,2
422	2009	8	16	8,4	3,1
422	2009	8	17	4,1	
422	2009	8	18	6,8	1,1
422	2009	8	19	9,2	0,5
422	2009	8	20	8,6	6,3
422	2009	8	21	5,2	0,3
422	2009	8	22	2,3	0,0
422	2009	8	23	4,4	
422	2009	8	24	9,2	3,0
422	2009	8	25	11,5	5,4
422	2009	8	26	8,3	0,0
422	2009	8	27	8,2	0,0
422	2009	8	28	6,4	1,9
422	2009	8	29	5,5	1,9
422	2009	8	30	5,8	0,0
422	2009	8	31	5,9	0,1

Table 28: Temperature and precipitation in August 2009, Akureyri. Northern Iceland.

Station number	Year	Month	Day	Temperature (°C)	Precipitation (mm)
422	2009	9	1	6,7	1,2
422	2009	9	2	2,7	
422	2009	9	3	5,9	
422	2009	9	4	5,4	
422	2009	9	5	2,1	
422	2009	9	6	4,0	

422	2009	9	7	4,9	0,4
422	2009	9	8	8,4	1,9
422	2009	9	9	5,9	4,4
422	2009	9	10	8,5	0,0
422	2009	9	11	7,7	1,6
422	2009	9	12	9,9	0,0
422	2009	9	13	13,3	
422	2009	9	14	12,9	
422	2009	9	15	9,3	0,0
422	2009	9	16	5,1	0,0
422	2009	9	17	10,3	0,8
422	2009	9	18	7,3	
422	2009	9	19	6,1	2,1
422	2009	9	20	2,0	
422	2009	9	21	6,0	0,3
422	2009	9	22	2,6	0,9
422	2009	9	23	-1,1	0,0
422	2009	9	24	3,6	6,4
422	2009	9	25	3,1	17,4
422	2009	9	26	4,2	0,9
422	2009	9	27	0,6	3,1
422	2009	9	28	-3,6	1,1
422	2009	9	29	-1,9	
422	2009	9	30	1,8	0,2

Table 29: Temperature and precipitation in September 2009, Akureyri. Northern Iceland.

Station number	Year	Month	Day	Temperature (°C)	Precipitation (mm)
422	2009	10	1	-0,9	2,9
422	2009	10	2	-1,2	2,9
422	2009	10	3	-0,4	6,0
422	2009	10	4	-6,6	2,2
422	2009	10	5	-3,2	0,3
422	2009	10	6	-1,3	0,0
422	2009	10	7	-1,1	0,4
422	2009	10	8	-5,1	0,0
422	2009	10	9	-2,2	
422	2009	10	10	3,3	3,3
422	2009	10	11	1,4	3,3
422	2009	10	12	-1,8	0,0
422	2009	10	13	4,2	1,7
422	2009	10	14	5,6	0,0
422	2009	10	15	7,2	0,6

422	2009	10	16	7,3	0,0
422	2009	10	17	5,5	0,0
422	2009	10	18	0,5	14,3
422	2009	10	19	-1,2	0,1
422	2009	10	20	-1,5	
422	2009	10	21	-3,1	0,0
422	2009	10	22	2,1	4,7
422	2009	10	23	2,4	4,2
422	2009	10	24	1,8	0,0
422	2009	10	25	1,4	
422	2009	10	26	-1,9	
422	2009	10	27	-2,2	
422	2009	10	28	-0,6	
422	2009	10	29	1,0	0,8
422	2009	10	30	5,1	0,6
422	2009	10	31	3,5	3,7

Table 30: Temperature and precipitation in October 2009, Akureyri. Northern Iceland.

Torfur

2007:

Station number	Year	Month	Day	Temperature (°C)	Precipitation (mm)
425	2007	8	1	7,2	2,4
425	2007	8	2	6,2	0,0
425	2007	8	3	-1,8	0,0
425	2007	8	4	7,2	0,5
425	2007	8	5	6,7	0,7
425	2007	8	6	7,2	0,0
425	2007	8	7	1,0	
425	2007	8	8	8,1	
425	2007	8	9	8,1	0,5
425	2007	8	10	10,5	0,7
425	2007	8	11	9,4	0,6
425	2007	8	12	7,7	1,0
425	2007	8	13	6,3	0,5
425	2007	8	14	6,2	0,0
425	2007	8	15	5,6	0,0
425	2007	8	16	6,2	
425	2007	8	17	4,7	
425	2007	8	18	5,7	0,1
425	2007	8	19	2,0	
425	2007	8	20	7,2	0,0

425	2007	8	21	10,4	
425	2007	8	22	12,8	8,2
425	2007	8	23	10,7	1,8
425	2007	8	24	7,7	1,6
425	2007	8	25	6,2	0,2
425	2007	8	26	1,5	12,0
425	2007	8	27	-1,5	0,1
425	2007	8	28	-0,8	
425	2007	8	29	7,8	5,6
425	2007	8	30	7,8	11,2
425	2007	8	31	8,5	0,3

Table 31: Temperature and precipitation in August 2007, Torfur. Northern Iceland.

Station number	Year	Month	Day	Temperature (°C)	Precipitation (mm)
425	2007	9	1	8,3	0,5
425	2007	9	2	4,8	0,8
425	2007	9	3	-0,2	
425	2007	9	4	10,0	3,4
425	2007	9	5	11,2	0,0
425	2007	9	6	7,6	4,6
425	2007	9	7	8,0	1,2
425	2007	9	8	11,4	0,0
425	2007	9	9	7,5	6,3
425	2007	9	10	3,6	1,2
425	2007	9	11	6,7	0,2
425	2007	9	12	3,0	0,8
425	2007	9	13	2,6	21,3
425	2007	9	14	-2,8	1,7
425	2007	9	15	-5,4	
425	2007	9	16	1,0	0,0
425	2007	9	17	-3,0	0,1
425	2007	9	18	4,6	0,0
425	2007	9	19	-1,0	
425	2007	9	20	2,1	0,6
425	2007	9	21	2,1	2,6
425	2007	9	22	-1,8	0,0
425	2007	9	23	2,9	2,4
425	2007	9	24	2,2	4,6
425	2007	9	25	-3,5	0,2
425	2007	9	26	-0,8	
425	2007	9	27	6,2	0,0
425	2007	9	28	11,2	

425	2007	9	29	8,7	0,0
425	2007	9	30	5,3	3,0

Table 32: Temperature and precipitation in September 2007, Torfur. Northern Iceland.

Station number	Year	Month	Day	Temperature (°C)	Precipitation (mm)
425	2007	10	1	3,5	5,2
425	2007	10	2	7,1	0,3
425	2007	10	3	3,1	3,9
425	2007	10	4	6,2	
425	2007	10	5	2,5	2,5
425	2007	10	6	1,7	7,7
425	2007	10	7	-5,8	
425	2007	10	8	-3,9	
425	2007	10	9	-4,3	0,0
425	2007	10	10	0,2	4,1
425	2007	10	11	3,4	31,2
425	2007	10	12	3,8	0,0
425	2007	10	13	8,5	0,5
425	2007	10	14	1,3	0,0
425	2007	10	15	1,2	1,4
425	2007	10	16	-0,5	0,1
425	2007	10	17	-7,1	0,0
425	2007	10	18	-6,2	0,1
425	2007	10	19	10,7	0,6
425	2007	10	20	9,4	0,1
425	2007	10	21	0,4	3,8
425	2007	10	22	0,4	12,0
425	2007	10	23	1,3	2,2
425	2007	10	24	4,7	
425	2007	10	25	6,6	0,2
425	2007	10	26	1,5	0,2
425	2007	10	27	1,6	
425	2007	10	28	-2,8	
425	2007	10	29	-8,6	
425	2007	10	30	-3,8	0,4
425	2007	10	31	-1,4	18,3

Table 33: Temperature and precipitation in October 2007, Torfur. Northern Iceland.

2008:

Station number	Year	Month	Day	Temperature (°C)	Precipitation (mm)
425	2008	8	1	14,4	
425	2008	8	2	12,1	
425	2008	8	3	11,2	
425	2008	8	4	11,0	1,0
425	2008	8	5	10,9	
425	2008	8	6	10,0	
425	2008	8	7	9,7	
425	2008	8	8	9,9	0,0
425	2008	8	9	10,9	
425	2008	8	10	9,9	0,0
425	2008	8	11	10,2	0,0
425	2008	8	12	7,9	0,0
425	2008	8	13	10,5	0,0
425	2008	8	14	12,6	
425	2008	8	15	13,4	0,0
425	2008	8	16	13,9	
425	2008	8	17	14,9	
425	2008	8	18	12,9	
425	2008	8	19	10,2	0,0
425	2008	8	20	8,7	0,0
425	2008	8	21	13,1	
425	2008	8	22	12,9	0,2
425	2008	8	23	13,4	0,9
425	2008	8	24	10,0	0,2
425	2008	8	25	8,4	4,3
425	2008	8	26	11,1	11,0
425	2008	8	27	9,7	0,8
425	2008	8	28	9,3	
425	2008	8	29	12,2	1,8
425	2008	8	30	8,0	
425	2008	8	31	8,9	0,3

Table 34: Temperature and precipitation in August 2008, Torfur. Northern Iceland.

Station number	Year	Month	Day	Temperature (°C)	Precipitation (mm)
425	2008	9	1	9,7	1,4
425	2008	9	2	10,4	1,8
425	2008	9	3	6,6	
425	2008	9	4	5,7	
425	2008	9	5	8,8	
425	2008	9	6	11,3	

425	2008	9	7	11,8	
425	2008	9	8	10,7	
425	2008	9	9	9,6	
425	2008	9	10	13,9	
425	2008	9	11	10,4	2,6
425	2008	9	12	11,3	8,7
425	2008	9	13	11,1	
425	2008	9	14	12,4	
425	2008	9	15	12,4	0,1
425	2008	9	16	13,5	
425	2008	9	17	13,3	1,1
425	2008	9	18	9,2	0,3
425	2008	9	19	11,8	0,3
425	2008	9	20	8,3	1,8
425	2008	9	21	7,8	0,0
425	2008	9	22	9,5	1,9
425	2008	9	23	7,0	1,7
425	2008	9	24	11,9	5,5
425	2008	9	25	4,7	0,0
425	2008	9	26	6,2	3,9
425	2008	9	27	6,5	1,8
425	2008	9	28	7,5	0,2
425	2008	9	29	4,9	0,3
425	2008	9	30	1,4	0,1

Table 35: Temperature and precipitation in September 2008, Torfur. Northern Iceland.

Station number	Year	Month	Day	Temperature (°C)	Precipitation (mm)
425	2008	10	1	1,2	0,5
425	2008	10	2	-3,3	2,1
425	2008	10	3	-6,9	
425	2008	10	4	-1,1	1,4
425	2008	10	5	3,8	
425	2008	10	6	6,3	
425	2008	10	7	5,1	1,9
425	2008	10	8	5,7	3,0
425	2008	10	9	1,6	
425	2008	10	10	6,5	2,5
425	2008	10	11	3,3	1,1
425	2008	10	12	1,5	
425	2008	10	13	2,7	0,1
425	2008	10	14	-1,4	0,2
425	2008	10	15	-1,7	0,0

425	2008	10	16	4,8	0,1
425	2008	10	17	5,9	0,2
425	2008	10	18	-2,3	0,1
425	2008	10	19	-2,0	
425	2008	10	20	0,1	0,0
425	2008	10	21	-3,5	0,1
425	2008	10	22	-9,7	
425	2008	10	23	0,6	7,5
425	2008	10	24	-3,4	0,0
425	2008	10	25	-1,2	0,7
425	2008	10	26	-0,5	2,7
425	2008	10	27	-4,4	0,3
425	2008	10	28	-3,7	0,4
425	2008	10	29	-10,0	0,2
425	2008	10	30	-8,5	
425	2008	10	31	9,1	

Table 36: Temperature and precipitation in October 2008, Torfur. Northern Iceland.

2009:

Station number	Year	Month	Day	Temperature (°C)	Precipitation (mm)
425	2009	8	1	7,1	0,5
425	2009	8	2	3,5	0,2
425	2009	8	3	9,5	2,8
425	2009	8	4	9,2	0,5
425	2009	8	5	11,8	2,0
425	2009	8	6	13,5	0,1
425	2009	8	7	5,1	
425	2009	8	8	11,5	
425	2009	8	9	9,0	
425	2009	8	10	9,0	4,3
425	2009	8	11	9,5	1,1
425	2009	8	12	9,2	0,2
425	2009	8	13	7,2	2,3
425	2009	8	14	1,2	0,3
425	2009	8	15	3,5	0,7
425	2009	8	16	7,2	0,0
425	2009	8	17	1,5	0,0
425	2009	8	18	4,8	1,5
425	2009	8	19	8,5	0,2
425	2009	8	20	9,8	2,4
425	2009	8	21	4,8	0,1
425	2009	8	22	-2,5	0,3

425	2009	8	23	1,0	0,0
425	2009	8	24	9,2	10,8
425	2009	8	25	11,4	1,9
425	2009	8	26	4,2	0,1
425	2009	8	27	8,2	
425	2009	8	28	6,6	0,8
425	2009	8	29	5,6	0,2
425	2009	8	30	5,8	
425	2009	8	31	5,5	0,1

Table 37: Temperature and precipitation in August 2009, Torfur. Northern Iceland.

Station number	Year	Month	Day	Temperature (°C)	Precipitation (mm)
425	2009	9	1	6,7	0,3
425	2009	9	2	1,1	
425	2009	9	3	4,5	
425	2009	9	4	1,1	
425	2009	9	5	-2,8	
425	2009	9	6	0,7	
425	2009	9	7	1,7	4,8
425	2009	9	8	2,7	1,1
425	2009	9	9	2,0	1,0
425	2009	9	10	8,5	0,1
425	2009	9	11	7,8	4,4
425	2009	9	12	9,8	1,8
425	2009	9	13	13,3	
425	2009	9	14	12,7	
425	2009	9	15	8,7	0,0
425	2009	9	16	6,0	
425	2009	9	17	10,9	0,0
425	2009	9	18	5,2	
425	2009	9	19	4,7	1,5
425	2009	9	20	-2,0	0,4
425	2009	9	21	4,2	1,3
425	2009	9	22	2,4	1,6
425	2009	9	23	-3,0	
425	2009	9	24	3,6	8,7
425	2009	9	25	3,3	22,2
425	2009	9	26	2,6	2,9
425	2009	9	27	1,6	1,5
425	2009	9	28	-7,5	1,6
425	2009	9	29	-4,9	
425	2009	9	30	1,2	0,5

Table 38: Temperature and precipitation in September 2009, Torfur. Northern Iceland.

Station number	Year	Month	Day	Temperature (°C)	Precipitation (mm)
425	2009	10	1	-2,3	0,4
425	2009	10	2	-2,8	4,4
425	2009	10	3	-0,8	4,5
425	2009	10	4	-11,8	0,5
425	2009	10	5	-4,6	0,4
425	2009	10	6	-3,3	
425	2009	10	7	-2,5	0,3
425	2009	10	8	-7,5	0,0
425	2009	10	9	-3,8	0,0
425	2009	10	10	2,4	13,0
425	2009	10	11	0,1	3,7
425	2009	10	12	-3,8	0,0
425	2009	10	13	0,6	7,8
425	2009	10	14	4,7	
425	2009	10	15	6,2	0,4
425	2009	10	16	6,2	0,0
425	2009	10	17	5,2	
425	2009	10	18	0,1	12,9
425	2009	10	19	-1,8	0,0
425	2009	10	20	-2,3	
425	2009	10	21	-4,7	0,1
425	2009	10	22	1,3	2,9
425	2009	10	23	1,4	2,3
425	2009	10	24	-0,7	
425	2009	10	25	-0,5	0,3
425	2009	10	26	-2,7	
425	2009	10	27	-5,8	
425	2009	10	28	-6,0	0,0
425	2009	10	29	-1,1	3,1
425	2009	10	30	2,5	0,4
425	2009	10	31	1,3	4,1

Table 39: Temperature and precipitation in October 2009, Torfur. Northern Iceland.

Precipitation and temperature, Tafjord, western Norway

Tafjord

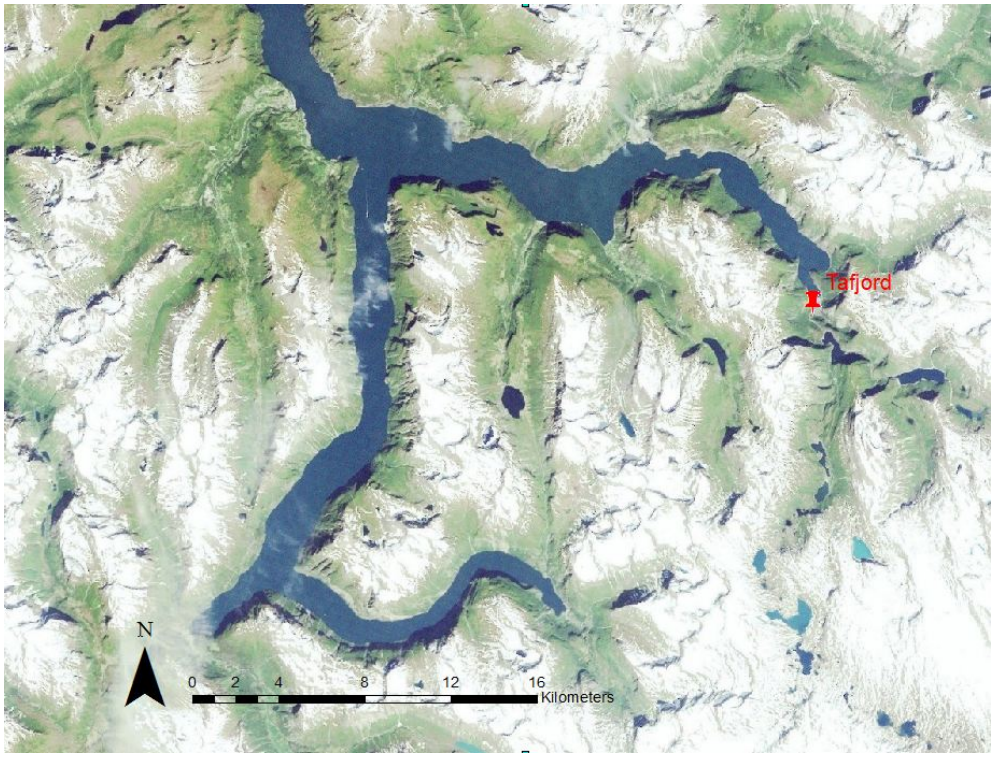

Figure 3: Location of the weather station in Tafjord, western Norway. Norge i Bilder background image, downloaded 25.09.2012.

2007:

Station number	Year	Month	Day	Temperature (°C)	Precipitation (mm)
60500	2007	9	1	6,7	
60500	2007	9	2	11,3	1,1
60500	2007	9	3	5,6	9,1
60500	2007	9	4	9,1	32,2
60500	2007	9	5	11,6	2,1
60500	2007	9	6	11,6	
60500	2007	9	7	11,7	18,9
60500	2007	9	8	11,1	19,5
60500	2007	9	9	10,4	15,2
60500	2007	9	10	10,2	9,2
60500	2007	9	11	11	2,2
60500	2007	9	12	9,6	3,4
60500	2007	9	13	8,8	2,7
60500	2007	9	14	12,6	
60500	2007	9	15	6,2	28,4

60500	2007	9	16	10,2	8,6
60500	2007	9	17	6,9	5,4
60500	2007	9	18	5,5	19,7
60500	2007	9	19	8,3	0,9
60500	2007	9	20	10,6	0,2
60500	2007	9	21	9,7	6,6
60500	2007	9	22	9,8	5,3
60500	2007	9	23	13,5	
60500	2007	9	24	16,1	0,5
60500	2007	9	25	15,4	1,2
60500	2007	9	26	8,7	7,8
60500	2007	9	27	5,4	4,2
60500	2007	9	28	5,4	
60500	2007	9	29	10,2	
60500	2007	9	30	12,1	

Table 40: Temperature and precipitation in September 2007, Tafjord, western Norway.

2008:

Station number	Year	Month	Day	Temperature (°C)	Precipitation (mm)
60500	2008	9	1	18,4	0,4
60500	2008	9	2	14,1	
60500	2008	9	3	11,1	12,4
60500	2008	9	4	11,7	11,3
60500	2008	9	5	11,2	4
60500	2008	9	6	9,6	0,6
60500	2008	9	7	9,9	
60500	2008	9	8	11,4	
60500	2008	9	9	15,9	
60500	2008	9	10	16,4	
60500	2008	9	11	17,5	
60500	2008	9	12	17	
60500	2008	9	13	14	
60500	2008	9	14	11,9	
60500	2008	9	15	11,5	
60500	2008	9	16	10,6	
60500	2008	9	17	9,9	
60500	2008	9	18	13	
60500	2008	9	19	11,6	0,5
60500	2008	9	20	10,9	1

60500	2008	9	21	13	
60500	2008	9	22	12,2	0,3
60500	2008	9	23	10,3	3,1
60500	2008	9	24	8,5	
60500	2008	9	25	8,1	
60500	2008	9	26	11,5	0,1
60500	2008	9	27	13,5	0,2
60500	2008	9	28	7,2	34,5
60500	2008	9	29	7,2	1,2
60500	2008	9	30	7,9	

Table 41: Temperature and precipitation in September 2008, Tafjord, western Norway.

2009:

Station number	Year	Month	Day	Temperature (°C)	Precipitation (mm)
60500	2009	9	1	16,3	2,5
60500	2009	9	2	13,3	10,6
60500	2009	9	3	13,3	0,2
60500	2009	9	4	11,8	0
60500	2009	9	5	12,1	6,1
60500	2009	9	6	10,1	0,1
60500	2009	9	7	13,8	0,2
60500	2009	9	8	14,7	1,3
60500	2009	9	9	14,5	3,1
60500	2009	9	10	12,3	0,3
60500	2009	9	11	11,4	0,2
60500	2009	9	12	10,9	13,4
60500	2009	9	13	11,6	18,8
60500	2009	9	14	9,1	
60500	2009	9	15	10,1	
60500	2009	9	16	9,9	3
60500	2009	9	17	9,4	7,1
60500	2009	9	18	12,2	4,1
60500	2009	9	19	11,7	
60500	2009	9	20	12,7	0,3
60500	2009	9	21	12,6	
60500	2009	9	22	15	1,4
60500	2009	9	23	9	5,4
60500	2009	9	24	9,3	11,4
60500	2009	9	25	13,3	4,5

60500	2009	9	26	16,2	0,7
60500	2009	9	27	10,9	1,1
60500	2009	9	28	5,4	14,8
60500	2009	9	29	4,6	33,4
60500	2009	9	30	5,7	13,7

Table 42: Temperature and precipitation in September 2009, Tafjord, western Norway.